Thèse de doctorat

Pour l'obtention du titre de

DOCTEUR EN PHYSIQUE

délivré par

CY Cergy Paris Université

École doctorale n°405 : Économie, Management, Mathématiques, Physique et Sciences Informatiques (EM2PSI).

Décoder la complexité des oscillations neuronales

---

par

Ferdinand Tixidre

préparée au Laboratoire de Physique Théorique et Modélisation (LPTM, UMR 8089)

présentée et soutenue publiquement le 4 décembre 2025.

Directeur de thèse: Alessandro Torcini

Co-directeur de thèse: Gianluigi Mongillo

Jury :

Prof. Mathias Quoy	CY Cergy Paris Université	Président du jury
Prof. Srdjan Ostojic	École Normale Supérieure	Rapporteur
Prof. Magnus J.E. Richardson	University of Warwick	Rapporteur
Dr. Simona Olmi	Istituto dei Sistemi Complessi	Examinateur
Prof. Alessandro Torcini	CY Cergy Paris Université	Examinateur

CERGY PARIS UNIVERSITÉ

Labex MME-DII
Modèles Mathématiques et Économiques de la Dynamique, de l'Incertitude et des Interactions

LPTM
laboratoire de physique théorique et modélisation

"Just when things looked their worse, they changed for the best. I have marveled often at the thin line that divides success from failure and the sudden turn that leads from apparently certain disaster to comparative safety."
— Ernest Shackleton

Préface

En premier lieu mes remerciements s'adressent à mon directeur de thèse Alessandro Torcini, que j'ai rencontré lors de ma première année de Master au cours d'un projet sur le modèle de Kuramoto. Ce projet m'a fait découvrir les phénomènes de synchronisation, un sujet qui m'a immédiatement captivé. Notre collaboration s'est poursuivie au-delà de ce projet et quand l'opportunité de continuer en doctorat s'est présentée, sa personnalité sympathique et bienveillante a largement participé à ma décision. Au cours des années il est devenu plus qu'un simple directeur de thèse, je garderai en mémoire les moments passés ensemble au laboratoire et en dehors, entre Prato et Cergy. Pour ses conseils, son soutien et son dévouement je tiens à exprimer toute ma gratitude.

Je tiens ensuite à remercier Gianluigi Mongillo, qui a co-dirigé cette thèse. Son expertise et sa rigueur scientifique ont été déterminantes dans ce projet, chaque échange aura été l'occasion d'apprendre et de progresser. Pour son temps, son engagement et la confiance qu'il m'a accordée je souhaite le remercier chaleureusement.

Je souhaite aussi remercier tous les collaborateurs avec lesquels j'ai eu la chance de travailler. Parmi eux Rainer Engelken se distingue par sa pédagogie et ses conseils avisés en matière de simulation numérique. Mes co-auteurs Denis Goldobin, Maria Ageeva et Matteo di Volo pour leur participation précieuse sur l'article publié ensemble. Alejandro Carballosa, quant à lui, a su créer un pont entre les approches physiques d'Alessandro Torcini et Gianluigi Mongillo, et les aspects biologiques portés par Alberto Bacci, que je remercie pour son accueil à l'Institut du Cerveau.

Cette thèse a également été marquée par des rencontres enrichissantes: Simona Olmi que je remercie pour m'avoir donné l'opportunité de présenter mes travaux au cours d'un atelier, et pour les soirées passées avec Alessandro à Prato. Mais aussi Serhiy Yanchuk et Magnus Richardson qui m'ont gentiment ouvert la porte de leurs bureaux pour des discussions scientifiques très intéressantes. Je salue aussi toutes les personnes que j'ai pu rencontrer lors de différentes conférences à travers le monde.

Un remerciement particulier va à tous les membres du jury, Mathias Quoy, Alessandro Torcini et Simona Olmi, et tout particulièrement les rapporteurs Srdjan Ostojic et Magnus Richardson, pour avoir accepté d'évaluer ce travail.

Ce projet a bénéficié d'un financement intégral par le Labex MME-DII (Grant No. ANR-11-LBX-0023-01). Des financements de la part de SLOWBRain et CY Generations (Grant No ANR-21-EXES-0008) ont également soutenu ce projet. Une partie de ces recherches a été menée à l'Istituto dei Sistemi Complessi (CNR) à Sesto Fiorentino en Italie, que je remercie pour l'accueil offert en 2023, 2024 et 2025.

Au LPTM, ma reconnaissance va d'abord à Guy Trambly de Laissardière qui a été mon premier contact à CYU Cergy Paris Université, dont la bienveillance lors de mon entretien d'admission en Master avait marqué un contraste bienvenue avec le processus administratif d'autres universités. Je salue aussi le directeur du LPTM, Jean Avan, pour la dynamique positive et l'ambiance de travail agréable qu'il a insuflées au laboratoire.

Je veux aussi remercier tous mes collègues doctorants au LPTM, pour les discussions et moments passés ensemble. En particulier Maxime Lucas et Jawad Allam avec qui j'ai partagé un bureau pendant trois années. Leur bonne humeur a rendu ces années encore plus agréables.

Enfin je souhaite remercier tout mon entourage: ma partenaire Gabrielle, ma famille et mes amis, en particulier Lucas, Josselin, Corentin, Amélie, Matthieu et Lucie pour leur soutien continu qui m'a permis de continuer en dépit des difficultés.

Ferdinand Tixidre
Pontoise, Octobre 2026

À ma mère.

Contents

Preface ii

Introduction 1

1 Elements of neuronal systems 4
- 1.1 Neurons in brief . . . 4
- 1.2 Membrane potential . . . 5
  - 1.2.1 Resting potential . . . 6
  - 1.2.2 Membrane capacity . . . 7
  - 1.2.3 Membrane resistance . . . 8
- 1.3 The membrane as an electrical circuit . . . 8
- 1.4 Action potential . . . 11
- 1.5 Synapses and signal transmission . . . 12
  - 1.5.1 Chemical synapses . . . 12
  - 1.5.2 Electrical synapses . . . 13
  - 1.5.3 Neurotransmitters and receptors . . . 15

2 Spiking neuron models 17
- 2.1 Introduction . . . 17
- 2.2 Leaky integrate-and-Fire model. . . . 17
  - 2.2.1 Limitations of the LIF model . . . 19
- 2.3 Nonlinear Integrate-and-Fire models . . . 20
  - 2.3.1 Stability of the fixed points . . . 21
  - 2.3.2 Excitability types . . . 21
  - 2.3.3 Exponential Integrate-and-Fire . . . 22
  - 2.3.4 Quadratic Integrate-and-Fire . . . 24
- 2.4 Neural networks. . . . 29
  - 2.4.1 Modeling synaptic currents . . . 29

3 Balanced spiking neural networks 30
- 3.1 Irregular, asynchronous spike trains in the cortex . . . 30
- 3.2 The balanced network . . . 32
  - 3.2.1 Static balance . . . 32
  - 3.2.2 Dynamical balance. . . . 33
- 3.3 Experimental confirmations . . . 37
- 3.4 Balance with weak currents . . . 38

4 Numerical study in partially symmetric networks of spiking neurons 39
- 4.1 Introduction . . . 39
- 4.2 Methods . . . 41
  - 4.2.1 The network model . . . 41
  - 4.2.2 Observables . . . 44
- 4.3 Results . . . 46
- 4.4 Discussion . . . 54

5 Synaptic shot noise triggers fast and slow global oscillations in balanced neural networks **57**
5.1 Introduction . . . 57
5.2 Model and methods . . . 59
5.2.1 The network model . . . 59
5.2.2 Simulation protocols . . . 60
5.2.3 Indicators . . . 60
5.3 Mean-field description . . . 62
5.3.1 Derivation of the macroscopic evolution equations . . . 64
5.3.2 Diffusion and third-order approximations . . . 67
5.3.3 Linear stability of the asynchronous regime . . . 68
5.3.4 Weakly nonlinear analysis . . . 70
5.4 Network Simulations . . . 73
5.4.1 Finite-size characterization of the observed transitions . . . 74
5.4.2 Frequency range of the global oscillations . . . 77
5.4.3 Two different types of GOs . . . 78
5.5 Summary and Discussion . . . 82

Conclusion **86**

Appendices **89**

A Non-ergodic dynamics in quadratic integrate-and-fire networks **90**
A.1 Model and methods . . . 90
A.1.1 Event-driven simulations of the QIF network . . . 90
A.1.2 Overlap observables . . . 91
A.2 Results . . . 91
A.2.1 Homogeneous network and synaptic weights . . . 92
A.2.2 Erdős-Rényi network and homogeneous weights . . . 95
A.2.3 Erdős-Rényi network with heterogeneous synaptic weights . . . 100
A.3 Summary . . . 101

B Methods and additional analysis for chapter 5 **102**
B.1 Integration of the Langevin equations . . . 102
B.2 Integration of the continuity and Fokker-Planck equations . . . 102
B.2.1 Time-splitting pseudo-spectral method . . . 103
B.3 Synaptic Filtering . . . 105
B.4 Complete mean field approach for excitatory-inhibitory networks . . . 105
B.5 Biological Relevance . . . 106

References **108**

List of Figures **119**

Introduction

The science of complex systems is a relatively recent field of research that studies how individual elements interact to produce collective behaviour that are more than the sum of their parts. It is an interdisciplinary field with applications in physics, biology, economics, sociology, and many other areas [1]. Complex systems can be natural or artificial, living or inanimate, they can even be composed of other complex systems.

Think of a flock of birds, each bird has many properties (size, age, needs...) and interacts with many other birds. Yet, the flock moves as a whole, changing direction in a coordinated manner. This collective behaviour emerges from simple rules followed by each bird, such as aligning with neighbours, avoiding collisions, and staying close to other birds of the flock. Complexity can emerge from simplicity.

The precise nature of the interaction between the elements is often irrelevant to understand the collective behaviour. For example, the internet is a complex system made up of millions of devices that communicate with each other through a network of cables and wireless connections. The precise nature of the communication protocol is not important to understand the large-scale structure of the internet, which can be described as a network of nodes and edges. Such abstraction is what allows us to build mathematical models that reveal the fundamental organising principles of complex systems.

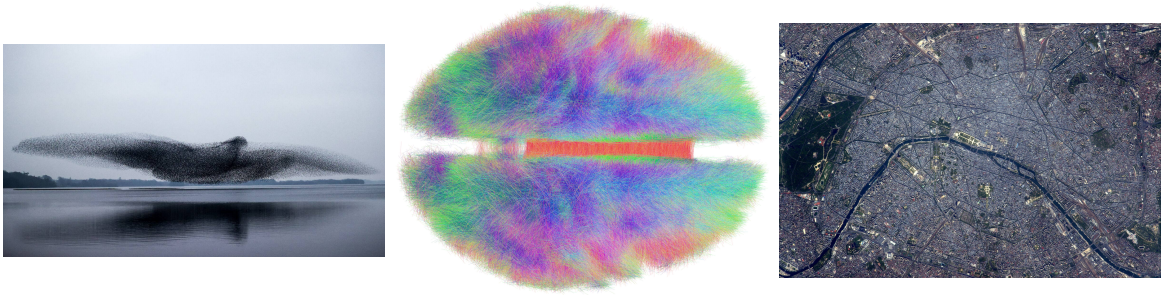

Figure 1: Left: the murmuration of starlings over Lough Ennell. Credit: James Crombie. Middle: group-averaged structural connectome reconstructed from 20 human brains. White-matter fiber pathways are shown with colors indicating their direction (x, y, z directions mapped to red, green, and blue). Credit: Andreas Horn. Right: the city of Paris as a complex system: a dynamic network of people, infrastructures, institutions, and interactions that together give rise to emergent social, economic, and spatial patterns. Credit: Thomas Pesquet.

The human brain is one of the most, if not the most, complex system that we know of. It is made up of approximately 10^{11} neurons, each of them connected to about 10^4 other neurons [2, 3, 4]. The resulting number of connections is monumental: there are more connections in a cubic centimeter of human brain tissue than there are stars in the Milky Way galaxy. Neurons communicate with each other through electrical impulses called action potentials or spikes. The collective activity of neurons gives rise to various brain functions, including perception, cognition, memory, and motor control. Understanding how these functions emerge from simple neuronal interactions is a major challenge in neuroscience and has important implications for medicine, psychology, and artificial intelligence.

A central puzzle of cortical physiology is the nature of its in vivo dynamics. Recordings from

awake animals reveal that cortical activity is highly irregular: single neurons fire with irregular, seemingly stochastic spike trains [5, 6], population activity fluctuates strongly, and yet these dynamics remain stable and robust over time. Moreover, the cortex exhibits a rich dynamical repertoire from asynchronous irregular states to oscillations spanning multiple frequency bands, which are thought to underlie information processing and communication between brain regions. Explaining how such complex dynamics emerge from the interactions of large populations of simple neurons is a fundamental theoretical problem.

A key conceptual advance in addressing this problem was the balanced network theory proposed by van Vreeswijk and Sompolinsky in the 1990s [7, 8]. They showed that large recurrent networks with strong but dynamically balanced excitation and inhibition naturally generate asynchronous irregular activity similar to that observed in vivo. In these networks, fluctuations in synaptic input persist even as the network size grows, and neuronal variability arises as a collective property of the circuit rather than from external noise. This framework has since become a cornerstone of theoretical neuroscience, providing a powerful explanation of cortical-like dynamics in terms of simple connectivity statistics and scaling principles.

The dynamical balance theory reproduces many aspects of cortical dynamics, however it does not capture all of them. In particular, the presence of long relaxation times [9, 10, 11] cannot be accounted by such a theory without the introduction of additional mechanisms. Furthermore, the emergence of oscillations in the γ frequency band (30-100 Hz) in the cat visual cortex and rat hippocampus due to an ensemble of inhibitory neurons sharing few connections [12, 13, 14] cannot be explained by the classical balanced network theory.

The work presented in this thesis builds on and extends this theoretical framework in two complementary directions. First, we explore how structural features of the network, in particular, partial symmetry in the synaptic connectivity, affect the dynamics. We show that partial symmetry can lead to long-lived fluctuations and signatures of ergodicity breaking. Second, we develop a *complete* mean-field theory of balanced networks that goes beyond the traditional diffusion approximation. By incorporating the discrete, non-Gaussian nature of synaptic input, we derive a new theoretical description capable of capturing dynamical regimes, such as oscillations and multistability, that are inaccessible to classical approaches, corresponding to the so-called diffusion approximation [15].

This thesis is structured as follows: **Chapter 1** introduces the fundamental biological and physical properties of neurons. We will review the mechanisms of action potential generation and propagation, the role of synapses in neuronal communication, and how these processes can be modelled mathematically. In **Chapter 2**, we present simplified spiking neuron models. From the Leaky integrate-and-Fire (LIF) to more biologically realistic nonlinear extensions such as the Exponential integrate-and-fire (EIF) and Quadratic integrate-and-fire (QIF). **Chapter 3** introduces the theoretical framework of balanced networks. We begin with the experimental observations that motivated this theory and then review the chronological development of balanced network models, from classical mean-field approaches to recent extension relaxing key assumption such as the strong external current. In **Chapter 4**, we investigate how topological features of the network, specifically, symmetry in the synaptic connectivity, can alter the dynamics of the network. We demonstrate that even partially symmetric network can give rise to long-lived temporal correlations and signatures of ergodicity breaking. These results reveal a simple and robust mechanism that leads to long-lived fluctuations in the network, providing insights into how structural properties may shape the temporal organisation of cortical activity. Finally, in **Chapter 5**, we address a limitation of classical diffusion approximations that neglect the the discrete nature of synaptic input. We develop a complete mean-field (CMF)

theory for balanced QIF network receiving Poisson synaptic shot noise. This framework predicts the emergence of global oscillations trough sub- and supercritical Hopf bifurcations, identifies regions of coexistence between asynchronous and oscillatory states, and reveals two distinct mechanisms of oscillation generation. The CMF reproduces network simulations with remarkable accuracy, where the classical diffusion approximation fails.

1

Elements of neuronal systems

Summary In this chapter we introduce the fundamental biological concepts on which mathematical models are based. We do not aim to provide a complete biological understanding of the neuron's functioning, therefore we will not detail every biological mechanism in full complexity. Yet these building blocks are general enough to form the basis of accurate neuronal models. We start with an overview of the neuron morphology. We then develop how nerve cells generate and transmit electrical signals. Building on this we introduce a biophysical model of the neuronal membrane represented as an RC circuit. Finally we turn to the mechanisms of neuronal communication, showing how neurons interact with each other through synaptic connections.

1.1. Neurons in brief

Neurons are specialized cells that act as the main information messenger in the nervous system. They transmit electrical signals, i.e. information, using electrical and chemical mechanisms. Experiments have shown variations between 62 and 94 billion neurons in the human brain [3, 2]. They come in many different shapes and sizes as shown in the founding work of neurobiology by Ramón y Cajal [16] whose remarkable illustrations are still relevant today; for a recent review see [17]. Despite their enormous variety neurons have common morphological features.

- *The soma*, or *cell body*, is a compact, almost spherical, structure which contains the nucleus of the cell.
- *The dendrites* collect information from other neurons and bring it to the soma. There are receptors on dendrites designed to pick up signals from other neurons that often come in the form of chemicals called neurotransmitters.
- *The axons* is a long tubular structure, connected to the cell body. Information is carried along the axons, as it propagates electrical activity from one region of the neuron to another, eventually passing it to other neurons. They can be covered by an insulating sheath called myelin, which increase the speed and efficiency of electrical signal transmission [18]. At the end of its structure the axon gives rise to small branches.
- *The synapses* are located at the terminal region of the axon branches. Synapses are junctions between neurons, allowing information to be transferred. We will see more about the synapses in Sec. 1.5.

A peculiarity of neurons is that they are polarised cells, meaning that different regions have

distinct biological functions. Information is carried from the soma to the synapse along the axon and passed to the next neuron via the dendritic tree. As signals flows one way only we have upstream neurons and downstream neurons. Because neurons are bridged by synapses, we speak of *presynaptic* and *postsynaptic* neurons. On Fig. 1.1 (A), the postsynaptic teal coloured neuron gets activated as a result of a release of neurotransmitter substance from the presynaptic orange neuron. Neurons can receive synaptic inputs from many other neurons, similarly they can make contacts with potentially thousands of other neurons. We can understand the potential complexity of the networks they form, see Fig. 1.1 (B) for a visualisation. Figure 1.1 (A) shows the orange neuron receiving inputs from three others (the green, red and blue neurons). Note that this orange neuron was presynaptic to the teal neuron but is also a postsynaptic neuron to the green, red and blue neurons.

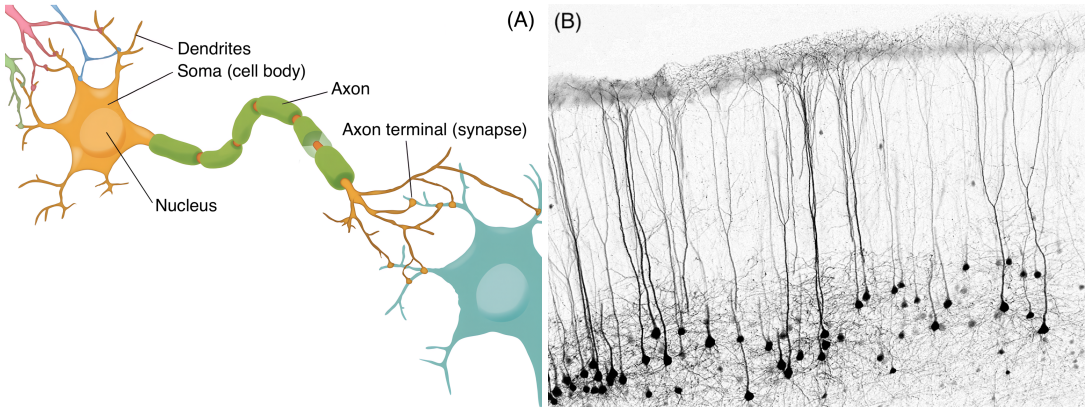

Figure 1.1: (A) Typical representation of a neuron Taken from [19]. Green cylinders around the axon represented the myelin sheath. In different colours we see pre- and postsynaptic neurons of the orange neuron. Taken from [19]. (B) Pyramidal neurons of the prefrontal cortex are sparsely labeled with a fluorescent protein to visualize their morphology. Joseph Zak, Lab of Venkatesh Murthy, Harvard University

1.2. Membrane potential

We have mentioned that neurons send electrical signals but we have not explained the origins of these electrical signals. The cell membrane is made of an electrical insulator separating two electrically conducting fluids: the cytoplasm (intracellular) and the extracellular fluid. However, the membrane also has a lot of channels on its surface which enable ions to pass through. Ions flow induce a change in the voltage across the membrane. This voltage change is the electrical signal at the basis of neuronal communication. The most common ions are sodium ions (Na^+), potassium ions (K^+), chloride ions (Cl^-) and calcium ions (Ca^{2+}). Negatively charged ions such as chloride are called anions while positively charged ions such has sodium, potassium and calcium are called cations.

Because the membrane blocks charged particles and water, the intracellular fluid can have a different composition than the extracellular fluid. In particular, their concentrations of ions are different: when a neuron is at rest, there is a higher concentration of potassium inside the cell than outside while there is more sodium and chloride outside the cell compared to inside, see Fig. 1.2. The movement of charged particles is only possible thanks to proteins embedded in the membrane, these proteins are in contact with both the interior and exterior of the cell. They can be *active*, in which case they are sometimes called *transporters*, or *passive*, in that case they are called *channels*. Channels are simply a pore through the membrane that allows specific ions to flow passively, down their electrochemical gradient; for that reason they are very fast. Channels can be open all the time (leak channel) or be opened by some trigger

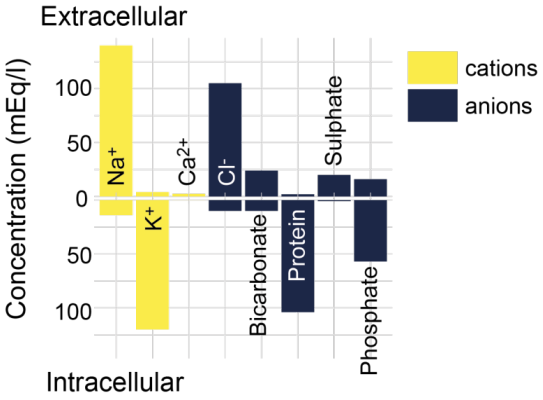

Figure 1.2: Constituents of extra- and intracellular fluids for a resting neuron, in milliequivalents per liter. Taken from [20].

such as voltage changes (voltage-gated ion channels) or binding of molecules (ligand-gated ion channels). Transporters, however, use an external energy source (for example: adenosine triphosphate, ATP) to move ions against their electrochemical gradient. For example the sodium-potassium pump is a transport protein that can exchange three intracellular sodium ions for two extracellular potassium ions, at the cost of one ATP molecule. Pumping more cations out than in helps to keep the membrane potential negative; this process alone is a significant part of the nervous system's total energy needs.

1.2.1. Resting potential

If we penetrate this membrane with an electrode, as done by Hodgkin and Huxley in 1939 [21], we notice an electrical potential across it. Most of the time this difference between the intracellular and extracellular potentials is negative.

$$V_m(t) = V_i(t) - V_e(t)$$

The existence of a steady potential difference across this membrane was first reported by Bernstein in 1902 [22]. We call it the rest potential V_{rest}, despite its name it is a state of dynamic equilibrium.

When the neuron is at rest potassium leak channels are open. Because the concentration of potassium is higher inside than outside the cell, potassium ions tend to diffuse out. As these positively charged ions leave, a charge imbalance develops: the inside of the cell becomes more negatively compared to the outside. This difference in charge eventually grows strong enough that the outward diffusion of potassium is opposed, since the positively charged potassium ions are repelled by the accumulating positive charge outside the cell. Eventually the electrical and chemical gradients will balance, the membrane potential that is reached at this thermodynamic equilibrium is called the equilibrium potential for K^+. At this point there is no net flow of potassium ions.

If the membrane was only permeable to potassium ions, the membrane rest potential V_{rest} would be equal to the potassium equilibrium potential V_K. In reality the situation is more complicated because the membrane has many different ions channels which can open and close. Other ions follow a similar logic and each have an equilibrium potential. The equilibrium potential of any given ion, V_{eq} can be calculated using the Nernst equation:

$$V_{eq} = \frac{k_B T}{q} \ln\left(\frac{[X]_e}{[X]_i}\right),$$

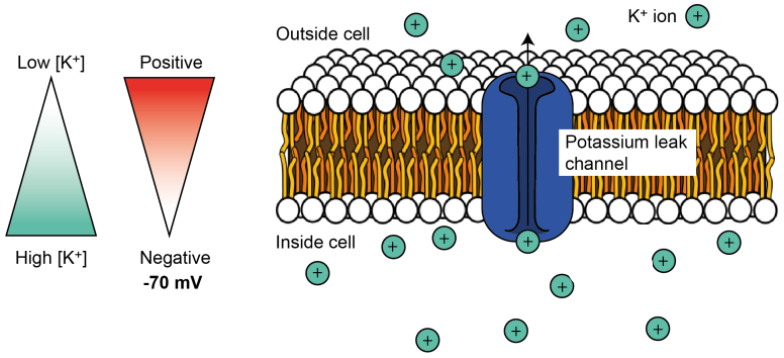

Figure 1.3: The density of potassium ion is higher inside the cell than outside, this chemical gradient tends to make ions cross the membrane via specific leak channels. As theses positively charged particles move out, an electrical gradients builds up. Eventually the two processes balance out. Taken from [20].

Where k_B is the Boltzmann constant, T is the temperature in Kelvin and q is the ion charge in coulomb. Typically we these values are $V_{K^+} = -75$ mV, $V_{Na^+} = +55$ mV, $V_{Ca^{2+}} = 145$ mV and $V_{Cl^-} = -66$ mV.

But not all ions are equal, the membrane is most permeable to potassium ions, so the rest potential of the membrane is close to the equilibrium potential of potassium. The Goldman-Hodgkin-Katz equation gives the membrane potential given the permeability p to different ions and their concentrations:

$$V_m = \frac{k_B T}{q} \ln\left(\frac{p_K[\mathrm{K}^+]_e + p_{Na}[\mathrm{Na}^+]_e + p_{Cl}[\mathrm{Cl}^-]_i}{p_K[\mathrm{K}^+]_i + p_{Na}[\mathrm{Na}^+]_i + p_{Cl}[\mathrm{Cl}^-]_e}\right).$$

In squids, $p_K = 1$, $p_{Na} = 0.03$ and $p_{Cl} = 0.1$, which gives $V_{rest} = -70$ mv. In agreements with the famous experiments of Hodgkin and Huxley in 1939 [21]. In humans, the resting potential is typically around -65 to -70 mV.

1.2.2. Membrane capacity

As we have said before, the plasma membrane of the cell is an electrical insulator. It is made of two lipid layers of phospholipid molecules which have a hydrophilic head and two hydrophobic tails. The tails will mix together while the heads will align themselves facing the intracellular and extracellular fluids, mostly composed of water; see Fig. 1.4. This thin insulator separating two conducting fluids effectively creates a capacitor which accumulates charge Q. The capacitance C measures how much charge needs to be accumulated on the membrane for a potential V_m to develop. These three quantities are linked together by the following relation:

$$Q = C \cdot V_m \,. \tag{1.1}$$

In practice, one often refers to the membrane capacitance C_m, defined as the capacitance per unit area of membrane, with typical values ranging from 0.7 to 1 μF/cm^2. For illustration, a spherical cell of 5 μm radius with a resting potential of -70 mV and a membrane capacitance of 1 μF/cm^2, would hold a charge of about 0.22×10^{-12} coulombs, on each side of the membrane with opposite polarity.

When the membrane voltage changes, the membrane must either take on extra charge or release charge. This movement of charge is the capacitive current; it is simply the time differential of Eq. (1.1):

$$I_C = C \cdot \frac{dV_m(t)}{dt} \,. \tag{1.2}$$

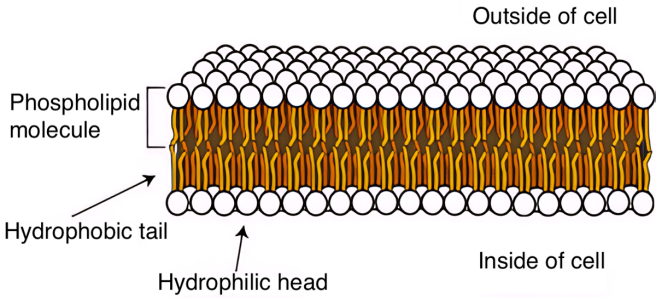

Figure 1.4: The two layers of phospholipid molecules making up the cell membrane, typically the membrane is 30–50 Åthick. Taken from [20].

1.2.3. Membrane resistance

It is only thanks to channels embedded in the membrane that ions are able to cross it. These conductive pathways give the membrane a finite resistance, permitting a passive *leak* of ions. As for the capacitance, the resistance is usually referred to as the membrane resistance R_m, expressed as a resistance times unit area ($\Omega \cdot \text{cm}^2$). Sometimes the inverse of the membrane resistance, the leak conductance $G_m = 1/R_m$, is used, expressed in siemens per square centimetre (S/cm^2).

1.3. The membrane as an electrical circuit

We now have three elements: an electrically insulating membrane that separates and stores charges on both its sides, ion channels that allow current to leak across the membrane, and resting potential resulting from ionic concentration gradients across the membrane. These elements can be modelled by simple electrical components: the membrane acts as a capacitor, the ion channels as a resistor, and the resting potential as a battery. Together they form an RC circuit, illustrated in Fig. 1.5. Let us consider a simple circuit with one ion channel.

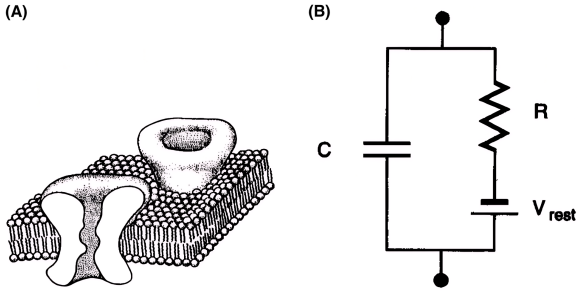

Figure 1.5: (A) An illustration of the neuronal membrane. The lipid bilayer, which width ranges around 30–50 Åelectrically isolates the cell. Ionic channels, embedded in the membrane act as gates, letting charged particles cross. (B) The electrical circuit modelling the membrane. The membrane acts as a capacitor, the channels can be modelled by a resistance and the resting potential of the cell as a battery. Taken from [23].

If we inject a current $I(t)$ of positive charges in the system, an imbalance appears, as adding a positive charge on one side will effectively kick out another on the other side. These charge movements create a current across the capacitor, I_C, given by Eq.(1.2). The current going through the resistor can be evaluated using Ohm's law,

$$I_R = \frac{V_m - V_{rest}}{R} \tag{1.3}$$

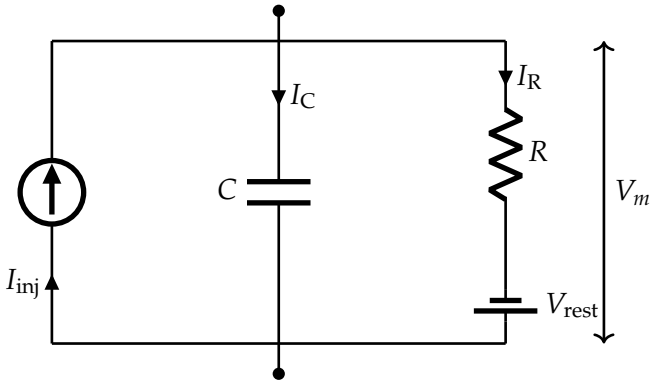

Figure 1.6: RC circuit modeling a passive membrane with injected current.

The current injected *inward* with the electrode is balanced by the sum of the *outward* membrane currents. By convention, a positive membrane current corresponds to positive charge leaving the cell, which *hyperpolarises* the membrane; on the contrary, a negative membrane current corresponds to inward positive charge, which *depolarises* the membrane. However, electrode currents are defined in the opposite way: a positive electrode current is inward, depolarising the cell, while a negative electrode current is outward, hyperpolarising it. From Kirchhoff's law we find that the total input current is $I(t) = I_C + I_R$. Using Eq. (1.2) and Eq. (1.3) we get the following expression:

$$I(t) = C\frac{dV_m(t)}{dt} + \frac{V_m(t) - V_{rest}}{R}\,. \tag{1.4}$$

The capacitance C is measured in farads ($\mathrm{kg}^{-1} \cdot \mathrm{m}^{-2} \cdot \mathrm{s}^4 \cdot \mathrm{A}^2$) and the resistance R in ohms ($\mathrm{kg} \cdot \mathrm{m}^2 \cdot \mathrm{s}^{-3} \cdot \mathrm{A}^{-2}$). Therefore the product RC defines a characteristic time of the neuron, τ. This characteristic time τ, called the *membrane time constant*, determines how quickly the membrane respond to stimulations. A small τ means a "fast" neuron which will quickly "forget" about past inputs, while a large τ allows the neuron to integrate inputs over longer periods. Typically it is around $\tau \simeq 10$–20 ms. We can multiply both sides of Eq. (1.4) by R and insert τ, we rearrange and obtain the following form:

$$\boxed{\tau\,\frac{dV_m(t)}{dt} = -V_m(t) + V_{rest} + R\,I(t)\,.} \tag{1.5}$$

This linear differential equation is called the equation of a passive membrane, it is the basic model of a single neuron. Suppose that, at time $t = 0$ the membrane potential has value $V_m(t = 0) = V_{rest}$, therefore we also have $dV_m/dt = 0$, which means that without input, once the system is at rest it stays there. Now, let us inject a step current of amplitude I_0 at time $t = 0$, we can integrate Eq. (1.5) and get the following equation:

$$V_m(t) = V_{rest} + R\,I_0\left(1 - e^{-t/\tau}\right)\,. \tag{1.6}$$

This equation describes how the membrane potential deviates from its resting state as an exponential function of time. If the current is sustained for long enough the membrane potential reaches a steady state, we define its asymptotic value as $V_\infty = V_{rest} + R\,I_0$. We illustrate this behaviour in Fig 1.7. The left panel shows the effect of step currents of varying amplitude on the membrane potential. As we can see, while the current can change instantaneously, the membrane potential takes time to adjust. As explained in the previous section, the speed of the membrane potential's response to inputs is determined by the product of the membrane

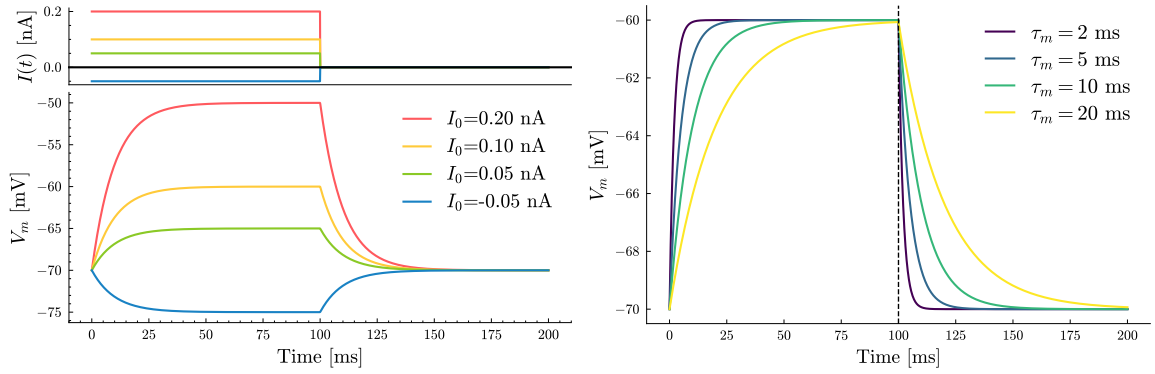

Figure 1.7: Time course of the membrane potential when a step current is applied. We turn on the current at $t = 0$ and turn it off at $t = 100$ ms. The left panel shows the current above and the membrane potential below. Different colours represent different values of the current $I(t)$. On the right side we see the rise and fall of the membrane potential when the current is turn on and off. Different colours represent different values of the membrane time constant τ_m.

resistance and capacitance. The right panel shows the effect of τ on the rise and decay of V_m when the current is turned on and off.

An intuitive property of this simple RC circuit is that it behaves as a low-pass filter: as we have seen, the voltage reaches its peak some time after the stimulus itself peaks. Imagine a stimulus that changes repeatedly, faster than the membrane reacts, the voltage would never manages to reach the peak it would attain if the stimulus remained stable long enough. Rapid current fluctuations are smoothed out, while slow inputs accumulate into significant voltage changes. This is shown on the left panel of Fig. 1.8 with a sinusoidal input current. We can also observe that the membrane potential lags behind the input current. The delay is a consequence of the membrane capacitance charging and discharging slower than the input rate of change, resulting in a phase shift that increases with input frequency and membrane time constant, as shown in Fig. 1.8 (C).

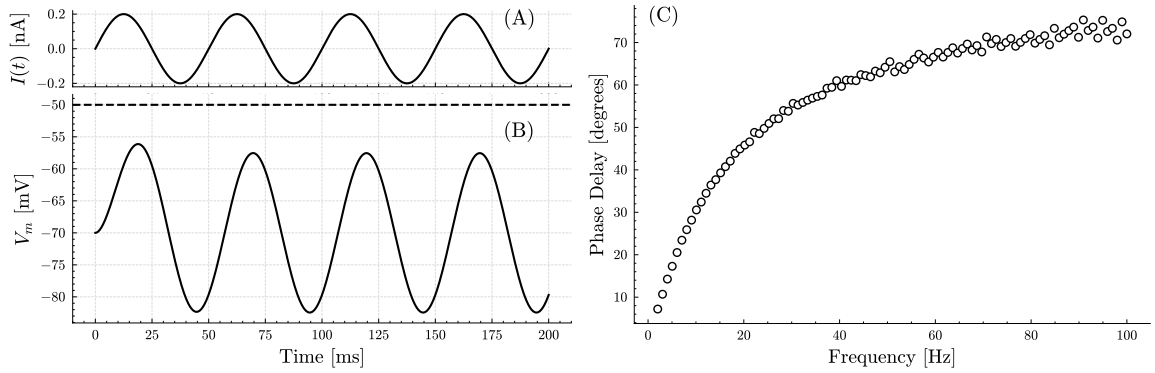

Figure 1.8: Low-pass filtering property of the RC membrane circuit. (A) Sinusoidal input current with frequency $f = 20$ Hz. (B) The resulting membrane potential, $V_m(t)$. The dashed line denote the steady state potential V_∞. (C) The phase delay in degrees as a function of the input frequency. $I_0 = 0.20$ nA, $R = 100$ MΩ, $V_{rest} = -70$ mV and $\tau = 10$ ms.

We denoted the membrane potential by $V_m(t)$ when discussing the equivalent electrical circuit. In what follows, we drop the subscript and simply write $V(t)$, since no other voltages are considered. Thus, unless otherwise stated, V always denotes the membrane potential of the neuron.

1.4. Action potential

The neuronal membrane can respond to a depolarising input current in two different ways. If the amplitude of the pulse is not large enough the membrane potential will rise slightly and come back to its resting state. This is shown in Fig. 1.9 as "Failed initiations". However if the stimulus is strong enough that the membrane potential reaches a specific threshold, it will induce an action potential. Action potential, or *spikes*, are the elementary unit of information that neurons exchange. They consist of a quick depolarisation and repolarisation, followed by a hyperpolarisation phase, before returning to the resting state potential [24]. They typically last 1-2 ms and have an amplitude of 100-120 mV. Figure 1.9 shows the time course of an action potential.

During repolarisation the neuron is in its absolute refractory period. The period where the neuron cannot fire another action potential no matter how strongly it is stimulated. This prevent emitting another spike too quickly and prevents action potential from travelling backwards, along the axon. For a brief period the membrane potential is hyperpolarised, it's more negative than the resting potential. During hyperpolarisation the neuron *could* fire again, but it would take a larger than usual stimulus to reach threshold. This is called the relative refractory period [23].

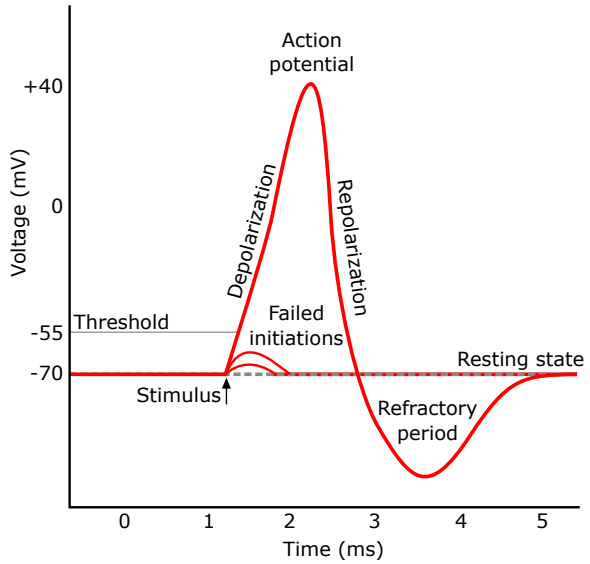

Figure 1.9: Representation of a typical action potential showing its various phases. The membrane potential starts out at approximately -70 mV at time zero. A stimulus is applied at time = 1 ms, which raises the membrane potential above -55 mV (the threshold potential). After the stimulus is applied, the membrane potential rapidly rises to a peak potential of +40 mV at time = 2 ms. Just as quickly, the potential then drops below the resting state potential to -90 mV at time = 3 ms, and finally the resting potential of -70 mV is re-established at time = 5 ms.

The amplitude of the action potential of a given neuron does not change. An action potential does not get bigger with a bigger stimulus. It either happens or it does not happen. Because they are roughly identical, we can conclude that the shape of the action potential carries no information. What can change is the frequency of firing, therefore only the time of spiking can be used to encode information.

1.5. Synapses and signal transmission

So far we have described neurons as single elements capable of generating action potentials; in a biological context, the importance of a spike lies not in its generation within a single neuron but in its ability to influence the activity of other neurons. This interaction occurs at synapses, specialized junctions that allow neurons to communicate with one another, estimates place the number of synapses in the human brain on the order of 100 trillion [25]. Synapses transform discrete stereotyped events of presynaptic spikes into graded changes in the postsynaptic membrane potential. They constitute the essential link between single-neuron excitability and the collective dynamics of neural circuits. We can distinguish two types of synapses: electrical and chemical synapses. They differ in their mechanisms of transmission, speed, and functional role in networks. In the following sections, we will briefly describe them.

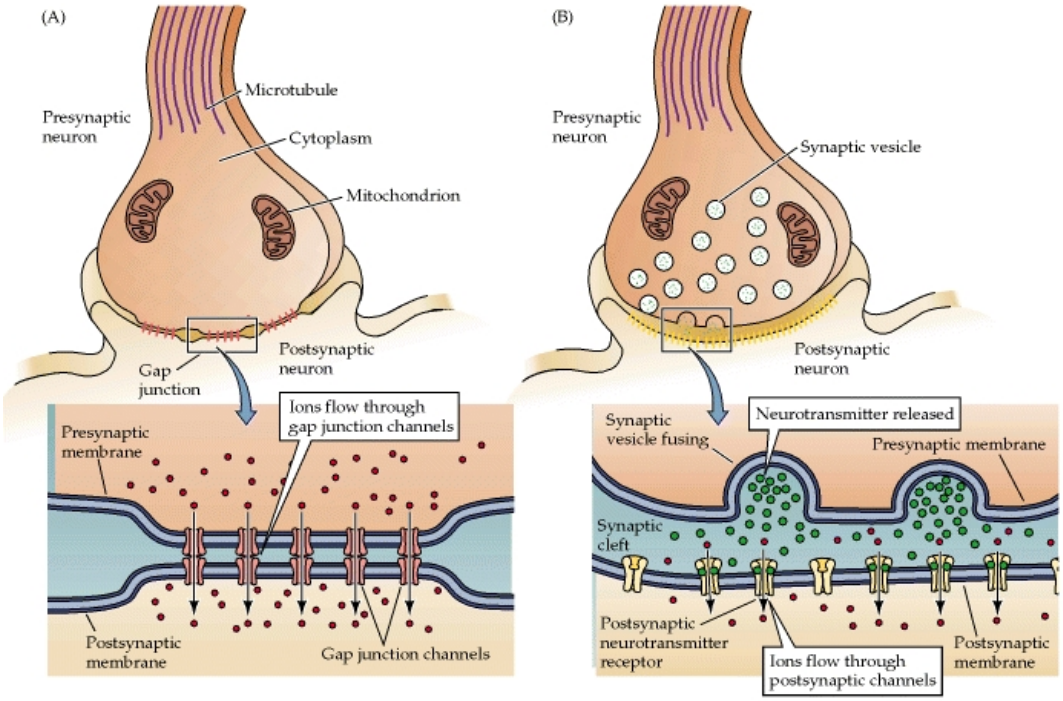

Figure 1.10: (A) Electrical synapses allow a continuous transmission of ions through gap junctions from one cell to the next. (B) Chemical synapses are separated by the synaptic cleft. The presynaptic neuron releases neurotransmitters, which open or close ion channels in the postsynaptic membrane. The movement of ions then generates a synaptic current through the postsynaptic neuron. Taken from [26].

1.5.1. Chemical synapses

The vast majority of synapses in the mammalian brain are chemical [27]. Here, transmission is mediated by the release of neurotransmitters from presynaptic vesicles in response to an incoming action potential. The arrival of the spike opens voltage-gated calcium channels, triggering vesicle fusion and neurotransmitter release into the synaptic cleft, a narrow extracellular space of about 20–40 nm. Neurotransmitter molecules then diffuse across the cleft and bind to receptors on the postsynaptic membrane, opening ion channels that generate a postsynaptic current, see the entire process in Fig 1.11. This series of events introduce a synaptic delay of up to 1–2 ms [28, 29]. Unlike electrical synapses, chemical synapses are typically unidirectional with distinct features found in the *pre-* and *post*synaptic parts. They also offer greater functional diversity, as the type of neurotransmitter and receptor determines whether the postsynaptic

response is excitatory or inhibitory, fast or slow, transient or sustained.

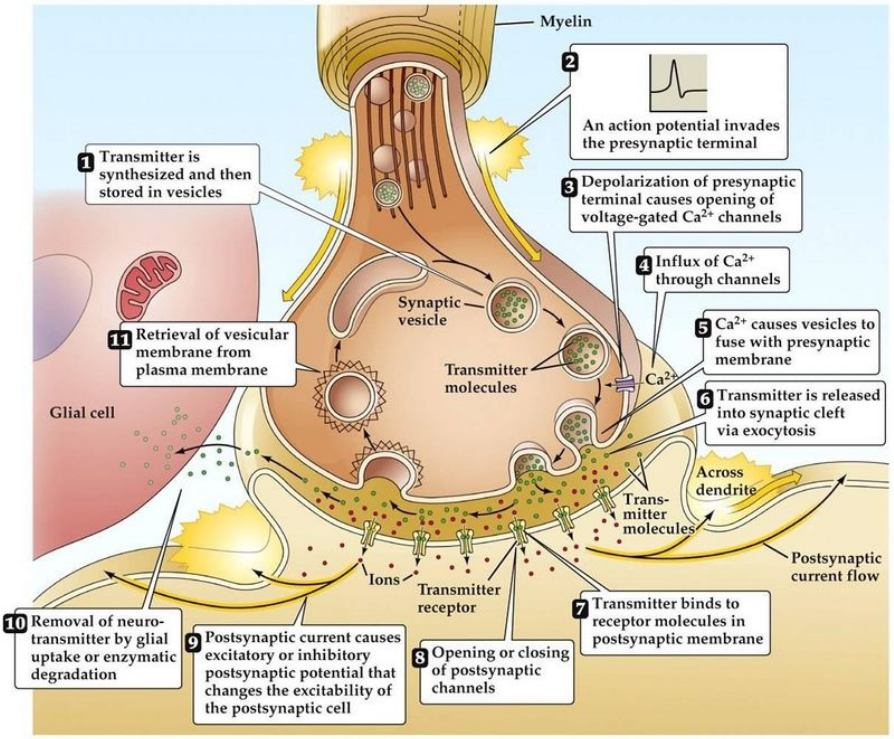

Figure 1.11: Chronological description of the different events allowing the transmission of electrical signals via a chemical synapse. Taken from [26]

1.5.2. Electrical synapses

Illustrated in Fig 1.10(A), electrical synapses provide a direct ionic coupling between neurons, allowing current to pass directly from one neuron to the other. The source of the current is the potential difference created locally by an action potential. Transmission occurs at *gap junctions*, regions where the membranes of the two neurons are particularly close to each other (~ 3.5 nm, against ~ 20 nm for other cells). Gap junctions contain specialized channels, called connexons, which let ions flow. Though they are a minority in the brain, electrical synapses have some significant advantages. Electrical synapses are extremely fast, the flux of the passive current through connexons is almost instantaneous, this was first identified by Furshpan and Potter in the synapses of the crayfish [30]. They report a postsynaptic signal only 0.12 ± 0.01 ms after the presynaptic neuron had emitted an action potential, see Fig. 1.12.

Another advantage of electrical synapses is that current can flow bidirectionally through the gap junction channels, allowing subthreshold voltage fluctuations to spread rapidly between neurons. This allows electrical synapses to synchronise the activity of a neuronal population, see Fig. 1.13. In the neocortex, it was shown that low-threshold-spiking interneurons can become synchronized through electrical synapses alone [31]. Even when chemical synapses and action potentials were blocked, these cells still displayed correlated oscillations. When electrical coupling was blocked, synchrony disappeared, showing that gap junctions are essential for this effect. The synchronized interneurons then produced rhythmic inhibition in nearby excitatory and inhibitory cells, spreading the synchrony to the local network. Electrical synapses also play an important synchronizing role in other parts of the brain such as the thalamus of the hippocampus. From a physical point of view, a gap junction can be modeled as a resistor

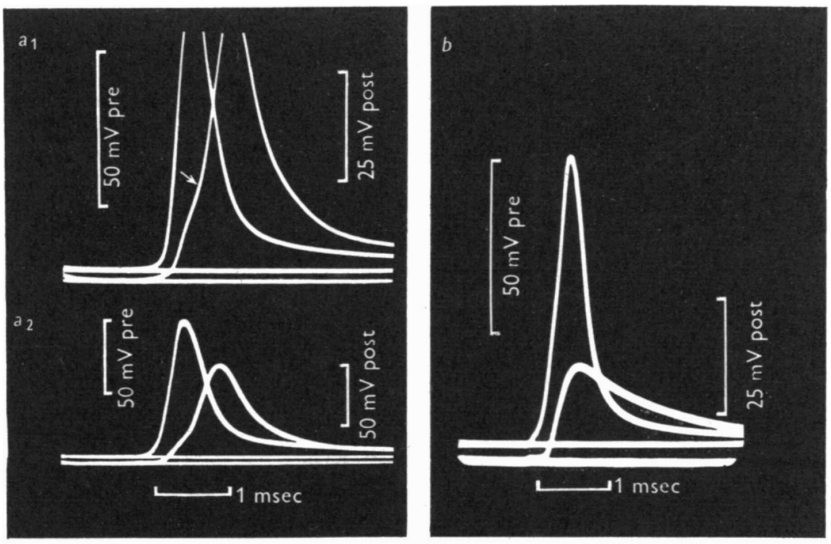

Figure 1.12: Transmission at the crayfish giant motor synapse. Simultaneous intracellular recordings from the presynaptic lateral giant axon (upper trace) and the postsynaptic motor giant axon (lower trace). (a) One-to-one transmission: the presynaptic spike evokes a postsynaptic potential that reaches threshold and triggers a postsynaptic action potential. The arrow indicates the point where the postsynaptic potential crosses threshold and triggers a postsynaptic spike (a_1) and (a_2) were recorded from the same synapse at different amplifications. (b) Subthreshold cases in which the presynaptic spike evokes a fast depolarisation in the postsynaptic axon without triggering a spike. Taken from [30]

connecting two RC circuits (the neuronal membranes). Such a system behaves as a low-pass filter: slow voltage changes, corresponding to low frequencies, charge and discharge the membrane and are transmitted efficiently, whereas rapid spikes are strongly attenuated. This explains why gap junctions are so effective at transmitting and synchronizing subthreshold oscillations [32, 33].

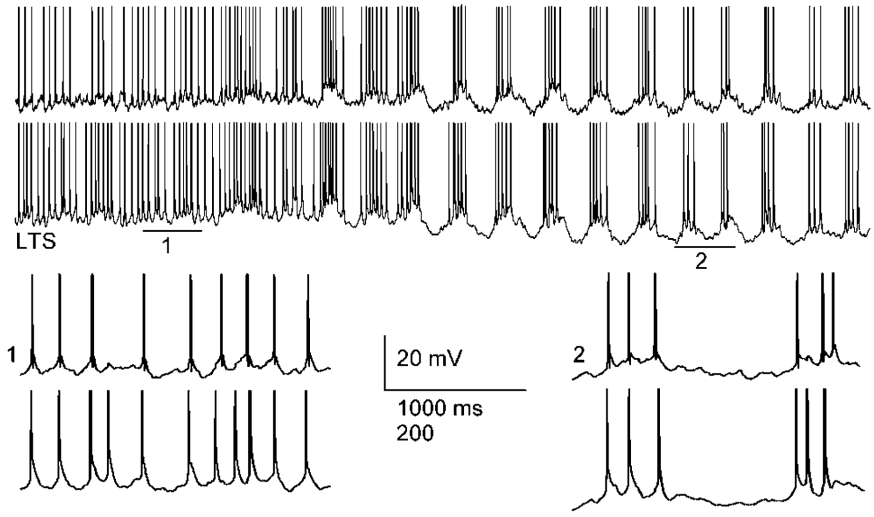

Figure 1.13: A pair of electrically coupled low-threshold-spiking neurons. An action potential in one cell often triggers a synchronized spike in the other cell. The periods marked 1 and 2 on top traces are expanded in time in the lower traces. Taken from [31].

1.5.3. Neurotransmitters and receptors

The idea of electrical signals transmitted via a chemical process was subject to debate at the beginning of the 20th century. The decisive breakthrough came with Otto Loewi's classic frog heart experiments, which demonstrated that vagus nerve stimulation released a chemical substance, later identified as acetylcholine, that could slow the heartbeat. This discovery provided the first clear evidence of chemical neurotransmission. Today, hundreds of neurotransmitters have been identified. Different neurotransmitters mean different responses, a neuron can, for example, be inhibited by one substance and excited by another. The speed of responses triggered by neurotransmitters also varies, allowing for a variety of timescales in the electrical activity.

Ultimately, the mechanism is the same for all chemical synapses: the neurotransmitter, binding to the receptor, modifies the postsynaptic conductance by opening (conductance increases) or closing (conductance decreases) channels through the membrane. This variation of conductance produces a postsynaptic current (PSC), which in turn, modifies the postsynaptic membrane potential (PSP). This variation in the membrane potential modifies the likelihood of the cell emitting an action potential. A PSP that increases the chances of firing of a neuron is called *excitatory* (EPSP); in contrast, a PSP that reduces the chances of firing is called *inhibitory* (IPSP). Because each PSP is usually small in amplitude, the combined effect of many inputs determines whether a neuron reaches the threshold. Postsynaptic potentials can add up over time if several signals arrive in quick succession at the same synapse, a process called temporal summation, see Fig 1.14. Through this interplay, excitatory and inhibitory inputs are continuously integrated, shaping the overall probability of generating an action potential.

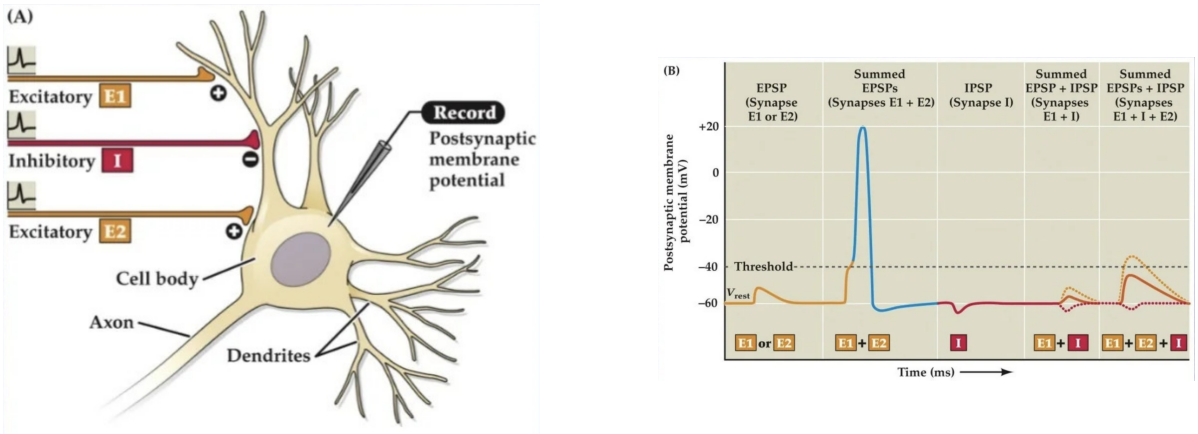

Figure 1.14: Summation of postsynaptic potentials. (A) A neuron receives inputs from excitatory (E_1 and E_2) and inhibitory (I) synapses. An electrode records the membrane postential of the postsynaptic neuron. (B) Effect of different input combinations on the postsynaptic membrane potential. Taken from [26].

Excitatory neurotransmitters Most excitatory communication relies on glutamate, acting primarily through AMPA (α-Amino-3-hydroxy-5-methyl-4-isoxazolepropionic acid) and NMDA (N-methyl-D-aspartate) receptors. AMPA-mediated excitatory postsynaptic currents (EPSCs) are very rapid, appearing and decaying within just a few milliseconds [34, 35, 36]; they provide the main component of fast synaptic excitation. NMDA-mediated EPSCs are slower, particularly in their decay, and can persist for hundreds of milliseconds [34, 37], thus contributing to longer-lasting integration of inputs. The time courses of AMPA- and NMDA-receptor mediated EPSCs are shown in Fig. 1.15.

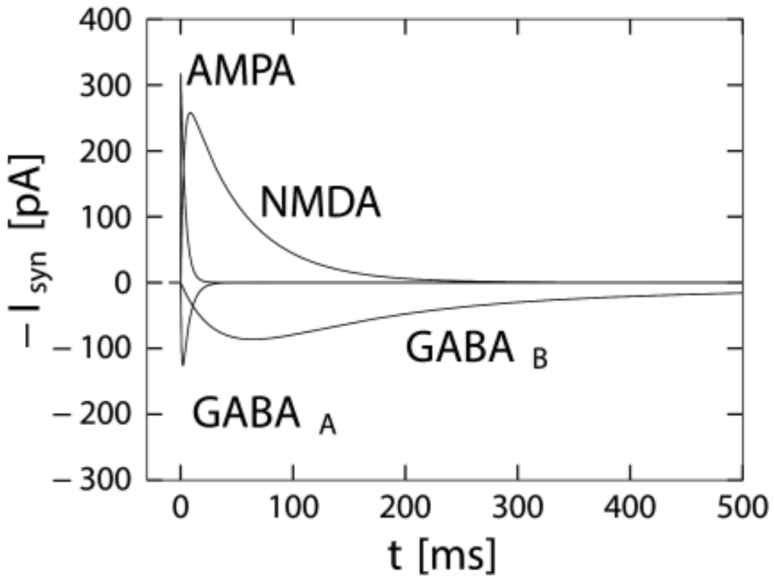

Figure 1.15: Time course of postsynaptic current following a presynaptic spike at time $t = 0$. Typical time constants: AMPA: $\tau_{rise} \simeq 0.2$–1 ms, $\tau_{decay} \simeq 2$–5 ms; NMDA: $\tau_{rise} \simeq 3$–5 ms, $\tau_{decay} \simeq 50$–200 ms. GABA$_A$: $\tau_{rise} \simeq 1$–2, $\tau_{decay} \simeq 5$–10 ms. GABA$_B$: $\tau_{rise} \simeq 50$–150, $\tau_{decay} \simeq 300$–1000 ms. Taken from [38].

Inhibitory neurotransmitters The main inhibitory neurotransmitter in the brain is γ-aminobutyric acid, also called GABA. It interacts with two types of receptors: GABA$_A$ and GABA$_B$ receptors. GABA$_A$ receptors are ionotropic, when GABA binds to the GABA$_A$ receptor, it causes the opening of an associated channel, permeable only to ion chloride. These negatively charged ions hyperpolarise the membrane potential of the neuron and make it less likely to fire an action potential. This is a fast process, typically the induced IPSC rises in 1–2 ms and decays within 5–10 ms [39]. GABA$_B$ receptors are metabotropic, they don't form an ion channel themselves, instead they trigger a cascade of chemical signals ultimately resulting in the opening of potassium channels, which let positively charged ions flow out of the cell, hyperpolarising it. GABA$_B$ receptors have a much slower kinetics than GABA$_A$, the rise time of associated currents varies around 50 ms and the decay last hundreds of milliseconds [40]. See Fig. 1.15. By providing inhibition over this extended time window, GABAergic input suppresses excessive activity and coordinates the timing of excitatory signals [41].

Beyond glutamate and GABA, the nervous system also employs a wide variety of neurotransmitters, including neuromodulators such as dopamine, serotonin, and acetylcholine. These typically act on slower timescales and regulate neuronal excitability and network states rather than mediating fast synaptic transmission. In this chapter, however, we focus on the fast excitatory and inhibitory mechanisms provided by glutamatergic and GABAergic synapses, as they form the core of most computational models of neural circuits.

2

Spiking neuron models

Summary In this chapter we introduce three standard integrate-and-fire models, starting with the simple leaky integrate-and-fire. We then study non-linear models, specifically, the quadratic and the exponential integrate-and-fire models. These widely used models are analytically tractable and simple to simulate despite their simplicity they can reproduce many features of real neurons [38, 42, 43, 44]. We will explore the single neuron dynamics and how we can use them for network models.

2.1. Introduction

At the beginning of the 20th century, the understanding of how neurons function was still in its early days. The work of Santiago Ramón y Cajal had recently established the neuronal theory, confirming that the nervous system is composed of independent cells called neurons, but the precise mechanisms of excitability and nerve transmission remained to be elucidated. Neurophysiology, initiated by Galvani's research on electricity in tissues, sought to understand how electrical signals were generated and propagated in nerve cells. It is in this context that Louis Lapicque published a fundamental article in 1907, proposing a model of neuronal activity based on electrical analogy: he described the membrane of excitable cells as an equivalent electrical circuit and introduced the concept of discharge threshold [45]. Lapicque thus formalized the idea that the neuron sums linearly the signals received, and that a response is produced only if the membrane reaches a certain threshold of electrical charge. This model is now know as the leaky integrate-and-fire neuron and we will present it in details in section 2.2.

2.2. Leaky integrate-and-Fire model.

Integrate-and-fire models simplify neuronal dynamics as an integration process coupled with a reset mechanism [46].

We have covered the integration part, now, let us go through the other fundamental element, which is the firing of action potentials (APs). From Eq. 1.6 and Fig. 1.7 it is easy to see that given enough time the membrane potential approaches an asymptotic value $\lim_{t\to\infty} V(t) = V_{rest} + RI$. If the membrane potential V reaches a threshold value V_{th}, the neuron *fires* an action potential and is immediately reset to a resting value. The moment of where the threshold is crossed is the firing time t_f. The temporal sequence of action potentials generated by a neuron is called its *spike train*.

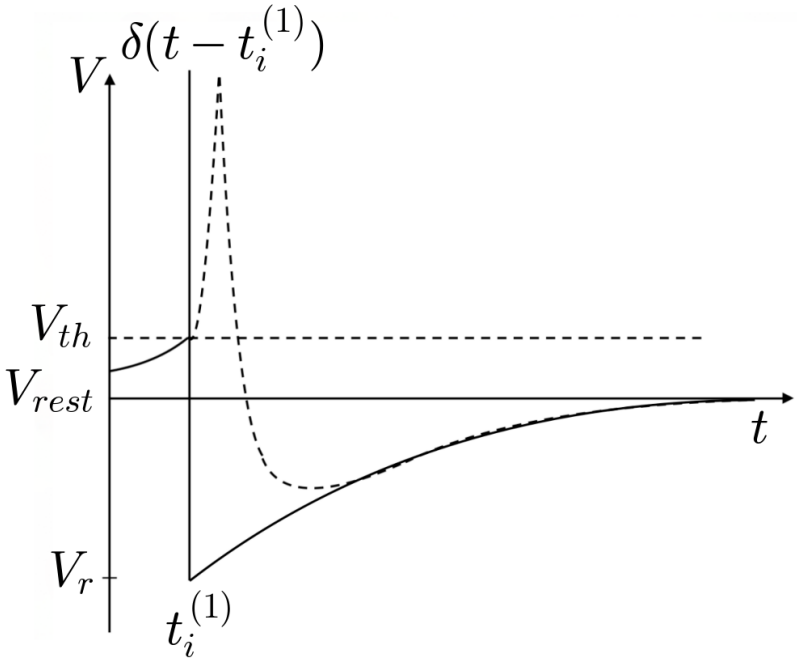

Figure 2.1: The typical shape of an action potential (dashed line) can be modeled by a δ pulse (solid vertical line). The hyperpolarisation after the pulse is replaced by a reset of the membrane potential to a chosen value V_r.

In simple phenomenological spiking neuron models, called integrate-and-fire, the shape of an action potential is not modeled and usually replace by a δ pulse, easier to analyze. Action potentials are described as events that happen at a precise moment, see Fig. 2.1. The simplest integrate-and-fire model only has two elements: (i) a linear differential equation to describe the evolution of the membrane potential; (ii) a threshold for spike firing. This model is called the "Leaky Integrate-and-Fire" (LIF) model. More realistic integrate-and-fire models that will be discussed in Sec. 2.3 of this thesis can be seen as variations of this basic model.

From Eq. (1.6), we have seen that the membrane charges up exponentially to its stationary value $V = RI$. When reaching the threshold V_{th}, a spike is initiated and the voltage is reset. We can deduce that the minimal sustained current that will lead to a spike is

$$I_{th} = \frac{V_{th}}{R}.$$

For any $I > I_{th}$, starting at $t = 0$, the membrane potential will reach the threshold at some time t_f. We can find this firing time using the threshold condition, $V(t_f) = V_{th}$. For simplicity we can also set $V_{rest} = 0$ in Eq. (1.6), we obtain the following expression:

$$V_{th} = RI \cdot \left(1 - e^{t_f/\tau_m}\right)$$

We can solve for t_f and obtain an equation for the time to spike:

$$\boxed{t_f = -\tau_m \cdot \ln\left(1 - \frac{V_{th}}{RI}\right)}. \tag{2.1}$$

After emitting a spike, the neuron's membrane potential is reset to V_r, and the integration process restarts. If the external current I remains constant, the neuron will reach the threshold after the same time interval. In this case, the neuron emits spikes periodically, and the time between two consecutive spikes, $T = t_i - t_{i-1}$, called the *interspike* interval, remains fixed. Given an input current we can establish the frequency response of a neuron. Such curves are called F-I curve, we will see more about them in Sec. 2.3.2.

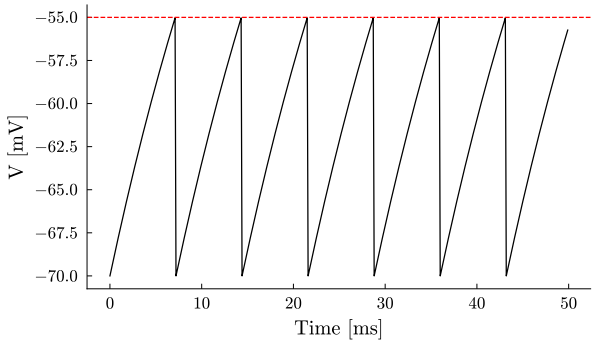

Figure 2.2: Periodic firing of a LIF neuron driven by constant current. Adapted from [46].

2.2.1. Limitations of the LIF model

The leaky integrate-and-fire model is the simplest model of spiking neuron and therefore neglects many aspects of neuronal dynamics. For example, it cannot reproduce spike-frequency adaptation, where most biological neurons, when stimulated with a sufficiently large current, respond with a spike train of increasing interspike intervals over time until they reach a steady state of periodic firing, (see Fig. 2.3 (b)). This progressive slowing of the firing rate is typically caused by slow ionic processes, such as the activation of potassium currents or sodium channel inactivation, which reduce the neuron's excitability as it continues to fire. The standard LIF model has no such slow process and no memory: after each spike the membrane potential is instantly reset to the same value and integration resumes regardless of past activity. Neurons that display spike-frequency adaptation are referred to as *regularly-firing* neurons.

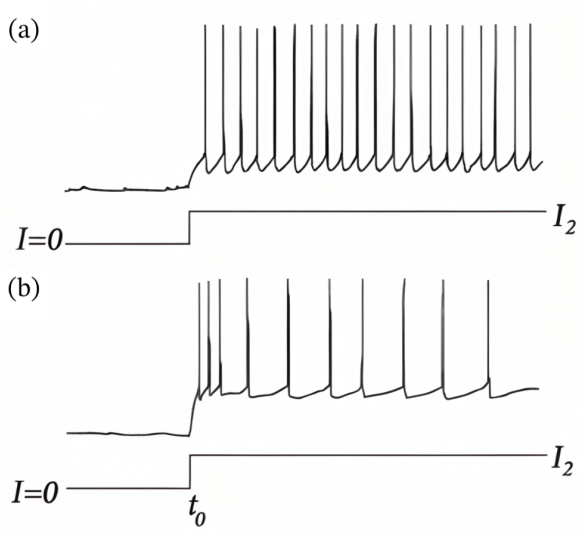

Figure 2.3: LIF neurons responding to a step current input. (A) A fast spiking neuron showing short interspike intervals with no adaptation. (C) A regular spiking neuron, showing adaptation. Adapted from [38].

Another class of neurons, called *fast-spiking* neurons, shows no adaptation, maintaining constant interspike intervals during sustained stimulation, see Fig. 2.3 (a). Many inhibitory neurons in the cortex fall in this category, and their behavior is well reproduced by the LIF model. Other biological features such as refractoriness or a synaptic transmission delay, representing the finite time for a spike to affect its post synaptic neurons, can be incorporated into the LIF model. However, these extensions will be ignored in this thesis.

2.3. Nonlinear Integrate-and-Fire models

To address the limitations of the LIF model, many extensions have been proposed. These models aim to capture the rapid nonlinear dynamics of spike initiation without resorting to the full complexity of conductance-based models like Hodgkin-Huxley. Two of the most widely studied nonlinear models are the exponential integrate-and-fire (EIF) and quadratic integrate-and-fire (QIF) models. Both introduce nonlinearities in the subthreshold membrane dynamics that lead to a more biologically realistic spike onset while remaining sufficiently simple to analyze numerically or analytically. We will study their derivations and discuss their dynamical properties in Sec. 2.3.3 and 2.3.4. A general non-linear integrate-and-fire model can be written as

$$\tau_m \frac{dV}{dt} = F(V) + RI \tag{2.2}$$

Where $F(V)$ is a nonlinear function of the membrane potential V and I denotes the input current. As before when V exceeds a threshold V_{th} the neuron emits a spike, at time t_f. The neuron then enters the refractory period of duration Δ_{abs}, at time $t_f + \Delta_{abs}$ the integration process resumes with initial condition $V = V_r$. Looking back at the LIF equation Eq. (1.5), this general nonlinearity $F(V)$ replaces the purely linear leak term. In the following sections we will introduce two of the most widely used models, the Quadratic integrate-and-fire (QIF) model and the exponential integrate-and-fire (EIF). Before going into details, let us see some general aspects of these nonlinear models.

2.3.1. Stability of the fixed points

Without external current ($I = 0$), fixed points satisfy $F(V^*) = 0$, their values and nature depend on the chosen nonlinearity. Let us consider a typical nonlinear integrate-and-fire model with two fixed points: V_{rest}, which is stable, and V_c, which is unstable.

In Fig. 2.4 (a) they are represented respectively by a black and a white dot. The black curve shows dV/dt as a function of V: for $V < V_c$, the slope is negative and the membrane potential relaxes to the resting potential V_{rest} while for $V > V_c$, the slope becomes positive and the potential increases until it reaches the threshold V_{th}, triggering a spike emission.

When the constant current I is increased, the curve is shifted upwards and the two fixed points approach each other. The critical value where they collide and annihilate in a saddle-node bifurcation is called the *rheobase* current I_c. For inputs larger than rheobase (super-threshold, $I > I_c$), dV/dt is strictly positive for all V. As shown in Fig.2.4 (b), the curve lies entirely above zero meaning that there is no fixed point and the membrane potential will monotonically increase until threshold, resulting in repetitive firing.

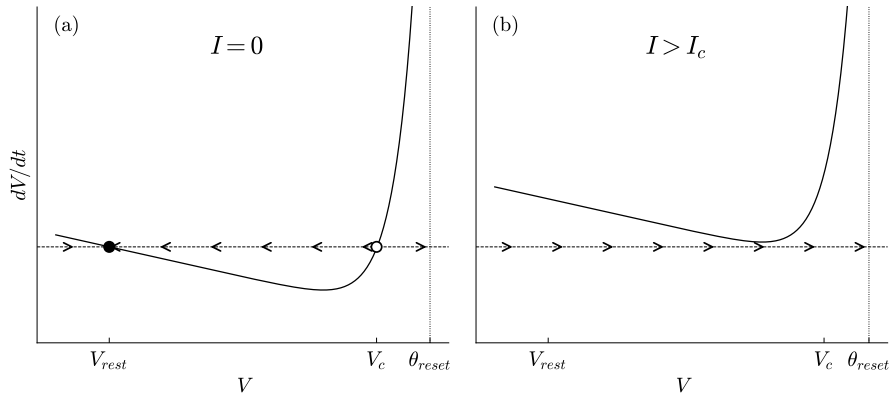

Figure 2.4: Fixed points in a nonlinear integrate-and-fire model. The black (white) dot represent a stable (unstable) fixed point. Arrows show the direction of flow: $dV/dt > 0$ to the right, $dV/dt < 0$ to the left. The horizontal dashed line shows the 0 and the vertical dotted line the threshold. (a) At $I = 0$, the zero crossings indicates the resting potential V_{rest} and the firing threshold V_c. (b) For inputs larger than the rheobase current I_c, no fixed points remains, the membrane potential is driven to threshold, leading to repetitive firing. Adapted from [46].

2.3.2. Excitability types

Neurons come in many different shapes and forms, with different dynamics. Despite these differences, we can classify them based on how they respond when driven by constant input current. There are two types of excitability: Type I neurons, which can emit action potentials with arbitrarily small frequencies as current is injected, and Type II neurons, which can only fire above a minimal frequency. Experimental recordings comparing these two types of neurons are shown in Fig 2.5. The figure reports the empirical F-I curves of two different neurons from a rat's brain. The left panel (Type I) shows data from the visual cortex while the right panel (Type II) shows data from a typical neuron in the rat's midbrain.

This biological distinction is carried on to mathematical models. As described by Ermentrout and Rinzel in [48, 49], the transition from a quiescent state to repetitive firing occurs through, typically, two different bifurcations corresponding to the two excitability types. In type I models, it occurs through a Saddle-Node bifurcation on an invariant circle (SNIC). In type II models, the transition occurs due to a Hopf bifurcation either supercritical or subcritical. All models used in this thesis are Type I, therefore we will only describe the SNIC bifurcation. An

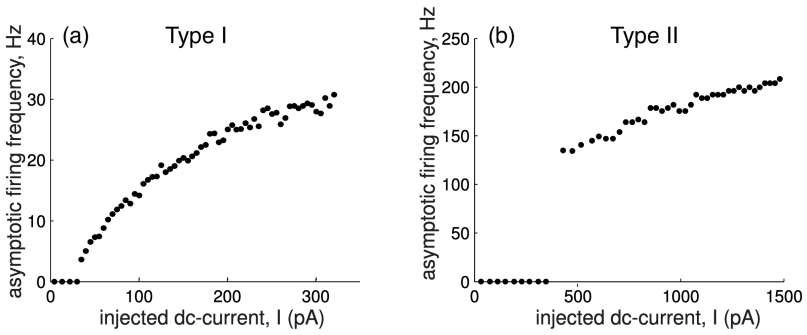

Figure 2.5: F-I curves from recordings of a rat's brain. Comparison of typical response of two neurons to steps of DC current of various magnitudes I. (a) Type I neuron: the frequency ν is almost a continuous function of I. (b) Type II neuron: the F-I curve has a discontinuity. Taken from [47].

example of a Type II model is the Hodgkin-Huxley model and the bifurcation analysis can be found in the following work of Rinzel [50].

The SNIC bifurcation arises in system of at least two dimensions, it is illustrated in Fig 2.6. For parameters below the critical value, three fixed points coexist: a stable node, an unstable saddle-point and an unstable focus. The unstable manifold of the saddle point is formed by two heteroclinic trajectories which, starting from the saddle, tend towards the stable node. Together, these two trajectories form a closed curve in the phase plane that encloses the unstable focus. The stable variety of the saddle point acts as a threshold: trajectories starting on the left relax directly to the stable node, while those on the right make a long excursion around the unstable focus before converging. The long path around the focus corresponds to the mechanism of generation of the action potential. This configuration defines the excitable state of the neuron. The center picture on Fig 2.6 shows the systems exactly at the critical bifurcation value. The saddle and node merges and the period of the action potential becomes infinite. On the right side of the panel the saddle and node have disappeared and we have a limit cycle of finite period, where the frequency of oscillations grow continuously.

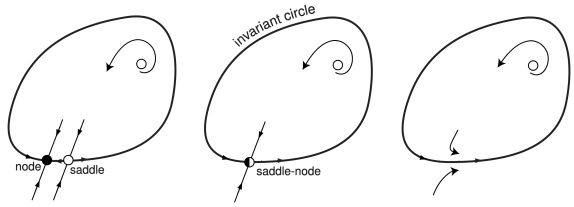

Figure 2.6: Sketch of the SNIC bifurcation. Black (white) dots show stable (unstable) fixed points. From left to right: excitable state, critical state, repetitive firing. Taken from [47].

2.3.3. Exponential Integrate-and-Fire

The exponential integrate-and-fire model was introduced by Fourcaud-Trocmé, Hansel, Van Vreeswijk and Brunel [51], as a one-dimensional reduction of biophysically detailed conductance-based neuron models, designed to capture the sharp onset of action potentials observed in recordings. Unlike the LIF model's abrupt threshold-reset mechanism, the EIF adds and exponential term that represents the rapid activation of sodium channels during spike initiation. This formulation produces a continuous, biologically plausible, transition to

spiking. The dynamics is given by the following equation:

$$\tau_m \frac{dV}{dt} = -(V - V_{rest}) + \Delta_T \cdot \exp\left(\frac{V - V_T}{\Delta_T}\right) + RI \tag{2.3}$$

Where Δ_T is the slope factor, and V_T is the threshold potential. This model is an extension of the LIF with an exponential term that more accurately captures the rapid membrane potential increase during spike initiation. This corresponds to Eq. (2.2) with $F(V) = -(V - V_{rest}) + \Delta_T \cdot \exp\left(\frac{V-V_T}{\Delta T}\right)$. In the limit where Δ_T goes to zero, the exponential term cancels out, only the linear term remains and we return to the LIF equation Eq. (1.5), this is show in figure 2.7. The

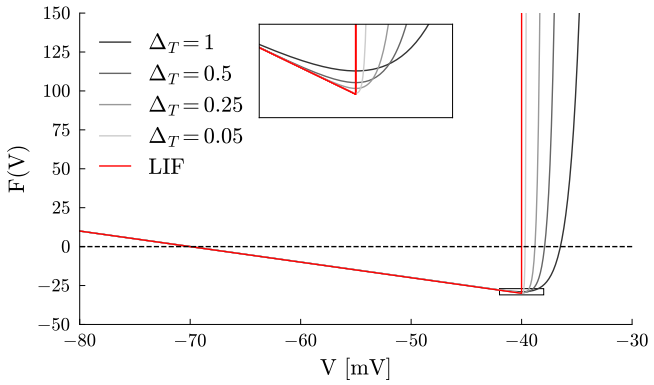

Figure 2.7: Comparing the sharpness of the threshold in the exponential and leaky integrate-and-fire models. We can see that as we reduce Δ_T (lighter shades of grey) in the EIF model, it becomes closer and closer to the LIF model represented by the red line. The inset shows a zoom around the boxed region. Taken from [38]

EIF model has been shown to fit remarkably well experimental data, this has been shown in the landmark article of Badel et al. [52], from which we show some results in Fig. 2.8.

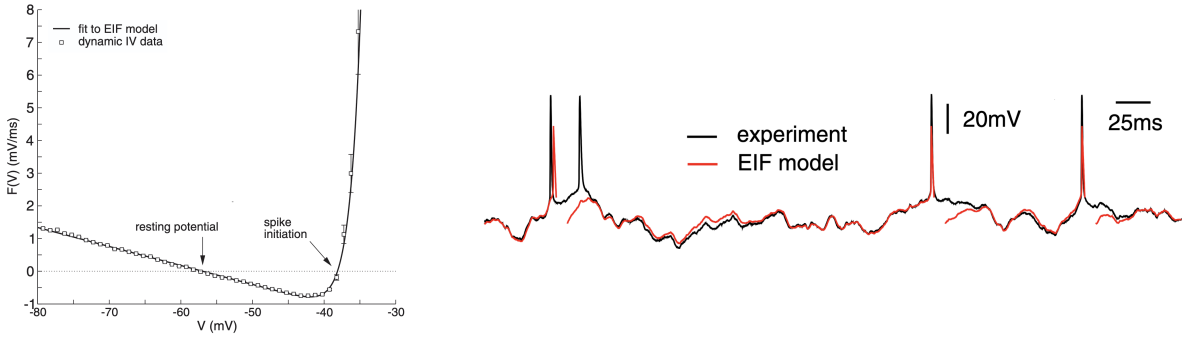

Figure 2.8: Experimental data fitted by the EIF model with parameters: τ_m = 17.2 ms, V_{rest} = −57.0 mV, V_T = −42.0 mV and ΔT = 1.51 mV. The curve crosses zero at two points: −57 mV and −38 mV, respectively the resting potential and spike initiation threshold.

2.3.4. Quadratic Integrate-and-Fire

Another instance of non-linear model is the *quadratic integrate-and-fire* model (QIF) [53, 54]. The QIF model provides the simplest mechanism for a continuous onset of firing. Unlike the EIF, which was designed to match the spike onset dynamics, the QIF prioritizes mathematical simplicity and analytical tractability. A key feature, that we will not use in this thesis, is that it can be mapped exactly to the theta neuron model [38, 55], allowing exact mean-field reductions for large, fully coupled networks. This is particularly useful for studying collective phenomena, such as synchronization and oscillations, where fully biophysical models would be intractable and the EIF offers no exact reduction. In summary the QIF model preserves the essential dynamical features of type I excitability while enabling analyses that are not feasible with more detailed models. It is described by the following equation:

$$\tau \frac{dV}{dt} = a_0(V - V_{rest})(V - V_c) + RI \tag{2.4}$$

For $I \simeq I_c$ the two fixed points merge together, in such a case the QIF model approximates well the EIF for $V_{rest} \leq V \leq V_c$. More generally, any type I neuron model close to repetitive firing (the bifurcation point) can be approximated by a quadratic integrate-and-fire model, this is why it is sometimes called the "canonical" type I model.

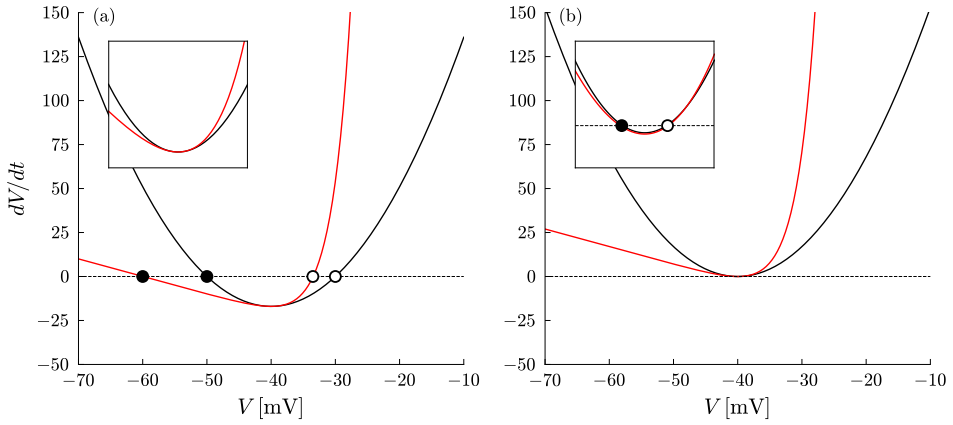

Figure 2.9: Quadratic (black) and exponential (red) integrate-and-fire models. (a) $I = 0$. Without external current the model has two fixed points, a stable one V_{rest} in black and another, unstable, V_c in white. (b) $I \simeq I_c$. The quadratic integrate-and-fire model can be seen as an approximation of an exponential integrate-and-fire model (or any other type I model) depolarised to a state close to repetitive firing. Adapted from [38].

With a shift of the voltage scale and constant current $I = I_c + \eta$ we can rewrite Eq. (2.4) as:

$$\dot{V}(t) = V^2(t) + \eta \tag{2.5}$$

This is the core equation of the QIF model, the form that we have used in this work, with $V_r = -\infty$ and $V_{th} = +\infty$. Equation (2.5) can be solved analytically, depending on the sign of η we can observe two different behaviors.

Tonic neuron $\eta > 0$

In the case where $\eta > 0$, the right hand side of Eq. (2.5) is strictly positive at all time. We can arrange Eq. (2.5) as $\frac{\dot{V}(t)}{V^2(t)+\eta} = 1$. Given an initial condition $(t_0, V(t_0))$, we can integrate the previous equation between t_0 and t_1 with $t_1 > t_0$:

$$\int_{t_0}^{t_1} \frac{\dot{V}(t)}{V^2(t) + \eta} dt = \int_{t_0}^{t_1} dt \tag{2.6}$$

Clearly the right hand sign is simply equal to $t_1 - t_0$. As for the left hand sign, notice that $V(t)$ is strictly monotonically increasing ($\dot{V}(t) > 0 \; \forall \, t$). Therefore we can make the change of variable $v = V(t)$, which gives $dv = \dot{V}(t)$. We write $v_0 = V(t_0)$ and $v_1 = V(t_1)$ and assume that t_1 is sufficiently close to t_0 so as not to include a singularity of the solution $V(t)$ in (t_0, t_1), we obtain the following integral:

$$\int_{v_0}^{v_1} \frac{1}{v^2 + \eta} dv = \left[\frac{1}{\sqrt{\eta}} \cdot \arctan\left(\frac{v}{\sqrt{\eta}} \right) \right]_{v=v_0}^{v=v_1}$$

We obtain the following, in term of $V(t)$:

$$\frac{1}{\sqrt{\eta}} \cdot \left[\arctan\left(\frac{V(t_1)}{\sqrt{\eta}} \right) - \arctan\left(\frac{V(t_0)}{\sqrt{\eta}} \right) \right] = t_1 - t_0 \tag{2.7}$$

Where we assume $t_1 - t_0 \in \left(0, \frac{\pi}{\sqrt{\eta}}\right)$, inverting the arctangent yields the analytical solution:

$$V(t_1) = \sqrt{\eta} \cdot \tan\left[\sqrt{\eta}(t_1 - t_0) + \arctan\left(\frac{V(t_0)}{\sqrt{\eta}} \right) \right] \tag{2.8}$$

shown in Fig. 2.10. This inversion is only valid as long as long as the argument of the tangent is smaller than $\frac{\pi}{2}$, because the tangent function has a singularity at that value. Therefore, for $\eta > 0$, given an initial solution we can extend the solution of Eq. (2.5) up to a time t_f such that

$$\sqrt{\eta} \cdot (t_f - t_0) + \arctan\left(\frac{V(t_0)}{\sqrt{\eta}} \right) = \frac{\pi}{2}$$

which gives

$$\boxed{t_f = t_0 + \frac{1}{\sqrt{\eta}} \cdot \left[\frac{\pi}{2} - \arctan\left(\frac{V(t_0)}{\sqrt{\eta}} \right) \right]} \tag{2.9}$$

At this instant, the neuron emits an action potential, and the membrane potential is instantaneously reset to minus infinity:

- $V(t_f^-) = +\infty$ spike emission
- $V(t_f^+) = -\infty$ membrane potential reset

At this point, the neuron restarts with a "limiting" initial condition given by, $t_0 = t_f^+$, $V(t_0) = -\infty$ and we can repeat the exact same reasoning as before by integrating over a time interval of $\frac{\pi}{\sqrt{\eta}}$ until a new singularity is encountered. We can deduce that a QIF neuron with $\eta > 0$ will emit trains of periodic impulses at times t_f given by the solutions of the following equation:

$$\sqrt{\eta} \cdot t_f + \arctan\left(\frac{V(t_0)}{\sqrt{\eta}} \right) = \frac{\pi}{2} \pm k\pi \qquad k \in \mathbb{Z}$$

Which are:

$$t_f = \frac{1}{\sqrt{\eta}} \left[\frac{\pi}{2} + \arctan\left(\frac{V(t_0)}{\sqrt{\eta}} \right) \right] \pm k \frac{\pi}{\sqrt{\eta}} \qquad k \in \mathbb{Z} \tag{2.10}$$

Moreover, from Eq. (2.10) we recover the formula that expresses the dependence of the period on the value of η

$$T = \frac{\pi}{\sqrt{\eta}} \tag{2.11}$$

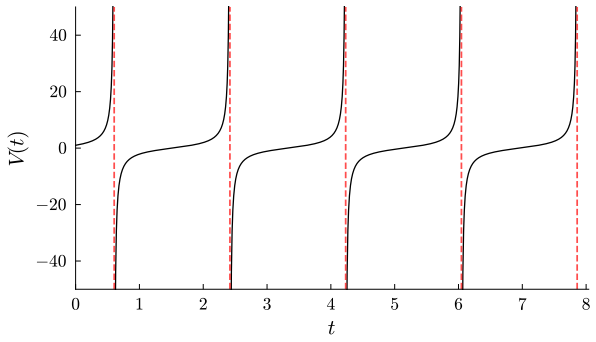

Figure 2.10: Tonic neuron. The red vertical asymptotes represent the firing times t_f, expressed by Eq. (2.10), in which the neuron emits an action potential. Function graph of V(t) in Eq. (2.8) with $\eta = 3$, $V(t0) = 1$.

Excitable neuron $\eta < 0$

As in the case of a tonic neuron, we proceed with the separation of variables. Given that $\eta \leq 0$, we must exclude from Eq. (2.5) the instants of time that provide constant solutions such that $V(t) = V_{stab}$ and $V(t) = V_{inst}$. Let us take an initial condition $(t_0, V(t_0))$ and choose a time t_1 such that the interval (t_0, t_1) do not contain the above mentioned times which achieve constant solutions. We have to distinguish two cases.

Sub-threshold dynamics: $|V(t_0)| \leq \sqrt{|\eta|}$

In this first case, $V(t_0)$ lies in the negative part of the parabola in Fig. 2.9 and therefore the evolution of the solution $V(t)$ will be strictly monotonically decreasing and will asymptotically approach the resting membrane potential value.

The strictly monotonically decreasing behavior allows us to perform the change of variable $v = V(t)$ in the integral on the left-hand side of Eq. (2.6), using again $V(t_0) > V(t_1)$, we obtain:

$$\int_{t_0}^{t_1} \frac{\dot{V}(t)}{V^2(t) + |\eta|} dt = \int_{v_0}^{v_1} \frac{1}{v^2 - |\eta|} dv$$

The right hand side is equivalent to:

$$-\int_{v_1}^{v_0} \frac{1}{v^2 - |\eta|} dv$$

which we can solve:

$$-\int_{v_1}^{v_0} \frac{1}{v^2 - |\eta|}\, dv = -\frac{1}{2\sqrt{|\eta|}} \left[\int_{v_1}^{v_0} \frac{1}{v - \sqrt{|\eta|}}\, dv - \int_{v_1}^{v_0} \frac{1}{v + \sqrt{|\eta|}}\, dv \right]$$

from which

$$-\frac{1}{2\sqrt{|\eta|}} \left[\ln\left(\sqrt{|\eta|} - v\right) - \ln\left(\sqrt{|\eta|} + v\right) \right]_{v=v_1}^{v=v_0}$$

For notation's clarity, we will use the hyperbolic arctangent function:

$$-\frac{1}{2\sqrt{|\eta|}} \ln\left(\frac{\sqrt{|\eta|} - v}{\sqrt{|\eta|} + v}\right) = +\frac{1}{\sqrt{|\eta|}} \operatorname{arctanh}\left(\frac{v}{\sqrt{|\eta|}}\right)$$

Rewriting everything in terms of the original variable $V(t)$, we obtain the relation:

$$\frac{1}{\sqrt{|\eta|}} \left[\operatorname{arctanh}\left(\frac{V(t_0)}{\sqrt{|\eta|}}\right) - \operatorname{arctanh}\left(\frac{V(t_1)}{\sqrt{|\eta|}}\right) \right] = t_1 - t_0$$

Finally, we can apply the hyperbolic tangent function and use the fact that this function is odd. We obtain the analytical solution

$$V(t_1) = -\sqrt{|\eta|} \cdot \tanh\left[\sqrt{|\eta|}\,(t_1 - t_0) - \operatorname{arctanh}\left(\frac{V(t_0)}{\sqrt{|\eta|}}\right)\right] \tag{2.12}$$

Which we plot in Fig. 2.11. In particular, a QIF neuron with $\eta < 0$ and initial condition $|V(t_0)| \leq \sqrt{|\eta|}$, if isolated, never emits any action potential.

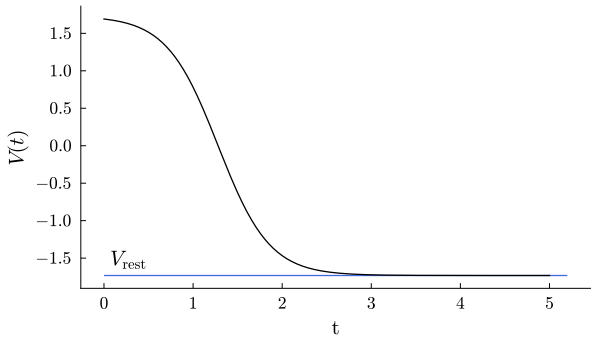

Figure 2.11: Excitable neuron, Sub-threshold dynamics. In blue, the value of the resting membrane potential, $V_{\text{rest}} = -\sqrt{-\eta}$, to which the neuron tends. Trend of $V(t)$ in Eq. (2.12) with $\eta = -3$ and $V(t_0) = -\eta - 0.05$.

Supra-threshold dynamics: $|V(t_0)| > \sqrt{|\eta|}$

If we now assume $|V(t_0)| \geq \sqrt{|\eta|}$, $V(t_0)$ now lies on the positive right part of the parabola from Fig. 2.9. In this configuration there exist a finite time t_f such that $V(t_f) = +\infty$. To demonstrate this it is sufficient to show that the following integral converges

$$\int_{v_0}^{+\infty} \frac{1}{v^2 - |\eta|}\,dv = \frac{1}{2\sqrt{|\eta|}}\left[\int_{v_0}^{+\infty} \frac{1}{v - \sqrt{|\eta|}}\,dv - \int_{v_0}^{+\infty} \frac{1}{v + \sqrt{|\eta|}}\,dv\right]$$

from which

$$\frac{1}{2\sqrt{|\eta|}}\left[\ln|v - \sqrt{|\eta|}| - \ln|v + \sqrt{|\eta|}|\right]_{v=v_0}^{v=+\infty} = \frac{1}{2\sqrt{|\eta|}}\left[\ln\left(\frac{v - \sqrt{|\eta|}}{v + \sqrt{|\eta|}}\right)\right]_{v=v_0}^{v=+\infty}$$

which is a finite real number, expressed as

$$-\frac{1}{2\sqrt{|\eta|}}\ln\left(\frac{v_0 - \sqrt{|\eta|}}{v_0 + \sqrt{|\eta|}}\right)$$

or, in terms of the hyperbolic arctangent, as

$$\frac{1}{\sqrt{|\eta|}} \cdot \operatorname{arctanh}\left(\frac{\sqrt{|\eta|}}{v_0}\right)$$

This means that if, at time t_0, the neuron has a membrane potential $V(t_0) > \sqrt{|\eta|}$, then at the time

$$t_f = t_0 + \frac{1}{\sqrt{|\eta|}} \cdot \operatorname{arctanh}\left(\frac{\sqrt{|\eta|}}{v_0}\right) \tag{2.13}$$

it will emit an action potential and will instantaneously reset its membrane potential to $-\infty$. At this point, as already observed, the value of $V(t)$ will tend towards $V_{\text{stab}} = -\sqrt{|\eta|}$ in a strictly monotonically increasing manner, and the analytical form of the solution can be obtained from Eq. (2.6), written as follows:

$$\int_{t_0}^{t_f} \frac{\dot{V}(t)}{V^2(t)+\eta}\,dt + \int_{t_f}^{t_1} \frac{\dot{V}(t)}{V^2(t)+\eta}\,dt = \int_{t_0}^{t_1} dt.$$

That is,

$$\int_{v_0}^{+\infty} \frac{1}{v^2+\eta}\,dv + \int_{-\infty}^{v_1} \frac{1}{v^2+\eta}\,dv = t_1 - t_0.$$

Giving,

$$\frac{1}{\sqrt{|\eta|}} \cdot \operatorname{arctanh}\left(\frac{\sqrt{|\eta|}}{V(t_0)}\right) - \frac{1}{\sqrt{|\eta|}} \cdot \operatorname{arctanh}\left(\frac{\sqrt{|\eta|}}{V(t_1)}\right) = t_1 - t_0.$$

from which we obtain the solution

$$V(t_1) = -\sqrt{|\eta|} \cdot \operatorname{cotanh}\left(\sqrt{|\eta|} \cdot (t_1 - t_0) - \operatorname{arctanh}\left(\frac{\sqrt{|\eta|}}{V(t_0)}\right)\right) \tag{2.14}$$

whose graph is shown in Fig.2.12.

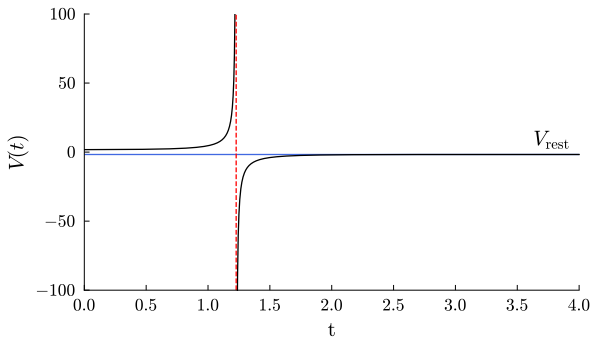

Figure 2.12: Excitable neuron, supra-threshold dynamics. The red vertical asymptote shows the time of spiking as predicted by Eq. (2.13). In blue, the resting value of the membrane potential, $V_{rest} = -\sqrt{-\eta}$ to which the neuron's potential converges after spiking. This curve represent eq.Eq. (2.14), with $\eta = -3$ and $V(t_0) = \sqrt{-\eta} + 0.05$.

Limit case $\eta = 0$

In this particular case, the differential equation of the QIF model takes the form

$$\dot{V}(t) = V^2(t)$$

Choosing an initial condition $V(t_0) \neq 0$, we can proceed with separation of variables to obtain the analytical solution

$$V(t) = \frac{V(t_0)}{1 - V(t_0) \cdot (t - t_0)}$$

Therefore, if $V(t_0) > 0$ the neuron fires at the time

$$t_f = t_0 + \frac{1}{V(t_0)}$$

The QIF neuron with $\eta = 0$ has dynamics qualitatively similar to those of the hyperbolic cotangent in Fig.2.12, although the analytical solution is different.

2.4. Neural networks.

So far, we have only considered single neurons. In the brain, however, neurons form large, complex networks in which the input current $I(t)$ to each neuron is generated by the activity of presynaptic neurons. The total input current received by neuron i is simply the linear sum over all current pulses.

2.4.1. Modeling synaptic currents

The representation of synaptic interactions, which shape how neurons integrate presynaptic activity is an important aspect of network modeling. The postsynaptic potential (PSP) elicited by an incoming spike can be modeled by different synaptic kernels $P(t)$, reflecting distinct levels of biological detail.

$$I_i(t) = \sum_j J_{ij} \sum_f P\left(t - t_j^{(f)}\right),$$

where J_{ij} denotes the synaptic coupling and $t_j^{(f)}$ the firing times of presynaptic neuron j.

A first, highly simplified choice is the *delta-function synapse*, $P(t) = \delta(t)$, where spikes are transmitted instantaneously to the postsynaptic neuron. This assumption, while biologically unrealistic, has the advantage of analytical tractability and allows for efficient implementation in event-driven simulations. In particular, it reduces the total input current to neuron i to a sum over weighted spike trains:

More realistic models introduce finite synaptic time constants. The simplest choice is the *exponential kernel*, $P(t) = \frac{1}{\tau_s} e^{-t/\tau_s} H(t)$, where τ_s sets the decay time of the postsynaptic response. To capture both the rise and decay phases of synaptic transmission, one can use a *double-exponential kernel*,

$$P(t) = \frac{1}{\tau_d - \tau_r} \left(e^{-t/\tau_d} - e^{-t/\tau_r}\right) H(t),$$

with τ_r and τ_d controlling the rise and decay timescales, respectively. Another frequently used alternative is the *alpha function*, $P(t) = \frac{t}{\tau_s} e^{-t/\tau_s} H(t)$, which provides a smooth onset and an exponential decay.

The choice of synaptic kernel reflects a compromise between biological realism and mathematical simplicity. While exponential or double-exponential functions more faithfully reproduce the time course of PSPs observed experimentally, delta synapses remain widely employed in theoretical work due to their analytical tractability and reduced computational cost. As a result, many network studies adopt simplified kernels depending on whether the emphasis lies on uncovering fundamental principles or on reproducing detailed physiological dynamics.

3

Balanced spiking neural networks

Summary In this chapter, we introduce the balanced network theory, the backbone of further work in this thesis. We first recall its motivations from experimental observations, then define what the balanced state is and how to be in such a regime. Two models will be discussed: on that reproduces cortical dynamics but requires fine tuning and a more robust formulation where balance emerges dynamically. We then mention some experimental confirmations of these ideas, followed by recent criticism and other mechanisms leading to balance.

3.1. Irregular, asynchronous spike trains in the cortex

The activity of spiking networks can be described at the individual and collectives levels by only four adjectives. Individual neurons can fire regularly or irregularly, and the population can be either synchronized or asynchronous. The cortex is characterized by irregular and asynchronous activity [5, 6], as we will see in this section.

Asynchronous simply means that neurons in a population fire independently, with no temporal coordination. Irregularity refers to the variability in the timing of spikes of a given neuron, usually measured by the coefficient of variation (CV) of the interspike interval distributions (ISI), defined as the ratio of the standard deviation to the mean ISI. Perfectly regularly firing neurons will have $CV = 0$ while a Poisson process gives $CV = 1$, this is illustrated in Fig. 3.1.

Consider a simple integrate-and-fire models, requiring n inputs to reach threshold. The output ISI is the time it takes for n input pulses to arrive. If the inputs arrive as a Poisson process with rate λ, then each interarrival time (the time between consecutive input spikes) is exponentially distributed and the output ISI (T) is the sum of n such interarrival times. Therefore T follows a Gamma distribution of shape n and rate λ:

$$T = \Gamma(n, \lambda)\,. \tag{3.1}$$

From the properties of the Gamma distribution, the mean and variance are:

$$\overline{T} = \frac{n}{\lambda}, \qquad \sigma_T^2 = \frac{n}{\lambda^2}. \tag{3.2}$$

Therefore,

$$CV = \frac{\sigma_T}{\overline{T}} = \frac{1}{\sqrt{n}}. \tag{3.3}$$

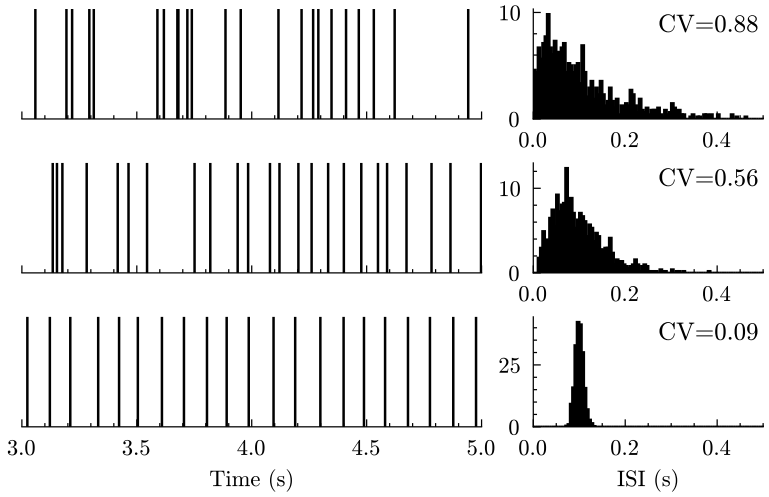

Figure 3.1: Spike trains (left) and their corresponding normalised interspike interval distributions (right). From top to bottom each row shows increasingly regular spike trains. The spikes trains are generated from Gamma renewal processes, they have a total duration of 100 s and a 10 Hz mean rate.

The coefficient of variation is expected to decrease as $1/\sqrt{n}$ [56], this follows from the central limit theorem. Humans have approximately 15 billion cortical neurons each making 7000 synaptic connections on average [2, 4], macaque have about 3 billions cortical neurons [57], and cats around 250 million [58]. Given those numbers the CV measured should be extremly small. This model predicts that cortical neurons should fire almost perfectly regularly.

Yet, empirical observations show the opposite: cortical neurons fire with high variability. In cats, for example, Smith and Smith found ISI distribution close to exponential, while Noda and Adey report state dependant levels irregularity [59, 60]. These results are illustrated in 3.2a and 3.2b, respectively. In primates , Softky and Koch reported values of CV ranging between $\simeq 0.5$ and 1, with some cases exceeding 1 [6]. See Fig. 3.3a. Experimental recordings consistently found cortical neurons to fire almost like a Poisson process.

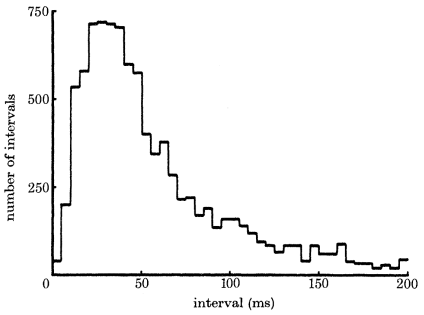

(a) Distribution of the interspike intervals from a cell in the cat auditory cortex. The horizontal axis shows the intervals and the vertical axis the number of such intervals in time bins of 5 ms. The distribution is a compilation of 2000 action potentials recorded in 166.6 s. Taken from [5].

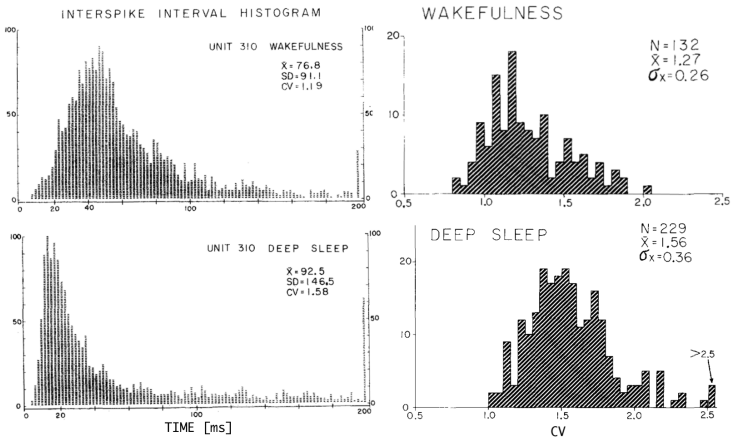

(b) Interspike interval histograms of a single neuron (left) and the distribution of CV of N neurons (right), during different states: awake (top row) and in deep sleep (bottom row). The ISI are counted in time bins of 2 ms, intervals longer than 200 ms are counted in the 100th bin, with those between 198 and 200 ms. All data come from the cat's visual cortex. Taken from [60].

Figure 3.2: Examples of experimental measurements of interspike interval variability in cortical neurons.

This suggests that the simple integrate-and-fire model fails to capture essential elements of cortical dynamics. Even a detailed Hodgkin-Huxley-like neuron failed to reproduce the dynamics observed in the macaque visual cortex, as we can see in (3.3a).

In contrast, in vitro experiments showed that neurons stimulated by a constant current fired regularly. Indicating that the irregularity observed in the brain is not an intrinsic property of neurons but is instead the result of strong temporal fluctuations in the synaptic inputs [61, 62]. What mechanisms in the brain generates these fluctuations and how do they persist despite the averaging effect of large number of inputs?

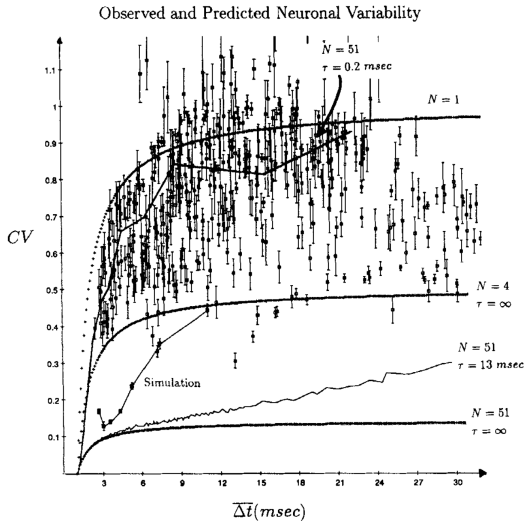

(a) CV as a function of interspike interval for three different data sets. (1) Individual squares: experimentally recorded, nonbursting, macaque cortical neurons [from middle temporal (MT) and primary visual cortex (V1)]. (2) Connected squares: detailed compartmental simulation of a reconstructed layer V pyramidal cell. (3) Crosses and jagged lines: different integrate-and-fire models with refractory period of 1.0 ms and N EPSPs required to fire. Crosses are predictions by integrate-and-fire models with $N = 1$ (top), $N = 4$ (middle), and $N = 51$ (bottom). Jagged lines show simulated leaky integrators with $N = 51$: $\tau_m = 0.2$ ms (top) or $\tau_m = 13$ ms (bottom). Conventional parameters (i.e., $\tau_m > 10$ ms and N > 50) fail to account for the high variability observed. Taken from [56].

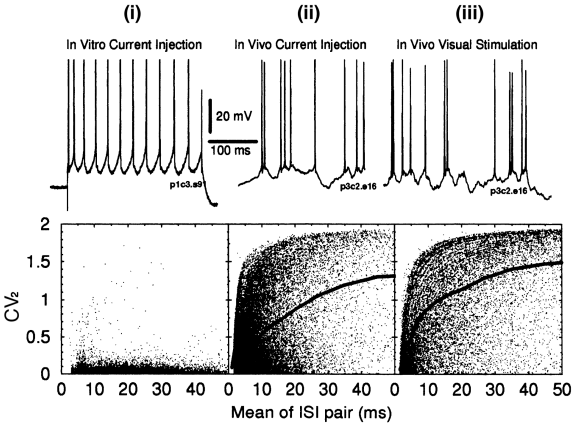

(b) Comparison of the activity of in vitro and in vivo stimulated cells from the adult cat primary visual cortex. The top row shows traces from two pyramidal neurons: one from a slice (i) and another, in vivo, stimulated with current (ii) or by a visual stimulus (moving bar) (iii). The bottom row shows the corresponding CV_2 of 89 cells from the slice, and 21 in vivo cells responding to the two different stimulations; larger lines show the average CV_2. CV_2 is a measure of spike train variability that looks at consecutive ISI instead of the entire distribution, defined as $CV_2 = 2|T_{i+1} - T_i|/(T_{i+1} + T_i)$. As for CV lower values indicates more regular spike trains. Taken from [61].

Figure 3.3: Observed and predicted neuronal variability.

3.2. The balanced network

3.2.1. Static balance

In 1994, Shadlen and Newsome [63] introduced the concept of excitation-inhibition balance. Their model consists of two populations, excitatory and inhibitory neurons, where each neuron receives a large number of weak inputs modeled as Poisson processes. The excitatory inputs are cancelled by the inhibitory ones, and thus it is possible to fine-tune the parameters so that the mean input into any neuron is close to zero. As a result, the neurons are driven by small input currents that fluctuate around zero, causing them to fire irregularly at low frequency. This model was able to reproduce the high temporal variability of cortical spike trains observed in vivo.

More precisely, the network is composed of N neurons, each neuron receives inputs of amplitude w from K presynaptic neurons, firing at a frequency ν. The number of synaptic connections per neuron is much smaller than the total number of neurons in the network ($K/N \ll 1$) such that the spike trains are uncorrelated. Each neuron is subject to a Poissonian spike train of rate $K\nu$. Thus, the mean excitatory and inhibitory currents are respectively:

$$\begin{aligned} I_E &= wK\nu \\ I_I &= -wK\nu \,. \end{aligned} \tag{3.4}$$

The total synaptic current is the sum of these two terms, $I_{syn} = I_E + I_I$, and the fluctuations are:

$$\sigma^2(I_{syn}) = 2w^2K\nu \,. \tag{3.5}$$

Neurons in the brain fire at relatively low rates and, more importantly, at a finite frequency. Meaning that $\langle I_{syn}\rangle$ and $\sigma(I_{syn})$ should remain finite when K gets large. For the average total synaptic current, it is the case when the excitatory and inhibitory inputs cancel each other $\langle I_{syn}\rangle = I_E + I_I = 0$. In this case the neurons fire because of current fluctuations. However, as we see from Eq. (3.5), the variance of the current will grow with the number of synaptic connections, making the neurons firing rate dependant of K and infinite. A simple way to prevent this is to scale the synaptic couplings as $w = g/\sqrt{K}$, making the variance independent of the connectivity:

$$\begin{aligned} \sigma^2\left(I_{syn}\right) &= 2w^2K\nu \\ &= 2\frac{g^2}{K}K\nu \\ &= 2g^2\nu \,. \end{aligned} \tag{3.6}$$

The condition $N \gg K \gg 1$ is crucial for the balanced state to emerge. $N \gg K$ ensures that the network is sparse, each neuron is connected to a small fraction of of the total population and presynaptic spike trains can be considered uncorrelated. At the same time, because $K \gg 1$, each neuron receives many inputs and, using the central limit theorem, we can consider the sum from many weak inputs as Gaussian noise with finite variance. This generates a regime where the mean excitatory and inhibitory current cancel each other, while the scaling of the synaptic weights guarantees that their fluctuations remain finite. As a result we obtain a fluctuation-driven regime with low firing rate, consistent to in vivo observations.

However, generating large excitatory and inhibitory currents that precisely cancel each other appears inefficient. Moreover, the brain does not fine tune its parameters to reach such a balanced state. Is it possible to build a model where balance dynamically emerge from the structure and dynamics of the network itself?

3.2.2. Dynamical balance.

This was the motivation behind the fundamental paper of Van Vreeswijk and Sompolinsky of 1996 [7]. They proposed that a dynamic balance of excitatory and inhibitory synaptic input is responsible for synaptic background noise. This theory and its extensions has come to be regarded as the standard model of cortical activity. Later, Monteforte and Wolf showed the existence of extensive chaos in balanced networks, demonstrating that the asynchronous irregular state is not just noisy in appearance but truly chaotic [64].

Let us consider a nonlinear integrate-and-fire model (this also works with the LIF model) made of excitatory (E) and inhibitory (I) neurons. To simplify, the PSP induced by presynaptic spikes are modeled as delta functions. In this approximation each presynaptic spike at time $t^{(f)}$ contributes a term $\delta(t - t^{(f)})$, producing an immediate "kick" in the membrane potential. The dynamics of neuron i can be written as:

$$\tau_m \frac{dV_i^{E/I}(t)}{dt} = F(V_i^{E/I}) + \frac{1}{\sqrt{K}} \left[g_{E\to E/I} \sum_{j\in \mathrm{pre}_E(i)}^{N} \sum_f \delta\left(t - t_j^{(f)}\right) - g_{I\to E/I} \sum_{k\in \mathrm{pre}_I(i)}^{N} \sum_f \delta\left(t - t_k^{(f)}\right) \right] + I_0 \tag{3.7}$$

Here, $V_i^{E/I}(t)$ is the membrane potential of neuron i which can belong either to the excitatory or inhibitory population. Here we write one equation that covers both cases, as indicated by the superscript of the membrane potential. $F(V_i)$ is the intrinsic dynamic of the neuron (LIF, EIF, ...) and τ_m is the membrane time constant. The term g is the relative synaptic weights between population, the subscripts indicates the presynaptic population and the arrow points to the postsynaptic population, for example $g_{E\to E}$ indicates is the weight of an excitatory neuron projecting onto another excitatory neuron. Later, when the duality in the membrane potential is no more present, we drop the arrow. The sums run over all presynaptic neurons from the excitatory $[pre_E(i)]$ or inhibitory $[pre_I(i)]$ populations, and over the spike times $t^{(f)}$. Finally, I_0 is an external current.

Assuming the excitatory/inhibitory populations have an average firing rate $\nu_{E/I}$,

$$\begin{aligned} \tau_m \frac{dV_i^{E/I}(t)}{dt} &= F(V_i^{E/I}) + \frac{1}{\sqrt{K}} \left[g_{E\to E/I} \cdot K\nu_E - g_{I\to E/I} \cdot K\nu_I \right] + I_0 \\ &= F(V_i^{E/I}) + \sqrt{K} \left[g_{E\to E/I} \cdot \nu_E - g_{I\to E/I} \cdot \nu_I \right] + I_0 \quad i = 1, \ldots, N \end{aligned} \tag{3.8}$$

This should remain finite even when the number of synaptic connections is very large, $K \gg 1$, as it does in the cortex. This can be achieved if the excitatory and inhibitory inputs cancel each other:

$$\begin{aligned} g_{EE} \cdot \nu_E - g_{IE} \cdot \nu_I = 0 \\ g_{EI} \cdot \nu_E - g_{II} \cdot \nu_I = 0\,. \end{aligned} \tag{3.9}$$

This homogeneous linear system has, for a generic g_E/I, only one solution: $\nu_E = \nu_I = 0$. This is not satisfactory, we want a solution with a positive and finite firing rate. To achieve this, we introduce a strong feedforward excitatory drive that scales as $\sqrt{K}$: $I_0 = \sqrt{K} i_0$. The balance equation gives:

$$g_{EE}\nu_E - g_{IE}\nu_I + i_0 = 0, \tag{3.10}$$

$$g_{EI}\nu_E - g_{II}\nu_I + i_0 = 0\,. \tag{3.11}$$

We can rewrite this in matrix form:

$$A \begin{pmatrix} \nu_E \\ \nu_I \end{pmatrix} = -i_0 \begin{pmatrix} 1 \\ 1 \end{pmatrix}, \qquad A = \begin{pmatrix} g_{EE} & -g_{IE} \\ g_{EI} & -g_{II} \end{pmatrix}. \tag{3.12}$$

We can solve this by multiplying Eq. (3.10) by g_{II} and Eq. (3.11) by g_{IE}:

$$g_{II}g_{EE}\,\nu_E - g_{II}g_{IE}\,\nu_I + g_{II}i_0 = 0, \tag{3.13}$$

$$g_{IE}g_{EI}\,\nu_E - g_{IE}g_{II}\,\nu_I + g_{IE}i_0 = 0. \tag{3.14}$$

Subtracting the second equation from the first gives

$$\left(g_{II}g_{EE} - g_{IE}g_{EI}\right)\nu_E + \left(g_{II} - g_{IE}\right)i_0 = 0. \tag{3.15}$$

We can recognize the determinant of the coupling matrix A:

$$\Delta = g_{EI}g_{IE} - g_{EE}g_{II}, \tag{3.16}$$

which simplifies the relation to

$$-\Delta\,\nu_E + \left(g_{II} - g_{IE}\right)i_0 = 0. \tag{3.17}$$

Therefore,

$$\nu_E = \frac{\left(g_{IE} - g_{II}\right)i_0}{\Delta}. \tag{3.18}$$

By symmetry,

$$\nu_I = \frac{\left(g_{EI} - g_{EE}\right)i_0}{\Delta}. \tag{3.19}$$

The rates are positive when one the these inequalities hold:

$$1 > \frac{g_{IE}}{g_{II}} > \frac{g_{EE}}{g_{EI}} \quad \text{or} \quad 1 < \frac{g_{IE}}{g_{II}} < \frac{g_{EE}}{g_{EI}}. \tag{3.20}$$

In this model the asynchronous chaotic activity naturally emerges when the synaptic couplings are sufficiently strong [8]. When it is the case we observe exponential firing rate distributions and large CV values. Yet the models are completely deterministic, the dynamic is the result of self-induced Gaussian fluctuations in the network, which have a variance $\sigma^2\left(I_{syn}\right) \propto g^2\nu$. Therefore the irregularity are due to chaotic dynamics.

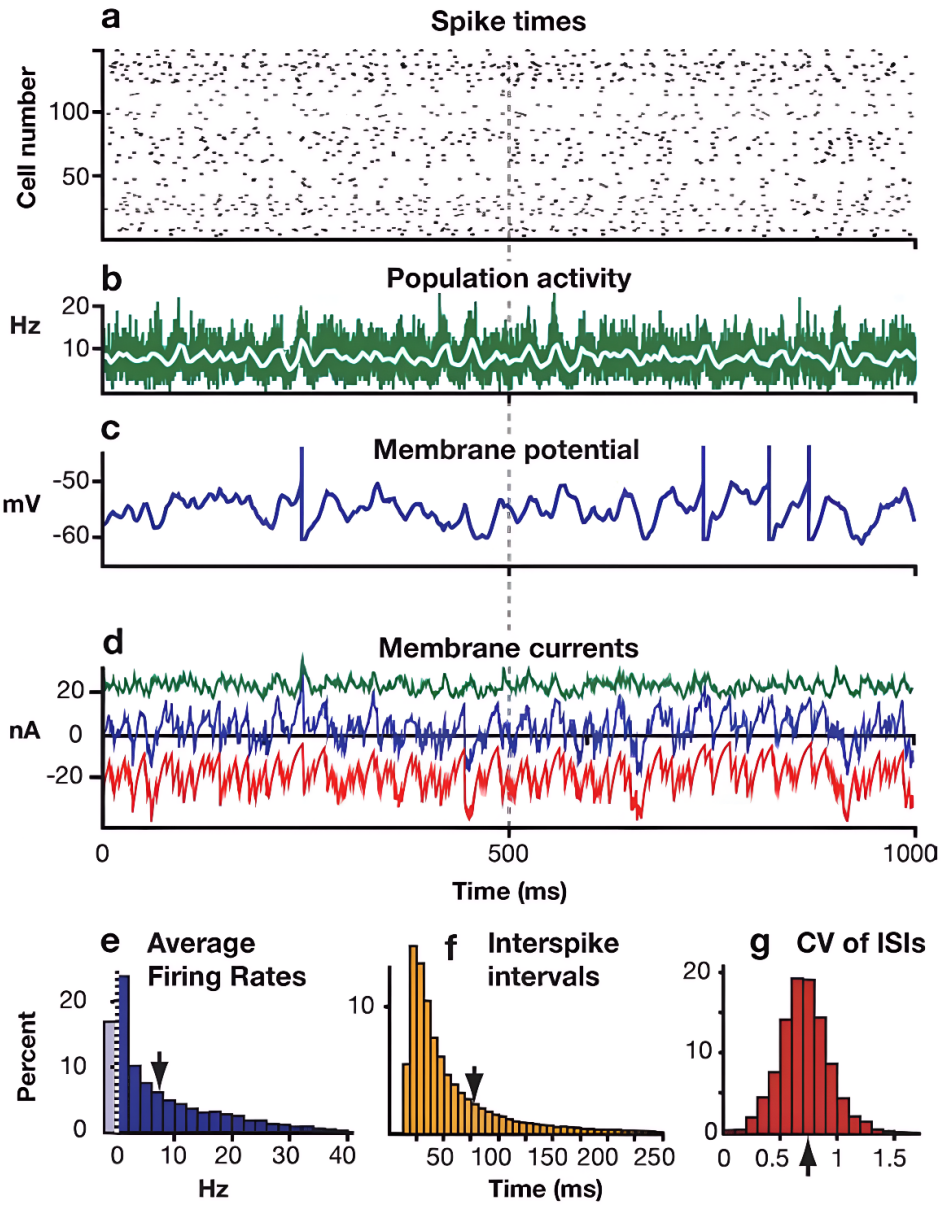

Figure 3.4: Asynchronous irregular activity in a balanced network of leaky integrate-and-fire neurons. (a) Raster plot showing 150 neurons from a network of 10 000. (b) The average firing rate (in green 0.1 ms binning, in white 5 ms binning) of the entire population is roughly constant and (c) the voltage trace of single randomly picked neuron shows that it fires irregularly. (d) The excitatory (green) and inhibitory (red) currents that the single neuron above receives in time. The total current (blue) fluctuates around zero. (e) Histogram of the time averaged firing rates of each neuron in the network. The arrow show the population average at 8 Hz. (f) Distribution of the time averaged interspike intervals of each neuron in the network. (g) Distribution of the CV for the network neurons. Arrows indicate the means of the distributions. Taken from [65].

3.3. Experimental confirmations

Experimental studies have provided strong confirmation of the main predictions of balanced network theory. Intracellular recordings in both in vitro and in vivo preparations have shown that excitatory and inhibitory synaptic conductances increase proportionally during spontaneous and stimulus-evoked activity, supporting the prediction that cortical neurons operate in a dynamically balanced regime. This was first demonstrated using in vitro intracellular recordings of ferret prefrontal and occipital cortex by [66]. They observed persistent states where the excitatory and inhibitory inputs were tightly correlated and scaled together. Subsequent in vivo studies, such as those by [67] and [68], confirmed this behavior under natural sensory stimulation.

But the main confirmation of Sompolinsky and Van Vreeswijk's theory came twenty years after the publication of their paper, from Barral and Reyes [69]. They used a culture of neurons where they could control exactly the number of neurons N, and accurately measure the number of synaptic connections K, the strength of the synaptic couplings g as well as the postsynaptic amplitudes of excitatory (EPSP) and inhibitory (IPSP) neurons. They found that the amplitudes of the postsynaptic potentials decreased as the network density increased, following a power-law relationship, as can be seen on Fig. 3.5.

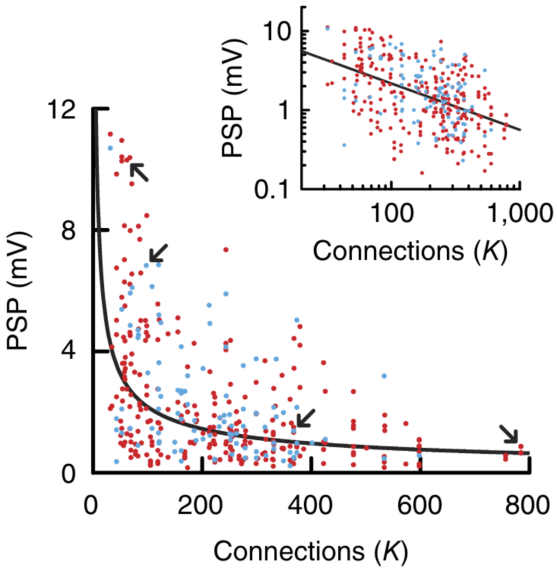

Figure 3.5: Amplitudes of unitary EPSPs (red, n = 261) and IPSPs (blue, n = 99) versus K. The inset shows the data in a log-log scale, the slope of the linear fit combining E-I data is −0.59. Taken from [69].

They report that the amplitude of EPSP scales as $K^{-0.60}$, and the IPSP as $K^{-0.52}$, in remarquable agreement with Sompolinsky and Van Vreeswijk's scaling as $1/\sqrt{K}$. As expected, they find that the action potential firing is irregular, consistent with a near-Poisson process. Confirming the $1/\sqrt{K}$ scaling hypothesis, they report that the variability in spiking activity does not decrease when increasing N. Moreover, the firing rate distribution is long-tailed and approximately log-normal, as anticipated by balanced network theory and reported in experimental observations [70].

Moreover, they directly tested, and confirmed, many other predictions of balanced network theory using optogenetic stimulation and intracellular recordings in cortical cultures. Using light pulses to activate subsets of neurons, they demonstrated that excitation and inhibition

varied linearly across stimulation conditions, preserving a stable excitatory/inhibitory ratio at the single-cell level. They also confirmed that fluctuation of the input current remains independent of K, as predicted by the theory if synaptic strength scales as $1/\sqrt{K}$. Finally, correlation analysis of excitatory and inhibitory currents showed that they tracked each other in time, such that their fluctuations largely cancelled and net inputs remained balanced.

3.4. Balance with weak currents

In their theory, Sompolinsky and Van Vreeswijk obtain a *tight* balanced regime using a strong feedforward excitatory drive, scaling with $\sqrt{K}$. This has been the subject of criticism [71, 72], backed by experimental observations of weak feedforward drive (of order $O(1)$). Such weak feedforward drive has been reported in several cortical areas: in the primary visual cortex of mice, [73, 74], in the auditory cortex [75] and in the olfactory cortex [76].

Ahmadian and Miller [71] presented evidence that the cortex often operates in a *loosely* balanced regime where partial, net, and external input currents are all of order $O(1)$. Most of these results concern sensory cortices where connectivity is lower than in the frontal cortex [77]. Higher connectivity is expected to push in the direction of tighter balance. Leaving open the possibility that tight balance may still dominate in areas with much higher connectivity (K $\sim$ 5000), such as frontal cortex.

Taken together results from [69, 71] show that strong excitation and inhibition are compatible with experimental observations, but there is no evidence for the strong feedforward drive required by the classical balanced network theory, and even some evidence against it. For this reason, alternative balance mechanisms have been explored. Notably the *sparse* balance model [72], which relies on weak external currents combined with broadly distributed synaptic weights (variance scaling as $1/\sqrt{K}$), making up for the reduced feedforward drive. This results in sparse activity, where only a small, dynamically changing subset of neurons is active at any given time, with the fraction of active neurons scaling as $1/\sqrt{K}$. While this scaling ensures finite mean input and fluctuations, it also implies that the fraction of active neurons vanishes in the thermodynamic limit ($K \to \infty$).

Alternatively, the balanced regime could rely on nonlinear mechanism. For instance, spike-frequency adaptation has been shown to restore balance in networks with highly heterogeneous connectivity [78], while facilitation can promote bistability in balanced regimes [79]. However, both studies assumed strong external inputs.Recently, Politi and Torcini [80] demonstrated that short-term synaptic depression (STD) [81] among excitatory neurons is sufficient to obtain a robust balanced state with weak external input. STD dynamically reduces the strength of excitatory synapses when neurons fire at high rates, preventing runaway excitation and allowing balance to emerge without the need for strong feedforward drive. This mechanism is robust to changes in network parameters and connectivity, and it produces irregular, asynchronous spiking activity consistent with experimental observations.

4

Numerical study in partially symmetric networks of spiking neurons

Summary Cortical activity in-vivo displays relaxational time scales much longer than the membrane time constant of the neurons or the deactivation time of ionotropic synaptic conductances. The mechanisms responsible for such slow dynamics are not understood. Here, we show that slow dynamics naturally and robustly emerges in dynamically-balanced networks of spiking neurons. This requires only partial symmetry in the synaptic connectivity, a feature of local cortical networks observed in experiments. The symmetry generates an effective, excitatory self-coupling of the neurons that leads to long-lived fluctuations in the network activity, without destroying the dynamical balance. When the excitatory self-coupling is suitably strong, the same mechanism leads to multiple equilibrium states of the network dynamics. Our results reveal a novel dynamical regime of the collective activity in spiking networks, where the memory of the initial state persists for very long times and ergodicity is broken.

4.1. Introduction

In the active cortex, neurons exhibit significant correlations in their spike counts, even when these counts are separated by lags as long as 1 second or more [9, 10, 11]. The dynamics of the membrane depolarization and the activation/deactivation of synaptic conductances have, instead, typical time scales on the order of 10ms [82]. Hence, these processes cannot account for the long-lived fluctuations of spiking activity observed in experiments.

Theoretically, there are two "minimal" scenarios to account for them. In one scenario, the long time scales are simply inherited from some slow underlying biophysical processes. For instance, both neurons [83, 84] and synapses [85] exhibit dynamics on multiple time scales, some of the order of 1-10s. We are not aware of any systematic investigation of this scenario. We note, however, that the relationship between the time scales of the microscopic (neuron/synapse) and the macroscopic (network) dynamics is far from trivial; slow microscopic dynamics does not automatically result in slow macroscopic dynamics [86]. In the other scenario, the long time scales emerge from the interaction of fast biophysical processes. In the following, we focus on this scenario.

The theory of balanced networks [87, 7, 88, 89] elegantly accounts for many non-trivial features of the cortical activity. According to this theory, in an active cortical network, the excitatory

and the inhibitory drive to single neurons are both large, but the level of activity in the network dynamically adjusts so that the net drive is around threshold. This leads to a dynamical state, the balanced regime, characterized by temporally-irregular spiking at the single-neuron level with low, heterogeneous firing rates [79, 90, 91, 92] and by weak pairwise correlations in the spiking of different neurons [89, 93], reproducing many characteristics of the patterns of activity observed in the cortex. Long relaxation times, however, are not a generic feature of *random* networks operating in the balanced regime; additional mechanisms have to be postulated.

There are presently three main proposals to explain the emergence of long time scales in cortical networks. According to one proposal, cortical networks operate close to the *edge of stability* [94, 95, 96]. Depending on the level of variability in the synaptic efficacies (synaptic gain), random networks of *rate* neurons display either a unique, stable fixed point or a chaotic attractor. Adjusting the synaptic gain suitably close to its critical level, one can achieve arbitrarily slow relaxational dynamics. As the network keeps operating in the balanced regime on both sides of the transition, pairwise correlations remain weak.

However, such a transition *does not* exist in spiking networks [94, 95]. More precisely, a "sharp" transition is recovered only when the *synaptic* time constant becomes infinitely long, so that spiking neurons effectively operate as rate elements [94, 95, 97]. Considering typical firing rates ($\sim$ 1Hz) and synaptic time constants ($10 - 100$ms) in the cortex, one expects a significant "smoothing" of the transition; in particular, the autocorrelation time remains finite regardless of the level of the synaptic gain [95]. In fact, numerical simulations show that the autocorrelation time remains of the order of the synaptic time constant when the network parameters, in particular synaptic time constants, are chosen within ranges of biological credibility [94].

According to another proposal, cortical networks are *metastable* [98, 99, 100]; see Ref. [101] for a general overview. With suitable synaptic structuring, model networks feature multiple steady states of activity, differing in the spatial distributions of "active" (high-rate) and "inactive" (low-rate) neurons. *Noise*, then, induces transitions between these states. Thus, single neurons exhibit fluctuations in their firing rate on time scales comparable with the lifetime of network's steady states. For suitably low levels of noise, these lifetimes can be significantly longer than the microscopic time constants. Furthermore, if pairs of neurons are co-active only in a small fraction of the steady states (sampled by the dynamics during the typical duration of the experiments), measured pairwise correlations remain weak [99, 100].

Achieving levels of noise suitable to match the experimental observations, however, requires significant fine-tuning; see Ref. [102] for a discussion of this point. The reason is easy to understand. Life-times much longer than the microscopic time scales require the existence of quasi-equilibrium states *à la* Kramers [103]. Accordingly, the transition rate between the different states will, to a good approximation, depend exponentially on the level of noise; see, e.g., Ref [99]. The level of noise, in turn, is controlled by the number of "active" neurons in a steady state, the strength of the recurrent synaptic couplings and the level of the external drive to the network. It is presently unclear, if neural and/or synaptic plasticity mechanisms can control these parameters with the required, exponential, precision; see, e.g., Ref [104] for a proposal based on synaptic plasticity.

A more recent and, hence, much less investigated proposal is that long time scales result from the symmetry in the synaptic connectivity [105, 106, 107]. In fact, local connectivity (i.e., on spatial scales of the order of 100 μm) in the cortex is not random. Rather, reciprocal synaptic connections are both over-represented, as compared to random networks, and stronger than average [108, 109, 110, 111, 112]. On first principles, then, one would expect a slowing down of the dynamics because of the *effective* positive self-coupling (i.e., the so-called *reaction term*; see

Sec. 4.3) generated by the symmetry. Indeed, the slowing down is observed in model networks, both of rate [105, 107, 113] and of spiking neurons [106]. A detailed investigation of the effects of symmetry on the dynamics of spiking networks, however, is still lacking. We provide here such an investigation.

We consider networks of inhibitory leaky-integrate-and-fire neurons, with arbitrary levels of symmetry in the synaptic connectivity and operating in the balanced regime, as a *minimal* model of a local cortical network. At increasing levels of symmetry, and for suitably large synaptic efficacies, we find that the neurons display large and long-lived fluctuations in their spiking rate, similarly to what is observed in *clustered* model networks and in experiments [98, 99, 100]. As the symmetry level is increased, the lifetime of the fluctuations becomes comparable to the duration of our simulations ($\sim 10^4$ seconds). Notably, this behavior is independent of the synaptic time constant and occurs in partially symmetric networks. In the parameter region where these exceptionally long-lived fluctuations exist, *interpolating* between spiking and rate neurons by progressively increasing the synaptic time constant, we find that the network dynamics exhibit multiple, *stable* fixed points.

Taken together, our results suggest that, for suitable levels of synaptic symmetry and of synaptic efficacies, the dynamics of a balanced network of spiking neurons is non-ergodic. In this parameter region, different initial conditions lead to different asymptotic states of activity.

4.2. Methods

4.2.1. The network model

We consider a network of N inhibitory LIF neurons sparsely connected so that each neuron makes and receives, K synaptic contacts on average [64, 94, 95, 114]. The neurons also receive a constant excitatory drive from outside the network. The membrane potential of neuron i, V_i, measured relative to the rest potential and in units of the threshold, evolves in time according to

$$\tau_m \dot{V}_i = -V_i + h_i(t) \tag{4.1}$$

where $\tau_m = 10$ ms is the membrane time constant and $h_i(t)$ is the total synaptic input (external and recurrent) to neuron i. Note that the synaptic input is measured in the same units as the voltage and is thus dimensionless. Whenever $V_i(t) \geq 1$, the voltage is reset to the rest potential $V_i = 0$, a spike is generated, and, as a result, postsynaptic currents (PSCs) are initiated at all the postsynaptic targets of neuron i. Then, the dynamics Eq. (4.1) resumes immediately after the spike, starting from $V_i = 0$.

The total synaptic input, $h_i(t)$, is given by

$$h_i(t) = h_{\text{ext}}\sqrt{K} - \tau_m E_i(t) \tag{4.2}$$

where $h_{\text{ext}}\sqrt{K} > 0$ is the external excitatory input and $E_i(t)$ is given by

$$\tau_s \dot{E}_i = -E_i + \frac{g_0}{\sqrt{K}} \sum_{j=1}^{N} A_{ij} \sum_n \delta(t - t_j^{(n)}) \tag{4.3}$$

where τ_s is the synaptic time constant, $g_0 > 0$ is a measure of the synaptic inhibitory strength, $A_{ij} = 1$ if there exists a synaptic connection from neuron j to neuron i ($A_{ij} = 0$ otherwise), and the sum over n is over all the spike times, $t_j^{(n)}$, of neuron j. In words, $E_i(t)$ is the linear superposition of all the PSCs generated by the spiking activity of the (presynaptic) neurons connected to neuron i. The unitary PSC, generated by a single spike (at time $t = 0$), is

$$\mathrm{PSC}(t) = \frac{g_0}{\tau_s\sqrt{K}} \mathrm{e}^{-t/\tau_s}\Theta(t) \tag{4.4}$$

where $\Theta(t)$ is the Heaviside function. Thus, the synaptic time constant, τ_s, controls the duration of the PSCs. In the limit $\tau_s \to 0$, instantaneous synaptic currents, $E_i(t)$ becomes (see Eq. (4.3))

$$E_i = \frac{g_0}{\sqrt{K}} \sum_{j=1}^{N} A_{ij} \sum_n \delta(t - t_j^{(n)}) \tag{4.5}$$

Note that synaptic currents are measured in units of 1/time (e.g., in Hz).

The unitary PSC, Eq. (4.4), is proportional to $1/\sqrt{K}$, so that $E_i(t) \sim \sqrt{K}$ scales with K as the external drive, see Eq. (4.2). To have $h_i(t) \sim 1$ when K is large ($1 \ll K \ll N$), the recurrent synaptic input, $\tau_m E_i(t)$, should cancel (i.e., to leading order) on average the external drive, $h_{\mathrm{ext}}\sqrt{K}$. Thus, the network operates in the dynamically-balanced regime when K is large [7, 89]. All the simulations described in Results are with $N = 4000$, $K = 1200$ and $h_{\mathrm{ext}} = 0.1$.

Synaptic connectivity

The synaptic connectivity matrix, $\mathbf{A} \equiv (A_{ij})$, is generated in the following way [106]. For each *ordered* pair of neurons (i, j), the probability, p_{B}, that they are reciprocally connected, i.e., $(A_{ij} = 1, A_{ji} = 1)$, is given by

$$p_{\mathrm{B}} = q \cdot \frac{K}{N} + (1 - q)^2 \cdot \frac{K^2}{N^2} \tag{4.6}$$

while the probability, p_{U}, that they are unidirectionally connected, i.e., $(A_{ij} = 1, A_{ji} = 0)$, is given by

$$p_{\mathrm{U}} = (1 - q) \cdot \frac{K}{N} - (1 - q)^2 \cdot \frac{K^2}{N^2} \tag{4.7}$$

where the parameter q, $0 \le q \le 1$, controls the over-representation of reciprocal connections, i.e., the level of symmetry. In experiments, this over-representation is often quantified in by the ratio, η, between the number of *observed* reciprocally-connected pairs of neurons divided by the *expected* number of reciprocally-connected pairs in a directed Erdős-Rényi network with the same probability of connection [108, 112]. The probability of connection is simply estimated by dividing the number of connected pairs by the number of pairs sampled in the experiment. In our case,

$$\eta = \frac{p_{\mathrm{B}}}{(p_{\mathrm{B}} + p_{\mathrm{U}})^2} = \frac{q}{K/N} + (1 - q)^2 \tag{4.8}$$

Hence, $\eta = 1$ for $q = 0$ and the network is simply a directed Erdős-Rényi network, while $\eta = N/K$ for $q = 1$ and all connections are reciprocal, i.e., the network is fully symmetric.

We note that, while q is independent of the probability of connection (i.e, K/N), η is not. In particular, the largest possible value of η is the reciprocal of the probability of connection. Hence, larger probabilities of connection necessarily result in lower values of η, regardless of the actual level of symmetry, measured more properly by q. For instance, in the cortex local excitatory-to-excitatory connections occur with probability ~ 0.1 and $\eta \simeq 5$ [112]; this leads to $q \simeq 0.5$ using Eq. (4.8) (taking, obviously, the solution with $0 \leq q \leq 1$). Inhibitory-to-inhibitory connections, instead, occur with probability ~ 0.3 and $\eta \simeq 3$ [112]; this leads to $q \simeq 0.9$. Hence, though η is larger for the excitatory-to-excitatory network, the inhibitory-to-inhibitory network is more "symmetric". Indeed, about 90% of its connections are bi-directional against only about 50% in the excitatory-to-excitatory network.

Network simulations

We have employed event-driven techniques to simulate the network dynamics. This allowed us to perform fast and accurate simulations of large networks. In fact, the differential equations, Eqs.(4.1)-(4.3), describing the network dynamics are exactly integrated between consecutive spikes. This can be done by rewriting the evolution of the V_i's and of the E_i's as a mapping between their value at a spiking event occurring at time t^n and their value at the next spiking event at t^{n+1} [115].

The identity of the neuron firing at the next spiking event and the time, t^{n+1}, at which the event occurs can be determined in the following way. Suppose that neuron k has fired at the current spiking event, at time t^n. Then, $V_k\left(t_+^n\right) = 0$ (as a result of the resetting) and

$$E_i\left(t^{n,+}\right) = E_i\left(t^{n,-}\right) + \frac{g_0}{\sqrt{K}}\frac{A_{ik}}{\tau_s} \tag{4.9}$$

where $t^{n,\pm} \equiv t^n \pm \epsilon$ for $\epsilon \to 0^+$ is the time immediately after/before the spike. After a time interval Δ, if no other spike occurs, we have

$$E_i\left(t^{n,+} + \Delta\right) = E_i\left(t^{n,+}\right) e^{-\Delta/\tau_s} \tag{4.10}$$

and

$$\begin{aligned} V_i\left(t^{n,+} + \Delta\right) = {} & h_{\text{ext}}\sqrt{K} + \left(V_i\left(t^{n,+}\right) - h_{\text{ext}}\sqrt{K}\right) e^{-\Delta/\tau_m} \\ & - e^{-\left(t^{n,+}+\Delta\right)/\tau_m} \int_{t^{n,+}}^{t^{n,+}+\Delta} \mathrm{d}t\; e^{t/\tau_m} E_i\left(t\right) \end{aligned} \tag{4.11}$$

The last term on the r.h.s. is

$$-E_i\left(t^{n,+}\right)\frac{\tau_m\tau_s}{\tau_m - \tau_s}\left(e^{-\Delta/\tau_m} - e^{-\Delta/\tau_s}\right) \tag{4.12}$$

Using Eqs. (4.11) and (4.12), we can determine the next spiking time, relative to t^n, for each neuron i if no other spike occurs before, i.e., Δ_i such that $V_i\left(t^{n,+} + \Delta_i\right) = 1$ for each i. Then, the next *actual* spiking event occurs at time

$$t^{n+1} = t^n + \min_i \Delta_i \tag{4.13}$$

and the identity of the neuron spiking at t_{n+1}, m, is simply

$$m = \arg\min_i \Delta_i \tag{4.14}$$

that is, the neuron i for which Δ_i achieves its minimum value.

In the case of instantaneous synapses, we use Eq. (4.5) into Eq. (4.11), and the last term on the r.h.s. of Eq. (4.11) is now

$$-\frac{g_0}{\sqrt{K}} A_{ik} e^{-\Delta/\tau_m} \tag{4.15}$$

4.2.2. Observables

Single-neuron firing activity

The single-neuron activity has been characterized in terms of the following observables:

The firing rate. For each neuron i, we obtained its *average* firing rate, ν_i, by counting all the spikes that the neuron fired during the simulation and then dividing the spike count by the total simulation time, T. The population-averaged firing rate, $\langle \nu \rangle$, is given by

$$\langle \nu \rangle = \frac{1}{N} \sum_{i=1}^{N} \nu_i \tag{4.16}$$

Estimates of the ν_i's were obtained by using simulations with $T = 1000$s or longer. In some cases (see, e.g., Fig. 4.4), we also estimated the *instantaneous* firing rate of neuron i, r_i, that is, the firing rate in a given time window of duration $\Delta < T$. This was obtained by counting only the spikes that the neuron fired *within* the time window and then dividing this spike count by Δ.

The coefficient of variation. The coefficient of variation of neuron i, CV_i, is the ratio between the standard deviation of its inter-spike intervals and the average of its inter-spike intervals [82]. CV_i provides a simple quantification of the degree of temporal irregularity of the spiking process. If neuron i spikes periodically, then $CV_i = 0$; if neuron i spikes according to a Poisson process, then $CV_i = 1$. The average and standard deviation of the inter-spike intervals have been estimated with simulations of $T = 1000$ s.

Pairwise spike-count correlations

We choose the bin size $\Delta = 100$ ms and divide the interval $[0, T]$, where T is the total duration of the simulation, into T/Δ non-overlapping bins. Then, for each neuron i we compute

$$\delta n_i(k) = -\nu_i \Delta + \int_{(k-1)\Delta}^{k\Delta} \mathrm{d}t \sum_a \delta(t - t_i^{(a)}) \tag{4.17}$$

where $k = 1, \ldots, T/\Delta$ is the bin number, ν_i is the average firing rate of neuron i estimated in $[0, T]$, and the sum over a is over all the spike times, $t_i^{(a)}$, of neuron i; $\nu_i \Delta$ is the expected spike count in a time bin Δ. Hence,

$$\langle \delta n_i \rangle \equiv \frac{\Delta}{T} \sum_{k=1}^{T/\Delta} \delta n_i (k) = 0 \tag{4.18}$$

for each $i = 1, \ldots, N$. Then, for each pair of neurons (i, j), ρ_{ij} is computed as

$$\rho_{ij} = \rho_{ji} = \frac{\langle \delta n_i \delta n_j \rangle}{\sqrt{\langle \delta n_i^2 \rangle \langle \delta n_j^2 \rangle}} \tag{4.19}$$

and it lies between -1 and 1.

Autocorrelation of the synaptic input
For each neuron i, we compute

$$\delta h_i (t) = h_i(t) - \frac{1}{T} \int_0^T \mathrm{d}t \; h_i (t) \tag{4.20}$$

where T is the total duration of the simulation. In the case of instantaneous synapses, we low-pass filter $h_i (t)$ with a cutoff frequency $f_c = 50$Hz before using Eq. (4.20). Hence,

$$\overline{\delta h_i} \equiv \frac{1}{T} \int_0^T \mathrm{d}t \; \delta h_i (t) = 0 \tag{4.21}$$

for each $i = 1, \ldots, N$. We define the *normalized* autocorrelation, $C_i (\tau)$, of the input to neuron i at a time lag τ as

$$C_i (\tau) \equiv \frac{1}{\overline{\delta h_i^2} (T - \tau)} \int_0^{T-\tau} \mathrm{d}t \; \delta h_i (t) \, \delta h_i (t + \tau) \tag{4.22}$$

so that $C_i (0) = 1$ for each $i = 1, \ldots, N$. Finally,

$$C (\tau) \equiv \frac{1}{N} \sum_{i=1}^{N} C_i (\tau) \tag{4.23}$$

Spike-triggered input
For each neuron i and lag τ, we define $Z_i (\tau)$ as the set of spike numbers, n, for which $t_i^{(n)} + \tau < t_i^{(n+1)}$ if $\tau > 0$, or the n's for which $t_i^{(n)} + \tau > t_i^{(n-1)}$ if $\tau < 0$. Thus, if $n \in Z_i (\tau)$, there are no spikes between $t_i^{(n)}$ and $t_i^{(n)} + \tau$.

The spike-triggered average input to neuron i at lag τ, $\mathrm{STA}_i (\tau)$, is given by

$$\mathrm{STA}_i(\tau) = \frac{1}{|Z_i(\tau)|} \sum_{n \in Z_i(\tau)} \left(h_i\left(t_i^{(n)} + \tau\right) - \overline{h_i} \right) \tag{4.24}$$

where $|Z_i(\tau)|$ is the number of elements in $Z_i(\tau)$, the sum is restricted to elements in $Z_i(\tau)$ and $\overline{h_i}$ denotes the average of $h_i(t)$ over time, i.e.,

$$\overline{h_i} \equiv \frac{1}{T} \int_0^T \mathrm{d}t \; h_i(t) \tag{4.25}$$

We low-pass filtered $h_i(t)$ with a cutoff frequency $f_c = 100$ Hz before computing Eqs. (4.24) and (4.25). By averaging over neurons, we finally obtain the spike-triggered average input, $\mathrm{STA}(\tau)$, shown in Fig. 4.2, i.e.,

$$\mathrm{STA}(\tau) = \frac{1}{N} \sum_{i=1}^{N} \mathrm{STA}_i(\tau) \tag{4.26}$$

Ergodic "distance"

To investigate the ergodicity of the network dynamics, we consider M different *physical* replicas of the same network. Each replica is the time evolution of the network starting from different initial conditions. Then, for two different replicas, α and β, we compute

$$\begin{aligned} D^{\alpha\beta}(T) &= \frac{1}{N} \sum_{i=1}^{N} \left[\frac{n_i^{\alpha}(T)}{T} - \frac{n_i^{\beta}(T)}{T} \right]^2 \\ &= \frac{1}{N} \sum_{i=1}^{N} \left[\nu_i^{\alpha}(T) - \nu_i^{\beta}(T) \right]^2 \end{aligned} \tag{4.27}$$

where $n_i^{\alpha}(T)$ is the spike count of the neuron i up to time T in replica α and $\nu_i^{\alpha}(T)$ is the corresponding firing rate. By averaging over all the distinct pairs of replicas, we finally obtain $D(T)$ [107], that is,

$$D(T) = \frac{2}{M(M-1)} \sum_{\alpha \neq \beta} D_{\alpha\beta}(T) \tag{4.28}$$

4.3. Results

As a paradigmatic example of a network operating in the balanced regime, we consider N randomly and sparsely connected inhibitory neurons receiving a constant, excitatory input from the outside [64, 94, 95, 114]. Single-neuron dynamics is described by the standard leaky integrate-and-fire (LIF) mechanism [82]. Each neuron randomly makes $K (\ll N)$ synaptic contacts, on average, with the other neurons. In order to obtain a dynamically-balanced dynamics [7, 89], we assume that the efficacy of the synaptic contacts is $-g_0/\sqrt{K}$ with $g_0 > 0$, so that the recurrent synaptic input is proportional to $\sqrt{K}$ and negative, and that the external excitatory input to each neuron is $h_{\mathrm{ext}}\sqrt{K}$ with $h_{\mathrm{ext}} > 0$.

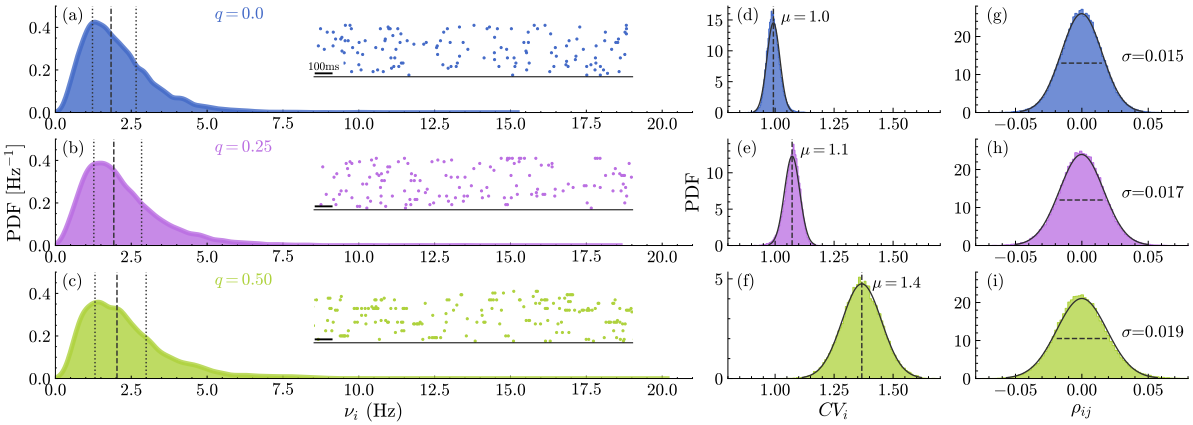

Figure 4.1: (a)–(c) PDFs of the single-neuron firing rates $\{\nu_i\}$. Dashed lines denote the mean and the dotted lines represent the first and third quartiles. The insets display the activity of thirty randomly selected neurons. (d)–(f) PDFs of the coefficients of variation $\{CV_i\}$ of individual neuron firing rates. The dotted vertical lines indicate the means of the PDFs. (g)–(i) PDFs of the pairwise correlation coefficients ρ_{ij} of the neuronal firing activity. The dotted horizontal lines indicate the full widths at half maximum of the PDFs. The solid black curves in (d)–(f) and (g)–(i) represents Gaussian fits to the data, the corresponding mean and standard deviation are denoted by μ and σ, respectively. The top row (blue) corresponds to $q = 0.0$; the middle row (magenta) to $q = 0.25$ and the bottom one (green) to $q = 0.5$. The PDFs were obtained by aggregating data from 10 independent replicas. Simulation parameters: $N = 4000$, $K = 1200$, $g_0 = 5$, and $h_{\text{ext}} = 0.10$.

We control the level of symmetry in the network by manipulating the probability of reciprocal connection between pairs of neurons [106]. The *excess reciprocity*, η, defined as the ratio between the probability of finding reciprocally connected neurons and the probability of reciprocal connections in a random network (i.e., directed Erdős-Rényi with the same probability of connection K/N) is given by (see Sec. 4.2 for details)

$$\eta = \frac{q}{K/N} + (1-q)^2 \tag{4.29}$$

where $0 \leq q \leq 1$. For $q = 0$, the network is simply a random network ($\eta = 1$), while for $q = 1$ the network is fully symmetric ($\eta = N/K$; all connections are reciprocal). Experimental estimates of the probability of local connections (0.1-0.3) and of the excess reciprocity (3-5) in the cortex [112] lead to $0.4 \leq q \leq 0.9$. In particular, we note that the inhibitory-to-inhibitory network in the cortex is close to fully symmetric, i.e., $0.8 \leq q \leq 0.9$.

We start by considering the case of instantaneous synaptic currents (see Sec.4.2.1 for details), i.e., when a neuron fires a spike, it instantaneously *reduces* the voltage of its postsynaptic targets by $g_0/\sqrt{K}$. In the absence of pairwise correlation in the synaptic connectivity (i.e., $q = 0$), our model network operates in the balanced regime when $K \gg 1$. In this regime, the large excitatory drive (the external input) is dynamically offset by the comparably large inhibitory drive (the recurrent input), resulting in the unsaturated, temporally irregular, and asynchronous spiking of the neurons in the network [7, 89]. This regime is illustrated in Fig. 4.1. In Fig. 4.1 (a) we show the distribution of firing rates in the network; as can be seen it is right-skewed and long-tailed, and, it can be well approximated by a log-normal distribution (not shown) [91, 92]. Moreover, the population-averaged firing rate, $\langle \nu \rangle = 2.1$Hz, is in good agreement with the value, ν_{B}, predicted by the balance condition in the limit $K \to \infty$, that is, $\nu_{\text{B}} = h_{\text{ext}}/(\tau_m g_0) = 2$ Hz where $\tau_m = 10$ ms is the membrane time constant [64, 114]. As expected in the balanced regime, spiking is irregular, as assessed by the coefficient of variation (CV) of the inter-spike intervals of single neurons (Fig. 4.1 (d)), and asynchronous, as assessed

by the zero-lag cross-correlation of the spike counts of different neurons (Fig. 4.1 (g)) [89, 93].

Increasing the levels of symmetry up to $q = 0.5$ does not affect these features qualitatively; spiking activity remains unsaturated, temporally irregular and asynchronous. There are some quantitative changes, however. First, the distribution of firing rates becomes more skewed while the population-averaged firing rate remains approximately constant, as can be seen by comparing Fig. 4.1 (b-c) with Fig. 4.1 (a): $\langle \nu \rangle$ varies from 2.1 Hz for $q = 0$ to 2.3 Hz for $q = 0.5$. Second, the temporal irregularity of the spike trains increases, as can be seen in Fig. 4.1(e-f); the population-averaged coefficient of variation, $\langle CV \rangle$, increases from 1 for $q = 0$ to 1.4 for $q = 0.5$. However, there are no noticeable changes in the level of "asynchrony", as can be seen in Fig. 4.1(h-i). Thus, the network continues to operate in the balanced regime.

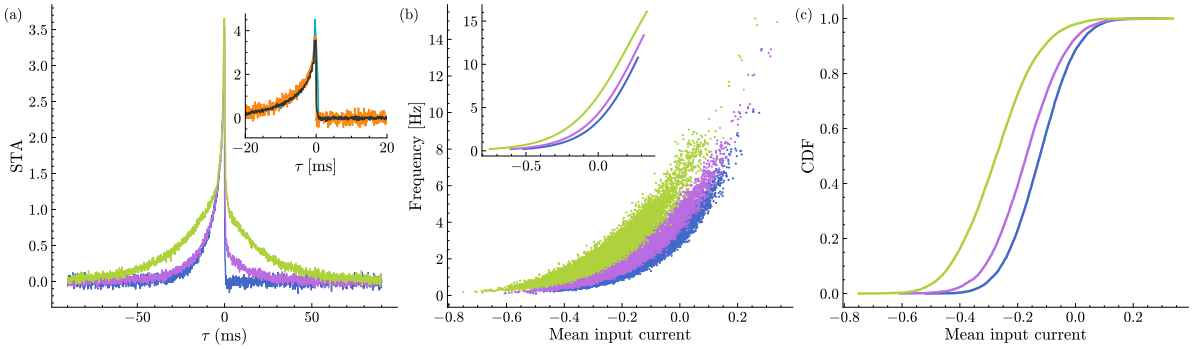

Figure 4.2: (a) Spike-triggered average input STA(τ) for $q = 0.0$ (blue), $q = 0.25$ (magenta) and $q = 0.5$ (green). In the inset of (a) we compare the STA obtained from the network simulations (grey), with a single neuron's dynamics under the diffusive approximation [15] (sky blue) and subject to Poissonian shot noise (orange). (b) Firing rates of the neurons versus the time averaged (mean) input currents for different levels of symmetry in the network $q = 0.0$ (blue), $q = 0.25$ (magenta), $q = 0.5$ (green); the Population Frequency-Input curves are shown in the inset and obtained by fitting the logistic function to the raw data (details in [116]). (c) Cumulative distribution functions (CDFs) of the mean input currents. The curves reported in (a) were obtained by averaging over 200, 000 spike events, while data in (b) and (c) has been obtained by averaging over a time interval of 250 seconds. Same parameters used as in Fig.4.1

As we shall explain shortly, these quantitative changes are a consequence of the *effective* positive feedback generated by the symmetry in the synaptic connectivity (see also Ref. [106]). First, let us discuss the mechanism generating the positive feedback.

Consider neuron i; every time it fires a spike, it delays spiking in its postsynaptic targets. Indeed, upon spiking, neuron i reduces the voltage of its postsynaptic targets by $g_0/\sqrt{K}$ and, hence, transiently reduces their instantaneous probability of spiking by a factor $\sim 1/\sqrt{K}$ (for $K \gg 1$). This is simply a consequence of the fact that the neurons are inhibitory. In the presence of symmetry, many of the postsynaptic targets of neuron i are also its presynaptic neurons, that is, a fraction q (on average). A reduction $\sim 1/\sqrt{K}$ in the probability of spiking of one of these neurons, then, leads to a reduction $\sim g_0/K$ in the (average) inhibitory input to neuron i. As there are $\sim qK$ of them, the total reduction is ~ 1 (i.e., independent of K, when $K \gg 1$). As a result, the *net* synaptic input received by neuron i *following* its spike is transiently increased, because of the (transiently) reduced probability of spiking of its inhibitory presynaptic neurons. The typical size of this positive feedback is ~ 1 and, hence, the balanced regime is unaffected by it [106].

The presence of such a positive feedback is readily revealed by the analysis of the spike-triggered average input, STA(τ) (see Sec. 4.2.2 for details), where τ is time relative to spike emission ($\tau = 0$). Let us consider first the case $q = 0$, where no positive feedback is expected. The corresponding STA(τ) is the blue curve in Fig. 4.2 (a). As can be seen, STA(τ) increases above

baseline briefly *before* the spike (i.e., $\tau < 0$), reflecting the fact that spikes are generated by suitably large, positive fluctuations in the input, and drops back to baseline immediately *after* the spike (i.e., $\tau > 0$), indicating that there is no *consistent* effect of the spike on subsequent inputs. As can be seen in the inset of Fig. 4.2 (a), this is the same STA(τ), for all practical purposes, that one obtains from a LIF neuron driven by white noise [15] or by shot noise (i.e., a Poissonian spike train inducing finite-amplitude postsynaptic potentials), where, by construction, there is no correlation between spikes and synaptic inputs.

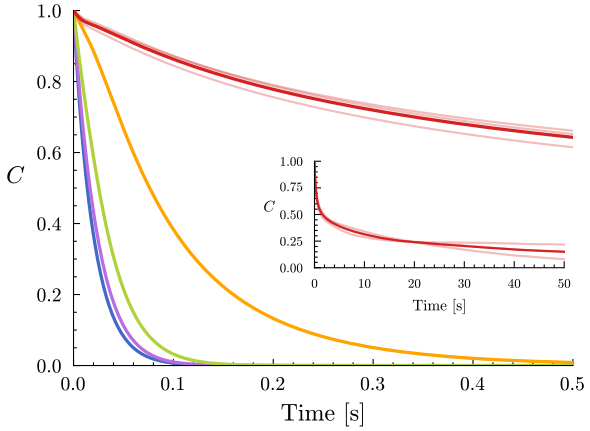

Figure 4.3: The autocorrelations are shown as a function of the time lag for different levels q of symmetry in the synaptic connections: $q = 0.0$ (blue), $q = 0.25$ (magenta), $q = 0.5$ (green), $q = 0.8$ (orange) and $q = 0.9$ (red). The inset shows a zoomed-in view for $q = 0.9$, where different shades of the red color denotes different initial conditions. The autocorrelations were averaged over 500 selected neurons and over 3 replicas. The same parameters as in Fig.4.1 were used.

As expected, the situation changes when the level of symmetry is increased. For $q = 0.25$, we see that STA(τ) remains significantly above the baseline for about 20 ms after the spike (magenta curve in Fig. 4.2 (a)). This "after-spike transient" in the synaptic input is further amplified, both in amplitude and duration, when $q = 0.5$ (green curve in Fig. 4.2 (a)). It is convenient to quantify the strength of the positive feedback, R, by integrating the spike-triggered average input for positive τ [117], i.e.,

$$R \equiv \int_0^{+\infty} \mathrm{d}\tau \ \mathrm{STA}\,(\tau) \tag{4.30}$$

For $q = 0$, we find $R \simeq 0.1$ ms, while $R \simeq 6$ ms for $q = 0.25$ and $R \simeq 24$ ms for $q = 0.5$.

With Fig. 4.2 (a) in mind, it becomes easier to understand the effects of the symmetry on the patterns of spiking activity, illustrated in Fig. 4.1. Let us start with the temporal structure of the spike trains. The presence of the positive feedback makes spiking a self-exciting process: firing a spike increases, transiently, the probability of firing another spike shortly. The strength of the self-excitation (i.e., R defined above) increases with increasing levels of symmetry (see Fig. 4.2 (a)) which, in turn, leads to an increasing tendency to fire spikes in "bursts". As a result, the mean coefficient of variation $\langle CV \rangle$ increases with q.

Next, let us consider the effect on the distribution of firing rates. At parity of synaptic input, the firing rate of a neuron increases with the level of symmetry q (and hence R). This is illustrated in Fig. 4.2 (b), where we plot the firing rates of the neurons in the network as a function of their time-averaged synaptic input, for the same values of q (and using the same color coding) as in Fig. 4.1. In the inset, we plot the population Frequency-Input (F-I) curves, obtained by fitting the data in the main panel with a logistic function [116].

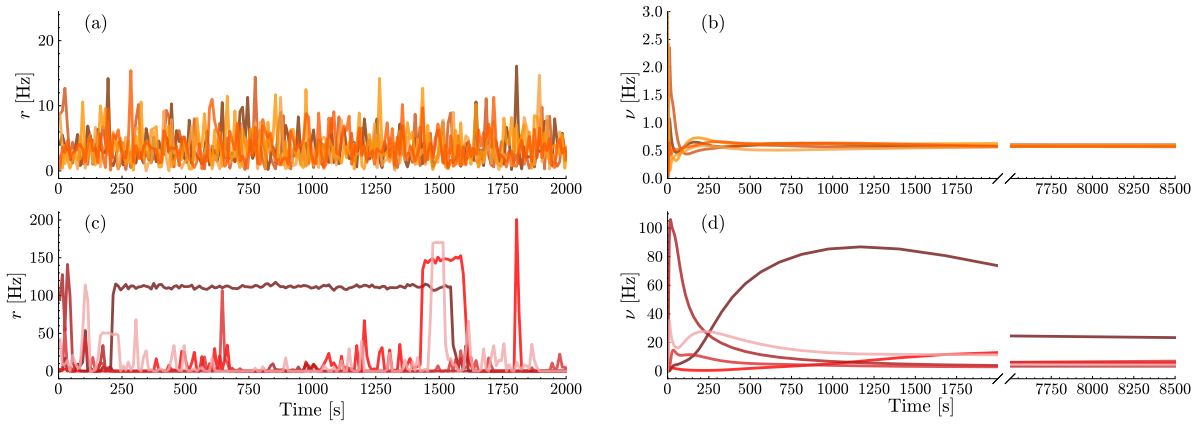

Figure 4.4: (a),(c) The "instantaneous" firing rate for the same neuron and replicas, using time bins of $\Delta = 10$ seconds, for 5 different replicas for $q = 0.8$ (orange) and $q = 0.9$ (red). Different shades of the main color represent different replicas. (b),(d) Running averages of the firing rate of a single selected neuron versus time. All other parameters are the same as in Fig. 4.1.

However, the population-averaged firing rate $\langle \nu \rangle$ cannot change dramatically. This is due to the fact that $\langle \nu \rangle$ is essentially fixed (i.e., within $O\left(1/\sqrt{K}\right)$) to ν_B by the balance condition, and the value of ν_B is independent of q. To "solve" this apparent contradiction, the distribution of the firing rates adjusts so as to reduce the time-averaged synaptic inputs while (approximately) preserving the population-averaged firing rate. This reduction is illustrated in Fig. 4.2 (c). The reduction of the time-averaged synaptic inputs leads to an increase in the fraction of both low-firing and high-firing neurons with increasing q, as clearly visible in the inset of Fig. 4.2 (b).

As a consequence of the increased tendency of neurons to fire spikes in bursts, we expect large, positive correlations between the synaptic inputs (to the same neuron) at time lags longer than the membrane time constant ($\tau_m = 10$ ms). We also expect these correlations to persist over longer lags as q increases. This is confirmed in Fig. 4.3, where we plot the population-averaged autocorrelation function of the synaptic inputs, $C(t)$, for different values of q (see Sec. 4.2.2 for details).

As can be seen, consistent with the expectations, $C(t)$ is non-negative, and the time it takes to decay to 0 gets longer with increasing q. For levels of symmetry up to $q = 0.8$, $C(t)$ is well fitted by a single exponential decay, i.e., $C(t) = e^{-t/\tau_C}$ for $t \geq 0$. The time constant τ_C, extracted from the fit, provides a simple quantification of the decay time. For $q = 0$ (blue curve), we find $\tau_C \simeq 20$ ms, while for $q = 0.8$ (orange curve), we find $\tau_C \simeq 100$ ms.

At $q = 0.9$ (red curve), however, the behavior of $C(t)$ changes dramatically. As can be seen in the inset of Fig. 4.3, $C(t)$ remains significantly different from 0 at $t = 50$ s; three orders of magnitudes larger than τ_m. Also, the decay of $C(t)$ is clearly different from a single exponential decay; indeed, it features at least two time scales. Finally, $C(t)$ displays noticeable fluctuations even at short lags when re-estimated (i.e., in the same network) starting from different initial conditions (lighter-red curves). For $q \leq 0.8$, the same re-estimation procedure produces virtually identical $C(t)$ (not visible in Fig. 4.3 since they are essentially overlapping).

Thus, the analysis of $C(t)$ reveals a *qualitative* change in the network dynamics, occurring between $q = 0.8$ and $q = 0.9$. For $q = 0.8$, the fluctuations in the activity decay exponentially at long time lags, suggesting that the network dynamics has reached a stationary state. For $q = 0.9$, the fluctuations in the activity do not decay exponentially; rather, they persist for a time comparable with the duration of the simulations, suggesting that the network dynamics

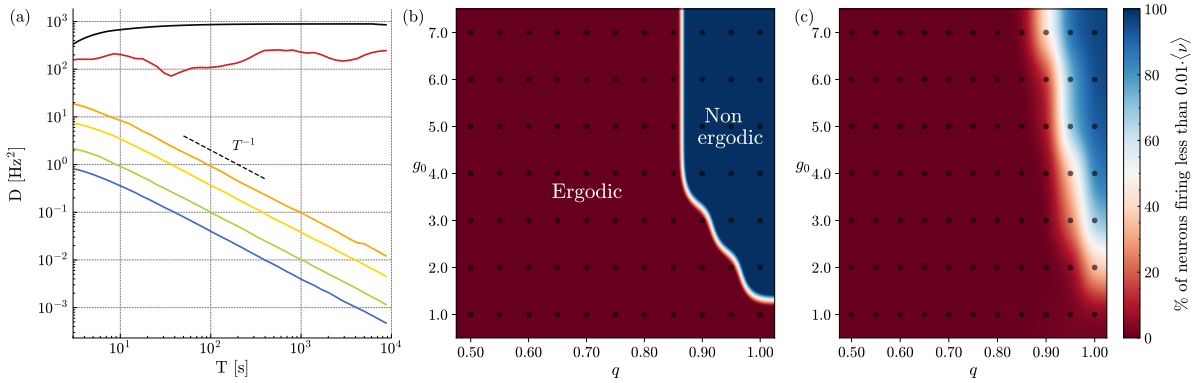

Figure 4.5: (a) D as a function of time for different values of q: $q = 0$ (blue), $q = 0.5$ (green), $q = 0.7$ (yellow), $q = 0.8$ (orange), $q = 0.9$ (red), $q = 1.0$ (black). Five realizations (replicas) of the same network have been considered to estimate D. (b) Bidimensional phase diagram in the (q, g_0) plane, showing the ergodic and non-ergodic regimes in the red and blue regions, respectively. (c) Percentage of neurons with a firing rate lower than $0.01\langle\nu\rangle$ (i.e., almost silent). The black dots in (b-c) indicate the parameter values for which the reported quantities in the plane have been measured. All other parameters are fixed as in Fig. 4.1.

has not reached a stationary state.

To better understand the dynamical mechanism responsible for such long memory in the fluctuations, we simulated the dynamics in the *same* network starting from *different* initial conditions, that is, different values of neurons' membrane potentials at time $t = 0$.

In Fig. 4.4 (a), we plot the time course of the firing rate of a randomly chosen neuron for 5 different initial conditions, at $q = 0.8$. The firing rate is estimated in consecutive, non-overlapping bins of duration 10s. The 5 corresponding time series appear "stationary", consistent with the analysis of $C(t)$ (see Fig. 4.3). Indeed, this is expected if the spike trains for the different initial conditions were simply different realizations of the same "underlying", constant (i.e., on time scales longer than τ_C) firing rate. To qualify this statement, for each initial condition, we have estimated the firing rate by counting all the spikes occurring between $t = 0$ and $t = T$. As can be seen in Fig. 4.4 (b), these estimates converge to the same value at increasing T, regardless of the initial condition.

The same analysis for $q = 0.9$ is shown in Fig. 4.4 (c). In this case, the time series for the different initial conditions clearly do not resemble different realizations of the same "underlying", constant firing rate. One can see large (up to $\sim$ 100 Hz) and very long-lived (up $\sim$ 1000 s) fluctuations in the firing rates (estimated in 10 s bins). It is not even clear that one can meaningfully define the "firing rate" of this neuron. Indeed, the procedure of estimating the firing rate, as above, by counting spikes in increasingly long time windows returns different values depending on the initial condition (Fig. 4.4 (d)).

By definition, the dynamics is ergodic when the long-time average of any (sufficiently well-behaved) observable asymptotically converges to the same value, independently of the initial condition. In our case, the observable is the number of spikes in a time window T, and its long-time average is the "firing rate", that is, the probability of observing a spike per unit of time. As just shown, this property is satisfied for $q = 0.8$, and it is not satisfied for $q = 0.9$. The foregoing analysis, thus, reveals that the network dynamics is *not* ergodic at $q = 0.9$.

We use the asymptotic convergence of firing rates to systematically study ergodicity breaking as a function of the level of symmetry, q, and of the synaptic efficacy, g_0. Specifically, we define a function of T, $D(T)$, which quantifies the difference among the firing-rate estimates, over a time

window T, obtained from different initial conditions (see Sec. 4.2.2 for details). We classify the dynamics as ergodic when $D(T)$ decays as $1/T$ for $T \to \infty$ [118], and as non-ergodic otherwise. Note that changes in g_0 at fixed h_{ext}, the strength of the external drive, result in changes in the population-averaged firing rate, $\langle \nu \rangle$. In the region of the (q, g_0) plane that we have explored numerically, $\langle \nu \rangle$ ranges between about 1 Hz (for $g_0 = 7$) and about 5 Hz (for $g_0 = 2$).

Consistent with the results illustrated in Figs. 4.3 and 4.4, $D(T) \to 0$ as $1/T$ for $q \leq 0.8$, while for $q \geq 0.9$, $D(T)$ does not decay, even when firing rates are estimated over time intervals as long as $T = 10^4$ s (see Fig. 4.5 (a)). In fact, as illustrated in Fig. 4.5 (b), ergodicity breaking occurs in a whole region of the (q, g_0) plane. As can be seen, ergodicity breaking requires large values of q, the level of symmetry in the synaptic connectivity. However, symmetry alone is not sufficient; synaptic efficacies have to be large enough. For instance, for $g_0 < 1.25$, the network dynamics is ergodic at $q = 1.0$ (Fig. 4.5 (b)).

The breaking of ergodicity is accompanied by the appearance of "silent" neurons. This is illustrated in Fig. 4.5 (c), where we report the fraction of neurons firing at less than $0.01\langle \nu \rangle$ as a function of q and g_0. These neurons would be hardly detectable in experiments [119]. As can be seen, for $q \geq 0.9$ and $g_0 \geq 3$, more than half of the neurons in the network are "almost silent" (up to 87% at $q = 1.0$). By contrast, there are no silent neurons at $q = 0.7$. The identity of the almost silent neurons and hence, of the active ones changes depending on the initial condition. In other words, in the region where ergodicity is broken, the network dynamics exhibits multiple, (very) long-lived states of activity differing in their spatial distribution of "active" and "silent" neurons. The fact that we were able to make such an observation by using a small number of initial conditions (i.e., 5) suggests that the network dynamics can, indeed, exhibit a very large number of such states.

What is the mechanism responsible for ergodicity breaking in our model network? Generally speaking, ergodicity breaking results from the fact that the dynamics is for very long times, or even permanently, restricted to different regions of the phase space depending on the initial conditions. Perhaps the simplest scenario for the emergence of such "trapping regions" is the co-existence of multiple, stable equilibria, e.g., different fixed points of the microscopic dynamics. However, our network does not have fixed points *stricto sensu*, i.e., states in which the voltage of all neurons is constant in time; this would correspond to a completely silent network. To assess the relevance of the above scenario in our model network, therefore, we introduce a synaptic time constant, τ_s (see Sec. 4.2.1 for details). Roughly speaking, this leads to synaptic inputs proportional to the "average", rather than the "instantaneous", presynaptic activity, effectively reducing their (fast) temporal fluctuations. The time window over which the presynaptic activity is averaged is controlled by τ_s. The network we have studied so far corresponds to $\tau_s = 0$. In the opposite limit, i.e., $\tau_s \to \infty$, the fast fluctuations due to spiking disappear, and the dynamics can be described by a rate model [95, 94]. Note that the time-averaged input to a neuron does not depend on τ_s.

We start by investigating how the ergodic properties of the network dynamics are affected by τ_s. To this end, we compute the ergodic distance, $D(T)$, for different values of τ_s and q, for $g_0 = 5$. For this value of g_0, ergodicity is broken between $q = 0.8$ and $q = 0.9$ in the network with $\tau_s = 0$ (see Fig. 4.5). To properly compare the behavior of $D(T)$ at different values of $\tau_s > 0$, we measure time in units of τ_s, i.e., $\tilde{T} = T/\tau_s$.

If the breaking of ergodicity in our model network is associated with the appearance of stable fixed points in the "corresponding" rate model (i.e., the same network in the limit $\tau_s \to \infty$), then one would expect that the region in the parameter space in which ergodicity is broken does not shrink with increasing τ_s; rather, it could increase. This is indeed what we observe.

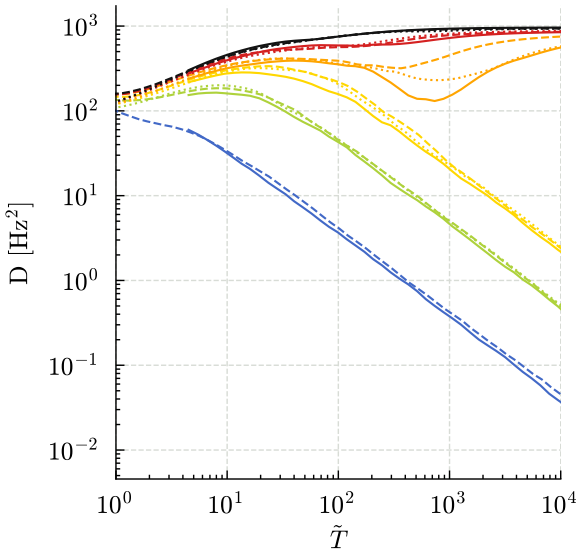

Figure 4.6: D as a function of $\tilde{T}$ for exponentially decaying synapses with different values of q and of the synaptic time constant: namely, $\tau_s = 0.02$ s (solid lines); 0.1 s (dashed lines); and 1 s (dotted lines). The colors refer to $q = 0$ (blue), $q = 0.5$ (green), $q = 0.7$ (yellow), $q = 0.8$ (orange), $q = 0.9$ (red), and $q = 1.0$ (black). These results were obtained using five replicas; other parameters are fixed as in Fig. 4.1

As can be seen in Fig. 4.6 (a), the dynamics remain non-ergodic for $q \geq 0.9$, regardless of the value of τ_s. However, now the dynamics is non-ergodic already at $q = 0.8$ for $\tau_s = 0.02$s, and remains so by further increasing τ_s. By contrast, the dynamics remain ergodic at $q = 0.7$ even for $\tau_s = 1$s. We conjecture that this is because there are no stable fixed points, in the limit $\tau_s \to \infty$, in the network at $q = 0.7$. However, it is also conceivable that, instead, stable fixed points will appear for $\tau_s > 1$s, and hence ergodicity will be broken for larger values of τ_s. For practical reasons, i.e., simulations run times, we have systematically explored only $\tau_s \leq 1$s. In any case, we do not expect the dynamics to become non-ergodic at $q = 0$ because there are no *stable* fixed points in the network, even in the limit $\tau_s \to \infty$.

It is very insightful to visualize ergodic and non-ergodic dynamics in the network. For this purpose, we use the "projection" of the network dynamics into the three-dimensional space (h_1, h_2, h_3), where h_i denotes the total synaptic input to neuron i. In Fig. 4.7, we show these projections for five different initial conditions in the same network, with different colors denoting different initial conditions. In the top row, we illustrate the case $q = 0.8$ and $\tau_s = 0$ (in this case, $\tilde{T} = T$). As can be seen, there is no evident separation between the representative points at any time; the orbits for the different initial conditions fill "densely" the *same* volume in the phase space. That this is not an artifact of the low-dimensional projection is, indeed, confirmed by the ergodic distance, $D(\tilde{T})$, that goes to 0 for $\tilde{T} \to \infty$. For comparison, in the bottom row, we illustrate the case $q = 0$ and $\tau_s = 1$ s. As is apparent, the qualitative behavior is the same as before. In fact, $D(\tilde{T}) \to 0$ for $\tilde{T} \to 0$ also in the case $q = 0$ and $\tau_s = 1$ s. By contrast, the behavior is qualitatively different in the case $q = 0.8$ and $\tau_s = 1$ s, which we illustrate in the middle row. In this case, while the orbits seem, as before, to fill the same volume at intermediate times, they asymptotically reach clearly separated regions of the phase space. Though it should be evident from the figure (see also Fig. 4.5), it is perhaps worth emphasizing the fact that such "asymptotic confinement" of the orbits—that is, reaching equilibrium—takes very long times, i.e., $\sim 10^3 \tau_s$.

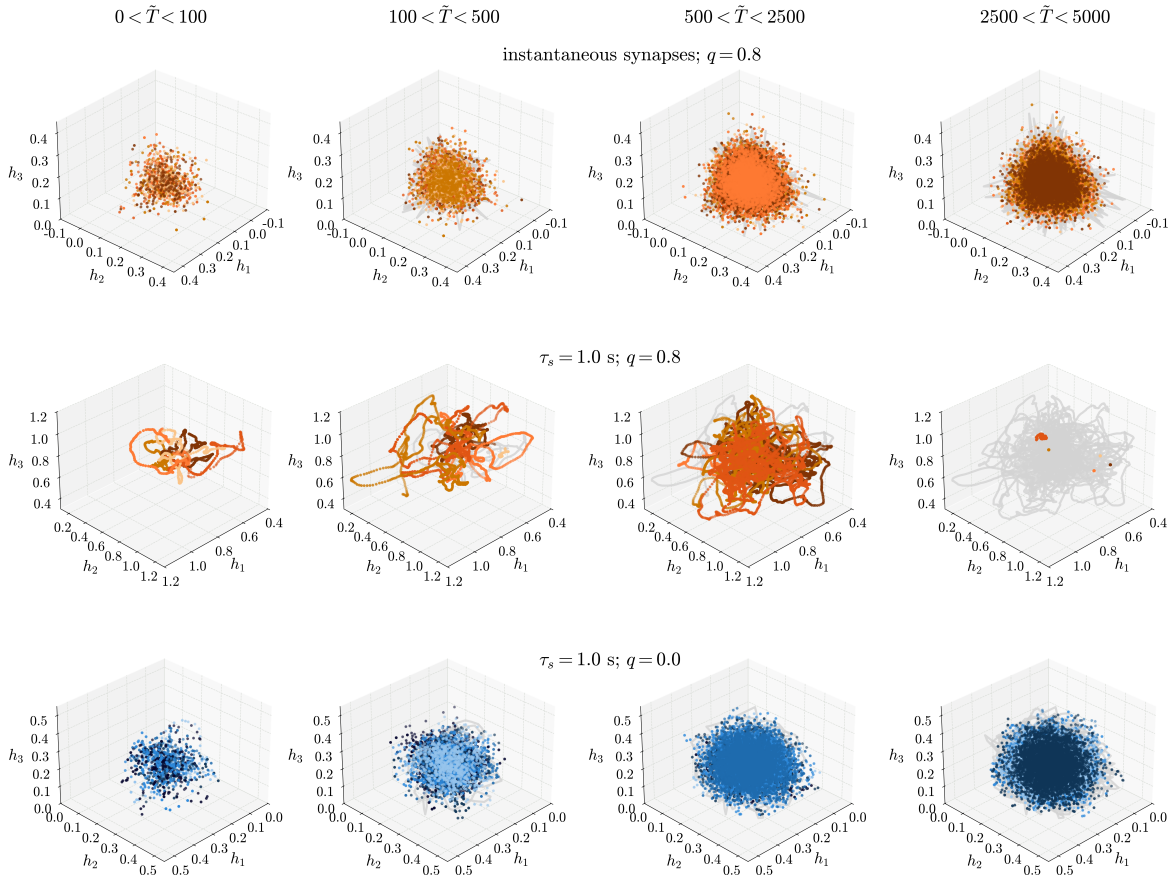

Figure 4.7: Trajectories in a 3D neural space defined by the total synaptic input of three random neurons; each point corresponds to $(h_1(\tilde{T}), h_2(\tilde{T}), h_3(\tilde{T}))$ at the same time. The different colors represent the five different replicas displayed. The upper row corresponds to instantaneous synapses with $q = 0.8$, while the other two refer to $\tau_s = 1$ s and $q = 0.8$ (middle row) and $q = 0$ (bottom row). The same parameters as in Fig.4.1 were used.

4.4. Discussion

We have shown that, in a spiking network operating in the dynamically-balanced regime, the over-expression of reciprocal synaptic connections, naturally and robustly leads to long-lived fluctuations in neural activity. In turn, these fluctuations lead to long relaxation times as estimated by the decay of the autocorrelation function, consistent with experimental observations in the active cortex [9, 10, 11]. The emergence of this slow dynamics is independent of both the size of the network and of the synaptic time constant, unlike in previous accounts (as discussed in the Introduction). Rather, it depends on the effective excitatory self-coupling generated by the symmetry in the synaptic connectivity, as already pointed out in [106] and further elaborated upon in the present study. Accordingly, we conclude that long relaxation times are a generic feature of the balanced regime, as soon as one includes in the model a more *realistic* description of the local synaptic connectivity [108, 109, 110, 111, 112].

Besides confirming previous results, here we significantly expand upon them. Specifically, we have shown that the network dynamics becomes non-ergodic when the excitatory self-coupling is suitably strong. Notably, the breaking of ergodicity also occurs in presence of significant levels of fast noise (i.e., for instantaneous synaptic currents) and in partially symmetric networks. By taking long synaptic time constants, we have shown that the network dynamics becomes multi-stable when ergodicity is broken. This suggests that the mechanism underlying the

ergodicity breaking in our model network could be a rather classical one, that is, the coexistence of multiple *stable* fixed points of the (rate) dynamics.

It is important to stress that, in our model network, the multi-stability does not result from some low-rank structure embedded in the synaptic connectivity, as is the case, for instance, in model networks of associative memory [88, 120, 121] or, more specifically, in clustered networks [98, 99, 100]. By contrast, the connectivity matrix in our network has no "structure" beyond a pre-assigned level of symmetry, and it is, indeed, full rank. Therefore, to the best of our knowledge, this is the first report of non-ergodic dynamics in an "unstructured" spiking network (see [107] for a related report in a network of rate neurons).

The usual caveats attached to any result based on numerical simulations apply to our results as well. We have probed the robustness of our results against finite-size effects by systematically varying, within "reasonable" bounds, both the number of neurons in the network ($1000 \leq N \leq 5000$) and the average number of connections they make ($100 \leq K \leq 3000$). In all cases, we observed the same phenomenology as described in Results; in particular, we found breaking of ergodicity for $q < 1$ and $\tau_s = 0$, for suitably large values of g_0.

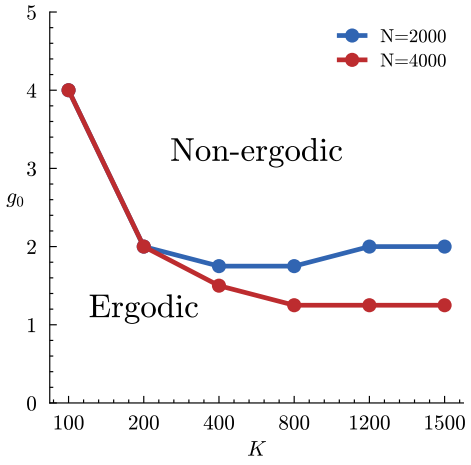

Figure 4.8: Ergodic to non-ergodic transition as a function of network connectivity and coupling strength. Phase boundary between the ergodic and non-ergodic regimes in networks of size N = 2000 (blue) and N = 4000 (red), shown in the (K, g_0) plane. Below the curves, network activity is ergodic: $D(T)$ eventually decays as $1/T$. Above the curves, activity becomes non-ergodic, $D(T)$ saturates for the entirety of the simulation ($1O^4$ s). The critical coupling decreases with increasing connectivity and saturates for large K, indicating a mean-field limit. The boundary also shifts downward with N, showing that larger networks enter the non-ergodic regime at weaker coupling strengths.

We have also verified that the basic phenomenology does not critically depend on the specific spiking-neuron model. Concretely, we have also studied networks of quadratic integrate-and-fire (QIF) neurons (see Appendix A). The QIF neuron is, in some respects, more *realistic* than the LIF neuron, since it can approximate reasonably well an entire class of neural models—Type I excitability according to Hodgkin classification—in proximity to the tonic firing threshold [38, 122]. We found, essentially the same phenomenology as for the LIF model. The results for a balanced network of QIF neurons will be presented in a forthcoming publication.

The best way to assess the robustness of our results would be, obviously, to develop an accompanying analytical theory. This is a formidable task for networks of LIF neurons [90]. On the other hand, using dynamical mean-field theory to achieve an analytical description of the steady states of networks, either of rate elements in presence of white noise or, even better, of spike-response models as in [95], appears feasible although very far from trivial.

Taken together, our results reveal the existence of a novel phase of the collective activity in dynamically-balanced spiking networks. In this phase, the dynamics reaches, asymptotically, different equilibrium states when starting from random initial conditions. In each of these states, the network operates in the balanced regime and, accordingly, the spiking activity of the neurons is unsaturated, temporally-irregular and asynchronous. In this respect, then, it resembles the pattern of activity that one observes in random, ergodic networks. However, unlike in random networks, the ergodicity is broken in this new phase; the memory of the initial conditions never fades away and reaching equilibrium is a very slow process.

An obvious question, then, is whether there is any evidence that the cortex operates in a non-ergodic phase. We are not aware of any experimental report definitively ruling out this possibility. As just discussed, many features of neural activity will be qualitatively the same in the ergodic and non-ergodic phases. Our work suggests a simple observable, easy to measure in an experiment (at least in principle), that could be help address this question. That is the ergodic distance, $D(T)$, originally introduced in [107], that we have also used in our spiking network. Note that $D(T)$ can be computed using only single-cell recordings. Deviations from $1/T$ in its decay at long times (e.g., $\sim$ 10s) would be supporting evidence of ergodicity breaking, at least in a weak sense (i.e., very long transients but only one equilibrium state). At present, we are actively pursuing this line of research.

5

Synaptic shot noise triggers fast and slow global oscillations in balanced neural networks

Summary Neural dynamics is determined by the transmission of discrete synaptic pulses (synaptic shot-noise) among neurons. However, the neural responses are usually obtained within the diffusion approximation modeling synaptic inputs as continuous Gaussian noise. Here, we present a rigorous mean-field theory that encompasses synaptic shot-noise for sparse balanced inhibitory neural networks driven by an excitatory drive. Our theory predicts new dynamical regimes, in agreement with numerical simulations, which are not captured by the classical diffusion approximation. Notably, these regimes feature self-sustained global oscillations emerging at low connectivity (in-degree) via either continuous or hysteretic transitions and characterized by irregular neural activity, as expected for balanced dynamics. For sufficiently weak (strong) excitatory drive (inhibitory feedback) the transition line displays a peculiar re-entrant shape revealing the existence of global oscillations at low and high in-degrees, separated by an asynchronous regime at intermediate levels of connectivity. The mechanisms leading to the emergence of these global oscillations are distinct: drift-driven at high connectivity and cluster activation at low connectivity. The frequency of these two kinds of global oscillations can be varied from slow ($\sim$ 1 Hz) to fast ($\sim$ 100 Hz), without altering their microscopic and macroscopic features, by adjusting the excitatory drive and the synaptic inhibition strength in a prescribed way. Furthermore, the cluster-activated oscillations at low in-degrees could correspond to the γ rhythms reported in mammalian cortex and hippocampus and attributed to ensembles of inhibitory neurons sharing few synaptic connections [14].

5.1. Introduction

Shot noise (or Poissonian noise) is a model of discontinuous noise characterised by a sequence of discrete pulses occurring at Poisson-distributed times. It is a ubiquitous process in nature, observable in electrical circuits and in optics due to the discrete nature of charges and photons [123, 124], as well as in population dynamics due to the discreteness of individuals [125]. Furthermore, the inclusion of shot noise is fundamental to fully characterize the considered phenomena in many fields of physics ranging from granular systems [126, 127, 128] to active matter [129], and from mesoscopic conductors [130] to Anderson localization [131].

Neural dynamics is also intimately linked to the discrete nature of the synaptic events [postsynaptic potentials (PSPs)] regulating the firing activity of the neurons. In the cortex, the PSPs received by a neuron are usually assumed to be of small amplitude and to have high arrival rates, due to the high number of presynaptic connections. Furthermore, since the number of presynaptic neurons is small with respect to the large number of neurons present in the cortex, the PSPs stimulating a specific neuron are assumed to be uncorrelated. Therefore, the synaptic inputs have been usually treated as white noise (as a continuous Gaussian process) giving rise to the so-called diffusion approximation (DA) for the mean-field description of the neural dynamics [15, 132].

However, experimental results challenge the hypotheses at the basis of the DA. First of all, there is clear evidence that synaptic weight distributions display heavy tails towards large values [70, 108, 133]. Moreover, rare large-amplitude synaptic connections are likely to contribute strongly to reliable information processing [134] and the synaptic weight distributions can be deeply modified by plasticity during learning processes and ongoing activity [135, 136]. A second important aspect is that neural circuits can display a connectivity definitely lower than expected. Indeed, networks of inhibitory neurons with very low number of presynaptic connections (in-degree $K \simeq 30$–80) have been found in the cat visual cortex [12] and in the rat hippocampus [13]; the latter population of interneurons is believed to be responsible for the emergence of global oscillations (GOs) in the γ-band (30–100 Hz) [14]. Along this direction goes a recent study reporting that primate excitatory and inhibitory neurons receive 2–5 times fewer excitatory and inhibitory synapses than similar mouse neurons [137].

These experimental indications call for the investigation of the dynamical regimes emerging in highly diluted neural networks under the effect of synaptic shot noise. Several works have been devoted to the development of mean-field approaches describing the population dynamics of integrate-and-fire neurons subject to synaptic shot noise, though mostly focused on asynchronous regimes [97, 138, 139, 140, 141, 142, 143].

However, oscillations are extremely relevant for the brain functioning, since they play a fundamental role in orchestrating cognitive functions and are often disrupted in neurological disorders [144, 145]. Oscillations in the brain are typically characterised by irregular neural firing, where neurons fire at frequencies much lower than those of the GOs both *in vivo* [146] and *in vitro* [147]. Several works have shown that this type of oscillations can arise in balanced excitatory-inhibitory sparse networks [7], due to the interplay between endogenous fluctuations and neural coupling [148, 149, 150, 151]. In particular, inhibition has been shown to play a critical role for the emergence of GOs, both in experimental data and in neural network models [152, 153]. Therefore, GOs have often been analysed within the simplified context of purely inhibitory networks, where the balance occurs between an external excitatory drive and the recurrent inhibition [64, 154, 155, 156, 157]. The characterization of the dynamical regimes exhibited by these models has been usually performed at a mean-field level within the context of the DA [154, 148]. Only quite recently, some of the authors of this paper have introduced in [158] a mean-field approach incorporating shot noise and sparsity in the connectivity to describe the emergence of GOs in balanced inhibitory neural networks.

In the present paper, we report in details the derivation of the *complete mean-field approach* (CMF) introduced in [158] for the quadratic integrate-and-fire (QIF) neurons [122, 159]. Furthermore, we will extend the analysis in [158] to the derivation of the diffusion (DA) and third-order approximation (D3A), obtained by expanding the source term in the continuity equation to the second and third-order, respectively. A weakly nonlinear analysis of the stationary solutions displayed by the CMF allows to identify hysteretic and non-hysteretic transitions towards GOs

with associated region of coexistence of GOs and asynchronous states. These forecasts are in good agreement with accurate numerical simulations, as shown via finite-size analysis of the observed transitions. On the other hand, DA and D3A fail in reproducing the network dynamics for sufficiently low excitatory drive (high inhibitory feedback). A peculiarity of the bifurcation diagram found with the CMF approach is a reentrant Hopf bifurcation line separating GOs observable at low and large in-degree K from an asynchronous irregular regime at intermediate K. These two kinds of GOs, induced by synaptic shot noise, are characterised, as the intermediate asynchronous state, by neurons spiking irregularly, but they emerge due to two different mechanisms. Moreover, both types of GOs can be observed at low frequencies [in the δ-band ($0.5 - 3.5$ Hz)] and at high frequencies (in the γ-band) by properly rescaling the external excitatory drive and the inhibitory synaptic strength, while the mean frequency of the irregularly firing neurons is always definitely slower.

The paper is organized as follows. Section II is devoted to the introduction of the network model, the simulation protocols, and the indicators employed to characterize microscopic and macroscopic dynamics. The mean-field formulation of the model is reported in Sec. III. In particular, we derive the macroscopic evolution equations for the CMF, the diffusion and third-order approximation, together with the corresponding linear and weakly nonlinear stability analysis of the asynchronous regime. The mean-field results are compared with network simulations in Sec. IV. This section reports a characterization of the observed transitions and macroscopic regimes, as well as an explanation of the two mechanisms that are at the origin of the two classes of GOs, induced by discrete synaptic events, observable at small and large in-degree. A summary and discussion of the results can be found in Sec. V. A detailed presentation of the integration methods employed for the network model and for the Langevin and continuity equations can be found in Appendices A.1.1, B.1 and B.2. Appendix B.3 compares the results for the macroscopic dynamics obtained by network simulations and mean-field analysis for noninstantaneous synapses.

5.2. Model and methods

5.2.1. The network model

As a prototype of a dynamically balanced system we consider a sparse inhibitory network made of N pulse-coupled QIF neurons [64, 156, 157] whose membrane potentials evolve according to the equation

$$\dot{v}_i(t) = v_i^2 + I - g \sum_{j=1}^{N} \sum_n \varepsilon_{ji} \delta(t - t_j^{(n)}) \quad v \in]-\infty, +\infty[; \tag{5.1}$$

where I represents an external DC current, g the synaptic coupling, and the last term on the right-hande side (r.h.s) the inhibitory synaptic current. The latter is the linear superposition of instantaneous inhibitory PSPs emitted at times $t_j^{(n)}$ from the presynaptic neurons connected to neuron i. ε_{ji} is the adjacency matrix of the random network with entries 1 (0) if the connection from node j to i exists (or not), and we assume the same in-degree $K = \sum_j \varepsilon_{ji}$ for all neurons.

We consider the quadratic integrate-and-fire (QIF) neuron [159], which is a current-based model of class I excitability. In particular, whenever the membrane potential v reaches infinity, a δ spike is emitted and instantaneously delivered to the postsynaptic neurons and v is reset to $-\infty$. In the absence of synaptic coupling, the QIF model displays excitable (oscillatory) dynamics for $I < 0$ ($I > 0$). Since we consider a purely inhibitory network in order to have nontrivial collective dynamics, the neurons should be suprathreshold, i.e., with $I > 0$, in this

case in absence of synaptic coupling the single neuron firing frequency is given by

$$\nu_0 = \frac{\sqrt{I}}{\pi} = \frac{1}{T_0}. \tag{5.2}$$

In the excitable case ($I < 0$) the neuron has a stable and an unstable fixed point located at $V^s = -\sqrt{-I}$ and $V^u = \sqrt{-I}$, respectively.

The DC current and the synaptic coupling are assumed to scale as $I = i_0\sqrt{K}$ and $g = g_0/\sqrt{K}$ as usually done, in order to ensure a self-sustained balanced state for sufficiently large K [7, 64, 156].

The times (frequencies) are reported in physical units by assuming as a time-scale a membrane time constant $\tau_m = 10$ ms.

5.2.2. Simulation protocols

The simulation of the QIF network model (5.1) has been performed due to an exact event-driven method (see Appendix A.1.1 for more details), which allowed us to reach very large system sizes from $N = 10\,000$ up to $N = 80\,000$ with $10 \leq K \leq 1000$, to integrate for long time spans up to 50–100 s and to average over 5–20 different network realizations.

The simulations performed to identify the emergence of collective oscillations are usually based on two quasiadiabatic protocols, where i_0 (K) is varied in steps Δi_0 (Δ_K) by maintaining all the other parameters constant. The simulations are performed for some value of i_0 (K) where the quantities of interest are evaluated over a certain time interval $t_E \simeq 20$–30 s after discarding a transient of durations $t_T \simeq 20$–30 s. At the end of the simulation the final values of the variables are stored and used to initialize the next simulation step with a parameter value $i_0 \pm \Delta i_0$ ($K \pm \Delta K$), whose duration will be again $t_T + t_E$. These steps are repeated until the final parameter value is achieved; to test for hysteresis the procedure can be reversed by decreasing (increasing) the parameter value in small steps to recover the initial value.

5.2.3. Indicators

The microscopic evolution of the neurons is typically measured in terms of the mean interspike interval (ISI) of each neuron $\langle T_i \rangle$ and of the corresponding firing rate $\nu_i = 1/\langle T_i \rangle$, where $\langle \cdot \rangle$ denotes a time average. The neural variability of each neuron is customarily measured via the so-called coefficient of variation

$$cv_i = \frac{\sqrt{\langle T_i^2 \rangle - \langle T_i \rangle^2}}{\langle T_i \rangle},$$

which is the ratio between the standard deviation and the mean of the ISIs of the neuron i. A value $cv_i = 0$ ($cv_i = 1$) corresponds to a periodic (Poissonian) activity of the considered neuron [132].

The activity of the neurons in the network can be therefore characterised in terms of the probability distribution functions (PDFs) of the firing rates $\{\nu_i\}$ and of the coefficient of variations $\{cv_i\}$ as well as of the corresponding population averages (denoted as $\overline{\cdots}$)

$$F = \overline{\nu_i} = \frac{1}{N}\sum_{i=1}^{N} \nu_i, \qquad CV = \overline{cv_i} = \frac{1}{N}\sum_{i=1}^{N} cv_i. \tag{5.3}$$

The population activity can be also analysed in terms of the population firing rate $\nu(t)$

$$\nu(t) = \frac{N_{sp}(T_W)}{T_W N}, \tag{5.4}$$

where $N_{sp}(T_W)$ is the number of spikes emitted by the N neurons in the network in a time interval T_W, which we typically consider of the order of 0.005 s.

The macroscopic evolution of the network can be characterised by the indicator introduced in [160]

$$\chi = \left(\frac{\sigma_V^2}{\overline{\sigma_i^2}} \right)^{1/2} \quad \text{where} \quad \sigma_i^2 = \langle v_i^2 \rangle - \langle v_i \rangle^2, \tag{5.5}$$

where $\overline{\sigma_i^2} = \frac{1}{N} \sum_{i=1}^N \sigma_i^2$ is the population average of the variances of the membrane potential of each neuron and σ_V^2 is the variance of the mean membrane potential $V(t) = \overline{v_i(t)} = \sum_{i=1}^N v_i(t)/N$. The actual value of χ is related to the level of synchronization among the neurons: asynchronous evolution (perfect synchrony) corresponds to $\chi \simeq O(1/\sqrt{N})$ ($\chi \equiv 1$). The presence of asynchronous dynamics or GOs can be inferred from the finite-size scaling of χ as explained in the following.

The global oscillations differentiated in terms of their frequency f_G and of the following two ratios:

$$R_G = \frac{f_G}{F}, \qquad R_0 = \frac{f_G}{\nu_0}, \tag{5.6}$$

where F is the ensemble average of the neuron firing rates (5.3) and ν_0 is the firing rate of the uncoupled neuron (5.2). Therefore, R_G represents the level of locking of the single neuron activity with respect to the population bursts and R_0 can be employed to understand the origin of GOs and the influence of inhibitory PSPs. As a general remark we have found that $R_G \geq 2$ in all simulations, indicating that in the studied model the firing rate of the neurons is always slower than the frequency of the GOs [161].

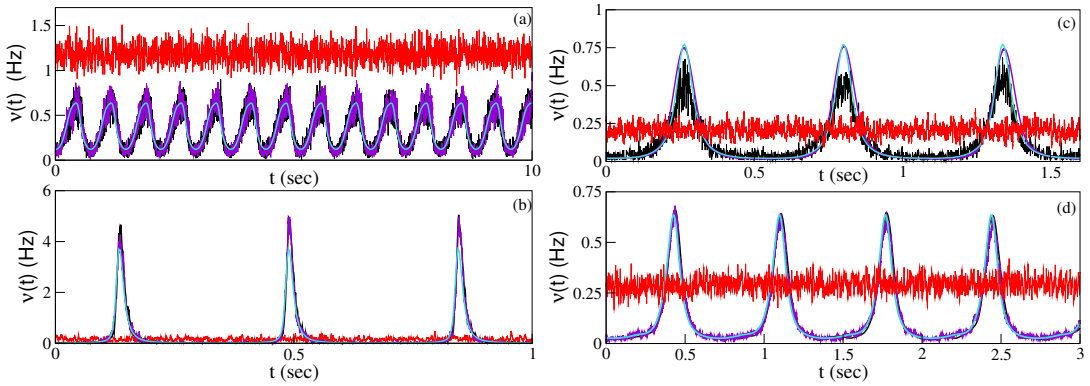

Figure 5.1: Population firing rates $\nu(t)$ versus time for $i_0 = 0.00055$: $K = 10$ (a) and $K = 210$ (b); $i_0 = 0.00033$: $K = 100$ (c) and $i_0 = 0.00027$ and $K = 60$ (d). The black lines represent network simulations with $N = 80\,000$ neurons, the violet lines to Langevin simulations with shot noise [Eq. (5.7)] and the red lines to Langevin simulations obtained within the DA [Eq. (5.9)] with $N = 20\,000$ (a, b) and $N = 80\,000$ (c, d). The solid turquoise lines denote the results of the CMF approach [Eq. (5.17) and (5.23)]. All data are for $g_0 = 1$. Details on the integration of the Langevin equations are reported in Appendix B.1.

5.3. Mean-field description

For a sufficiently sparse network with in-degree $K \ll N$, the spike trains emitted by K presynaptic neurons can be assumed to be uncorrelated and Poissonian [154]; therefore the mean-field dynamics of a QIF neuron can be represented in terms of the following shot noise Langevin equation:

$$\dot{V}(t) = V^2 + I - gS(t), \tag{5.7}$$

where $S(t)$ is a Poissonian train of δ spikes with rate $R(t) = K\nu(t)$, and $\nu(t)$ is the population firing rate self-consistently estimated.

Usually the Poissonian spike trains are approximated within the DA [15, 132] as

$$S(t) = R(t) + \sqrt{R(t)}\xi(t), \tag{5.8}$$

where $\xi(t)$ is a normalized Gaussian white noise signal. Therefore, the Langevin equation within the DA can be rewritten as

$$\dot{V}(t) = V^2 + [I - gK\nu(t)] + g\sqrt{K\nu(t)}\xi(t) = V^2 + \sqrt{K}[i_0 - g_0\nu(t)] + g_0\sqrt{\nu(t)}\xi(t), \tag{5.9}$$

where we have made explicit the dependence of I and g on the in-degree K: namely, for the balanced model here studied $g = g_0/\sqrt{K}$ and $I = i_0\sqrt{K}$.

However, the DA can fail in reproducing the neural dynamics. Indeed, as shown in Fig. 5.1 for sparse networks with different sets of parameters by employing the DA [Eq. (5.9)] one obtains an asynchronous dynamics (red curve), while the network evolution is characterised by GOs (black lines), that can be recovered only by explicitly taking into account the Poissonian spike trains in Eq. (5.7) (violet lines). As shown in Fig. 5.1 (b), the DA is unable to reproduce simulation results even with quite large in-degree ($K = 210$) for sufficiently small i_0. On the other hand, the Langevin mean-field data with shot noise are in good agreement with the simulations in all considered cases indicating the validity of this approach.

In the mean-field framework the population dynamics is usually described in terms of the membrane potential probability density function (PDF) $P(V,t)$, whose time evolution for the QIF model is given [according to (5.7)] by the continuity equation

$$\partial_t P(V,t) + \partial_V[(V^2 + I)P(V,t)] = R(t)\Delta P(V,T) \tag{5.10}$$

with boundary condition $\lim_{V\to\infty} V^2 P(V,t) = \nu(t)$ and where $\Delta P(V,T) = [P(V^+,t) - P(V,t)]$ with $V^+ = V + g$.

The r.h.s term in (5.10) represents the time variation of $P(V,t)$ due to the arrival of the Poissonian trains of instantaneous inhibitory kicks of amplitude g from K presynaptic neurons. By assuming that g is sufficiently small we can expand the latter term as

$$\Delta P(V,t) = \sum_{p=1}^{\infty} \frac{g^p}{p!}\partial_V^p P(V,t), \tag{5.11}$$

and by limiting to the first two terms in this expansion we recover the DA corresponding to the following Fokker-Planck equation (FPE) [162]:

$$\partial_t P(V,t) + \partial_V[(V^2 + A(t))P(V,t)] = D(t)\partial_V^2 P(V,t), \tag{5.12}$$

where $A(t) = \sqrt{K}[i_0 - g_0\nu(t)]$ is the effective input current and $D(t) = g_0^2\nu(t)/2$ represents the diffusion coefficient.

In the following we will also consider a generalized version of the FPE (GFPE) obtained by considering up to the third-order term in the expansion (5.11), which gives the following evolution equation for the $P(V,t)$:

$$\partial_t P(V,t) + \partial_V[(V^2 + A(t))P(V,t)] = D(t)\partial_V^2 P(V,t) + H(t)\partial_V^3 P(V,t), \tag{5.13}$$

where $H(t) = \frac{g_0^3 \nu(t)}{3!\sqrt{K}}$.

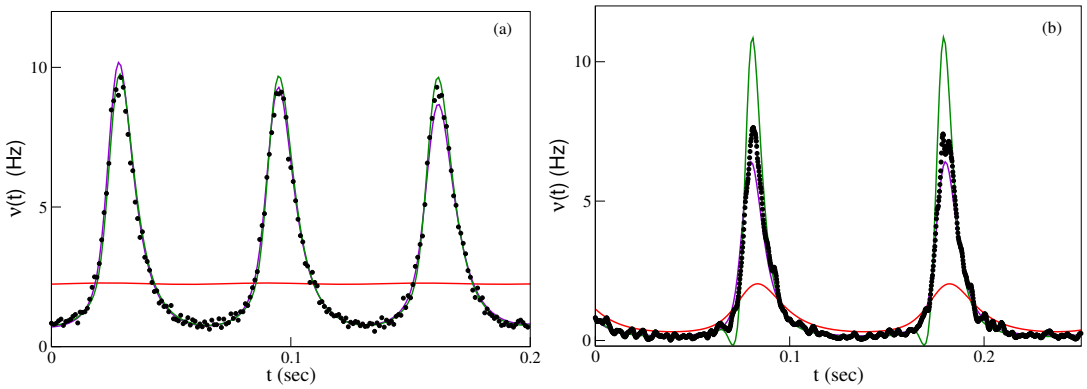

Figure 5.2: Population firing rates $\nu(t)$ versus time for $i_0 = 0.02$, $K = 200$ (a) and $i_0 = 0.006$, $K = 400$ (b). The black circles refer to network simulations with $N = 80\,000$ (a) and $N = 20\,000$ (b); the violet (red) solid lines to integration of the continuity equation (5.10) [FPE (5.12)]. The green solid lines denote the results of the integration of the GFPE including third-order terms (5.13). All data are for $g_0 = 1$; the numerical integration of the partial differential equations has been performed by employing time splitting pseudo-spectral methods with a time step $\Delta t = 10^{-4}$ ms and with 128–512 Fourier modes (for more details see Appendix B.2).

Comparisons among the network simulations (black circles) and the results obtained by integrating the partial differential equations (5.10) (violet line), (5.12) (red lines) and (5.13) (green lines) via time splitting pseudo-spectral methods (as explained in details in Appendix B.2) are shown in Fig. 5.2. These results show that DA can give incorrect predictions even at the level of population dynamics. Indeed, as shown in Fig. 5.2 (a) the network dynamics is oscillatory with $f_G \simeq 15$ Hz (black circles). This evolution is correctly captured by the continuity equation (5.10) (violet line). On the other hand, the FPE (5.12) (red line) converges to a stable fixed point corresponding to asynchronous dynamics. In this case, the inclusion of the third-order term of the expansion (5.11) in the evolution equation for $P(V,t)$ (5.13) gives a stable solution (green solid line) capturing quite well the network dynamics. Unfortunately, this is not always the case due to the intrinsic instability of the third-order expansion [163, 164], which, e.g., does not guarantee that the sign of the PDF remains positive, as observable in the case reported in Fig. 5.2 (b). In this latter situation, the DA is able to reproduce the oscillatory behaviour displayed by the network evolution; however, the amplitudes of such oscillations are definitely better captured by the continuity equation (5.10) (violet line).

In summary, to correctly reproduce the collective dynamical regimes observable in the network it is necessary to consider the complete continuity equation (5.10), even if in some cases the third-order expansion (5.13) could be sufficiently accurate. As a general remark the time-splitting pseudo-spectral integration methods here employed suffer of numerical instabilities in particular for small K, which render the approach not particularly reliable. Therefore, as we will explain in the following we have developed an accurate and stable formalism encompassing synaptic shot noise to identify the various possible regimes displayed by (5.10) and to characterize their linear and nonlinear stability.

5.3.1. Derivation of the macroscopic evolution equations

As already mentioned, the dynamical evolution of the QIF model can be transformed into that of a phase oscillator, the θ neuron [159, 165], by introducing the phase variable $\theta = 2\arctan V$. However, this transformation renders quite difficult to distinguish asynchronous from partially synchronized states [166, 167]. A more suitable phase transformation, able to take into account correctly the phase synchronization phenomena, is the following

$$\psi = 2\arctan\frac{V}{\sqrt{I}} \in [-\pi,\pi]\,, \qquad V = \sqrt{I}\tan\frac{\psi}{2} \in]-\infty,+\infty[\,,$$

where $I = i_0\sqrt{K}$. Indeed, for $I > 0$ and in the absence of incoming pulses the phase ψ is uniformly rotating with angular velocity $2\sqrt{I}$ at variance with the θ neuron where even for uncoupled oscillators the velocity depends on the phase.

The probability distribution function (PDF) $w(\psi)$ for the phase variables ψ is related to the one of the membrane potentials $P(V,t)$ via the relation

$$w(\psi,t) = P(V,t)\frac{I+V^2}{2\sqrt{I}}$$

due to the probability conservation under (nonlinear) transformations of stochastic variables. Therefore, the continuity equation (5.10) for $P(V,t)$,

$$\frac{\partial P(V,t)}{\partial t} = -\frac{\partial}{\partial V}\Big[(I+V^2)P(V,t)\Big] + K\nu(t)\Big[P(V+g,t) - P(V,t)\Big]\,, \tag{5.14}$$

can be recast as follows for $w(\psi,t)$:

$$\frac{\partial w(\psi,t)}{\partial t} = -\frac{\partial}{\partial\psi}\left[2\sqrt{I}w(\psi,t)\right] + K\nu(t)\left[\frac{I+V^2}{I+(V+g)^2}w(\psi_+,t) - w(\psi,t)\right]\,, \tag{5.15}$$

where ψ_+ is the shifted phase:

$$V+g = \sqrt{I}\tan\frac{\psi_+}{2}\,, \qquad \tan\frac{\psi_+}{2} = \alpha + \tan\frac{\psi}{2}\,, \qquad \alpha \equiv \frac{g}{\sqrt{I}} = \frac{g_0}{\sqrt{i_0}K^{3/4}}\,.$$

By making all the terms in the r.h.s of Eq. (5.15) explicit in terms of the variable ψ,

$$\frac{I+V^2}{I+(V+g)^2} = \frac{1+\tan^2\frac{\psi}{2}}{1+\left(\alpha+\tan\frac{\psi}{2}\right)^2} = \frac{1}{1+\frac{\alpha^2}{2}+\alpha\sin\psi+\frac{\alpha^2}{2}\cos\psi}\,,$$

we can finally rewrite Eq. (5.15) as

$$\frac{\partial w(\psi,t)}{\partial t} = -\frac{\partial}{\partial\psi}\left[2\sqrt{I}w(\psi,t)\right] + K\nu(t)\left[\frac{w(\psi_+,t)}{1+\frac{\alpha^2}{2}+\alpha\sin\psi+\frac{\alpha^2}{2}\cos\psi} - w(\psi,t)\right]\,. \tag{5.16}$$

In Fourier space the PDF $w(\psi,t)$ can be expressed as

$$w(\psi,t) = \frac{1}{2\pi}\sum_{n=-\infty}^{+\infty} z_n e^{-in\psi}\,,$$

with $z_0 = 1$ and $z_{-n} = z_n^*$, where the complex coefficients z_n are the so-called Kuramoto-Daido order parameters z_n [168, 169]. In terms of these coefficients the continuity equation (5.16) becomes

$$\dot{z}_n = i2n\sqrt{I}z_n + K\nu(t)\left[\sum_{m=-\infty}^{+\infty} I_{nm}z_m - z_n\right] , \tag{5.17}$$

where

$$I_{nm} \equiv \frac{1}{2\pi}\int_0^{2\pi} \frac{e^{in\psi}\left(e^{-i\psi_+}\right)^m \mathrm{d}\psi}{1+\frac{\alpha^2}{2}+\alpha\sin\psi+\frac{\alpha^2}{2}\cos\psi} . \tag{5.18}$$

In order to calculate the integrals I_{nm}, we need to express explicitly the term $e^{-i\psi_+} = \cos\psi_+ - i\sin\psi_+$ entering in Eq. (5.18). In particular, by noticing that

$$\cos\psi_+ = \frac{1-\tan^2\frac{\psi_+}{2}}{1+\tan^2\frac{\psi_+}{2}} , \qquad \sin\psi_+ = \frac{2\tan\frac{\psi_+}{2}}{1+\tan^2\frac{\psi_+}{2}} ,$$

and therefore that

$$e^{-i\psi_+} = \cos\psi_+ - i\sin\psi_+ = \frac{1-i\tan\frac{\psi_+}{2}}{1+i\tan\frac{\psi_+}{2}} = -\frac{\tan\frac{\psi}{2}+\alpha+i}{\tan\frac{\psi}{2}+\alpha-i} .$$

Moreover by expressing $\zeta \equiv e^{i\psi}$ as

$$\zeta \equiv e^{i\psi} = -\frac{\tan\frac{\psi}{2}-i}{\tan\frac{\psi}{2}+i} , \quad \text{and hence} \quad \tan\frac{\psi}{2} = i\frac{1-\zeta}{1+\zeta} ,$$

one finally finds

$$e^{-i\psi_+} = -\frac{\alpha+2i+\alpha\zeta}{\alpha+(\alpha-2i)\zeta} . \tag{5.19}$$

By employing the above expression the integral (5.18) can be rewritten as

$$I_{nm} = \int_0^{2\pi} \frac{(2\pi)^{-1}e^{in\psi}\left[-\frac{\alpha+2i+\alpha e^{i\psi}}{\alpha+(\alpha-2i)e^{i\psi}}\right]^m \mathrm{d}\psi}{1+\frac{\alpha^2}{2}-\frac{i\alpha}{2}(e^{i\psi}-e^{-i\psi})+\frac{\alpha^2}{4}(e^{i\psi}+e^{-i\psi})} = \oint_{|\zeta|=1} \frac{(i2\pi)^{-1}\zeta^{n-1}\left[-\frac{\alpha+2i+\alpha\zeta}{\alpha+(\alpha-2i)\zeta}\right]^m \mathrm{d}\zeta}{1+\frac{\alpha^2}{2}-\frac{i\alpha}{2}(\zeta-\frac{1}{\zeta})+\frac{\alpha^2}{4}(\zeta+\frac{1}{\zeta})}$$

$$= \frac{1}{2\pi i}\oint_{|\zeta|=1} \frac{4(-\alpha)^m\zeta^n(\zeta+\frac{\alpha+2i}{\alpha})^{m-1}}{\alpha(\alpha-2i)^{m+1}(\zeta+\frac{\alpha}{\alpha-2i})^{m+1}}\mathrm{d}\zeta . \tag{5.20}$$

To evaluate the complex integral in (5.20) we employ the residue theorem and therefore we should identify the poles of the integrand. We can limit our consideration to $n \geq 1$ since $z_0 = 1$, and $z_{-n} = z_n^*$, for $m \leq 0$ the integrand has the following pole

$$\zeta_2 = -\frac{\alpha+2i}{\alpha} ,$$

which is always beyond the unit circle since $|\frac{\alpha+2i}{\alpha}|^2 = 1 + 4/\alpha^2 > 1$ and, therefore, does not contribute to the integral I_{nm}. However, for $m \geq 0$ the integrand displays another pole located at

$$\zeta_1 = -\frac{\alpha}{\alpha-2i}.$$

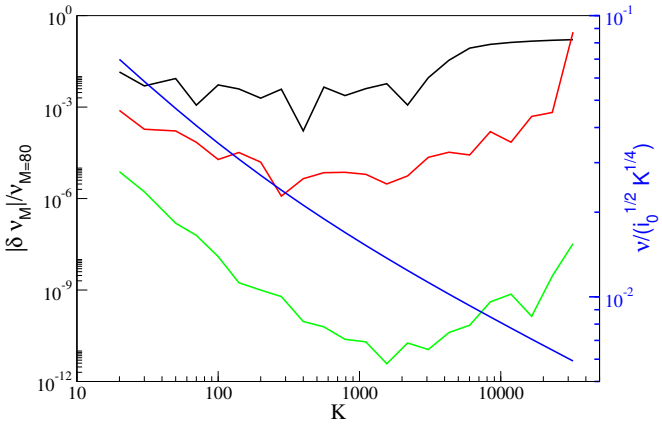

Figure 5.3: Relative error in the estimation of the firing rate ν for a stationary situation (asynchronous dynamics) computed with (5.17)–(5.23) plotted versus the in-degree K for $M = 10$ (black line), 20 (red line) and 40 (green line). The reference firing rate was estimated by employing $M = 80$, and it is shown in rescaled units as a blue line. Parameters: $(i_0, g_0) = (0.006, 1)$.

This pole is always within the integration contour $|\zeta| = 1$ since $|\frac{\alpha}{\alpha-2i}|^2 = \frac{\alpha^2}{\alpha^2+4} < 1$ and therefore it contributes to the integral (5.20).

We employ the residue theorem to evaluate the following integral:

$$\frac{1}{2\pi i}\oint_{|\zeta|=1}\frac{\zeta^n\left(\zeta+\frac{\alpha+2i}{\alpha}\right)^{m-1}}{\left(\zeta+\frac{\alpha}{\alpha-2i}\right)^{m+1}}\,\mathrm{d}\zeta = \begin{cases}\dfrac{1}{m!}\dfrac{\mathrm{d}^m}{\mathrm{d}\zeta^m}\left(\zeta^n(\zeta-\zeta_2)^{m-1}\right)\Big|_{\zeta=\zeta_1}, & m\geq 0;\\ 0, & m\leq -1\end{cases}$$

$$= \begin{cases}\displaystyle\sum_{j=0}^{\min(n,m)-1}\binom{m-1}{j}\binom{n+m-1-j}{m}\zeta_1^{n-1-j}(-\zeta_2)^j, & m\geq 1;\\ \dfrac{\zeta_1^n}{\zeta_1-\zeta_2}, & m=0;\\ 0, & m\leq -1,\end{cases}$$

where $\min(n,m)$ returns the minimal of two values, and the binomial coefficients are defined as $\binom{n}{m} = \frac{n!}{m!(n-m)!}$. In particular, to obtain the result reported in the latter line, we separately considered the cases for $1 \leq n \leq m$ and for $n > m$. Hence,

$$I_{nm}(\alpha) = \begin{cases}\displaystyle\sum_{j=0}^{\min(n,m)-1}\frac{(\zeta_1-\zeta_2)(n+m-1-j)!\zeta_1^{m+n-1-j}(-\zeta_2)^j}{mj!(m-1-j)!(n-1-j)!}, & m\geq 1\,;\\ \zeta_1^n\,, & m=0\\ 0, & m\leq -1.\end{cases} \tag{5.21}$$

After the substitution of the values of ζ_1 and ζ_2 in (5.21), the coefficients $I_{nm}(\alpha)$ take the form

$$I_{nm}(\alpha) \equiv \frac{1}{2\pi}\int_0^{2\pi}\frac{e^{in\psi}\left(e^{-i\psi_+}\right)^m\mathrm{d}\psi}{1+\frac{\alpha^2}{2}\alpha\sin\psi+\frac{\alpha^2}{2}\cos\psi} = \begin{cases}\left(\frac{\alpha}{2i-\alpha}\right)^n\,, & m=0\,;\\ \displaystyle\sum_{j=1}^{\min(n,m)}\frac{4(-1)^j(n+m-j)!\alpha^{m+n-2j}(4+\alpha^2)^{j-1}}{m(j-1)!(m-j)!(n-j)!(2i-\alpha)^{m+n}}, & m\geq 1.\end{cases} \tag{5.22}$$

In particular, for $n \geq 1$, one has $I_{nm} = 0$ for $m < 0$; therefore, the matrix I_{nm} has nonzero elements only for $n = 1, 2, 3, \ldots$ and $m = 0, 1, 2, 3, \ldots$:

$$\left(\frac{I_{nm}}{\zeta_1 - \zeta_2}\right) = \begin{pmatrix} \frac{\zeta_1}{\zeta_1-\zeta_2} & \zeta_1 & \zeta_1^2 & \zeta_1^3 & \ldots \\ \frac{\zeta_1^2}{\zeta_1-\zeta_2} & 2\zeta_1^2 & 3\zeta_1^3 - \zeta_1^2\zeta_2 & 4\zeta_1^4 - 2\zeta_1^3\zeta_2 & \ldots \\ \frac{\zeta_1^3}{\zeta_1-\zeta_2} & 3\zeta_1^3 & 6\zeta_1^4 - 3\zeta_1^3\zeta_2 & 10\zeta_1^5 - 8\zeta_1^4\zeta_2 + \zeta_1^3\zeta_2^2 & \ldots \\ \frac{\zeta_1^4}{\zeta_1-\zeta_2} & 4\zeta_1^4 & 10\zeta_1^5 - 6\zeta_1^4\zeta_2 & 20\zeta_1^6 - 20\zeta_1^5\zeta_2 + 4\zeta_1^4\zeta_2^2 & \ldots \\ & \ldots & & & \end{pmatrix}.$$

In the continuity equation (5.15) appears the population firing rate $\nu(t)$, which should be evaluated self-consistently during the time evolution. The instantaneous firing rate is given by the flux at the firing threshold, therefore

$$\nu(t) = \lim_{V\to\infty} V^2 P(V,t) = 2\sqrt{I}\, w(\pi, t) = \frac{\sqrt{I}}{\pi}\mathrm{Re}\big(1 - 2z_1 + 2z_2 - 2z_3 + 2z_4 - \cdots\big). \tag{5.23}$$

The dynamical system (5.17), (5.23) has been numerically integrated with the exponential time differencing method [170, 171] for time-dependent regimes and numerically solved (in the Maple analytical calculation package) for time-independent regimes, stability and weakly nonlinear analyses by truncating the series z_n at $n = M$ terms. Usually we fixed $M = 100$, and, where necessary, M was increased in order to keep the relative simulation error below 10^{-12} [172] (see Fig. 5.3).

5.3.2. Diffusion and third-order approximations

Consider the continuity equation (5.13), which yields the DA with $H(t)$ set to zero and the D3A for $H(t) = g_0^3\nu(t)/(3!\sqrt{K})$, but recast it as

$$\partial_t P(V,t) + \partial_V[(V^2 + I)P(V,t)] = K\nu(t)\left[g\partial_V P(V,t) + \frac{g^2}{2}\partial_V^2 P(V,t) + \frac{g^3}{3!}\partial_V^3 P(V,t)\right]. \tag{5.24}$$

For the probability density $w(\psi, t)$ of the phase variable $\psi = 2\arctan(V/\sqrt{I})$, continuity equation (5.24) yields a modified version of (5.15):

$$\frac{\partial w(\psi,t)}{\partial t} = -\frac{\partial}{\partial\psi}\left[2\sqrt{I}w(\psi,t)\right] + K\nu(t)\left[\frac{g}{\sqrt{I}}\mathcal{Q}w(\psi,t) + \frac{g^2}{2I}\mathcal{Q}^2 w(\psi,t) + \frac{g^3}{3!I^{3/2}}\mathcal{Q}^3 w(\psi,t)\right], \tag{5.25}$$

where the operator

$$\mathcal{Q}(\cdots) \equiv \frac{\partial}{\partial\psi}\Big[(1 + \cos\psi)(\cdots)\Big].$$

Hence, for the Kuramoto-Daido order parameters z_n, one finds a modified version of equation system (5.17):

$$\dot{z}_n = i2n\sqrt{I}z_n + K\nu(t)\sum_{m=0}^{+\infty} I_{nm}^{[\mathrm{tr}]} z_m\,, \quad n = 1, 2, 3, \ldots, \tag{5.26}$$

where $z_0 = 1$; for DA, the "truncated" matrix

$$I_{nm}^{[\mathrm{tr}]} = I_{nm}^{[\mathrm{DA}]} \equiv \alpha Q_{nm} + \frac{\alpha^2}{2}(\boldsymbol{Q}^2)_{nm};$$

and, for D3A,

$$I_{nm}^{[\mathrm{tr}]} = I_{nm}^{[\mathrm{D3A}]} \equiv \alpha Q_{nm} + \frac{\alpha^2}{2}(\boldsymbol{Q}^2)_{nm} + \frac{\alpha^3}{3!}(\boldsymbol{Q}^3)_{nm}.$$

In Fourier space, operator $\boldsymbol{Q}$ has the following matrix form:

$$Q_{nm} = \begin{pmatrix} 0 & 0 & 0 & 0 & 0 & \dots \\ -\frac{i}{2} & -i & -\frac{i}{2} & 0 & 0 & \dots \\ 0 & -i & -2i & -i & 0 & \dots \\ 0 & 0 & -\frac{3i}{2} & -3i & -\frac{3i}{2} & \dots \\ & \dots & & & & \end{pmatrix},$$

where the numbers of rows and columns run from $n = 0$ and $m = 0$, respectively; and matrices $\boldsymbol{Q}^2$, $\boldsymbol{Q}^3$ can be easily calculated via conventional matrix multiplication. By substituting the matrix coefficients, one can recast Eq. (5.26) as follows:

$$\begin{aligned} \dot{z}_n = i2n\sqrt{i_0\sqrt{K}}z_n + K\nu(t)\Big\{ & \tfrac{n\alpha}{i}\left(z_n + \tfrac{z_{n\pm1}}{2}\right) - \tfrac{n\alpha^2}{2}\left[\tfrac{3n}{2}z_n + \left(n \pm \tfrac{1}{2}\right)z_{n\pm1} + \tfrac{n\pm1}{4}z_{n\pm2}\right] \\ & + \tfrac{in\alpha^3}{6}\left[\tfrac{5n^2+1}{2}z_n + \tfrac{15n(n\pm1)+6}{8}z_{n\pm1} + \tfrac{3(n\pm1)^2}{4}z_{n\pm2} + \tfrac{(n\pm1)(n\pm2)}{8}z_{n\pm3}\right]\Big\}, \end{aligned} \tag{5.27}$$

where the terms with ± are not alternative, but they should be considered as both present in the sum of the terms on the right-hand side and the diffusion approximation can be obtained by omitting the α^3term. By employing Eq. (5.26) (or (5.27)) we can deal with the DA and the D3A in technically the same way as done for the CMF model (5.17), once we replace the matrix $(I_{nm}(\alpha) - \delta_{nm})$ with $I_{nm}^{[\mathrm{tr}]}(\alpha)$.

5.3.3. Linear stability of the asynchronous regime

In order to analyse the stability of the asynchronous dynamics and the emergence of global oscillations in the macroscopic evolution, we rewrite the system (5.17,5.23) as follows:

$$\begin{aligned} \frac{\mathrm{d}z_n}{\mathrm{d}t} &= F_n(z_1, z_2, z_3, \cdots) \\ &= \sqrt{i_0}K^{\frac{1}{4}}\left(i2nz_n + K\widetilde{\nu}\left[I_{n0}(\alpha) + \sum_{m=1}^{+\infty} I_{nm}(\alpha)\, z_m - z_n\right]\right), \end{aligned} \tag{5.28}$$

with

$$\widetilde{\nu} = \frac{\nu}{\sqrt{I}} = \frac{1}{\pi}\mathrm{Re}(1 - 2z_1 + 2z_2 - 2z_3 + 2z_4 - \dots). \tag{5.29}$$

We first notice that the dynamical evolution of the system (5.28), (5.29) is controlled by two dimensionless parameters, namely

$$K \quad \text{and} \quad \alpha = \frac{g_0}{\sqrt{i_0}K^{3/4}},$$

while the time can be rescaled by the factor $\sqrt{I} = \sqrt{i_0}K^{1/4}$. Therefore a bifurcation diagram in the plane $(K, i_0/g_0^2)$ is sufficient to capture all possible dynamical regimes observable for the system (5.28), (5.29).

In order to analyse the stability of the stationary regimes in this plane, we should linearize the system (5.28), (5.29) around a fixed point solution $\{z_n^{(0)}\}$. In particular, since F_n depend on $\widetilde{\nu}$, which is non analytic function of z_m, the linearization of (5.28) should be performed by considering as independent variables the real and imaginary parts of the Kuramoto-Daido order parameters, namely, $z_n^{\rm re} = {\rm Re}(z_n)$ and $z_n^{\rm im} = {\rm Im}(z_n)$ (here and hereafter, superscripts "re" and "im" denote the real and imaginary parts).

Therefore the linearization of (5.28) can be written as

$$\delta\dot{x}_{2n-1} = \frac{\partial F_n^{\rm re}}{\partial z_m^{\rm re}}\delta x_{2n-1} + \frac{\partial F_n^{\rm re}}{\partial z_m^{\rm im}}\delta x_{2n}\,, \tag{5.30}$$

$$\delta\dot{x}_{2n} = \frac{\partial F_n^{\rm im}}{\partial z_m^{\rm re}}\delta x_{2n-1} + \frac{\partial F_n^{\rm im}}{\partial z_m^{\rm im}}\delta x_{2n}\,, \tag{5.31}$$

where δx_{2n-1} and δx_{2n} are the infinitesimal perturbations of the real and imaginary parts of z_n, respectively. Moreover, the other terms entering in (5.30) and (5.31) can be explicitly written as

$$\frac{\partial F_n^{\rm re}}{\partial z_m^{\rm re}} = \sqrt{i_0}K^{\frac{1}{4}}\left(K\widetilde{\nu}\left(I_{nm}^{\rm re} - \delta_{nm}\right) + \frac{4n(-1)^m}{\pi\widetilde{\nu}}\left[z_n^{(0)}\right]^{\rm im}\right), \tag{5.32a}$$

$$\frac{\partial F_n^{\rm im}}{\partial z_m^{\rm re}} = \sqrt{i_0}K^{\frac{1}{4}}\left(2n\delta_{nm} + K\widetilde{\nu}I_{nm}^{\rm im} - \frac{4n(-1)^m}{\pi\widetilde{\nu}}\left[z_n^{(0)}\right]^{\rm re}\right), \tag{5.32b}$$

$$\frac{\partial F_n^{\rm re}}{\partial z_m^{\rm im}} = \sqrt{i_0}K^{\frac{1}{4}}\left(-2n\delta_{nm} - K\widetilde{\nu}I_{nm}^{\rm im}\right)\,, \tag{5.32c}$$

$$\frac{\partial F_n^{\rm im}}{\partial z_m^{\rm im}} = \sqrt{i_0}K^{\frac{5}{4}}\widetilde{\nu}\left(I_{nm}^{\rm re} - \delta_{nm}\right)\,. \tag{5.32d}$$

The linear stability analysis of time-independent solutions $\mathbf{z}^{(0)} = \{z_n^{(0)}\}$ of system (5.28), (5.29) can be performed by solving the eigenvalue problems associated with Eqs. (5.30) and (5.31). In particular, by truncating the system (5.28), (5.29) to the Mth Kuramoto-Daido order parameter the eigenvalue problem can be solved for a $(2M \times 2M)$ matrix with real-valued elements given by (5.32) to find the associated complex eigenvalue spectrum $\{\lambda_j\}\quad j = 1, \ldots, 2M$. The stationary solution is stable whenever Re $\lambda_j < 0 \quad \forall j$.

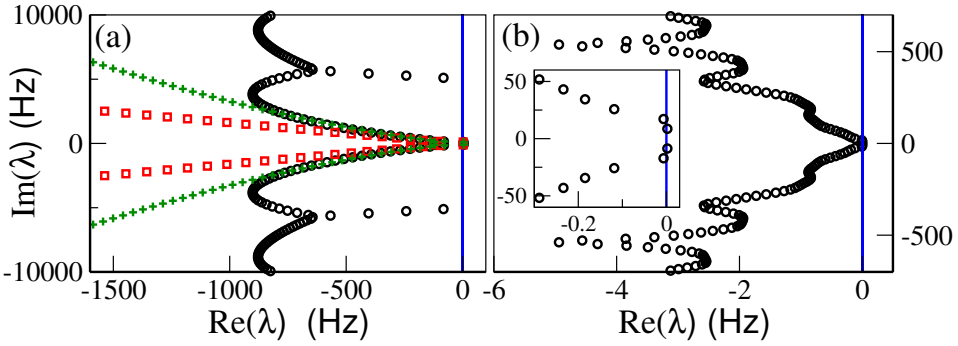

Figure 5.4: Spectrum of the eigenvalues $\{\lambda_i\}$ for a stationary solution of the system (5.17,5.23) for $(i_0/g_0^2, K) = (0.02, 400)$ (a) and $(0.00055, 10)$ (b). An enlargement is reported in the inset in (b). Black circles represent the CMF, the red squares the DA and the green plus signs are for the D3A.

Let us compare the spectra obtained within the CMF, DA and D3A to better understand the origin of the instabilities leading to oscillatory dynamics in the presence of microscopic shot noise. As a first remark, we observe that the DA and D3A spectra are characterised besides

the most unstable modes, which can give rise to the oscillatory instability, by modes that are strongly damped as shown in Fig. 5.4 (a). The case shown in Fig. 5.4 (a) refers to a situation where the dynamics is well reproduced already within the DA (red squares), in this case the DA and D3A (green plus signs) eigenvalues corresponding to small Im λ_j in proximity of the Hopf instability approximate quite well the CMF spectrum (black circles). However, while the CMF eigenvalues appear to saturate at some finite Re λ value, the DA and D3A ones do not. We also notice that the D3A captures extremely well the central part of the CMF spectrum, while the DA deviates quite soon from it. Despite these differences in this case the collective dynamics of the system is essentially controlled by the two most unstable modes, typical of a Hopf bifurcation, that practically coincide within the three approaches.

In Fig. 5.4 (b) we report the CMF spectrum for a situation where the oscillatory regime is definitely due to the finitness of the synaptic stimulations and not captured at all by the DA and D3A. In this case, we observe that a large part of the eigenmodes are now practically undamped, compare the scales over which Re λ_j varies in Figs. 5.4 (a) and (b). Therefore, we expect that the collective dynamics is no longer dominated by only the two most unstable modes as usually observable in the DA, but that also the marginally stable or slightly unstable modes will contribute in the coherent dynamics, see the inset of Fig. 5.4 (b).

In summary, the shot noise promotes the emergence of weakly damped eigenmodes that have a relevant role in the instability of the asynchronous regime at sufficiently small i_0/g_0^2 and in-degrees and that are neglected in the DA.

5.3.4. Weakly nonlinear analysis

As for the linear stability, also for the weakly nonlinear analysis required to characterize the nature of the observed Hopf bifurcations, one must handle $z_n^{\rm re}$ and $z_n^{\rm im}$ as independent real-valued variables. In particular, it is important to stress that the dynamical system (5.28,5.29) is quadratic with respect to the variables $z_n^{\rm re}$ and $z_n^{\rm im}$. The absence of cubic terms makes the calculation of the coefficients of the amplitude equations quite simple as we will see in the following.

Let us now analyse the Hopf instability of the stationary solution $\mathbf{z}^{(0)} = \{z_1^{(0)}, z_2^{(0)}, z_3^{(0)}, \dots\}$ in proximity to the critical value $K_{\rm cr}$, where the in-degree K acts as the control parameter and i_0 and g_0 are maintained constant. In order to perform this analysis we have considered *finite* perturbations $\mathbf{x} = \{x_1, x_2, x_3, x_4, \dots\}$ of the stationary solution, where x_m are real-valued variables defined as follows: $z_n^{\rm re} \equiv (z_n^{(0)})^{\rm re} + x_{2n-1}$, $z_n^{\rm im} \equiv (z_n^{(0)})^{\rm im} + x_{2n}$. To obtain an *exact* evolution equation for the perturbations, we have substituted $z_n = z_n^{(0)} + x_{2n-1} + i x_{2n}$ into the system (5.28,5.29). Furthermore, by remembering that $\mathbf{z}^{(0)}$ solves the r.h.s of the system (5.28,5.29), and rearranging the terms, one can arrive to the following system of differential equations ruling the dynamics of $\mathbf{x}$:

$$\frac{{\rm d}x_n}{{\rm d}t} = F_{nm} x_m + \widetilde{F}_{nml} x_m x_l \,, \tag{5.33}$$

where we imply the Einstein summation rule over repeated indices and odd-indexed(even-indexed) x_n are the perturbations of the real (imaginary) part of z_m. All the linear in $\mathbf{x}$ terms appearing in (5.33) correspond to those obtained within the linear stability analysis; therefore,

the coefficients (5.32) calculated at $\mathbf{z}^{(0)}$ correspond to the coefficients F_{nm} as follows:

$$F_{2n-1\,2m-1} = \left.\frac{\partial F_n^{\mathrm{re}}}{\partial z_m^{\mathrm{re}}}\right|_{\mathbf{z}^{(0)}}, \qquad F_{2n\,2m-1} = \left.\frac{\partial F_n^{\mathrm{im}}}{\partial z_m^{\mathrm{re}}}\right|_{\mathbf{z}^{(0)}},$$
$$F_{2n-1\,2m} = \left.\frac{\partial F_n^{\mathrm{re}}}{\partial z_m^{\mathrm{im}}}\right|_{\mathbf{z}^{(0)}}, \qquad F_{2n\,2m} = \left.\frac{\partial F_n^{\mathrm{im}}}{\partial z_m^{\mathrm{im}}}\right|_{\mathbf{z}^{(0)}}.$$

Further, we need to collect all the terms quadratic in $\mathbf{x}$ which can only originate from the following term in Eq. (5.28):

$$K\left(\widetilde{\nu} - \pi^{-1}\right)\sum_{m=1}^{+\infty}(I_{nm} - \delta_{nm})z_m = \sum_{m,m'}\frac{2K(-1)^{m'}}{\pi}(I_{nm} - \delta_{nm})z_m z_{m'}^{\mathrm{re}};$$

substituting $z_n = z_n^{(0)} + x_{2n-1} + ix_{2n}$ into the latter expression and taking the real and imaginary parts, one can collect all the quadratic $x_m x_l$ terms:

$$\widetilde{F}_{2n-1\,ml}x_m x_l = \sum_{m,m'}\frac{2\sqrt{i_0}K^{\frac{5}{4}}(-1)^{m'}}{\pi}\left[\left(I_{nm}^{\mathrm{re}} - \delta_{nm}\right)x_{2m-1} - I_{nm}^{\mathrm{im}}x_{2m}\right]x_{2m'-1},$$
$$\widetilde{F}_{2n\,ml}x_m x_l = \sum_{m,m'}\frac{2\sqrt{i_0}K^{\frac{5}{4}}(-1)^{m'}}{\pi}\left[\left(I_{nm}^{\mathrm{re}} - \delta_{nm}\right)x_{2m} + I_{nm}^{\mathrm{im}}x_{2m-1}\right]x_{2m'-1}.$$

Since the original equation system (5.28,5.29) contained only quadratic in $\mathbf{z}$ terms, we will also only have linear and quadratic in $\mathbf{x}$ terms.

For the weakly nonlinear analysis of a bifurcation, we have to consider dynamical system (5.33) in a small vicinity of the bifurcation point $K_{\mathrm{cr}}(i_0, g_0)$, where

$$\frac{\mathrm{d}x_n}{\mathrm{d}t} = F_{nm}(K_{\mathrm{cr}})\,x_m + \widetilde{F}_{nml}(K_{\mathrm{cr}})\,x_m x_l + (K - K_{\mathrm{cr}})\left(\frac{\partial F_{nm}}{\partial K}\right)_{i_0,g_0}x_m, \tag{5.34}$$

and $\left(\frac{\partial \ldots}{\partial K}\right)_{i_0,g_0}$ indicates the derivative with respect to K for fixed i_0, g_0. Below we will omit the argument K_{cr} for coefficients F_{nm} and $\widetilde{F}_{nml}$ for brevity.

At a Hopf instability, the most unstable modes are associated with two purely imaginary and complex conjugate eigenvalues. Therefore the linear stability matrix (F_{nm}) has a pair of eigenvalues $\pm i\Omega \equiv \pm i2\pi f^H$ with eigenvector $\mathbf{Y}$ and $\mathbf{Y}^*$, namely,

$$i\Omega Y_n = F_{nm}Y_m, \qquad -i\Omega Y_n^* = F_{nm}Y_m^*, \tag{5.35}$$

and the Hermitian conjugate problem possesses eigenvalues $\mp i\Omega$ with eigenvectors $\mathbf{Y}^+$ and $(\mathbf{Y}^+)^*$:

$$-i\Omega Y_n^+ = F_{mn}Y_m^+, \qquad i\Omega(Y_n^+)^* = F_{mn}(Y_m^+)^*. \tag{5.36}$$

To find the amplitude equation we employ the standard multiple scale method [168, 173] with formal small parameter ε : $\frac{\mathrm{d}}{\mathrm{d}t} = \frac{\partial}{\partial t_0} + \varepsilon\frac{\partial}{\partial t_1} + \varepsilon^2\frac{\partial}{\partial t_2} + \cdots$, $x_n = \varepsilon x_n^{(1)} + \varepsilon^2 x_n^{(2)} + \varepsilon^3 x_n^{(3)} + \cdots$, where t_0 is the time-scale related to the period of the emergent oscillation and t_1, t_2 are the "slow" time-scales, associated with the modulation of the oscillation amplitude. In proximity of a Hopf bifurcation one expects the scaling $|\mathbf{x}| \sim (K - K_{\mathrm{cr}})^{1/2}$ for the oscillation amplitude, thus

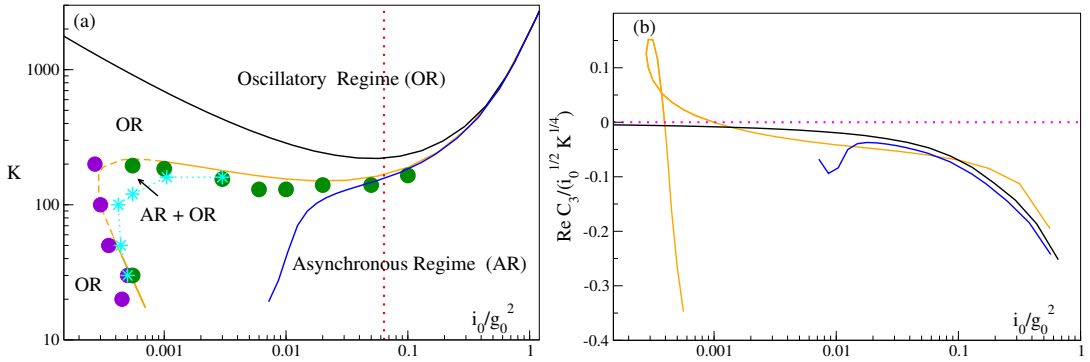

Figure 5.5: (a) Phase diagram for the QIF network in the plane $(i_0/g_0^2, K)$: the black (blue) solid line is the supercritical HB line obtained within the DA (D3A); the orange solid (dashed) line is the super- (sub-) critical HB line given by the CMF; the symbols refer to numerical estimations of the HBs and SNBs. The green (violet) circles denote HBs obtained by performing quasiadiabatic simulations by varying K (i_0) for constant i_0 (K) values; the cyan stars indicate SNBs. The dimension of symbols takes into account for the error bar in the transition point evaluation. The vertical red dotted line is the critical value defined in [157] within the DA for the emergence of fluctuation-driven balanced asynchronous dynamics (for more details see the text). (b) The coefficient $\mathrm{Re}\, C_3$ in rescaled units at the critical points $K = K_{cr}$ versus i_0/g_0^2: CMF (orange solid line), DA (black line), and D3A (blue line). In all simulations we set $g_0 = 1$.

suggesting to expand the control parameter as $K = K_{\rm cr} + \varepsilon^2 K_2$, where $\varepsilon^2 K_2$ is the deviation from the bifurcation point.

By substituting these expansions in Eq. (5.34) we obtain at the first order in ε the following expression

$$x_n^{(1)} = A(t_1, t_2, \dots) Y_n e^{i\Omega t_0} + c.c.\,;$$

and at the order ε^2,

$$\frac{\partial x_n^{(2)}}{\partial t_0} + \frac{\partial A}{\partial t_1} Y_n e^{i\Omega t_0} + \text{c.c.} = F_{nm} x_m^{(2)} + \widetilde{F}_{nml}\left[A^2 Y_m Y_l e^{i2\Omega t_0} + \text{c.c.} + |A|^2 (Y_m Y_l^* + Y_m^* Y_l)\right].$$

One finds $\partial A/\partial t_1 = 0$ and

$$x_n^{(2)} = A^2 \Xi_n e^{i2\Omega t_0} + \text{c.c.} + |A|^2 \phi_n\,,$$

where ϕ_n is the solution of the linear equation system

$$F_{nm}\phi_m = -\widetilde{F}_{nml}(Y_m Y_l^* + Y_m^* Y_l)\,,$$

and Ξ_n is the solution of

$$(F_{nm} - i2\Omega\delta_{nm})\Xi_m = -\widetilde{F}_{nml} Y_m Y_l\,.$$

At the order ε^3, we find the solvability condition,

$$\frac{\partial A}{\partial t_2}(Y_{n'}^+)^* Y_{n'} = K_2 A (Y_n^+)^* \left(\frac{\partial F_{nm}}{\partial K}\right)_{i_0, g_0} Y_m$$
$$+ A|A|^2 (Y_n^+)^* \widetilde{F}_{nml}\left(Y_m^* \Xi_l + \Xi_m Y_l^* + Y_m \phi_l + \phi_m Y_l\right)\,.$$

The latter is the so-called amplitude equation and it can be recast in the standard form

$$\frac{\partial A}{\partial t} = (K - K_{\rm cr})\frac{\mathrm{d}\lambda}{\mathrm{d}K} A + C_3 A|A|^2\,, \tag{5.37}$$

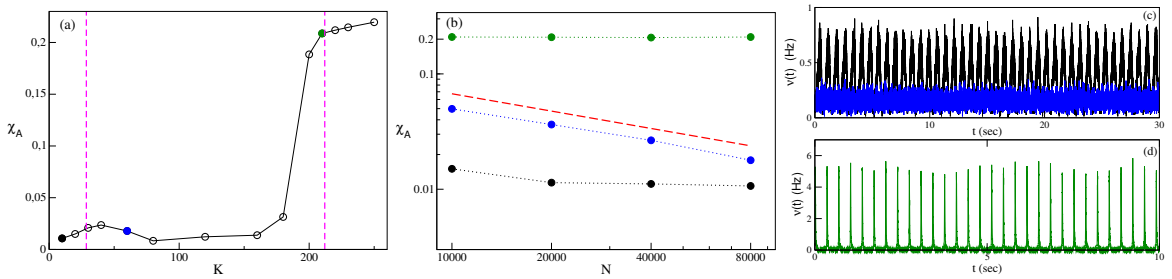

Figure 5.6: Average order parameter χ_A versus K (a) and versus the system size N (b) for $K = 10$ (black circles), $K = 60$ (blue circles) and $K = 210$ (green circles). In (a) the vertical magenta lines denote the HBs obtained within the CMF approach. In (b) the dotted lines are a guide for the eye, while the red dashed line denotes a power-law decay $\propto N^{-1/2}$. The values of χ_A have been averaged over 5–20 network realizations for a time interval $t_E = 20$–30 s following a transient of $t_T = 20 - 30$ s. (c-d) Firing rates $\nu(t)$ versus time t for $K = 10$ (black line) and $K = 60$ (blue line) in (c) and $K = 210$ (green line) in (d). The data in (a) refer to quasiadiabatic simulations for fixed i_0 obtained by increasing (decreasing) K in steps $\Delta K = 10 - 20$. All are for $i_0 = 0.00055$ and $g_0 = 1$; the simulations in (a), (c) and (d) concern networks of size $N = 80\,000$.

where A is the complex amplitude of oscillations, $x_n = AY_n e^{i\Omega t} + \text{c.c.} + O(A^2)$; λ is the exponential growth rate of the leading mode. The expression of the coefficient C_3 is the following:

$$C_3 = \frac{(Y_n^+)^* \widetilde{F}_{nml} \left(Y_m^* \Xi_l + \Xi_m Y_l^* + Y_m \phi_l + \phi_m Y_l \right)}{(Y_{n'}^+)^* Y_{n'}} \,. \tag{5.38}$$

The sign of the real part of C_3 identifies the Hopf bifurcation as subcritical (supercritical) for Re $C_3 > 0$ (Re $C_3 < 0$).

The Hopf bifurcation lines obtained in the plane $(i_0/g_0^2, K)$ with this approach are reported for CMF (orange line), DA (black line) and D3A (blue line) in Fig. 5.5 (a). For the DA and D3A the Hopf lines are always supercritical; this is not the case for the CMF, where they can be either supercritical (solid orange line) or subcritical (dashed orange line). The sub- or supercritical nature of the Hopf bifurcation is decided on the basis of the sign of Re C_3 displayed in Fig. 5.5 (b) as a function of i_0/g_0^2 at the critical points $K = K_{cr}$.

A peculiarity of the CMF results is that the HB line is reentrant; thus in a certain range of i_0/g_0^2 we have an asynchronous regime only within a finite interval of in-degrees and GOs at sufficiently small and large K. As explained in the following these two oscillatory regimes are due to different mechanisms.

Furthermore, there is a dramatic difference among the CMF and D3A approaches and the DA at small i_0 (large g_0): within the DA GOs are observable only above a critical K diverging to infinity for $i_0/g_0^2 \to 0$, while for the CMF (D3A) analysis GOs are present at any K value for $i_0/g_0^2 < 0.00029$ ($i_0/g_0^2 < 0.007$).

5.4. Network Simulations

In order to verify the CMF predictions we have performed extremely accurate numerical simulations of QIF networks, according to (5.1), by employing an event-driven integration scheme (see Appendix A.1.1 for more information), which allowed us to follow the network dynamics for long times, up to 60–100 seconds, for systems of size $N = 10\,000 - 80\,000$. The CMF (5.17,5.23) is able to reproduce reasonably well network simulations (black curves) as shown by the data reported in Fig. 5.1 for various values of K and i_0. Furthermore, also the

agreement between the Langevin results with shot noise (violet curve) and the CMF (turquoise curve) is definitely good for all K, as shown in Fig. 5.1. These comparisons confirm the validity of the considered CMF approach.

Let us now compare the bifurcation diagrams obtained within the CMF approach and via extensive numerical simulations. In particular, to characterize the macroscopic evolution of the network we measured the indicator χ_A (5.5) averaged over several different network realizations. As we will show in the following a finite-size analysis of this order parameter has allowed us to identify numerically the Hopf bifurcations (HBs) and the saddle-node bifurcations (SNBs). This analysis is essentially based on the fact that a coherent macroscopic activity is characterised by a value of χ_A remaining finite in the thermodynamic limit (irrespective of its value), while asynchronous dynamics is associated with a vanishing χ_A; indeed from the central limit theorem one expects that $\chi_A \propto N^{-1/2}$ for $N \to \infty$ [174, 156].

The results of this analysis are reported in Fig. 5.5(a) green (violet) circles refer to HBs identified via quasiadiabatic simulations by varying K (i_0) for constant i_0 (K) values, while the cyan stars indicate SNBs. Numerical simulations are in good agreement with the CMF results and allowed us also the identification of a coexistence region for asynchronous and oscillatory collective dynamics.

In large part of the phase diagram (namely, for $i_0/g_0^2 < 0.1$), in both the AR and OR we observe an irregular firing activity of the neurons associated with the population-averaged coefficient of variations $CV \simeq 0.8 - 1.0$, as expected in sparse balanced networks. This is consistent with the analysis reported in [157], where within the DA a critical value $i_0/g_0^2 = 0.0637\ldots$ separating fluctuation-driven from mean-driven balanced asynchronous dynamics [90] has been identified in the thermodynamic limit. This value, shown in Fig. 5.5 (a) as a red dotted vertical line, can be considered as a lower limit, below which the spiking activity is definitely irregular.

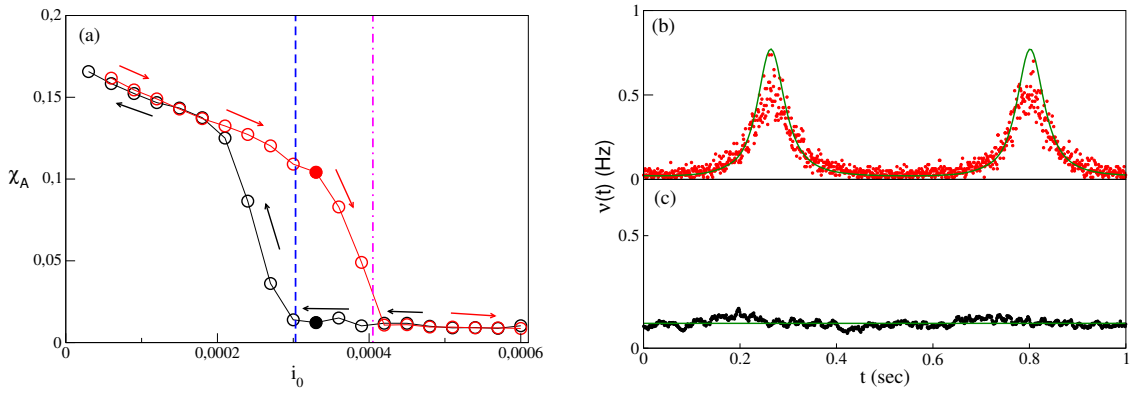

Figure 5.7: (a) Average order parameter χ_A versus i_0 for $K = 100$. The blue dashed line in (a) denotes the subcritical HB given by the CMF and the magenta dot-dashed line: numerically estimated SNB. In (b-c) the population firing rates $\nu(t)$ versus time are reported for the states indicated by the corresponding coloured filled circles; the results for the CMF are also shown as green solid lines. The data in (a) refer to quasiadiabatic simulations for fixed in-degree obtained by increasing (decreasing) i_0 in steps $\Delta i_0 = 0.00003$. The values of χ_A in (a) have been averaged over five network realizations for $t_E = 30$ s following a transient of $t_T = 20$ s. For all data $N = 80\,000$ and $g_0 = 1$.

5.4.1. Finite-size characterization of the observed transitions

Let us now explain in detail for two characteristic cases how we proceeded to estimate numerically the transitions. In order to compare simulations done for a finite network to the CMF results obtained in the limit $N \to \infty$ it is necessary to average over different network realizations, to reduce finite-size effects. The HBs and SNBs reported in Fig. 5.5 (a) have

been obtained by performing finite-size analysis of the order parameter χ_A obtained during quasiadiabatic simulations of the QIF network by varying K (i_0) for constant i_0 (K). In particular, the average value of the order parameter χ_A for each system size N has been obtained by averaging over a time t_E = 20–30 s after discarding a transient of t_T = 20–30 s and over 5 to 20 different network realizations. Therefore, χ_A is obtained as a double average over time and over different random realizations of the connections among the neurons by maintaining K constant; the latter amounts to average over realizations of the quenched disorder present in the network. According to the central limit theorem and analogously to what done in [156], we have classified the dynamical regimes by estimating the parameter χ_A for increasing system sizes N: if the indicator χ_A decreases as $1/\sqrt{N}$ (saturates to some constant value), then the dynamics is identified as asynchronous (oscillatory). The actual value of χ_A is just related to the level of synchronization in the neuronal population, not to the specific macroscopic regime (asynchronous or GOs) displayed by the network.

Furthermore, as shown in Fig. 5.6 (a) for sufficiently small i_0/g_0^2 values, GOs are observable at small ($K \leq 30$) and large ($K \geq 200$) in-degrees, while the AR is present only at intermediate in-degrees ($K \in [40, 180]$). The dynamics in these three intervals is visualized by reporting in Fig. 5.6 (c-d) the firing rates $\nu(t)$ at $K = 10$ (black line), $K = 60$ (blue line) [Fig. 5.6 (c)], and $K = 210$ (green line) [Fig. 5.6 (d)].

In particular, we have estimated, for these three different values of the in-degree $K = 10, 60$, and 210, the scaling of χ_A for system sizes N = 10 000, 20 000, 40 000, and 80 000. From Fig. 5.6 (a) we observe that for $K = 10$ and $K = 210$ (black and green symbols, respectively) χ_A saturates to some constant value and therefore we expect oscillatory dynamics as confirmed by the evolution of the population firing rate $\nu(t)$ reported in Fig. 5.6 (c-d). The value to which the indicator converges is irrelevant for the observation of GOs, it only indicates a different level of synchronization among the neurons. Indeed the neurons are much more synchronized for $K = 210$ as shown in Fig. 5.6 (d) (green line), as compared to the case $K = 10$ reported in Fig. 5.6 (c) (black line). For $K = 60$ we observe that χ_A decreases as $1/\sqrt{N}$ as shown in Fig. 5.6 (b)(blue symbols) and as expected the population firing rate displays irregular fluctuations around a constant value, see Fig. 5.6 (c)(blue line), therefore the dynamics can be safely identified as asynchronous in this case. In this case we do not observe any hysteretic effect, consistent with what predicted by the CMF theory.

A hysteretic transition from AR to OR is instead obtained by varying quasiadiabatically i_0 as displayed in Fig. 5.7 (a) for $K = 100$ and $g_0 = 1$, and the coexistence region can be clearly identified between the subcritical HB (blue dashed line) and the SNB of limit cycles (magenta dot-dashed line). Two coexisting solutions are reported in Fig. 5.7 (b-c) confirming the good agreement between CMF (green lines) and the network simulations (red and black circles).

The bifurcations reported in Fig. 5.7 (a) have been identified as a subcritical HB and a SNB of limit cycles, since they were associated with a hysteretic transition from asynchronous to oscillatory dynamics. The subcritical HB, as identified from the CMF approach, is located at $i_0^{(HB)} \simeq 0.00303$, while the SNB at $i_0^{(SN)} \simeq 0.0040(1)$ has been identified numerically by finite-size scaling of the order parameter χ_A as explained in the following.

It is known that subcritical HBs (SNBs of limit cycles) are characterised by an abrupt transition from an asynchronous to an oscillatory state (from an oscillatory to a stationary state); however from Fig. 5.7 (a) both transition appear as smoothed over a finite interval of the current i_0. This is due to two facts: (1) in the present case the asynchronous regime corresponds to a focus, and therefore damped oscillations forced by finite-size fluctuations are present in the asynchronous state and (2) the indicator χ_A is averaged over different network realizations. This average

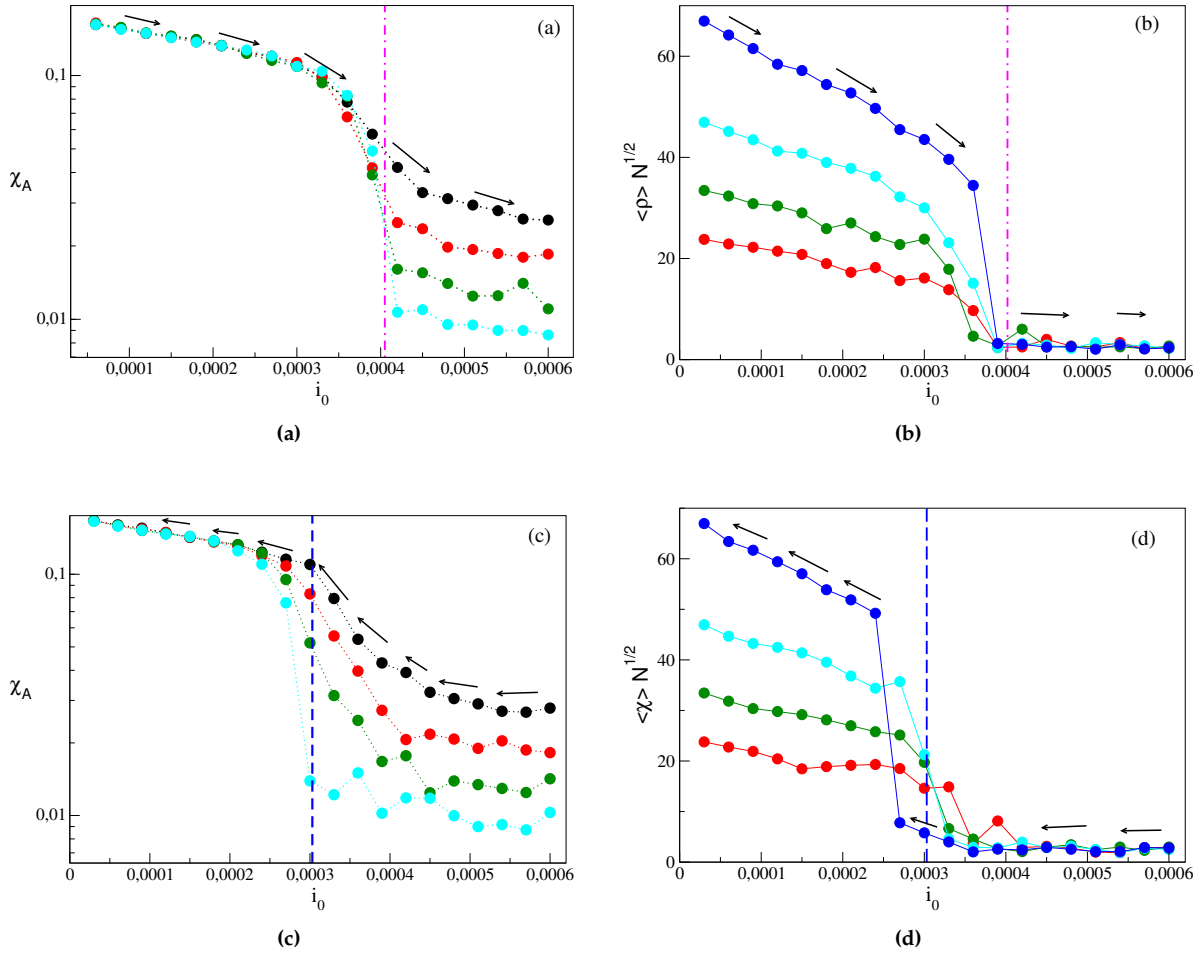

Figure 5.8: (a,c) Average order parameter χ_A versus i_0 for different system sizes: $N = 10\,000$ (black circles), 20 000 (red circles), 40000 (green circles) and 80000 (cyan circles). The values of χ_A have been averaged over 5-20 network realizations for a time interval $t_E = 20 - 30$ s following a transient of $t_T = 20 - 30$ s. (b,d) Order parameter $\langle\chi\rangle$ for a single network realization multiplied by $\sqrt{N}$ versus i_0 for different network sizes. The sizes are identified by the same symbols as in panel (a) apart $N = 160000$ (blue circles). The parameter χ has been averaged in time for a time interval $t_E = 20$ s following a transient of $t_T = 60$ s and refers to a single network realization. The magenta dash-dotted line in (a) and (b) is the SNB numerically estimated via finite-size scaling analysis of χ_A, while the blue dashed line in (c-d) is the subcritical HB obtained from the CMF approach. All data refer to quasiadiabatic simulations of QIF networks with $g_0 = 1$ for fixed in-degree $K = 100$ by varying i_0: the data in (a) and (b) (in (c) and (d)) have been obtained by increasing (decreasing) i_0 in steps $\Delta i_0 = 0.00003$.

allows us to give a better estimate of the transition points, but it has also the drawback of smoothing out the transition over a finite interval, since different networks will have slightly different transition points. However, we expect that for increasing system sizes the transition region will become narrower, since the network realization will be less statistically different and finite-size fluctuations will decrease.

Let us describe in detail the finite-size analysis we have performed. As a first analysis we consider χ_A versus i_0 as obtained by quasiadiabatic simulations by increasing (decreasing) i_0 from the value 6×10^{-5} (6×10^{-4}) to 6×10^{-4} (6×10^{-5}) in steps of $\Delta i_0 = 3\times10^{-5}$ for system sizes $N = 10\,000$, $20\,000$, $40\,000$ and $80\,000$ [the data are shown in Figs. 5.8 (a) and (c)]. It is evident from the figures that the transition region shrinks for increasing N and at the same time for $i_0 > i_0^{(SN)}$ ($i_0 > i_0^{(HB)}$) the value of the parameter decreases drastically with N indicating that the dynamics above such current is asynchronous. On the other hand for $i_0 < i_0^{(SN)}$ ($i_0 < i_0^{(HB)}$) χ_A either remains essentially constant or does not present a clear decrease with N, in this range of currents we can affirm that we have a coherent behaviour characterised by GOs. Furthermore by increasing N the jumps of the order parameter at the transition become higher and steeper, but still at $N = 80\,000$ they seem not to be abrupt. As previously stated, we believe that the origin of this smoothing is related not only to the finite-size effects, but also to the fact that χ_A is obtained as an average over different network realizations, typically presenting slightly different values of the bifurcation points $i_0^{(SN)}$ and $i_0^{(HB)}$.

To verify this conjecture we have considered the time average of the indicator $\langle\chi\rangle$ for only one realization of the network and for systems sizes increasing from $N = 20\,000$ to $N = 160\,000$, the results of this analysis are reported in Figs. 5.8 (b) and (d). To make more evident the transitions we have now reported $\langle\chi\rangle$ multiplied by $\sqrt{N}$ in the figures; in this case for increasing N one will observe an almost constant (growing) value of $\langle\chi\rangle\sqrt{N}$ for asynchronous (oscillatory) dynamics. As a matter of fact, in Fig. 5.8 (b) we observe that for $i_0 \leq 0.00039 < i_0^{(SN)}$ the quantity $\langle\chi\rangle\sqrt{N}$ grows as $N^{1/2}$, while above such value it is almost constant. Furthermore, at $N = 160\,000$ we see an abrupt transition from a value $\langle\chi\rangle\sqrt{N} \simeq 34$ at $i_0 = 0.00036$ to a value $\langle\chi\rangle\sqrt{N} \simeq 2$ at $i_0 = 0.00039$. Similar effects are observable in Fig. 5.8 (d) where the subcritical Hopf is characterised, and also in this case at $N = 160\,000$ the jump from asynchronous to oscillatory dynamics is abrupt. Furthermore, the single realization gives values of the bifurcation points slightly different from that obtained from the analysis of the average χ_A as expected. These indications are consistent with the interpretation we have given of the smoothing of the transitions observable in this case over a finite interval of i_0 and of the lack of abrupt variations of the measured order parameter.

5.4.2. Frequency range of the global oscillations

At the HBs, GOs emerge with a frequency f^H that is reported as a function of i_0/g_0^2 in Fig. 5.9 (a). The comparison between the CMF results (solid line) network simulations with $N = 20\,000$ (blue stars) is very good along the whole bifurcation line predicted by the CMF. Furthermore, f^H covers a wide range of frequencies ranging from 1.77 Hz (δ band) to $\simeq 100$ Hz (γ band), according to the usual classification of the brain rhythms [144]. As visible in the upper part of the panel the population averaged coefficient of variation CV is significantly greater than zero for $i_0/g_0^2 < 0.1$, where, as previously discussed, the firing activity is driven by fluctuations, as expected in the balanced regime. The fluctuation-driven regime is associated with quite high values of the ratio $R_G \simeq 6$–11, indicating that only 9–16% of neurons participate to each population burst and that their activity is definitely slower than the collective one. Instead,

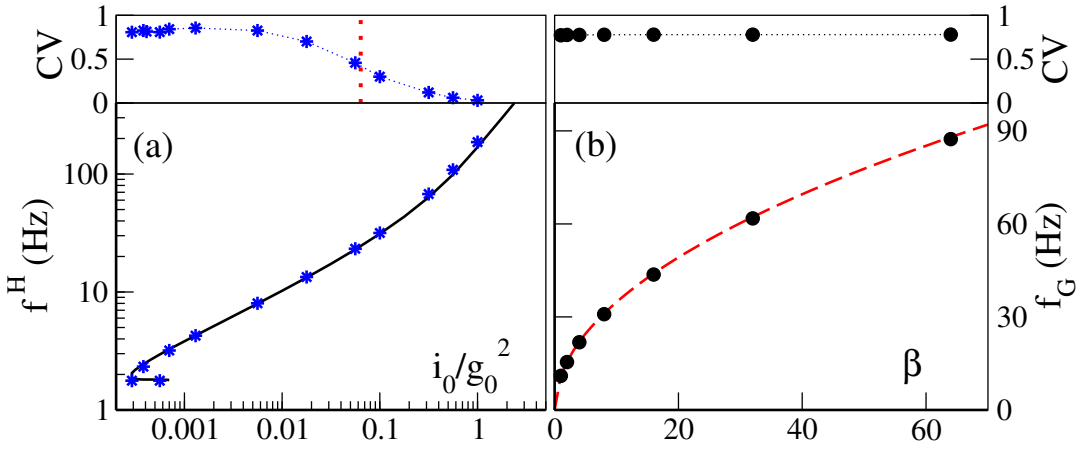

Figure 5.9: (a) Frequency f^H of the GOs at the HB versus i_0/g_0^2: symbols are simulations for $N = 20\,000$ and the solid line is the CMF result. (b) Frequency f_G of the GOs as a function of the parameter β, where $i_0 = \beta \times 0.01$, $g_0 = \sqrt{\beta}$, $K = 200$. Circles are network simulation data with $N = 20\,000$ and the red dashed line represents the curve $\nu_{GO} = 11\sqrt{\beta}$ Hz. The corresponding population averaged coefficients of variation CVs are shown above the two panels with the same symbols employed to denote simulation data. The vertical red dotted line shown in the upper part of panel (a) is the critical value defined in [157] within the DA for the emergence of fluctuation-driven balanced asynchronous dynamics (for more details see the text). All data have been obtained by considering a time interval $t_E = 100$ s, after discarding a transient of $t_T = 20$ s. In (a) we set $g_0 = 1$.

in the mean-driven regime $R_G \to 2$, indicating that we observe the emergence of a peculiar cluster synchronization characterised by two groups (clusters) of neurons alternating their participation to the population bursts with low irregularity. This dynamics is quite similar to the one recently reported in [175] for globally coupled QIF networks subject to additive Gaussian noise. Furthermore, across the examined range, $R_0 \simeq 0.9$–1, suggesting that the GOs are associated with those neurons receiving few/no inhibitory PSPs during the global oscillation period.

As predicted by the CMF, the same dynamics should be observable at fixed K by maintaining the ratio i_0/g_0^2 constant. We verified this by considering a state in the oscillatory regime corresponding to $(K, i_0/g_0^2) = (200, 0.01)$ and by varying, as a function of a control parameter β, the synaptic coupling and the current as $g_0 = \sqrt{\beta}$ and $i_0 = \beta \times 0.01$, while K stays constant. In particular, we observed irregular dynamics characterised by a mean coefficient of variation $CV \simeq 0.78$, as shown in the upper part of Fig. 5.9 (b), associated with GOs in the whole examined range $\beta \in [1, 64]$. As expected, only the time-scale varies, decreasing as $1/\sqrt{I}$, as previously shown, and consequently the frequency f_G of the GOs grows proportionally to $\sqrt{\beta}$ [as shown in Fig. 5.9 (b)] as well as the population average of the firing rates F. Obviously, the ratio of the two frequencies remains constant, and in the present case the ratio $R_G \simeq 7.05$ indicating that one has always a slow firing activity of the neurons with respect to the GOs. Moreover, also R_0 stays almost constant around $\simeq 0.91$ implying that the frequency of the GOs essentially coincides with the frequency of the free neuron ν_0 (5.2). Thus one can observe GOs with the same dynamical features in a wide frequency range by simply varying the parameter β.

5.4.3. Two different types of GOs

As previously mentioned, we can identify two classes of GOs induced by discrete synaptic events in the interval $i_0/g_0^2 \in [0.00036 : 0.00070]$. These two classes correspond to GOs observed at sufficiently low K and high K; in particular for $i_0/g_0^2 = 0.00055$, we have the first

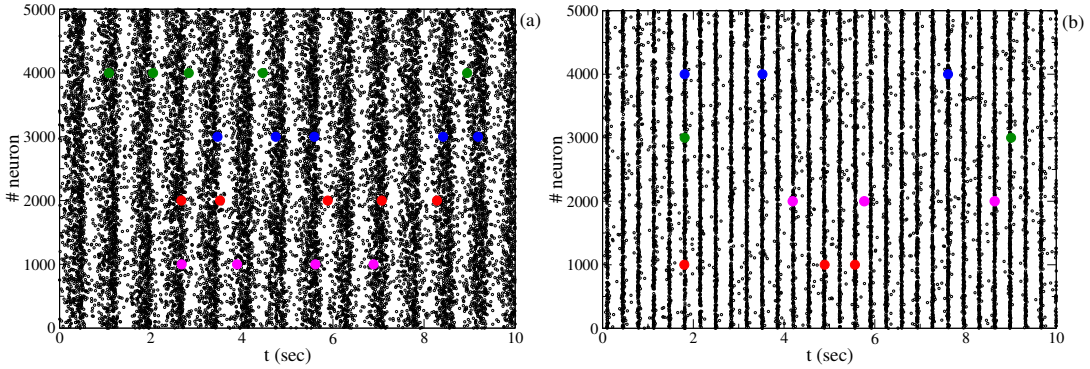

Figure 5.10: Raster plots of 5000 neurons for $K = 10$ (a) and $K = 250$ (b). In both cases the firing times of four neurons are evidenced by coloured circles. Parameters $g_0 = 1$, $i_0 = 0.00055$, and $N = 20\,000$.

type for $K \leq 30$ and the second one for $K \geq 200$, and asynchronous dynamics at intermediate in-degrees (as shown in Fig. 5.6). Raster plots corresponding to $K = 10$ ($K = 250$) are shown in Fig. 5.10 (a) [Fig. 5.10 (b)]. The GOs are characterised by sparser (less synchronized) activity at low K, while at higher K the neurons contributing to the population bursts fire almost at the same moment, with few outliers. However, the neurons participate in a quite random manner to the bursts in both cases (see the red circles in Fig. 5.10). Since the percentage of neurons contributing to a burst is 25% (since $R_G = 4$) for $K = 10$ and 10% for $K = 250$ (here $R_G = 9.6$), in the first case each neuron takes part in many more bursts than in the second case.

Moreover, GOs at $K \leq 30$ are associated with $R_G = 4$–7, while those at $K \geq 200$ to much larger $R_G > 10$, since R_G grows with K, as evident from the lower panel of Fig. 5.11 (a) where data for $i_0/g_0^2 = 0.00055$ are reported for different values of $g_0 = 1$ (black circles) and $g_0 = 20$ (red stars). At the same time the spiking activity of the neurons is always quite irregular being $CV \simeq 0.75$–0.92 in all the examined range of K both in the asynchronous and in the oscillating regime and for $g_0 = 1$ and $g_0 = 20$, as shown in the upper panel of Fig. 5.11 (a).

As shown in Fig. 5.11 (b) and as noticed in the previous sub-section, the frequency of the GOs f_G is well approximated by the frequency of the free neuron ν_0 (5.2), for both $g_0 = 1$ (lower panel) and $g_0 = 20$ (upper panel). The only difference among these two cases being the range of explored frequencies: for $g_0 = 1$ the frequencies are in the δ-range between 1-4 Hz, smaller than 2 Hz for $K \leq 30$ and around 3-4 Hz for $K > 200$, while for $g_0 = 20$ the frequencies are slow γ (< 40 Hz) for $K \leq 30$ and fast γ (60–80 Hz) for large K [176].

The difference among these two GOs becomes clearer by considering the mean-field membrane potential evolution $V_0(t)$ given by the following *zeroth-order* Langevin equation:

$$\dot{V}_0(t) = V_0^2 + \sqrt{K}[i_0 - g_0 \nu(t)] = V_0^2 + A(t) \qquad ; \tag{5.39}$$

where $A(t)$ is the effective input current, $\nu(t)$ is the population firing induced by the shot noise and where current fluctuations have been neglected. Whenever $A < 0$ ($A > 0$) the QIF neuron will display excitable dynamics (periodic firing) [122].

The GOs reported in Fig. 5.6 (c) corresponding to $K = 10$ are characterised by $A(t)$ always being negative, while the GOs shown in Fig. 5.6 (d) for $K = 210$ display an effective current that is positive for a large part of the oscillation period, as shown in Fig. 5.12 (a) and Fig. 5.12 (b), respectively. Therefore, for $K = 10$ $V_0(t)$ displays subthreshold oscillations, while for $K = 210$ it has large excursions from negative to positive values driven by $A(t) > 0$, as evident from the signal denoted by the black solid line in Fig. 5.12 (c) and Fig. 5.12 (d), respectively. In

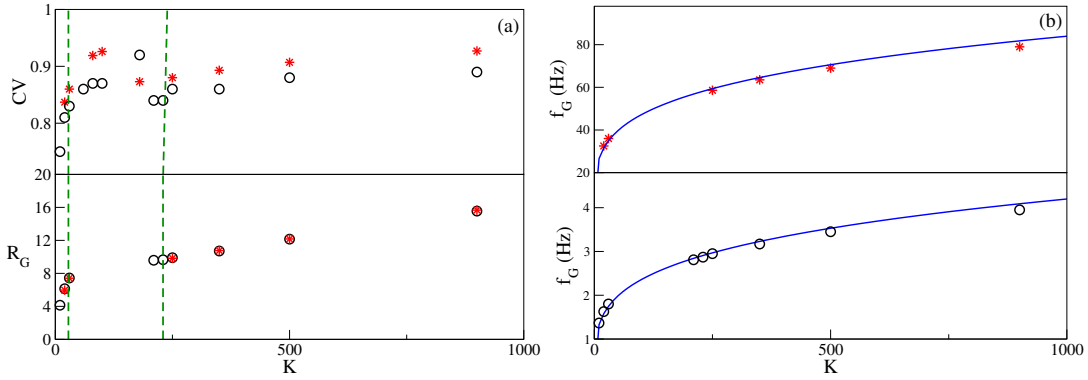

Figure 5.11: (a) R_G versus K in the lower panel, while in the upper panel is reported the population averaged coefficients of variation CVs versus K. The green dashed lines refer to the HBs found within the CMF: GOs are expected for $K \leq 28$ and $K \geq 230$ in this case. (b) f_G versus K, the blue solid lines denote ν_0. Parameters $g_0 = 1$, $i_0 = 0.00055$, and $N = 40\,000$ for the empty black circles, $g_0 = 20$, $i_0 = 0.22$, and $N = 20\,000$ for the red stars.

the same figures we report the time evolution of the membrane potential $v_i(t)$ of four generic neurons (characterised by coloured lines), it is immediately evident that low (high) in-degree GOs are characterised by a low (high) level of coherence among the neurons. For $K = 210$ the single neurons $v_i(t)$ essentially follow the mean-field evolution $V_0(t)$ for a large part of the evolution. However, current fluctuations induce irregular firings of the neurons in proximity of the threshold, indeed $CV \simeq 0.85$. In contrast the dynamics of the neurons is quite uncorrelated over the whole evolution from reset to threshold for $K = 10$ and also in this case the coefficient of variation is reasonably large $CV \simeq 0.75$.

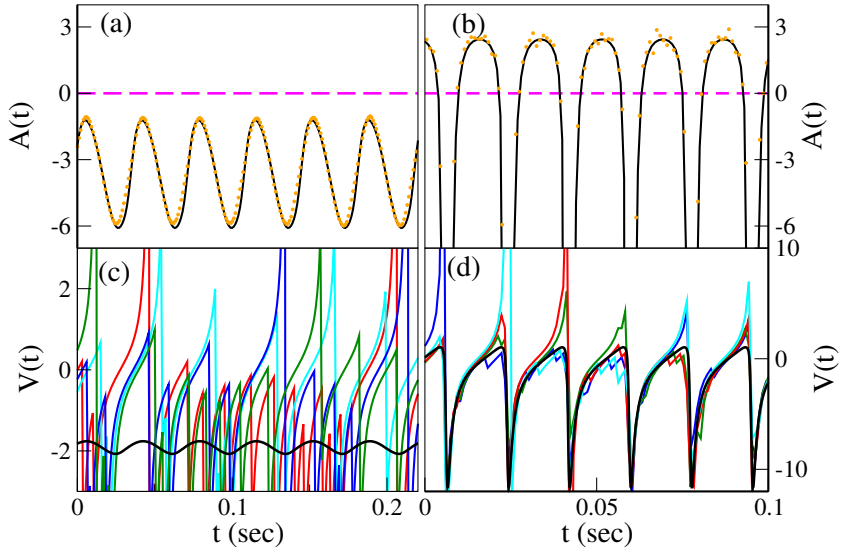

Figure 5.12: (a, b) Effective input currents $A(t)$ versus time: black lines (orange dots) refer to CMF (network simulations) results. (c, d) Membrane potential evolution in time: black lines (other colors) refer to $V_0(t)$ (single-neuron dynamics). Data correspond to $i_0/g_0^2 = 0.00055$ (with $g_0 = 20$) and to $K = 10$ (a, c), $K = 210$ (b, d), network simulations realised for $N = 80\,000$

These behaviours can be somehow explained by two different mechanisms once remembering that for both cases the GO frequency f_G is extremely close to the firing frequency of an isolated neuron $\nu_0 = 1/T_0$. This suggests that at a first approximation the GOs are due to the neurons not receiving any inhibitory PSP from reset to threshold. For low K, whenever a neuron fires large amplitude inhibitory PSPs are delivered since their amplitude is $g_0/\sqrt{K}$. These lead the

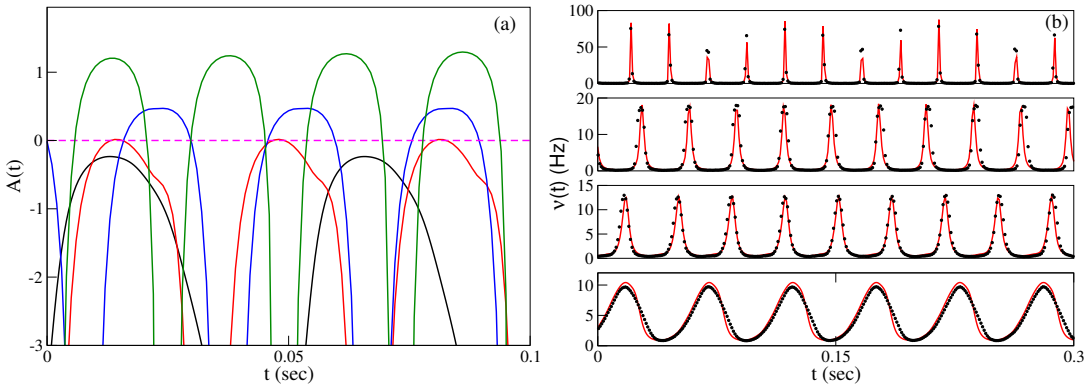

Figure 5.13: (a) Effective input currents $A(t)$ versus time : black line ($K = 10$), red line ($K = 60$), blue line ($K = 100$), and green line $K = 250$. (b) Population firing rates $\nu(t)$ versus time the panels from bottom to top are for $K = 10$, $K = 60$, $K = 100$ and $K = 250$. Solid lines are CMF results obtained via the integration of Eq. (5.10); black symbols denote network simulation for $N = 80\,000$. Data correspond to $i_0/g_0^2 = 0.00027$ (with $g_0 = 20$).

membrane potentials of the K postsynaptic neurons to have quite similar values, and therefore the presynaptic neuron spiking induces a transient synchronization of the K postsynaptic neurons. A subgroup of these, not receiving any further PSPs, can eventually reach threshold together at a time $\simeq T_0$. This transient synchronizing effect of small clusters of neurons (termed *cluster activation*) is at the origin of the GOs observable for $K = 10$. For increasing K, the amplitude of the PSPs decreases, therefore above some critical in-degree ($K \simeq 30$ in this case) a single inhibitory PSP is no longer able to induce a sufficiently strong synchronizing effect on the postsynaptic neurons and the dynamics become asynchronous [as shown in Fig. 5.6 (c) (blue line)].

For larger K, the postsynaptic neurons receive many small inhibitory PSPs at each population burst, whenever K is sufficiently large a non negligible part of the neurons can get synchronized by the discharge of inhibitory PSPs. As shown in Fig. 5.13 (d), the time courses of the membrane potentials are now extremely coherent by approaching the threshold, where fluctuations lead to irregular firing of the neurons. However, a sufficient percentage of these drift-driven neurons is always able to fire together with a period $\simeq T_0$ giving rise to the GOs.

The one described above is the scenario in the interval $i_0/g_0^2 \in [0.00036 : 0.00070]$, where for fixed i_0/g_0^2 one has GOs at low and large K separated by a region of intermediate K where the dynamics is asynchronous. For larger $i_0/g_0^2 > 0.00070$ we have only *drift-driven* GOs, since oscillatory dynamics is observable only for sufficiently large K. At low K either the value of g_0 is too small to promote transient synchronization among the postsynaptic neurons or the period $T_0 = \pi/\sqrt{I} = \pi/\sqrt{i_0\sqrt{K}}$ becomes too long to allow the cluster of postsynaptic neurons to reach threshold without receiving other PSPs.

However, it is unclear what happens for $i_0/g_0^2 < 0.00036$, in this region there are GOs for any value of the in-degree, as shown in Fig. 5.5 (a). The main question is if we pass from one mechanism to the other in a continuous or discontinuous way. Therefore, we have analysed in detail the behaviour in this region by fixing $i_0/g_0^2 = 0.00027$ and by exploring the collective dynamics at different in-degrees. In Fig. 5.13 (a) we report for various K the effective current $A(t)$ obtained within the CMF approach, estimated via the integration of Eq. (5.10) with the pseudo-spectral methods (see Appendix B.2 for more details). From the figure it is evident that $A(t)$ begins to become partially positive for $K \geq 60$; therefore we could speak of the *cluster activation* mechanism for lower K and of the *drift-driven* mechanism for larger K. At the same

time the neurons become more and more synchronized within each population burst, as shown in Fig. 5.13 (b), thus indicating that the effect of a positive $A(t)$ leads them to be more and more coherent as expected. Despite the number of neurons participating to a population burst declines with K, analogously to what seen already for $i_0/g_0^2 = 0.00055$, indeed R_G passes from value 4 at $K = 10$ to value 10 at $K = 250$. At the same time the firing activity remains always irregular with $CV \simeq 0.75$–0.85 in the whole examined range. However, all the indications suggest that the transition from one type of GO to the other occurs smoothly by increasing K in this case.

5.5. Summary and Discussion

In this paper we have presented a mean-field theory for balanced QIF neural networks encompassing synaptic Poisson noise and sparsity in the network connections. This approach, termed complete mean-field (CMF), has allowed us to perform linear and weakly nonlinear stability analysis of the asynchronous state, revealing sub- and supercritical Hopf instabilities leading to global oscillations (GOs). Therefore, besides asynchronous and oscillatory regimes, there is also a region of coexistence of these two solutions near the hysteretic transitions associated with the subcritical Hopf bifurcations. As a further result of this analysis it emerges that the phase diagram depends only on two parameters: the in-degree K (number of presynaptic neurons) and the ratio i_0/g_0^2 between the external excitatory drive and the square of the synaptic coupling. A peculiarity of the Hopf bifurcation line is that it is reentrant at low i_0/g_0^2: in a limited range of i_0/g_0^2 one has GOs at low K and high K values, and asynchronous dynamics at intermediate in-degrees. Furthermore, the GOs observable at low and high K, despite being both associated with the irregular firing of single cells, are promoted by two different mechanisms: "cluster activation" at low in-degree and a "drift-driven" mechanism at high in-degree.

The network dynamics is well captured by the CMF, but not by the diffusion approximation (DA) [157] valid in the limit of small PSPs (large K) and high neuronal activity (large i_0 and/or small g_0). Indeed, the DA works well for large $i_0/g_0^2 > 0.5$, but fails at low i_0/g_0^2 where it is completely unable to reproduce the scenario. In particular, the DA predicts the emergence of GOs only via supercritical Hopf bifurcations and that in the limit $i_0/g_0^2 \to 0$ the critical in-degree K_c required to observe GOs should diverge to infinity. Instead, at sufficiently low $i_0/g_0^2 < 0.00036$ GOs are observable for any K value, as predicted by the CMF and in agreement with simulations.

An intermediate approximation going in the direction of the CMF can be obtained by considering an expansion to the third-order of the source term in the continuity equation. This gives rise to the D3A approximation that we have studied in this paper. This approximation also predicts the emergence of GOs only via supercritical Hopf bifurcations and it is unable to reproduce the reentrant Hopf bifurcation line found within the CMF. On the positive side, D3A captures well the network dynamics already for $i_0/g_0^2 > 0.02$ (i.e. for a parameter value an order of magnitude smaller than the DA) and it forecasts correctly that the GOs are present for sufficiently low i_0/g_0^2 for any in-degree, even if it gives a higher bound for this value with respect to CMF.

To understand the mechanisms responsible for the emergence of GOs at sufficiently low and high in-degree one should consider the effective input current $A(t)$ driving the mean-field dynamics in the two cases: at low K $A(t)$ always induces subthreshold dynamics, while at large K this is mostly suprathreshold. In the first case GOs are promoted by small groups of neurons transiently synchronized by a large inhibitory PSP traveling together towards

threshold, without being affected by further inhibitory PSPs. This is the origin of the name of the mechanism: "cluster activation". At large K a large part of neurons, highly synchronized due to the previously received barrage of small inhibitory PSPs, are "drift driven" towards the threshold by the positive effective input current; however only a small part of them, receiving few or no PSPs, will reach threshold almost at the same time giving rise to the GO. The Hopf bifurcations leading to these two types of GOs are characterised by distinct features. For large K the collective dynamics is clearly dominated by the two most unstable (complex conjugate) eigenvalues. At low K, the spectrum is not only characterised by a pair of complex-conjugate eigenvalues responsible for the instability, but also by additional undamped pairs of eigenvalues that lie very close to the unstable ones. This suggests that, in this case, the instability is no longer controlled only by the two most unstable modes, but also by additional modes, which contribute to the coherent dynamics. Indeed, the population bursts are not generated by highly synchronized neurons, as is the case at high in-degrees.

From analytic investigations performed within the DA in [157], it emerges that the asynchronous balanced dynamics could be either fluctuation-driven (mean-driven) for sufficiently small (large) values of i_0/g_0^2 [90, 177]. Indeed, we have verified that in a large region of the phase space (namely, for $i_0/g_0^2 < 0.1$) the single neuron dynamics remains highly irregular, characterised by $CV > 0.75$, regardless of the in-degree and whether the global activity is asynchronous or oscillatory.

As mentioned in the Introduction, this paper can be considered as the natural completion of the DA analysis reported in two well-known papers devoted to the emergence of GOs in sparse inhibitory [154] and excitatory-inhibitory neural networks [148]. However, the model we consider is the quadratic integrate-and-fire, while the one analysed in [148, 154] is the leaky integrate-and-fire. As already reported in [156], GOs can be observed in QIF sparse networks even for instantaneous synapses in the absence of any synaptic delay. This is not the case for LIF. Indeed, for inhibitory LIF networks the period of GOs is two or three times the synaptic delay (assumed to be on the order of few ms), thus the observable frequencies f_G are limited to a range of 100–200 Hz. Instead, in our case f_G can range from the δ-band (0.5–3.5 Hz) to the γ range (30–100 Hz), where f_G is essentially proportional to the square root of the external excitatory drive I. One would naively expect that slow GOs observable for low I are associated with irregular spiking dynamics, while fast GOs at high I are linked to almost regular neuronal spiking. However, the microscopic dynamical behaviour (fluctuation-driven or mean-driven) is controlled by the value of the ratio i_0/g_0^2. Irregular or regular spiking is observable at fixed in-degree K by maintaining the ratio constant, the only effect of rescaling i_0 and g_0 being the modification of the time-scale of the model. Therefore, GOs of any frequency (fast or slow) can be obtained by conveniently rescaling i_0 and g_0 with either irregular or regular firing.

In [148] Brunel, by considering an excitatory-inhibitory network in the inhibition-dominated regime was able to identify slow ($f_G \simeq$ 20–60 Hz) and fast ($f_G \simeq$ 120–180 Hz) GOs separated by an asynchronous regime. This scenario closely resembles the one we have identified at low i_0/g_0^2. However, the analysis in [148], besides considering excitatory and inhibitory neurons, is performed within the DA, and for purely inhibitory networks only fast oscillations have been reported in [154]. Furthermore, the frequency of the slow (fast) oscillations is controlled by the membrane time constant (synaptic time scale), while in our case it is always related to the external excitatory drive. As a further difference, the parameter R_G (which is the ratio of f_G with respect to the population firing rate) takes values around 3-4 in both the slow and fast oscillation regimes, while in our case $R_G \simeq$ 4–6 for low K and $R_G > 10$ for high K. Therefore, it is worth extending our approach to excitatory-inhibitory networks in order to understand in more detail the origin of these differences and similitudes and to investigate how the scenario

will be modified by the presence of excitatory neurons. A synthetic formulation of the CMF approach for excitatory-inhibitory neural populations is reported in Appendix B.4, where also the possibility to extend our model to distributed synaptic weights and in-degrees K is briefly discussed. The analysis of the excitatory-inhibitory QIF networks is left to future studies.

Our theoretical results are rigorously derived for the continuity equation (5.10) obtained in the thermodynamic limit $N \to \infty$. This equation is valid even for a finite network as long as (1) the firing events of the presynaptic neurons can be treated as independent and (2) all emitting and receiving neurons can be considered to be statistically equivalent. This introduces a lower and upper bound on the in-degree K. On one side, the network must be sparse, $K \ll N$, otherwise, the presynaptic spike trains will no longer be independent. On the other side, for the statistical equivalence any neuron should be connected to any other (no closed loop should emerge), and this is achieved in an Erdős-Rényi network, analogous to the setup we considered, when the in-degree is larger than the percolation threshold, i.e. $K > 1$ [178]. The role of finite N effects for the macroscopic behaviour of sparse LIF networks has been considered in [148, 154] and more recently in [179, 180] for globally coupled QIF networks. Future studies should be devoted to the inclusion of finite-size effects in the framework of the CMF for balanced neural networks.

The limits of applicability of our approach can be summarised as follows : (i) the system size should be sufficiently large to neglect finite-size corrections, in practice we found that at $N = 40\,000 - 80\,000$ finite-size fluctuations are usually negligible; (2) the spike train should be Poissonian, and this is largely verified for $i_0/g_0^2 < 0.1$, as stated above; (3) the in-degree should be in the range $1 < K \ll N$. Despite these limitations, we are indeed surprised by the wide range of parameters where the CMF approach works definitely very well.

Clustering instabilities observed in globally coupled neural networks in the presence of additive noise for LIF [181] and QIF neurons [175] should not be confused with the mechanism of "cluster activation" here reported. The dynamics induced by the clustering instability is characterised by GOs with a frequency that is a multiple of the single neuron frequency and by low irregularity in the firing activity, whereas the GOs emerging due to the "cluster activation" mechanism exhibit stochastic synchrony (in contrast to regular synchrony where neurons resonantly lock with the oscillatory input) with associated high values of the coefficient of variation $CV \simeq 0.75$–0.85 denoting a quite irregular firing activity. Clustered dynamics can be observed in this model only in the mean-driven regime, for large $i_0/g_0^2 > 0.1$ and large $K > 200$. The clustered phase is characterised by population bursts where neurons are split in two equally populated clusters firing in alternation. Although the global activity appears regular, the single neurons display switching between the two clusters due to fluctuations in the input currents, but with a low level of irregularity in their dynamics. This clustering phenomenon has been already reported for heterogeneous and homogeneous globally coupled QIF networks subject to weak additive noise [175].

In the paper we have always considered instantaneous synapses; however a fundamental question is if the introduction of finite synaptic times or the specific shape of PSPs [182] will alter the observed scenario. We can expect that, as long as the burst duration is large compared to the duration of the spike, the fine details of the PSP should be irrelevant for the collective dynamics. Indeed, as shown in Appendix B.3, the introduction of (short) synaptic times does not alter substantially the scenario depicted for instantaneous synapses: namely, for sufficiently low i_0/g_0^2 or K, the DA is unable to capture the network dynamics and the inclusion of discrete synaptic events is fundamental in order to reproduce the network simulations. These results call for the inclusion in the CMF of more biologically realistic features, such as the delay in

the pulse transmission or the finite duration of the PSPs. These generalizations are technically feasible, but they require a careful derivation that goes beyond the scopes of the present analysis and that will be considered in future analysis.

As previously stated, GOs with tunable frequencies can emerge even in extremely sparse inhibitory networks due to the mechanism of "cluster activation". This mechanism can be at the origin of the γ oscillations observed in the cat visual cortex and rodent hippocampus and generated by a population of interneurons with low in-degree $K \simeq 30$–80 [12, 13, 14]. Our results can be even more important for primate where inhibitory and excitatory neurons of the primary visual cortex receive from 3 to 5 times fewer synaptic connections than in the mouse [137]. We must also mention the relevance of our analysis for extremely sparse connectome, such as the one of the Fly *Drosophila melanogaster* where neurons have connection probability of only 0.016 % and a median in-degree $K = 11$ [183] and a prevalence of strong inhibitory connections [184]. A concise discussion of the biological relevance of our results is reported in Appendix B.5.

Conclusion

The main objective of this thesis has been to investigate the emergence of different dynamical phases in random networks of spiking neurons and how these dynamics are shaped by structural features of connectivity and by the statistics of synaptic transmission. Starting from the foundational framework of dynamically balanced networks we explored two major directions that extend this classical theory.

In chapter 4 we demonstrated that in a spiking network operating in the balanced regime, the over-representation (as compared to a random network) of reciprocal synaptic connections produces long-lived fluctuations in neural activity and, consequently, long relaxation times, consistent with in vivo observations [9, 10, 11]. This slow dynamics is independent of the network size and synaptic time constant and instead arises from the effective excitatory self-coupling introduced by the symmetry in the synaptic connectivity. Thus, we conclude that long relaxation times are a generic feature of balanced networks when *realistic* local connectivity is considered [108, 109, 110, 111, 112].

Real cortical networks are not only partially symmetric but also exhibit modularity, clustering, and distance-dependent connectivity [185]. Extending the current analysis to networks combining partial symmetry with structured connectivity [186, 187] could reveal new collective phenomena and clarify how structural heterogeneity interacts with balanced dynamics.

Beyond reproducing previous findings, our study reveals that sufficiently strong self-coupling drives the system into a non-ergodic phase, where network trajectories become history-dependent and fail to explore the full state space. This ergodicity breaking persists even with fast synaptic noise or partial symmetry and leads to multistability when synaptic time constants are long. Notably, this behaviour emerges without low-rank patterns typical of associative memory or clustered networks [120, 188, 189], to our knowledge this is the first report of non-ergodic dynamics in an "unstructured" spiking network.

We confirmed the robustness of these results against finite-size effects ($1000 \leq N \leq 5000$, $100 \leq K \leq 3000$) and across neuron models by reproducing the same phenomenology in networks of leaky integrate-and-fire (LIF) and quadratic integrate-and-fire (QIF) neurons. Developing a dynamical mean-field theory would be the next step to achieve an analytical description of the steady states of networks, though it remains nontrivial.

Our findings thus identify a novel phase of the collective activity in dynamically balanced spiking networks. In this phase, the dynamics reaches, asymptotically, different equilibrium states when starting from random initial conditions, memory of initial conditions persists indefinitely, and convergence to equilibrium becomes extremely slow. This raises the question whether a real cortical network could operate in such a non-ergodic regime. To test this experimentally, we propose measuring the ergodic distance $D(T)$ introduced in [107], which, in principle should be possible. Deviations from $1/T$ in its decay at long times (e.g., $\sim$ 10s) would be supporting evidence of ergodicity breaking, at least in a weak sense (i.e., very long transients but only one equilibrium state). At present, we are actively pursuing this line of research.

This work, which has been conducted in collaboration with Gianluigi Mongillo and Alessandro

Torcini, is currently under revision for publishing [190].

The second original contribution is chapter 5 which has been published in Physical Review E [191], with Denis Goldobin, Maria Ageeva, Matteo di Volo, and Alessandro Torcini.

In this work we developed a *complete* mean-field theory (CMF) for balanced networks of quadratic integrate-and-fire neurons that explicitly incorporates Poissonian synaptic shot noise and network sparsity. The CMF approach reveals that the asynchronous state can loose stability through both subcritical and supercritical Hopf bifurcations, giving rise to global oscillations (GOs). The resulting phase diagram depends only on two key parameters: the in-degree K and the ratio i_0/g_0^2 of external input current to the square of the synaptic strength. Importantly, this phase diagram features a re-entrant Hopf bifurcation line: oscillations can emerge at both low and high in-degree, separated by a region of asynchronous activity. These two oscillatory regimes arise from distinct mechanisms: Cluster activation (low K) and Drift-driven synchrony (high K).

The CMF accurately reproduces network dynamics in regions where the DA fails, particularly at low i_0/g_0^2, where oscillations occur but the diffusion model predicts none. It also captures key features such as highly irregular single-neuron activity and a broad range of oscillation frequencies, from δ to γ bands, determined by the external input strength. These results establish a direct link between the discrete nature of synaptic events and the emergence of collective rhythms and suggest a potential mechanism for experimentally observed oscillations in sparse inhibitory networks, such as those found in the visual cortex, hippocampus, and even in extremely sparse connectomes like that of the drosophila [184, 192].

The results presented in Chapter 5 focus on the impact of discrete synaptic events on network dynamics under the simplifying assumption that inputs are independent Poisson processes. While this assumption enabled a tractable theoretical framework and led to the discovery of novel oscillatory regimes and bifurcation structures, recent experimental evidence suggests that real cortical input statistics deviate significantly from pure Poissonian behavior.

In particular, the work of Pattadkal et al. [193] shows that weak but structured synchrony in presynaptic activity (pairwise correlations on the order of $\rho \sim 0.01$–0.03 and characteristic timescales of tens to hundreds of milliseconds) is a major determinant of neuronal variability in vivo. This synchrony shapes the statistics of synaptic input, modulates single neuron firing irregularity, and underlies transitions between different dynamical regimes across brain states. These recent findings suggest that variability is not simply stochastic "noise" but rather a deterministic consequence of network-level synchrony that varies across behavioral or cognitive conditions.

Considering these findings, a natural extension of the work presented here is to incorporate correlated synaptic input into the complete mean-field (CMF) framework. By enriching the CMF framework with realistic correlation structure, future work could bridge the gap between the microscopic statistics of cortical inputs and the macroscopic phenomena of variability, oscillations, and state-dependent transitions. This integration would bring theoretical models one step closer to the complexity of real cortical dynamics.

Taken together, the results of this thesis advance our understanding of the mechanisms that generate and shape neural dynamics. Structurally, we have shown that even subtle features of the network architecture, such as partial synaptic symmetry, can induce profound changes in temporal organization, leading to long-lived correlations, ergodicity breaking, and memory-like behaviors without requiring structured connectivity. Dynamically, we have demonstrated that the discrete nature of synaptic transmission can give rise to rich oscillatory phenomena beyond

the reach of Gaussian approximation, providing a more realistic theoretical account of cortical rhythms and state transitions.

Appendices

A

Non-ergodic dynamics in quadratic integrate-and-fire networks

We have investigated the effect over-representation of reciprocal synaptic connections in the quadratic integrate-and-fire model (QIF), introduced in Sec. 2.3.4. We will report results for this model under different conditions. Starting from the fully homogeneous case, (where in-degree and synaptic weights are constant for all neurons) to heterogeneous situations, where the in-degrees are distributed according to an Erdös - Reniy distribution and also with synaptic weights with different distributions.

A.1. Model and methods

A.1.1. Event-driven simulations of the QIF network

The QIF network model (5.1) can be integrated by employing an event driven method, since we always considered suprathreshold neurons $I > 0$ [194]. In particular, the method consists in integrating exactly the network evolution between one spike emitted by neuron j at time $T_1 = t_j^{(n)}$ and the next one emitted by the qth neuron at time $T_2 = t_q^{(n+1)}$.

The first step consists in identifying the next firing neuron, therefore one should evaluate the time $\mathcal{T}_i$ needed to each neuron i to reach the firing threshold $v_{th} = +\infty$. These times can be evaluated on the basis of the value of the neuron membrane potential at time T_1^+ (immediately after the spike emission), as follows:

$$\mathcal{T}_i(n+1) = \frac{1}{\sqrt{I}}\left[\frac{\pi}{2} - B_i(T_1^+)\right], \qquad \text{where} \qquad B_i(t) \equiv \arctan\left[\frac{v_i(t)}{\sqrt{I}}\right]. \tag{A.1}$$

The next firing neuron q will be the one associated with the smallest time $\mathcal{T}_q(n+1)$ and the next firing time will be $T_2 = T_1 + \mathcal{T}_q(n+1)$.

Once the next firing neuron is identified, the membrane potential evolution between $[T_1^+, T_2^-]$ is given by

$$v_i(T_2^-) = \sqrt{I}\tan\left(\frac{T_2 - T_1}{\sqrt{I}} + B_i(T_1^+)\right), \tag{A.2}$$

and the membrane potentials of the postsynaptic neurons connected to neuron q should be

modified as follows, due to the spike arrival,

$$v_k(T_2^+) = v_k(T_2^-) - g_0 \qquad \text{if} \qquad k \in \text{post}(q) \ , \tag{A.3}$$

while the others are left unchanged. At this point the adjoint variables $B_i(T_2^+)$ are evaluated by following their definition, apart from the one associated with the spiking neuron q that it is simply set to $B_q(T_2^+) = -\pi/2$ due to the reset condition for the membrane potential (namely, $v_q(T_2^+) = -\infty$). The iterative procedure can be now repeated to find the next firing neuron and so on.

See also [195] for a recently developed efficient event-driven simulations scheme for sparse random networks.

A.1.2. Overlap observables

To analyze the system behaviour, we introduce a further order parameter: the overlap between the firing rate fluctuations of the single neurons in different replicas by generalizing a definition given in [196] for random laser dynamics. For a given neuron we measure the fluctuations across replicas:

$$\Delta_i^\alpha = \overline{\nu_i^\alpha} - r_i \quad ; \tag{A.4}$$

where $\overline{\nu_i^\alpha}$ is the time averaged firing rate of neuron i in replica α and r_i is the replica averaged firing rate of neuron i, i.e.

$$r_i = \frac{1}{M} \sum_{\alpha=1}^{M} \overline{\nu_i^\alpha} \quad ; \tag{A.5}$$

with M the number of replicas. The overlap among two replicas α and β is then defined as:

$$Q^{\alpha\beta} = \frac{\sum_{k=1}^{N} \Delta_i^\alpha \, \Delta_i^\beta}{\sqrt{\sum_{k=1}^{N} (\Delta_i^\alpha)^2} \sqrt{\sum_{k=1}^{N} (\Delta_i^\beta)^2}} \quad . \tag{A.6}$$

where N is the number of neurons in the network. Two perfectly correlated replicas will have $Q^{\alpha\beta} = 1$, while two perfectly anti-correlated replicas will have $Q^{\alpha\beta} = -1$. If the replicas are completely uncorrelated, then $Q^{\alpha\beta} = 0$. We obtain one value of $Q^{\alpha\beta}$ for each pair, therefore for M replicas we will have $M(M-1)/2$ different values. We then estimate their distributions.

Physically, the overlaps $Q^{\alpha\beta}$ quantify the similarity between two microscopic activity patterns for two distinct replicas of the same network. Each replica shares the same synaptic connectivity but differs in the initial conditions of the membrane potentials.

A.2. Results

In the following section, we report results obtained using the Quadratic Integrate-and-Fire model as introduced in the chapter 2.3.4. To isolate the contribution of different sources of heterogeneity, we progressively increase the network complexity: starting from the *most homogeneous* network, i.e. a random network with constant in-degree and homogeneous parameters for all neurons. Then we consider more heterogeneous situations: first, we analyze networks where the in-degree is Erdös-Reniy distributed, then we add the heterogeneity also in the synaptic couplings. In all cases, we considered balanced networks of inhibitory neurons receiving a constant external excitatory input.

A.2.1. Homogeneous network and synaptic weights

In the *homogeneous* configuration, all neurons are randomly connected but receive exactly K inputs and where the synaptic weights are all equally fixed to $-g_0/\sqrt{K}$ and the external DC current to $\sqrt{K}i$. When reciprocal connections are introduced, each such pair occupies one in-degree and one out-degree slot for both neurons. Figure A.1 shows the degree distribution in this configuration for different levels of reciprocity in synaptic connections. Increasing the reciprocity makes the network more homogeneous, but also imposes structural and combinatorial constraints to its construction. In the limit $q = 1$, these constraints become overdetermined: it is generally impossible to make all pairs reciprocal while maintaining an identical number of incoming connections for every neuron. For this reason, we did not include the limit $q = 1.0$ in the fixed in-degree configuration.

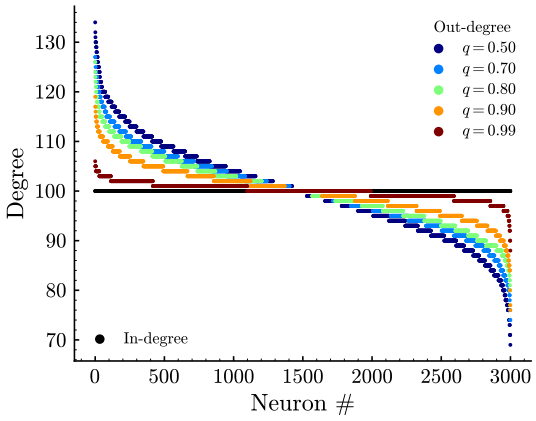

Figure A.1: In- and out-degree distributions for varying reciprocity q. $N = 3000$, $K = 100$.

We first identify, by varying synaptic coupling strength, an asynchronous irregular regime in the absence of excess reciprocity. We measured the level of synchronization among the neurons using the indicator χ previously defined (5.5) [197]. Setting $g_0 = 5$ seems a reasonable choice, as we can observe on Fig. A.2 (a) the coefficient of variation is high even for $q = 0.0$ ($CV = 0.85$), and the activity remains asynchronous for all values of q as shown on Fig. A.2 (b), the order parameter χ goes from ~ 0.12 at $q = 0.0$ to ~ 0.05 at $q = 0.99$. Thus indicating that the dynamics is not presenting coherent activity among neurons and that it can be assumed to be indeed asynchronous.

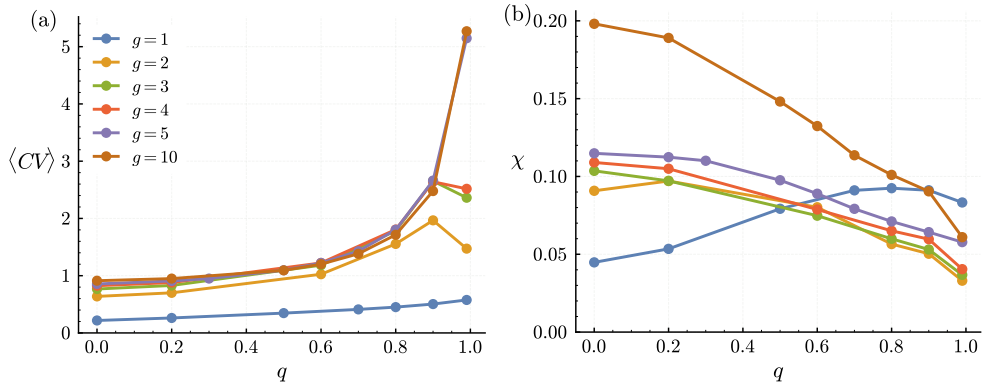

Figure A.2: (a) The population averaged CV (a) and order parameter χ (b) as a function of q and for different synaptic strengths. $N = 3000$, $K = 100$.

In this network configuration, for $q = 0.$, the dynamics of the single neuron is highly irregular ($\langle CV \rangle = 0.85$), and the distribution of the CV, shown in Fig A.3 (d), is very narrow. The average firing rate is relatively low, $\langle \nu \rangle = 3.1$ Hz at $q = 0.0$. However, as the level of symmetry increases, the firing rate distribution broadens as illustrated in Fig. A.3 (a). For $q = 0.9$ the maximum firing rate is around 7 Hz, while for $q = 0.99$ it reaches 30 Hz. This effect is mirrored in the CV histograms in Fig. A.3 (d) the distribution shifts towards CV > 1 for partially symmetric networks, a clear sign of bursting dynamics. The bursting is observable in the raster plots in Fig. A.3 (c).

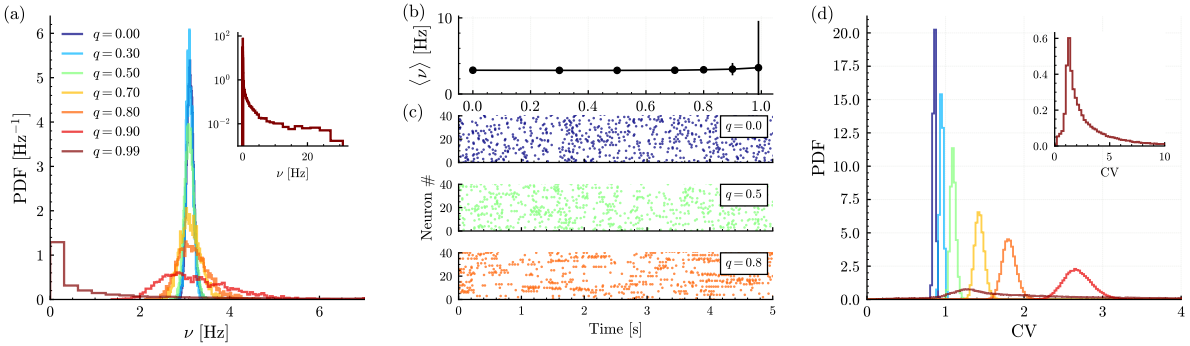

Figure A.3: (a) Probability density functions of the firing rate, the inset shows the distribution for $q = 0.99$ in a semi-logarithmic scale. (b) The population averaged firing rate as a function of q. (c) Raster plots for different values of q. (d) The distribution of the coefficient of variation of individual neurons. Again, the inset shows the distribution when $q = 0.99$. $N = 3000$, $K = 100$, $g_0 = 5$. In the distributions we have combined data from 25 realizations (5 networks and 5 replicas per network).

To assess the level of ergodicity of the networks we compute the distance between replicas $D(T)$, as defined earlier 4.28. We first study how $D(T)$ evolves in fully symmetric network for different values of the synaptic couplings (Fig. A.4).

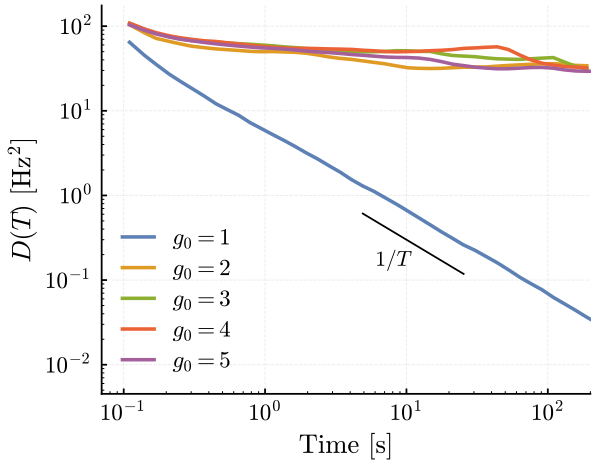

Figure A.4: Distance indicator in highly symmetric networks, $q = 0.99$, with homogeneous synaptic couplings. $N = 3000$, $K = 100$. The data have been obtained by considering 5 different replicas for each network realization, i.e. by averaging over 20 unique pairs of replicas for each network, and then by averaging over 5 different network realizations. In total this makes 100 unique pairs.

We see from figure A.5 (a) that in partially symmetric networks $D(T)$ eventually decays as $1/T$. However for highly symmetric networks, i.e. $q = 0.99$, $D(T)$ seems to saturate, even after 1000 s, we therefore label them as a non ergodic regimes. Non ergodicity for $q = 0.99$ is already

evident for $g_0 \geq 2$.

Another way to measure the breaking of ergodicity is by using the overlap indicator (A.6). Examples are reported in Fig A.5 (b) for a fixed synaptic coupling strength g_0 and different symmetry levels q. Note that for $q = 0$, all overlaps are centered around zero. The firing-rate fluctuations of two replicas are uncorrelated. This indicates that the network has completely lost memory of its initial state and that time averages coincide with ensemble averages, as expected for an ergodic system.

By increasing symmetry we observe a broadening of the overlap distributions. In highly symmetric networks the overlap Q reaches *large* positive values, indicating strong positive correlations in the firing activity. This is difficult to see on Fig A.5 (b), but on Fig. A.5 (c) we report the maximum value of the overlap distributions as a function of q. We see that few pairs are highly correlated $Q > 0.8$.

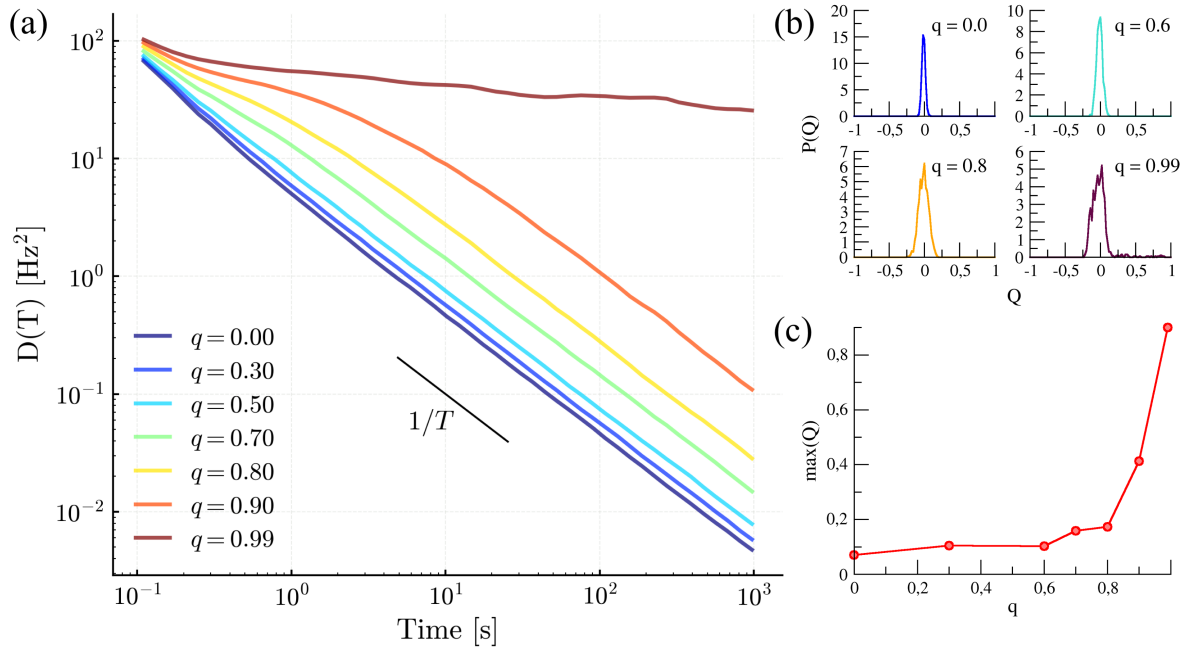

Figure A.5: (a) $D(T)$ for different level of symmetry, 5 networks with 5 to 45 replicas per network. (b) Overlap distributions, using 45 replicas. (c) The maximum value of the overlaps as a function of q. $N = 3000$, $K = 100$, $g_0 = 5$.

In this configuration, we have used 45 replicas, which make 990 distinct pairs. Interestingly, at $q = 0.99$, we find a few large positive overlaps but not one of the overlaps falls below -0.25, by symmetry one could expect to also find large negative values. When two replicas evolve from different initial conditions, their microscopic configurations may differ, but they do not form *anti-symmetric* patterns in which highly active neurons in one replica correspond to inactive neurons in the other.

This could be a consequence of the structural homogeneity of the network: since every neuron receives exactly K inputs of identical strength, the resulting input statistics are nearly uniform across the population. This is visible in the distribution of the time averaged synaptic input, Fig. A.6, the distribution gets shifted to the right and becomes narrower for larger q. Neurons receive stronger, and more similar inputs.

The global inhibitory balance further constrains the dynamics, enforcing a common population

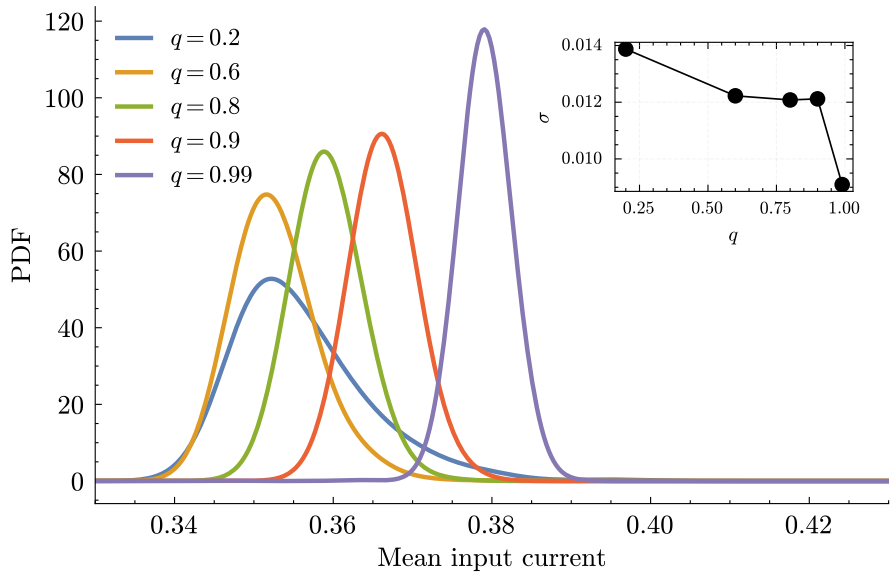

Figure A.6: Distribution of the time averaged input currents of individual neurons, for different symmetry levels of the network. In the inset we show the standard deviation of the distributions. $N = 3000$, $K = 100$, $g_0 = 4$.

firing rate and coupling fluctuations across neurons. There is (almost) no heterogeneity in connectivity that could single out specific neurons as more excitable or more inhibited than others.

As a consequence, deviations from the mean activity in different replicas tend to remain positively correlated, leading to overlap values distributed around zero or positive but never strongly negative. Only when structural heterogeneity is introduced (through variable in-degree or distributed synaptic weights) can large negative overlaps appear, reflecting partial inversions between subsets of neurons.

A.2.2. Erdős-Rényi network and homogeneous weights

We now introduce random connectivity while keeping the synaptic weights homogeneous. The degree of the nodes are normally distributed, as shown in Fig. A.7.

The resulting dynamics remain irregular and asynchronous for $g_0 = 5$, see Fig. A.8.

We illustrate the dynamics of the network using $g_0 = 5$ in Fig. A.9, where we show that the firing rate distribution in the network is right-skewed and long-tailed. As we increase the level of symmetry we observe that the distribution of firing rates becomes more skewed, see how the value of the 95th percentile increases with q in A.9 (c). For high levels of symmetry we can also observe that many neurons are almost silent or even completely silent, in the fully symmetric network, see the large peak in the first bin on Fig. A.9(a). The result of these two effects is that the average firing rate remains relatively unchanged, but its standard deviation increases.

The irregularity of the spike trains is also drastically increased, this is measured, as done in the LIF model, with the population averaged CV. For example, with $g_0 = 5$, it increases from 0.85 for $q = 0$ to 1.5 for $q = 0.8$ and 2.8 for $q = 1.0$. Typically a coefficient of variation larger than one indicates bursting activity, indeed we observe some neurons firing many times consecutively in the inset of Fig A.9 (d) for $q = 0.8$.

As can be seen on Fig. A.8 (b) increasing the strength of inhibition tends to make the dynamics

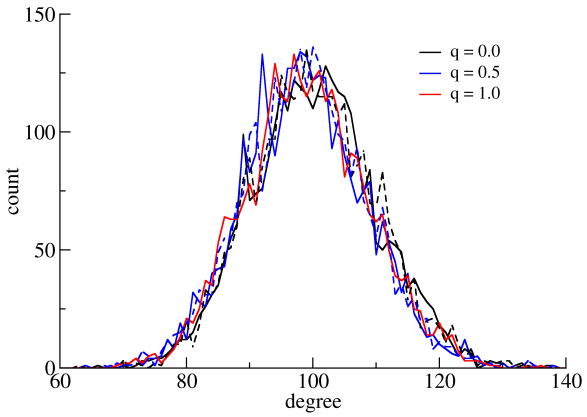

Figure A.7: In- (solid lines) and out-degree (dashed lines) distributions of nodes in the network, for different levels of symmetry.

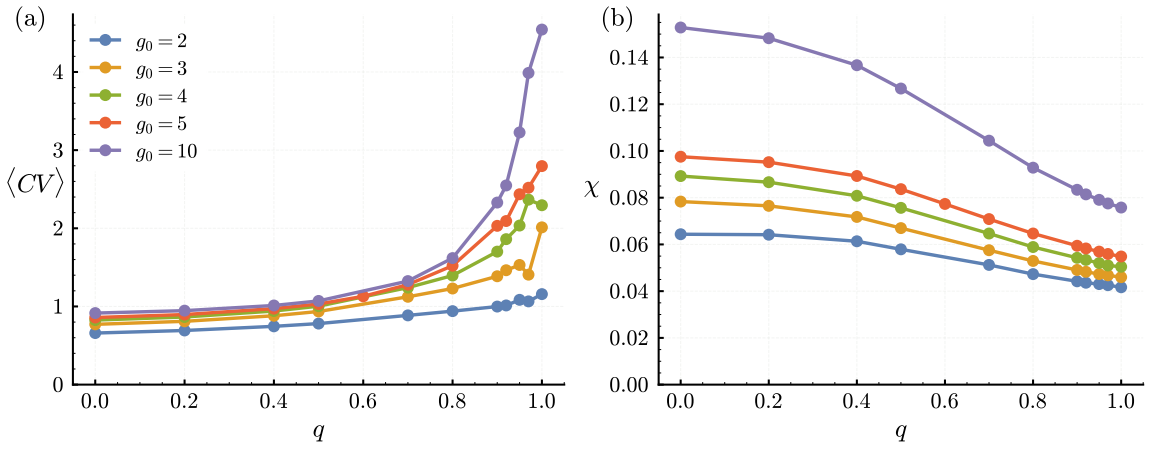

Figure A.8: The coefficient of variation (a) and the order parameter χ (b) as a function of q for different synaptic strength. $N = 3000$, $K = 100$.

more synchronized, but increasing the symmetry does not. As a matter of fact, χ is decreasing with larger q.

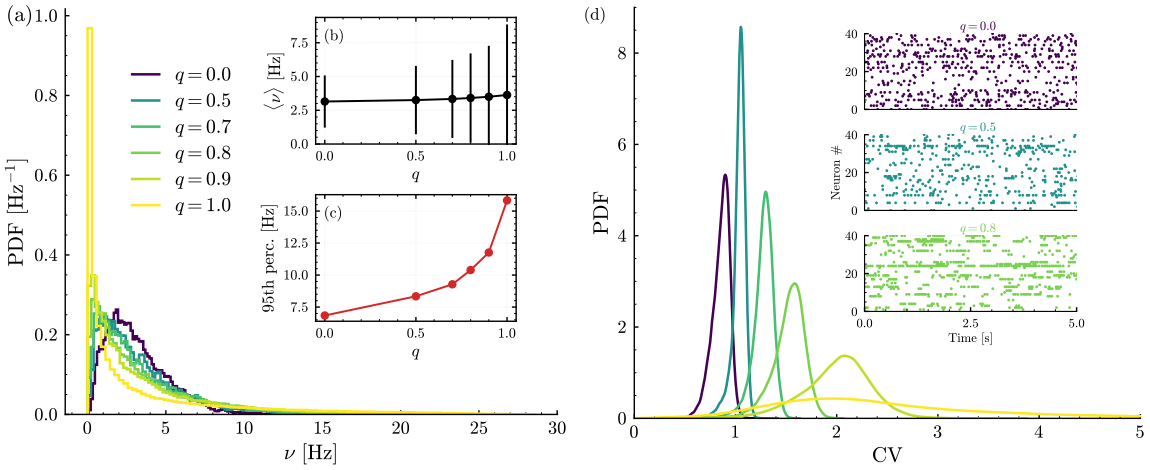

Figure A.9: (a) Firing rate distribution for different levels of symmetry in the network. 2 networks and 50 replicas of each. The inset (b) shows the population averaged firing rate as a function of q, the error bars represent the standard deviation. (c) The 95th percentile as a function of q. (d) Distribution of the coefficient of variation of individual neurons firing rate. Data aggregated from 5 networks using 3–5 realisations of each. The insets show the firing activity for different levels of symmetry. We used the following parameters: $N = 3000$, $K = 100$ and $g_0 = 5$.

Let us now study the ergodic properties of such a network. We see from figure A.10 (a) that in a fully symmetric network, $D(T)$ tends to decay slower than $1/T$, this effect is increased by the strength of inhibition. We note that now, the level of reciprocity alone is not enough to make $D(T)$ saturate, strong enough inhibition is also necessary. This is unlike the homogeneous configuration, see Fig. A.4, thus, we conclude that heterogeneity in the network has reduced the effect of reciprocal connections. For $g_0 = 5$, the fully symmetric network $D(T)$ does not decay as $1/T$ even after 1000 s, we therefore label it as a non ergodic regime. For a fixed $g_0 = 5$ and varying levels of symmetry, we see on Fig. A.10 (b) that $D(T)$ only saturates in the fully symmetric network.

These results are similar to what we observed in the network with fixed in-degree. However the situation changes if we look at the overlap distributions. Examples are reported in Fig A.10 (c) for a fixed synaptic coupling strength $g_0 = 5$ and different symmetry levels q, and in Fig A.11 as a function of q and g_0.

Up to $q = 0.7$, in Fig A.11, all overlaps are centered around zero. The firing-rate fluctuations of two replicas are uncorrelated. This indicates that the network has completely lost memory of its initial state and that time averages coincide with ensemble averages, as expected for an ergodic system. By increasing the symmetry we observe a broadening of the overlap distributions, when the inhibition is sufficiently strong (i.e. $g_0 > 2$). In highly symmetric networks the overlap Q assumes all possible values in the range $[-1, 1]$, highlighting the fact that correlation between firing rates fluctuations in a given pair of replica depends on the replicas selected.

Each replica settles into a specific pattern of activity. Different replicas may fall into different patterns, but those patterns are not random: they can share partial correlations, the overlap measures the similarity of those attractors. Contrary to the fixed in-degree configuration, we now observe large negative correlations, meaning that it is possible for a neuron to behave completely differently across realisations of the same network.

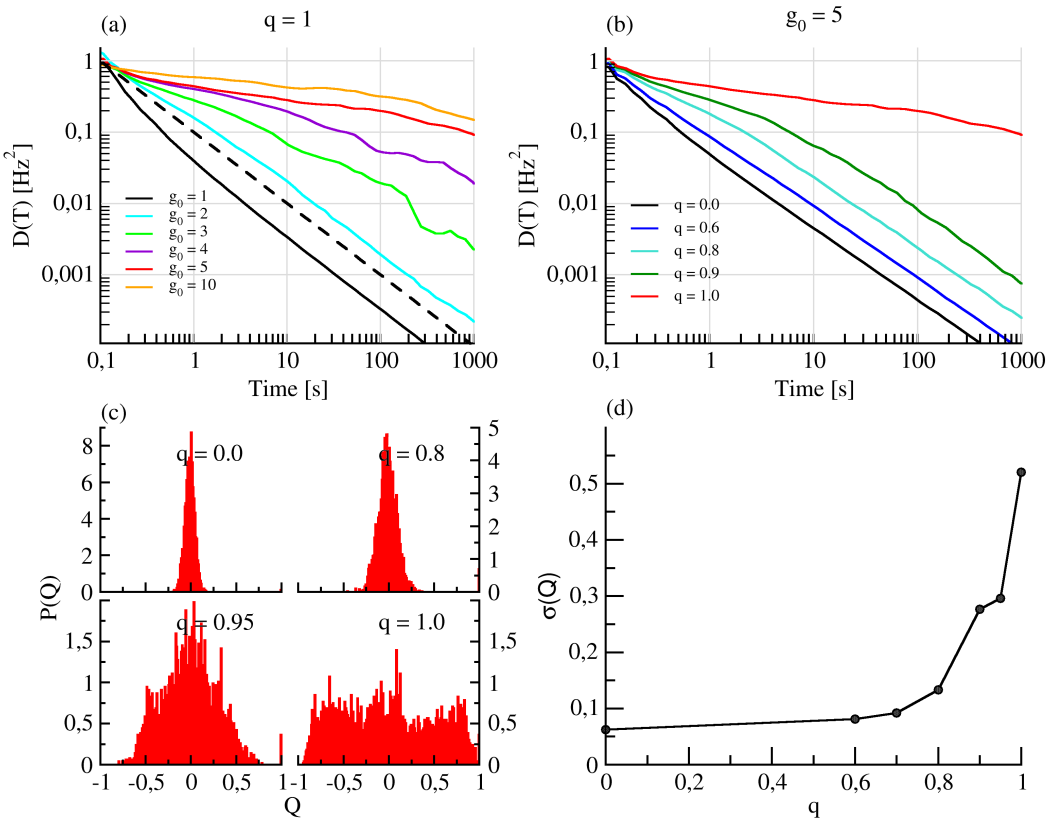

Figure A.10: (a) The distance $D(t)$ as a function of time in fully symmetric networks, for different synaptic couplings strength. (b) Fixing the synaptic couplings to $g_0 = 5$, we vary the level of symmetry q in the connectivity matrix. (c) The distribution of the overlaps Q for $g_0 = 5$ and different symmetry levels. (d) The standard deviation of the overlaps distributions as a function of the symmetry.

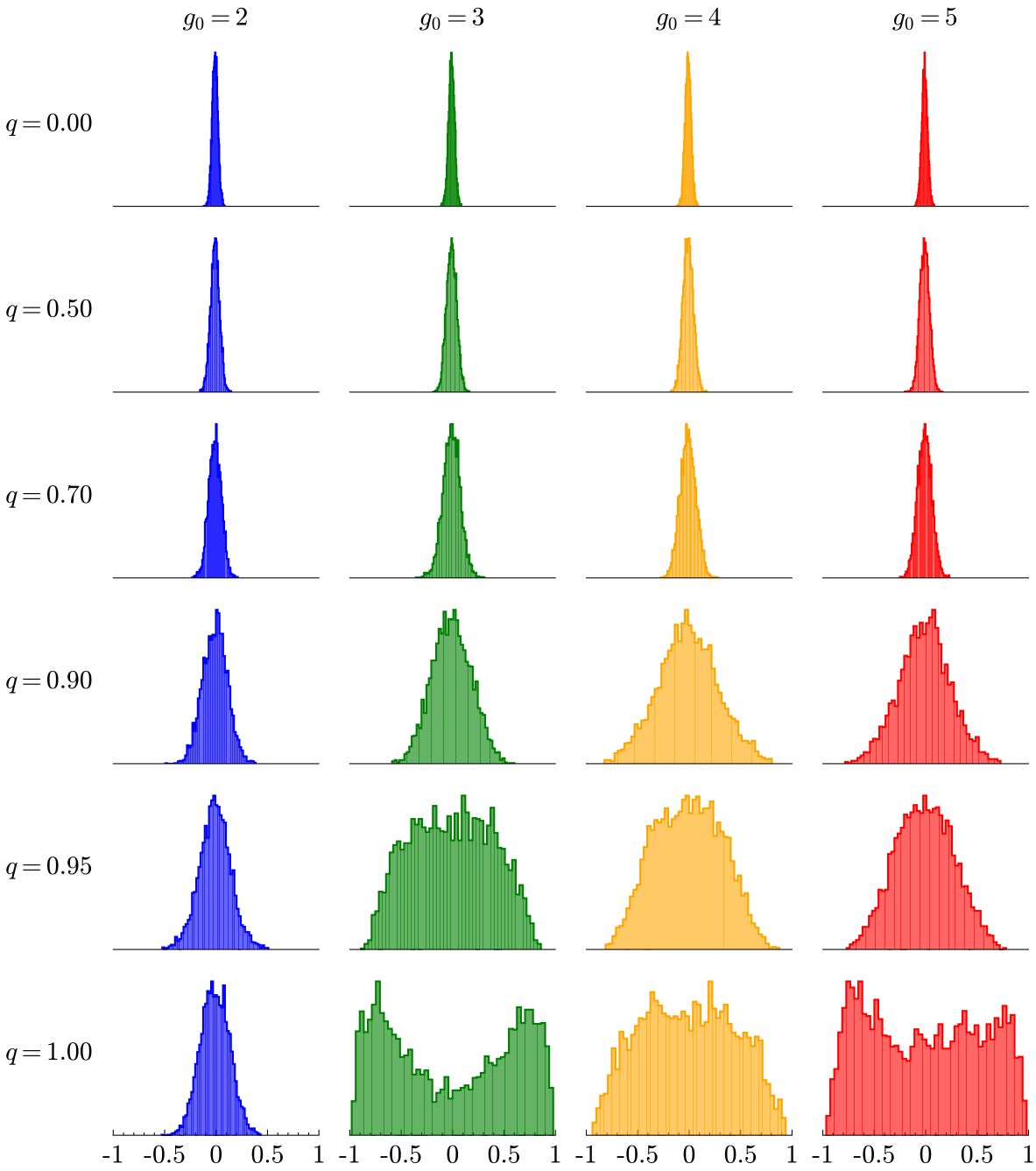

Figure A.11: Left: distribution of the overlaps Q between different replicas for different levels of symmetry q and different synaptic couplings. Right: the absolute maximum value of the overlaps. 100 replicas of a single network with $N = 3000$, $K = 100$.

A.2.3. Erdős-Rényi network with heterogeneous synaptic weights

We will now consider the case where the synaptic couplings are distributed according to a uniform distribution of mean g_0 and width A. Therefore the effective couplings will range across $\left[(g_0 - A)/\sqrt{K},\ (g_0 + A)/\sqrt{K}\right]$. The general dynamic of the network is very similar to the case with homogeneous synaptic weights. We can note that the standard deviation of the population averaged firing rate is already large at $q = 0.0$, see Fig. A.12, which was not the case previously.

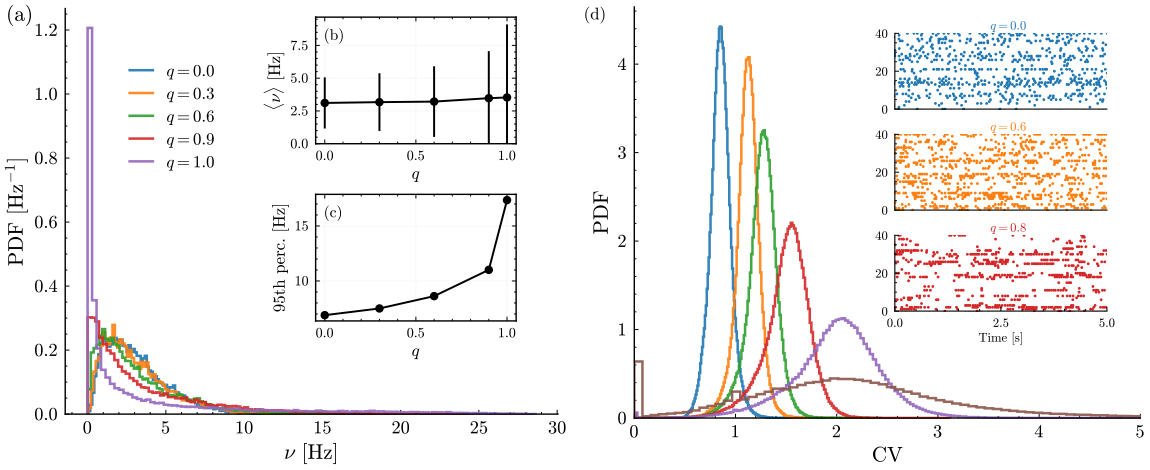

Figure A.12: (a) Firing rate distribution for different levels of symmetry in the network. The inset (b) shows the population averaged firing rate as a function of q, the error bars represent the standard deviation. (c) The 95th percentile as a function of q. (d) Distribution of the coefficient of variation of individual neurons firing rate. The insets show the firing activity for different levels of symmetry. We used the following parameters: $N = 3000$, $K = 100$ and $g_0 = 5$, data aggregated from 4 networks and 45 replicas of each.

However, heterogeneity in the synaptic couplings does seem to reduce the effect of saturation in $D(T)$. See Fig. A.13, lighter shades of the main colors indicates wider coupling distributions.

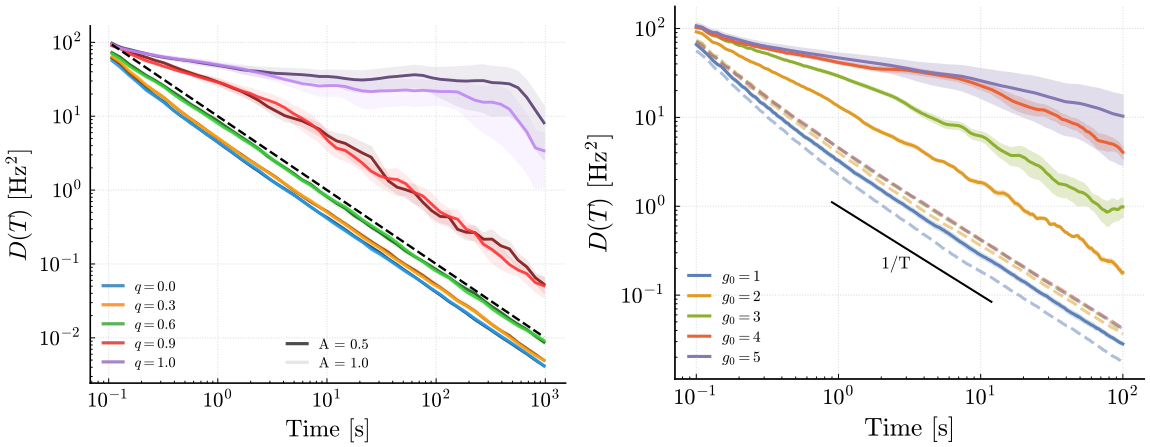

Figure A.13: Left: effect of the width A of the synaptic strength distribution on the average distance $D(t)$ between replicas. The black dashed line show the decay of $1/T$. Right: Effect of the mean synaptic strength g_0 on the average distance $D(t)$ between replicas. Solid lines represent simulations with a fully symmetric network ($q = 1$), while dashed lines are for a fully random network ($q = 0$). In both cases synaptic weights were uniformly distributed $g_{ij} \sim \mathcal{U}(g_0, A)$, 5 replicas of the same network were used to compute the distances, other parameters were set to $N = 3000$, $K = 100$, $\eta = 0.1$.

A.3. Summary

We have studied the effect of synaptic reciprocity on the dynamics and ergodicity of inhibitory QIF neuronal networks. In particular we have carefully analysed the role of heterogeneity, both in the synaptic couplings and in the topology of the network. In all three configurations, increasing the reciprocity enhanced the firing variability while maintaining asynchronous macroscopic activity. In the limit of fully symmetric networks, the system becomes non-ergodic.

In homogeneous networks some replicas remained correlated, even after long times, but when we observed large correlations, only positive were found. As we have seen, in the network with fixed in-degree, increasing the reciprocity effectively also fixes the out-degree. Due to the high homogeneity of the network all neurons experience nearly identical inputs, preventing anti-correlated microscopic configurations.

When degree heterogeneity is introduced, negative overlaps emerge: distinct replicas can evolve towards anti-correlated microscopic states. The system thus explore a wider set of attractors. Adding heterogeneity in synaptic strengths reduces these correlations and tends to restore ergodicity. Variability in the strengths counteracts the self-consistency of geometric motifs.

Overall, reciprocity promotes the emergence of structured, long-lived and non-ergodic activity patterns. Heterogeneity seems to reduce this effect, although, interestingly, adding heterogeneity in the node degree extended the overlap distributions into the negative range, indicating that replicas can settle in anti-correlated microscopic configurations.

B

Methods and additional analysis for chapter 5

B.1. Integration of the Langevin equations

Regarding the integration of the mean-field Langevin equations for shot noise (5.7) and DA (5.9), we considered $N = 20\,000$–$80\,000$ replica of such equation, corresponding to N *uncoupled* QIF neurons. In particular, we integrated such N uncoupled evolution equations either (5.7) or (5.9) by employing an Euler integration scheme with Δt. The population firing rate $\nu(t)$ entering in Eq. (2) at time t is estimated self-consistently by counting the number of spikes $N_{sp}(\Delta t)$ emitted by the N neurons in the preceding time window T_w, as follows:

$$\nu(t) = \frac{N_{sp}(\Delta t)}{T_w N} \,. \tag{B.1}$$

For the shot noise case (5.7), at the end of every time interval T_w, every neuron receives an inhibitory postsynaptic input of finite amplitude g with a probability $K \times \nu(t) \times \Delta t$ mimicking a Poissonian process with rate $K\nu(t)$.

To simulate the Langevin evolution within the DA, we considered N uncoupled neurons whose membrane potential obeys the stochastic differential equation (5.9). The firing rate is estimated also in this case by the activity of the N neurons via (B.1) by performing an average on a sliding time window of duration T_w and the integration is performed again via an Euler scheme. We fixed $\Delta t = 5 \times 10^{-4}\tau_m$ and $T_w = 0.005\tau_m$, and an initial transient time $t_t = 10$ s is discarded in all the simulations.

B.2. Integration of the continuity and Fokker-Planck equations

In order to integrate the CMF and the FPE we transformed the membrane potential V in the angular variable $\theta = 2 \arctan V$ with $\theta \in [-\pi, +\pi]$; in the present case we used the standard transformation to pass from the QIF to the θ model.

Accordingly, the PDF $P(V, t)$ for the membrane potentials is related to the PDF $R(\theta, t)$ of the corresponding angular variables as follows

$$P(V, T) = (1 + \cos\theta) R(\theta, t) \,. \tag{B.2}$$

The CMF equation then takes the following form

$$\frac{\partial R(\theta,t)}{\partial t} = -\frac{\partial}{\partial \theta}\left[((I+1)+(I-1)\cos\theta)R(\theta,t)\right] + K\nu(t)\left[R(\theta^+,t)\frac{1+\cos\theta^+}{1+\cos\theta} - R(\theta,t)\right] . \quad \text{(B.3)}$$

where

$$\theta^+ = 2\arctan\left[\tan\left(\frac{\theta}{2}\right) + g\right] . \quad \text{(B.4)}$$

By expanding the term within square brackets on the r.h.s in (B.3) up to the second order in g we obtain the corresponding FPE in the angular space,

$$\frac{\partial R}{\partial t} = -\frac{\partial}{\partial \theta}\left\{\left[(1-\cos\theta)+(A(t)+D(t)\sin\theta)(1+\cos\theta)\right]R - D(t)(1+\cos\theta)^2\frac{\partial R}{\partial \theta}\right\} , \quad \text{(B.5)}$$

where $A(t) = \sqrt{K}[i_0 - g_0\nu(t)]$, $D(t) = [g_0^2\nu(t)]/2$ and $R = R(\theta,t)$.

The Fokker-Planck formulation can be extended by including the third-order term in the expansion, this amounts to add on the r.h.s of (B.5) the following term:

$$H(t)\frac{\partial}{\partial \theta}\left[(1+\cos\theta)^3\frac{\partial^2 R}{\partial \theta^2} - 3\sin\theta(1+\cos\theta)^2\frac{\partial R}{\partial \theta} + (1+\cos\theta)(1-\cos\theta-2\cos^2\theta)R\right] , \quad \text{(B.6)}$$

where $H(t) = \frac{g_0^3}{3!\sqrt{K}}\nu(t)$.

In all the cases listed above we assumed that the flux at the threshold determines the instantaneous population firing rate, therefore this sets the following boundary condition for the PDFs

$$\lim_{V\to\infty} V^2 P(V,t) = 2R(\pi,t) = \nu(t) .$$

B.2.1. Time-splitting pseudo-spectral method

The above partial differential equations can be integrated by employing time-splitting pseudo-spectral methods developed for spatially extended systems, such as the complex Ginburg-Landau equation [198], surface growth models [199] and asymmetrically coupled Swift-Hohenberg and Cahn-Hilliard equations [200]. In particular, in order to perform the numerical integration we considered a discrete grid for the angular values of resolution $\Delta\theta$ and a discrete time evolution with a constant time step Δt. The discretized PDF can be written as $R(i,n)$, where the integer indices i and n represent the angular and temporal variables, respectively. Periodic boundary conditions are assumed for the PDF: $R(i,n) = R(i+I,n)$, where I is the number of sites of the grid namely $2\pi = I\Delta\theta$.

In general the evolution equations for the PDF $R(\theta,t)$ can be rewritten as follows

$$\partial_t R(\theta,t) = (\mathcal{L}+\mathcal{N})R(\theta,t) , \quad \text{(B.7)}$$

where $\mathcal{L}$ and $\mathcal{N}$ are a linear and nonlinear operator, respectively. For a sufficiently small time step Δt the formal solution of (B.7) is the following

$$R(\theta,t+\Delta t) = e^{(\mathcal{L}+\mathcal{N})\Delta t}R(\theta,t) . \quad \text{(B.8)}$$

The evolution operator appearing in (B.8) can be approximated via the Trotter formulas as follows:

$$e^{(\mathcal{L}+\mathcal{N})\Delta t} \approx e^{\mathcal{N}\Delta t/2}e^{\mathcal{L}\Delta t}e^{\mathcal{N}\Delta t/2} + \mathcal{O}(\Delta t^3) . \quad \text{(B.9)}$$

For a finite time-interval $T = M\Delta t$ we can lump together $M-1$ integration steps and approximate the evolution operator over the interval T as

$$e^{(\mathcal{L}+\mathcal{N})T} \approx e^{\mathcal{N}\Delta t/2}\left(e^{\mathcal{L}\Delta t}e^{\mathcal{N}\Delta t}\right)^{M-1} e^{\mathcal{L}\Delta t}e^{\mathcal{N}\Delta t/2}\ ; \tag{B.10}$$

this amounts to perform successive integration of the linear and nonlinear part. The linear part

$$\partial_t R(\theta,t) = \mathcal{L}R(\theta,t) \tag{B.11}$$

is usually solved in Fourier space where it takes the form

$$\partial_t \tilde{R}(p,t) = f(p)\tilde{R}(p,t), \tag{B.12}$$

where $\tilde{R}(p,t)$ is the Fourier transform of the PDF $R(\theta,t)$ over the angular variable, p is an integer defined in the interval $p \in [-I/2, I/2-1]$ representing the wave number and $f(p)$ is a polynomial in p. The time evolution for $\tilde{z}$ over a time step Δt is given by

$$\tilde{R}(p,t+\Delta t) = e^{f(p)\Delta t}\tilde{R}(p,t)\ ; \tag{B.13}$$

therefore the integration of (B.11) in the original space can be written as

$$\tilde{R}(\theta,t+\Delta t) = \mathcal{F}^{-1}e^{f(p)\Delta t}\mathcal{F}R(\theta,t)\ , \tag{B.14}$$

where $\mathcal{F}$ ($\mathcal{F}^{-1}$) is the direct (inverse) Fourier transform.

The integration of the nonlinear part amounts to solve

$$\partial_t R(\theta,t) = \mathcal{N}R(\theta,t), \tag{B.15}$$

and this can be integrated by employing some standard integration method. Specifically we have employed the Euler scheme, and therefore the time evolution of the PDF is given by

$$R(\theta,t+\Delta t) = R(\theta,t) + [\mathcal{N}R(\theta,t)]\Delta t. \tag{B.16}$$

In order to increase the precision of the integration, the angular derivatives of R eventually entering in $\mathcal{N}R(\theta,t)$ have been evaluated in the Fourier space.

In the following we will explicitly report the linear and nonlinear operators considered in the article.

The CMF

The linear operator for the CMF is

$$\mathcal{L}R(\theta,t) = -(I+1)\frac{\partial R(\theta,t)}{\partial\theta} - K\nu(t)R(\theta,t), \tag{B.17}$$

and the nonlinear one is

$$\mathcal{N}R(\theta,t) = -\frac{\partial}{\partial\theta}\left[(I-1)\cos\theta R(\theta,t)\right] + K\nu(t)\left[R(\theta^+,t)\frac{1+\cos\theta^+}{1+\cos\theta}\right]. \tag{B.18}$$

The linear integration can be performed as in (B.14) with

$$f(p) = -K\nu(t) - (I+1)ip,$$

where i is the imaginary unit.

The FPE
The linear operator for the FPE can be written as

$$\mathcal{L}_{FP}R(\theta,t) = D(t)\left[R(\theta,t) + \frac{\partial^2 R(\theta,t)}{\partial\theta^2}\right] - (1+A(t))\frac{\partial R(\theta,t)}{\partial\theta} \tag{B.19}$$

and the nonlinear one as

$$\begin{aligned}
\mathcal{N}_{FP}R(\theta,t) &= f(\theta,t)R(\theta,t) + g(\theta,t)\frac{\partial R(\theta,t)}{\partial\theta} + h(\theta,t)\frac{\partial^2 R(\theta,t)}{\partial\theta^2}, && \text{(B.20)}\\
f(\theta,t) &= \sin\theta(A(t)-1) - D(t)(2\cos^2\theta + \cos\theta), && \text{(B.21)}\\
g(\theta,t) &= \cos\theta(1-A(t)) - 3D(t)\sin\theta(1+\cos\theta), && \text{(B.22)}\\
h(\theta,t) &= D(t)\cos\theta(2+\cos\theta). && \text{(B.23)}
\end{aligned}$$

The term needed for the linear integration appearing in (B.14) has the following expression

$$f(p) = D(t)(1-p^2) - (1+A(t))ip.$$

The extention to the third-order is algebraically complicated, but straightforward; we do not report here the expressions of the linear and nonlinear operators but they can be easily derived from (B.5) and (B.6).

B.3. Synaptic Filtering

In the paper we have always considered instantaneous synapses; however a fundamental question is if the introduction of finite synaptic times will alter the observed scenario. In particular, to generalize our findings we have considered a network of QIF neurons with exponentially decaying PSPs, this amounts to rewriting the model (5.1) as follows:

$$\begin{aligned}
\dot{v}_i(t) &= v_i^2 + I - gS_i(t) \quad i = 1,\dots,N,\\
\tau_s\dot{S}_i(t) &= -S_i(t) + \sum_{j=1}^{N}\sum_n \varepsilon_{ji}\delta(t - t_j^{(n)}),
\end{aligned} \tag{B.24}$$

where $S_i(t)$ represents the synaptic input current due to the linear super-position of the exponential PSPs emitted by the presynaptic neurons connected to neuron i and τ_s is the synaptic decay time of the PSP.

We have considered the same case reported in Fig. 1 (b) in [158], but this time the PSPs have a finite duration, namely $\tau_s = 0.1\tau_m$. As shown in Fig. B.1, analogously to what found for instantaneous synapses the DA (red line) fails in reproducing the network simulations (black line), while the inclusion of shot noise in the Langevin dynamics allows us to recover the correct evolution (violet line).

Therefore we can conclude that for finite τ_s we find the same scenario reported for instantaneous synapses. A detailed investigation of the role of the synaptic filtering is left to future analysis.

B.4. Complete mean field approach for excitatory-inhibitory networks

One can extend the continuity equations (5.17) to the case of excitatory-inhibitory networks with excitatory (inhibitory) in-degree K_e (K_i) and excitatory (inhibitory) synaptic coupling

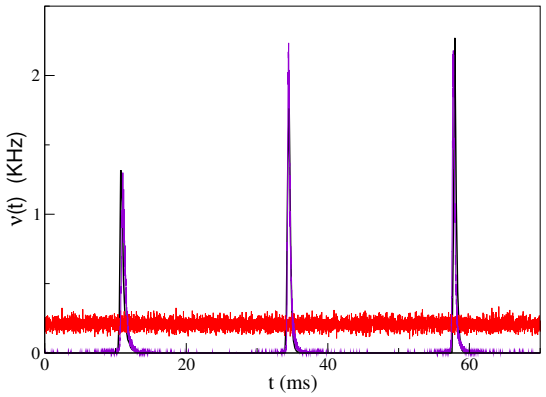

Figure B.1: Population firing rates $\nu(t)$ versus time for exponentially decaying PSPs. The black line refers to network simulations with $N = 20\,000$, and the red (violet) line to Langevin simulations for diffusive (shot) noise with $N = 20\,000$ uncoupled neurons. The data are from QIF networks with exponentially decaying PSPs (B.24) with $K = 200$, $i_0 = 0.16$, $g_0 = 4$, and $\tau_s = 0.1\tau_m$.

strength g_e (g_i), where both populations are subject to the same external excitatory drive I. The CMF formulation becomes in this case the following:

$$\dot{z}_n = i2n\sqrt{I}z_n + \nu(t)\left\{\sum_{m=0}^{+\infty}\left[K_i I_{nm}(\alpha_i) + K_e I_{nm}(-\alpha_e)\right]z_m - (K_i + K_e)z_n\right\}\,, \tag{B.25}$$

where $\alpha_{i/e} = g_{i/e}/\sqrt{I}$; the relation between $\nu(t)$ and $\{z_n(t)\}$ remains the same reported in Eq. (5.23). For distributed synaptic weights, the main modification is in the expression of $I_{nm}(\alpha_{i/e})$, since now the coefficients (5.22) should be averaged over $g_{i/e}$ with the weights given by the distribution of $\alpha_{i/e} = g_{i/e}/\sqrt{I}$.

For distributed in-degrees $K_{i/e}$, the Kuramoto-Daido order parameters now depend also on the values of the in-degree; however the dynamics of $z_n(K_i, K_e, t)$ is still given by (B.25) and one can estimate self-consistently $\nu(t)$ from $z_n(K_i, K_e, t)$ weighted with the distribution of the in-degrees $K_{i/e}$.

B.5. Biological Relevance

In this appendix we will try establish in which regime our results can have a biological relevance for real brain circuits. The first relevant quantity entering in our model is the amplitude $g = g_0/\sqrt{K}$ of the postsynaptic potentials, or synaptic weights; this quantity has been experimentally measured revealing PDFs with heavy tails towards large values [133, 108, 70]. This would require us in the future to extend our model by including distributed synaptic weights. So far, it has been shown that analytical results for the stationary solutions of the shot noise continuity equation can be found for balanced and purely excitatory LIF networks only when the synaptic weights are exponentially distributed [138, 141]. A generalization to generic distributions can be obtained only for purely inhibitory LIF populations; see [140]. It is interesting to notice that for QIF neurons, the problems related to the overshoots over the threshold v_{th} induced by excitatory finite PSPs should be not present since the threshold value is now at $v_{th} = +\infty$, and therefore one would not be limited to consider exponentially decaying PDF for the synaptic weights even in excitatory-inibitory networks. For a discussion of how to include distributed synaptic weights in the CMF see Appendix B.4. Nonetheless, the maximal synaptic weights reported in the literature for excitatory synapses range from 2–5 mV in the cortex to 0.5 mV in the hippocampus, to 0.3 mV for cerebellar granule cell-Purkinje cell

synapses [136]. For inhibitory synapses, synaptic weights in the range 0.3 – 2.6 mV have been reported for the guinea-pig hippocampus *in vitro* [133]. To give an estimation of the synaptic weights employed in our model we should first introduce a scale for the membrane potential. Unfortunately for QIF the membrane potential varies from $v_{re} = -\infty$ to $v_{th} = +\infty$; therefore the model does not have an intrinsic scale for v. A possibility is to approximate threshold and reset to some finite value, e.g., by setting $v_{th} = +100$ and $v_{re} = -100$. This choice introduces a quite small mistake in the integration, as shown in [201], and we can map the reset (rest) to threshold distance $v_{th} - v_{re} = 200$ to the one usually measured in real neurons which is of the order of 20 mV [202]. Thus, one can give a rough estimate of the synaptic weight S in mV units as follow

$$S = \frac{g_0}{\sqrt{K}} \frac{20\text{mV}}{200} = \frac{g_0}{\sqrt{K}} 0.1 \text{ mV}.$$

If we assume that, consistent with experimental measurements, S should be at most 0.1–1 mV, this implies that for $g_0 = 1$ (the value most used in the article) these upper limits are satisfied whenever $K \geq 1$. For the data reported in Fig. 5.12 where $g_0 = 20$ and $i_0 = 0.22$, we obtain for $K = 10$ ($K = 210$) $S = 0.63$ mV ($S = 0.14$ mV), mean firing rate of the single neurons $F = 5$ Hz ($F = 5.18$ Hz), mean coefficient of variation $CV = 0.85$ ($CV = 0.88$) and frequency of the global oscillations in the γ range: namely $f_G = 35$ Hz ($f_G = 57$ Hz). All values consistent with the cortical dynamics, e.g. the dendritic inhibitory interneurons have been found to fire with a mean firing rate of $F \simeq 8$ Hz during hippocampal γ oscillations *in vitro* [203]. Furthermore, for the data reported in Fig. 5.9 (b) with $K = 200$ we found $0.007 \text{ mV} \leq S \leq 0.056$ mV with $g_0 = \sqrt{\beta}$, $i_0 = 0.01\beta$, $f_G = 11\sqrt{\beta}$ Hz for $\beta \in [1 : 64]$, and the dynamics was always irregular with $CV \simeq 0.78$ and with neurons spiking quite slowly with respect to GOs, since $R_G \simeq 7$, with F ranging from 1.6 Hz to 13 Hz.

Another fundamental quantity entering in our model is the in-degree K; here we have considered a simplified approach where K is the same for all neurons. However this is not always the case, as shown, for example, in developing hippocampal networks, where GABAergic hubs have been identified [204], or in the rodent somatosensory cortex, where nonrandom structures of connectivity have been identified at different scales [205]. A possible extension of the CMF model to the case of distributed in-degrees is discussed briefly in Appendix B.4. However, even when restricting the discussion to the case of a fixed mean in-degree, the inclusion of shot noise in the mean-field formulations is already relevant to capture the network dynamics for $K < 500$–1000 for sufficiently low values of $i_0/g_0^2 < 0.001$ [as shown in Fig. 5.5 (a)].

Therefore, we expect that shot noise will play a major role in sparse neural circuits. Examples of inhibitory circuits with low connectivity ($K = 30$–80) have been reported in the cat visual cortex [12] and in the rodent hippocampus [13], where they are considered to be at the origin of global oscillations in the γ range [14]. Due to recent accurate analyses of the primary visual cortex [137], the authors have concluded that this cortical circuit is definitely more sparse in primates with respect to mice (from 3 to 5 times), and there are indications that this sparsity will apply to other cortex region of the primates. Therefore, the cortical circuits of the primates can represent an ideal benchmark to test for the relevance of our results with respect to those obtained within the DA. Another neural circuit where our findings can find application is the connectome of the fly *Drosophila melanogaster*, that is extremely sparse with very low median in-degree ($K \simeq 11$) [183], and where inhibitory connections are particularly strong [184].

References

[1] Melanie Mitchell. *Complexity: A guided tour*. Oxford university press, 2009.

[2] Frederico AC Azevedo et al. "Equal numbers of neuronal and nonneuronal cells make the human brain an isometrically scaled-up primate brain". In: *Journal of Comparative Neurology* 513.5 (2009), pp. 532–541.

[3] Alain Goriely. "Eighty-six billion and counting: do we know the number of neurons in the human brain?" In: *Brain* 148.3 (2025), pp. 689–691.

[4] Bente Pakkenberg et al. "Aging and the human neocortex". In: *Experimental gerontology* 38.1-2 (2003), pp. 95–99.

[5] Benedict Delisle Burns and AC Webb. "The spontaneous activity of neurones in the cat's cerebral cortex". In: *Proceedings of the Royal Society of London. Series B. Biological Sciences* 194.1115 (1976), pp. 211–223.

[6] William R Softky and Christof Koch. "The highly irregular firing of cortical cells is inconsistent with temporal integration of random EPSPs". In: *Journal of neuroscience* 13.1 (1993), pp. 334–350.

[7] Carl Van Vreeswijk and Haim Sompolinsky. "Chaos in neuronal networks with balanced excitatory and inhibitory activity". In: *Science* 274.5293 (1996), pp. 1724–1726.

[8] Carl van Vreeswijk and Haim Sompolinsky. "Chaotic balanced state in a model of cortical circuits". In: *Neural computation* 10.6 (1998), pp. 1321–1371.

[9] Tadashi Ogawa and Hidehiko Komatsu. "Differential temporal storage capacity in the baseline activity of neurons in macaque frontal eye field and area V4". In: *Journal of neurophysiology* 103.5 (2010), pp. 2433–2445.

[10] John D Murray et al. "A hierarchy of intrinsic timescales across primate cortex". In: *Nature neuroscience* 17.12 (2014), pp. 1661–1663.

[11] Satoshi Nishida et al. "Discharge-rate persistence of baseline activity during fixation reflects maintenance of memory-period activity in the macaque posterior parietal cortex". In: *Cerebral Cortex* 24.6 (2014), pp. 1671–1685.

[12] Zoltán F Kisvárday, Clermont Beaulieu, and Ulf T Eysel. "Network of GABAergic large basket cells in cat visual cortex (area 18): implication for lateral disinhibition". In: *Journal of Comparative Neurology* 327.3 (1993), pp. 398–415.

[13] A Sik et al. "Hippocampal CA1 interneurons: an in vivo intracellular labeling study". In: *Journal of Neuroscience* 15.10 (1995), pp. 6651–6665.

[14] György Buzsáki and Xiao-Jing Wang. "Mechanisms of gamma oscillations". In: *Annual Review of Neuroscience* 35 (2012), pp. 203–225.

[15] RM Capocelli and LM Ricciardi. "Diffusion approximation and first passage time problem for a model neuron". In: *Kybernetik* 8.6 (1971), pp. 214–223.

[16] Santiago Ramón y Cajal. *Histologie du système nerveux de l'homme & des vertébrés: Cervelet, cerveau moyen, rétine, couche optique, corps strié, écorce cérébrale générale & régionale, grand sympathique*. Vol. 2. A. Maloine, 1911.

[17] Hongkui Zeng and Joshua R Sanes. "Neuronal cell-type classification: challenges, opportunities and the path forward". In: *Nature Reviews Neuroscience* 18.9 (2017), pp. 530–546.

[18] DK Hartline and DR Colman. "Rapid conduction and the evolution of giant axons and myelinated fibers". In: *Current biology* 17.1 (2007), R29–R35.

[19] John H. Byrne, ed. *Neuroscience Online: An Electronic Textbook for the Neurosciences*. Department of Neurobiology and Anatomy, McGovern Medical School, The University of Texas Health Science Center at Houston (UTHealth), 1997. URL: http://nba.uth.tmc.edu/neuroscience/.

[20] Catherine N. Hall, ed. *Introduction to Biological Psychology*. Open textbook, licensed under CC BY-NC. Brighton, UK: University of Sussex Library, 2023. URL: https://openpress.sussex.ac.uk/introductiontobiologicalpsychology/.

[21] Alan L Hodgkin and Andrew F Huxley. "Action potentials recorded from inside a nerve fibre". In: *Nature* 144.3651 (1939), pp. 710–711.

[22] Julius Bernstein. "Untersuchungen zur Thermodynamik der bioelektrischen Ströme: Erster Theil". In: *Archiv für die gesamte Physiologie des Menschen und der Tiere* 92.10 (1902), pp. 521–562.

[23] Christof Koch. *Biophysics of computation: information processing in single neurons*. Oxford university press, 2004, pp. 154–6.

[24] Alan L Hodgkin and Andrew F Huxley. "A quantitative description of membrane current and its application to conduction and excitation in nerve". In: *The Journal of physiology* 117.4 (1952), p. 500.

[25] Eric R Kandel et al. *Principles of neural science*. Vol. 4. McGraw-hill New York, 2000.

[26] George J Augustine et al. *Neurosciences*. De Boeck Superieur, 2015.

[27] MJ Caire, V Reddy, and M Varacallo. "Physiology, Synapse.[Updated 2023 Mar 27]". In: *StatPearls. Treasure Island (FL): StatPearls Publishing* (2023).

[28] John C Eccles. "The nature of synaptic transmission in a sympathetic ganglion". In: *The Journal of Physiology* 103.1 (1944), p. 27.

[29] Sami Boudkkazi, Laure Fronzaroli-Molinieres, and Dominique Debanne. "Presynaptic action potential waveform determines cortical synaptic latency". In: *The Journal of physiology* 589.5 (2011), pp. 1117–1131.

[30] EJ Furshpan and DD1356828 Potter. "Transmission at the giant motor synapses of the crayfish". In: *The Journal of physiology* 145.2 (1959), p. 289.

[31] Michael Beierlein, Jay R Gibson, and Barry W Connors. "A network of electrically coupled interneurons drives synchronized inhibition in neocortex". In: *Nature neuroscience* 3.9 (2000), pp. 904–910.

[32] Michael V L Bennett. "Gap junctions as electrical synapses". In: *Journal of neurocytology* 26.6 (1997), pp. 349–366.

[33] Yair Manor et al. "Low-amplitude oscillations in the inferior olive: a model based on electrical coupling of neurons with heterogeneous channel densities". In: *Journal of neurophysiology* 77.5 (1997), pp. 2736–2752.

[34] Maria Cecilia Angulo, Jean Rossier, and Etienne Audinat. "Postsynaptic glutamate receptors and integrative properties of fast-spiking interneurons in the rat neocortex". In: *Journal of neurophysiology* 82.3 (1999), pp. 1295–1302.

[35] Ingo C Kleppe and Hugh PC Robinson. "Determining the activation time course of synaptic AMPA receptors from openings of colocalized NMDA receptors". In: *Biophysical Journal* 77.3 (1999), pp. 1418–1427.

[36] Jörg RP Geiger et al. "Submillisecond AMPA receptor-mediated signaling at a principal neuron–interneuron synapse". In: *Neuron* 18.6 (1997), pp. 1009–1023.

[37] Alejandro F Schinder, Benedikt Berninger, and Mu-ming Poo. "Postsynaptic target specificity of neurotrophin-induced presynaptic potentiation". In: *Neuron* 25.1 (2000), pp. 151–163.

[38] Wulfram Gerstner et al. *Neuronal dynamics: From single neurons to networks and models of cognition*. Cambridge University Press, 2014.

[39] Alain Destexhe and Denis Paré. "Impact of network activity on the integrative properties of neocortical pyramidal neurons in vivo". In: *Journal of neurophysiology* 81.4 (1999), pp. 1531–1547.

[40] Leah B Gerrard, Malinda LS Tantirigama, and John M Bekkers. "Pre-and postsynaptic activation of GABAB receptors modulates principal cell excitation in the piriform cortex". In: *Frontiers in Cellular Neuroscience* 12 (2018), p. 28.

[41] David A McCormick, Zhong Wang, and John Huguenard. "Neurotransmitter control of neocortical neuronal activity and excitability". In: *Cerebral cortex* 3.5 (1993), pp. 387–398.

[42] Werner M Kistler, Wulfram Gerstner, and J Leo van Hemmen. "Reduction of the Hodgkin-Huxley equations to a single-variable threshold model". In: *Neural computation* 9.5 (1997), pp. 1015–1045.

[43] Alain Destexhe et al. "Fluctuating synaptic conductances recreate in vivo-like activity in neocortical neurons". In: *Neuroscience* 107.1 (2001), pp. 13–24.

[44] Alexander Rauch et al. "Neocortical pyramidal cells respond as integrate-and-fire neurons to in vivo–like input currents". In: *Journal of neurophysiology* 90.3 (2003), pp. 1598–1612.

[45] L Lapicque. "Recherches quantitatives sur l'excitation electrique des nerfs". In: *J. Physiol* 9 (1907), pp. 620–635. URL: https://gallica.bnf.fr/ark:/12148/bpt6k6446089w/f640.item.

[46] Wulfram Gerstner and Werner M Kistler. *Spiking neuron models: Single neurons, populations, plasticity*. Cambridge university press, 2002.

[47] Eugene M Izhikevich. *Dynamical systems in neuroscience*. MIT press, 2007.

[48] Bard Ermentrout. "Type I membranes, phase resetting curves, and synchrony". In: *Neural computation* 8.5 (1996), pp. 979–1001.

[49] John Rinzel and G Bard Ermentrout. "Analysis of neural excitability and oscillations". In: *Methods in neuronal modeling* 2 (1998), pp. 251–292.

[50] John Rinzel and James P Keaner. "Hopf bifurcation to repetitive activity in nerve". In: *SIAM Journal on Applied Mathematics* 43.4 (1983), pp. 907–922.

[51] Nicolas Fourcaud-Trocmé et al. "How spike generation mechanisms determine the neuronal response to fluctuating inputs". In: *Journal of neuroscience* 23.37 (2003), pp. 11628–11640.

[52] Laurent Badel et al. "Extracting non-linear integrate-and-fire models from experimental data using dynamic I–V curves". In: *Biological cybernetics* 99.4 (2008), pp. 361–370.

[53] Peter E Latham et al. “Intrinsic dynamics in neuronal networks. I. Theory”. In: *Journal of neurophysiology* 83.2 (2000), pp. 808–827.

[54] D Hansel and G Mato. “Existence and stability of persistent states in large neuronal networks”. In: *Physical Review Letters* 86.18 (2001), p. 4175.

[55] G Bard Ermentrout and Nancy Kopell. “Parabolic bursting in an excitable system coupled with a slow oscillation”. In: *SIAM journal on applied mathematics* 46.2 (1986), pp. 233–253.

[56] William R Softky, Christof Koch, and Neural Computation. “Cortical cells should fire regularly, but do not”. In: (1992).

[57] David C Van Essen et al. “Parcellations and connectivity patterns in human and macaque cerebral cortex”. In: *Micro-, meso-and macro-connectomics of the brain* (2016), pp. 89–106.

[58] Débora Jardim-Messeder et al. “Dogs have the most neurons, though not the largest brain: trade-off between body mass and number of neurons in the cerebral cortex of large carnivoran species”. In: *Frontiers in neuroanatomy* 11 (2017), p. 296229.

[59] DR Smith and Go Ko Smith. “A statistical analysis of the continual activity of single cortical neurones in the cat unanaesthetized isolated forebrain”. In: *Biophysical Journal* 5.1 (1965), pp. 47–74.

[60] Hiroharu Noda and W Ross Adey. “Firing variability in cat association cortex during sleep and wakefulness”. In: *Brain research* 18.3 (1970), pp. 513–526.

[61] Gary R Holt et al. “Comparison of discharge variability in vitro and in vivo in cat visual cortex neurons”. In: *Journal of neurophysiology* 75.5 (1996), pp. 1806–1814.

[62] Zachary F Mainen and Terrence J Sejnowski. “Reliability of spike timing in neocortical neurons”. In: *Science* 268.5216 (1995), pp. 1503–1506.

[63] Michael N Shadlen and William T Newsome. “Noise, neural codes and cortical organization”. In: *Current opinion in neurobiology* 4.4 (1994), pp. 569–579.

[64] Michael Monteforte and Fred Wolf. “Dynamical entropy production in spiking neuron networks in the balanced state”. In: *Physical review letters* 105.26 (2010), p. 268104.

[65] Tim P Vogels, Kanaka Rajan, and Larry F Abbott. “Neural network dynamics”. In: *Annu. Rev. Neurosci.* 28.1 (2005), pp. 357–376.

[66] Yousheng Shu et al. “Barrages of synaptic activity control the gain and sensitivity of cortical neurons”. In: *Journal of Neuroscience* 23.32 (2003), pp. 10388–10401.

[67] Michael Wehr and Anthony M Zador. “Balanced inhibition underlies tuning and sharpens spike timing in auditory cortex”. In: *Nature* 426.6965 (2003), pp. 442–446.

[68] Bilal Haider et al. “Neocortical network activity in vivo is generated through a dynamic balance of excitation and inhibition”. In: *Journal of Neuroscience* 26.17 (2006), pp. 4535–4545.

[69] Jérémie Barral and Alex D Reyes. “Synaptic scaling rule preserves excitatory–inhibitory balance and salient neuronal network dynamics”. In: *Nature neuroscience* 19.12 (2016), pp. 1690–1696.

[70] György Buzsáki and Kenji Mizuseki. “The log-dynamic brain: how skewed distributions affect network operations”. In: *Nature Reviews Neuroscience* 15.4 (2014), pp. 264–278.

[71] Yashar Ahmadian and Kenneth D Miller. “What is the dynamical regime of cerebral cortex?” In: *Neuron* 109.21 (2021), pp. 3373–3391.

[72] Ramin Khajeh, Francesco Fumarola, and LF Abbott. "Sparse balance: Excitatory-inhibitory networks with small bias currents and broadly distributed synaptic weights". In: *PLOS Computational Biology* 18.2 (2022), e1008836.

[73] Anthony D Lien and Massimo Scanziani. "Tuned thalamic excitation is amplified by visual cortical circuits". In: *Nature neuroscience* 16.9 (2013), pp. 1315–1323.

[74] Ya-tang Li et al. "Linear transformation of thalamocortical input by intracortical excitation". In: *Nature neuroscience* 16.9 (2013), pp. 1324–1330.

[75] Ling-yun Li et al. "Intracortical multiplication of thalamocortical signals in mouse auditory cortex". In: *Nature neuroscience* 16.9 (2013), pp. 1179–1181.

[76] Cindy Poo and Jeffry S Isaacson. "A major role for intracortical circuits in the strength and tuning of odor-evoked excitation in olfactory cortex". In: *Neuron* 72.1 (2011), pp. 41–48.

[77] Guy N Elston. "Cortex, cognition and the cell: new insights into the pyramidal neuron and prefrontal function". In: *Cerebral cortex* 13.11 (2003), pp. 1124–1138.

[78] Itamar D Landau et al. "The impact of structural heterogeneity on excitation-inhibition balance in cortical networks". In: *Neuron* 92.5 (2016), pp. 1106–1121.

[79] Gianluigi Mongillo, David Hansel, and Carl Van Vreeswijk. "Bistability and Spatiotemporal Irregularity in Neuronal Networks with Nonlinear<? format?> Synaptic Transmission". In: *Physical review letters* 108.15 (2012), p. 158101.

[80] Antonio Politi and Alessandro Torcini. "A robust balancing mechanism for spiking neural networks". In: *Chaos: An Interdisciplinary Journal of Nonlinear Science* 34.4 (2024).

[81] Misha Tsodyks, Klaus Pawelzik, and Henry Markram. "Neural networks with dynamic synapses". In: *Neural computation* 10.4 (1998), pp. 821–835.

[82] Peter Dayan and L Abott. *Theoretical Neuroscience*. 2001.

[83] Giancarlo La Camera et al. "Multiple time scales of temporal response in pyramidal and fast spiking cortical neurons". In: *Journal of neurophysiology* 96.6 (2006), pp. 3448–3464.

[84] Christian Pozzorini et al. "Temporal whitening by power-law adaptation in neocortical neurons". In: *Nature neuroscience* 16.7 (2013), pp. 942–948.

[85] Stephen A Fisher, Thomas M Fischer, and Thomas J Carew. "Multiple overlapping processes underlying short-term synaptic enhancement". In: *Trends in neurosciences* 20.4 (1997), pp. 170–177.

[86] Manuel Beiran and Srdjan Ostojic. "Contrasting the effects of adaptation and synaptic filtering on the timescales of dynamics in recurrent networks". In: *PLoS computational biology* 15.3 (2019), e1006893.

[87] Misha V Tsodyks and Terrance Sejnowski. "Rapid state switching in balanced cortical network models". In: *Network: Computation in Neural Systems* 6.2 (1995), p. 111.

[88] Daniel J Amit and Nicolas Brunel. "Model of global spontaneous activity and local structured activity during delay periods in the cerebral cortex." In: *Cerebral cortex (New York, NY: 1991)* 7.3 (1997), pp. 237–252.

[89] Alfonso Renart et al. "The asynchronous state in cortical circuits". In: *science* 327.5965 (2010), pp. 587–590.

[90] Alexander Lerchner et al. "Response variability in balanced cortical networks". In: *Neural computation* 18.3 (2006), pp. 634–659.

[91] Alex Roxin et al. “On the distribution of firing rates in networks of cortical neurons”. In: *Journal of Neuroscience* 31.45 (2011), pp. 16217–16226.

[92] Gianluigi Mongillo, Simon Rumpel, and Yonatan Loewenstein. “Inhibitory connectivity defines the realm of excitatory plasticity”. In: *Nature neuroscience* 21.10 (2018), pp. 1463–1470.

[93] Moritz Helias, Tom Tetzlaff, and Markus Diesmann. “The correlation structure of local neuronal networks intrinsically results from recurrent dynamics”. In: *PLoS computational biology* 10.1 (2014), e1003428.

[94] Omri Harish and David Hansel. “Asynchronous rate chaos in spiking neuronal circuits”. In: *PLoS computational biology* 11.7 (2015), e1004266.

[95] Jonathan Kadmon and Haim Sompolinsky. “Transition to chaos in random neuronal networks”. In: *Physical Review X* 5.4 (2015), p. 041030.

[96] David Dahmen et al. “Second type of criticality in the brain uncovers rich multiple-neuron dynamics”. In: *Proceedings of the National Academy of Sciences* 116.26 (2019), pp. 13051–13060.

[97] David Angulo-Garcia et al. “Death and rebirth of neural activity in sparse inhibitory networks”. In: *New Journal of Physics* 19.5 (2017), p. 053011.

[98] Gustavo Deco and Etienne Hugues. “Neural network mechanisms underlying stimulus driven variability reduction”. In: *PLoS computational biology* 8.3 (2012), e1002395.

[99] Ashok Litwin-Kumar and Brent Doiron. “Slow dynamics and high variability in balanced cortical networks with clustered connections”. In: *Nature neuroscience* 15.11 (2012), pp. 1498–1505.

[100] Luca Mazzucato, Alfredo Fontanini, and Giancarlo La Camera. “Dynamics of multistable states during ongoing and evoked cortical activity”. In: *Journal of Neuroscience* 35.21 (2015), pp. 8214–8231.

[101] Braden AW Brinkman et al. “Metastable dynamics of neural circuits and networks”. In: *Applied Physics Reviews* 9.1 (2022).

[102] Chengcheng Huang and Brent Doiron. “Once upon a (slow) time in the land of recurrent neuronal networks. . . ” In: *Current opinion in neurobiology* 46 (2017), pp. 31–38.

[103] Peter Hänggi, Peter Talkner, and Michal Borkovec. “Reaction-rate theory: fifty years after Kramers”. In: *Reviews of modern physics* 62.2 (1990), p. 251.

[104] Xiaoyu Yang and Giancarlo La Camera. “Co-existence of synaptic plasticity and metastable dynamics in a spiking model of cortical circuits”. In: *PLOS Computational Biology* 20.7 (2024), e1012220.

[105] Daniel Martí, Nicolas Brunel, and Srdjan Ostojic. “Correlations between synapses in pairs of neurons slow down dynamics in randomly connected neural networks”. In: *Physical Review E* 97.6 (2018), p. 062314.

[106] Shrisha Rao, David Hansel, and Carl van Vreeswijk. “Dynamics and orientation selectivity in a cortical model of rodent V1 with excess bidirectional connections”. In: *Scientific Reports* 9.1 (2019), p. 3334.

[107] Kevin Berlemont and Gianluigi Mongillo. “Glassy phase in dynamically-balanced neuronal networks”. In: *bioRxiv* (2022), pp. 2022–03.

[108] Sen Song et al. “Highly nonrandom features of synaptic connectivity in local cortical circuits”. In: *PLoS biology* 3.3 (2005), e68.

[109] Yumiko Yoshimura, Jami LM Dantzker, and Edward M Callaway. "Excitatory cortical neurons form fine-scale functional networks". In: *Nature* 433.7028 (2005), pp. 868–873.

[110] Ho Ko et al. "Functional specificity of local synaptic connections in neocortical networks". In: *Nature* 473.7345 (2011), pp. 87–91.

[111] Nicolas Brunel. "Is cortical connectivity optimized for storing information?" In: *Nature neuroscience* 19.5 (2016), pp. 749–755.

[112] Luke Campagnola et al. "Local connectivity and synaptic dynamics in mouse and human neocortex". In: *Science* 375.6585 (2022), eabj5861.

[113] Andrea Crisanti and Haim Sompolinsky. "Dynamics of spin systems with randomly asymmetric bonds: Ising spins and Glauber dynamics". In: *Physical Review A* 37.12 (1988), p. 4865.

[114] Matteo Di Volo and Alessandro Torcini. "Transition from asynchronous to oscillatory dynamics in balanced spiking networks with instantaneous synapses". In: *Physical review letters* 121.12 (2018), p. 128301.

[115] Rüdiger Zillmer et al. "Stability of the splay state in pulse-coupled networks". In: *Physical Review E—Statistical, Nonlinear, and Soft Matter Physics* 76.4 (2007), p. 046102.

[116] We used the function $S(x) = 25/(1 + e^{-k(x-x_0)})$ to approximate the data. The two free parameters, x_0 and k, were determined by least-squares fitting. We obtained: $x_0 = 0.32$ and $k = 5.67$ for $q = 0$, $x_0 = 0.29$ and $k = 5.40$ for $q = 0.25$, $x_0 = 0.22$ and $k = 4.94$ for $q = 0.5$.

[117] Clearly, since $\mathrm{STA}(\tau)$ is a rate, the integral in time R is dimensionless.

[118] Crispin W Gardiner et al. *Handbook of stochastic methods*. Vol. 3. springer Berlin, 1985.

[119] Shy Shoham, Daniel H O'Connor, and Ronen Segev. "How silent is the brain: is there a "dark matter" problem in neuroscience?" In: *Journal of Comparative Physiology A* 192 (2006), pp. 777–784.

[120] John J Hopfield. "Neural networks and physical systems with emergent collective computational abilities." In: *Proceedings of the national academy of sciences* 79.8 (1982), pp. 2554–2558.

[121] Emanuele Curti et al. "Mean field and capacity in realistic networks of spiking neurons storing sparsely coded random memories". In: *Neural computation* 16.12 (2004), pp. 2597–2637.

[122] Boris Gutkin. "Theta neuron model". In: *Encyclopedia of computational neuroscience*. Springer, 2022, pp. 3412–3419.

[123] W. Schottky. "Über spontane Stromschwankungen in verschiedenen Elektrizitätsleitern". In: *Annalen der Physik* 362.23 (1918), pp. 541–567.

[124] Charles H Henry and Rudolf F Kazarinov. "Quantum noise in photonics". In: *Reviews of Modern Physics* 68.3 (1996), p. 801.

[125] Branda Goncalves, Thierry Huillet, and Eva Löcherbach. "On decay–surge population models". In: *Advances in Applied Probability* 55.2 (2023), pp. 444–472.

[126] Kiyoshi Kanazawa. *Statistical mechanics for athermal fluctuation: Non-Gaussian noise in physics*. Springer, 2017.

[127] D Lucente et al. "Revealing the Nonequilibrium Nature of a Granular Intruder: The Crucial Role of Non-Gaussian Behavior". In: *Physical Review Letters* 131.7 (2023), p. 078201.

[128] Dario Lucente et al. “Langevin dynamics with generalized time-reversal symmetry”. In: *arXiv preprint arXiv:2504.05980* (2025).

[129] Étienne Fodor et al. “Non-Gaussian noise without memory in active matter”. In: *Physical Review E* 98.6 (2018), p. 062610.

[130] Ya M Blanter and Markus Büttiker. “Shot noise in mesoscopic conductors”. In: *Physics Reports* 336.1-2 (2000), pp. 1–166.

[131] HL Frisch and SP Lloyd. “Electron levels in a one-dimensional random lattice”. In: *Physical Review* 120.4 (1960), p. 1175.

[132] Henry Clavering Tuckwell. *Nonlinear and stochastic theories*. Vol. 2. Cambridge Univ. Press., 1988.

[133] R Miles. “Variation in strength of inhibitory synapses in the CA3 region of guinea-pig hippocampus in vitro.” In: *The Journal of Physiology* 431.1 (1990), pp. 659–676.

[134] Sandrine Lefort et al. “The excitatory neuronal network of the C2 barrel column in mouse primary somatosensory cortex”. In: *Neuron* 61.2 (2009), pp. 301–316.

[135] Guo-qiang Bi and Mu-ming Poo. “Distributed synaptic modification in neural networks induced by patterned stimulation”. In: *Nature* 401.6755 (1999), pp. 792–796.

[136] Boris Barbour et al. “What can we learn from synaptic weight distributions?” In: *TRENDS in Neurosciences* 30.12 (2007), pp. 622–629.

[137] Gregg A Wildenberg et al. “Primate neuronal connections are sparse in cortex as compared to mouse”. In: *Cell Reports* 36.11 (2021).

[138] Magnus J E Richardson and Rupert Swarbrick. “Firing-rate response of a neuron receiving excitatory and inhibitory synaptic shot noise”. In: *Physical Review Letters* 105.17 (2010), p. 178102.

[139] Ramakrishnan Iyer et al. “The influence of synaptic weight distribution on neuronal population dynamics”. In: *PLoS Computational Biology* 9.10 (2013), e1003248.

[140] Simona Olmi et al. “Exact firing time statistics of neurons driven by discrete inhibitory noise”. In: *Scientific Reports* 7.1 (2017), p. 1577.

[141] Felix Droste and Benjamin Lindner. “Exact analytical results for integrate-and-fire neurons driven by excitatory shot noise”. In: *Journal of Computational Neuroscience* 43 (2017), pp. 81–91.

[142] Magnus J E Richardson. “Spike shape and synaptic-amplitude distribution interact to set the high-frequency firing-rate response of neuronal populations”. In: *Physical Review E* 98.4 (2018), p. 042405.

[143] Magnus J E Richardson. “Linear and nonlinear integrate-and-fire neurons driven by synaptic shot noise with reversal potentials”. In: *Physical Review E* 109.2 (2024), p. 024407.

[144] Gyorgy Buzsaki. *Rhythms of the Brain*. Oxford University Press, 2006.

[145] Wolf Singer. “Neuronal oscillations: unavoidable and useful?” In: *European Journal of Neuroscience* 48.7 (2018), pp. 2389–2398.

[146] Jozsef Csicsvari et al. “Reliability and state dependence of pyramidal cell–interneuron synapses in the hippocampus: an ensemble approach in the behaving rat”. In: *Neuron* 21.1 (1998), pp. 179–189.

[147] Andre Fisahn et al. “Cholinergic induction of network oscillations at 40 Hz in the hippocampus in vitro”. In: *Nature* 394.6689 (1998), pp. 186–189.

[148] Nicolas Brunel. "Dynamics of sparsely connected networks of excitatory and inhibitory spiking neurons". In: *Journal of computational neuroscience* 8.3 (2000), pp. 183–208.

[149] Nicolas Brunel and Xiao-Jing Wang. "What determines the frequency of fast network oscillations with irregular neural discharges? I. Synaptic dynamics and excitation-inhibition balance". In: *Journal of neurophysiology* 90.1 (2003), pp. 415–430.

[150] Caroline Geisler, Nicolas Brunel, and Xiao-Jing Wang. "Contributions of intrinsic membrane dynamics to fast network oscillations with irregular neuronal discharges". In: *Journal of neurophysiology* 94.6 (2005), pp. 4344–4361.

[151] Hongjie Bi, Matteo Di Volo, and Alessandro Torcini. "Asynchronous and coherent dynamics in balanced excitatory-inhibitory spiking networks". In: *Frontiers in systems neuroscience* 15 (2021), p. 752261.

[152] Miles A Whittington et al. "Inhibition-based rhythms: experimental and mathematical observations on network dynamics". In: *International journal of psychophysiology* 38.3 (2000), pp. 315–336.

[153] Edward O Mann and Ole Paulsen. "Role of GABAergic inhibition in hippocampal network oscillations". In: *Trends in neurosciences* 30.7 (2007), pp. 343–349.

[154] Nicolas Brunel and Vincent Hakim. "Fast global oscillations in networks of integrate-and-fire neurons with low firing rates". In: *Neural computation* 11.7 (1999), pp. 1621–1671.

[155] Jonathan Kadmon and Haim Sompolinsky. "Transition to chaos in random neuronal networks". In: *Physical Review X* 5.4 (2015), p. 041030.

[156] Matteo Di Volo and Alessandro Torcini. "Transition from asynchronous to oscillatory dynamics in balanced spiking networks with instantaneous synapses". In: *Physical review letters* 121.12 (2018), p. 128301.

[157] Matteo Di Volo et al. "Coherent oscillations in balanced neural networks driven by endogenous fluctuations". In: *Chaos: An Interdisciplinary Journal of Nonlinear Science* 32.2 (2022), p. 023120.

[158] Denis S Goldobin, Matteo Di Volo, and Alessandro Torcini. "Discrete synaptic events induce global oscillations in balanced neural networks". In: *Physical Review Letters* 133.23 (2024), p. 238401.

[159] G Bard Ermentrout and Nancy Kopell. "Parabolic bursting in an excitable system coupled with a slow oscillation". In: *SIAM Journal on Applied Mathematics* 46.2 (1986), pp. 233–253.

[160] D. Golomb. "Neuronal synchrony measures". In: *Scholarpedia* 2.1 (2007), p. 1347. DOI: 10.4249/scholarpedia.1347.

[161] Pau Clusella and Ernest Montbrió. "Exact low-dimensional description for fast neural oscillations with low firing rates". In: *Physical Review E* 109.1 (2024), p. 014229.

[162] Evan Haskell, Duane Q Nykamp, and Daniel Tranchina. "Population density methods for large-scale modelling of neuronal networks with realistic synaptic kinetics: cutting the dimension down to size". In: *Network: Computation in Neural Systems* 12.2 (2001), pp. 141–174.

[163] J. Marcinkiewicz. "Sur une peropriété de la loi de Gauss". In: *Mathematische Zeitschrift* 44 (1939), pp. 612–618. URL: http://eudml.org/doc/168829.

[164] C. W. Gardiner. *Handbook of Stochastic Methods*. 2nd ed. Berlin: Springer, 1997.

[165] B. Ermentrout. "Ermentrout-Kopell canonical model". In: *Scholarpedia* 3.3 (2008). revision #122134, p. 1398. DOI: 10.4249/scholarpedia.1398.

[166] Björn Kralemann et al. "Uncovering interaction of coupled oscillators from data". In: *Physical Review E* 76.5 (2007), 055201(R).

[167] Anastasiya V Dolmatova, Denis S Goldobin, and Arkady Pikovsky. "Synchronization of coupled active rotators by common noise". In: *Physical Review E* 96.6 (2017), p. 062204.

[168] Yoshiki Kuramoto. *Chemical oscillations, waves, and turbulence*. Vol. 19. Springer Science & Business Media, 2012.

[169] Hiroaki Daido. "Order function and macroscopic mutual entrainment in uniformly coupled limit-cycle oscillators". In: *Progress of Theoretical Physics* 88.6 (1992), pp. 1213–1218.

[170] S. M. Cox and P. C. Matthews. "Exponential time differencing for stiff systems". In: *J. Comput. Phys.* 176.2 (2002), pp. 430–455. DOI: {10.1006/jcph.2002.6995}. URL: https://doi.org/10.1006/jcph.2002.6995.

[171] E. V. Permyakova and D. S. Goldobin. "High-order schemes of exponential time differencing for stiff systems with nondiagonal linear part". In: *J. Comput. Phys.* 520 (2025), p. 113493. DOI: {10.1016/j.jcp.2024.113493}. URL: https://doi.org/10.1016/j.jcp.2024.113493.

[172] For numerical calculations in the Maple package, whenever needed the length of the digital mantissa of the variables was increased significantly beyond 16 digits (environmental variable 'Digits') in order to maintain this accuracy. We adopted the following technical criterion for accuracy: the elevations of the decimal mantissa length by 20 and M by a factor of 1.5 induce the relative changes of the calculated quantity of interest below 10^{-12}.

[173] Ali H Nayfeh. *Introduction to perturbation techniques*. John Wiley & Sons, 2024.

[174] Ekkehard Ullner and Antonio Politi. "Self-sustained irregular activity in an ensemble of neural oscillators". In: *Physical Review X* 6.1 (2016), p. 011015.

[175] Yannick Feld, Alexander K Hartmann, and Alessandro Torcini. "Coexistence of asynchronous and clustered dynamics in noisy inhibitory neural networks". In: *New Journal of Physics* 26.6 (2024), p. 063017.

[176] Laura Lee Colgin and Edvard I Moser. "Gamma oscillations in the hippocampus". In: *Physiology* 25.5 (2010), pp. 319–329.

[177] Alfonso Renart et al. "Mean-driven and fluctuation-driven persistent activity in recurrent networks". In: *Neural computation* 19.1 (2007), pp. 1–46.

[178] Réka Albert and Albert-László Barabási. "Statistical mechanics of complex networks". In: *Reviews of modern physics* 74.1 (2002), p. 47.

[179] Vladimir V Klinshov and Sergey Yu Kirillov. "Shot noise in next-generation neural mass models for finite-size networks". In: *Physical Review E* 106.6 (2022), p. L062302.

[180] VV Klinshov, PS Smelov, and S Yu Kirillov. "Constructive role of shot noise in the collective dynamics of neural networks". In: *Chaos: An Interdisciplinary Journal of Nonlinear Science* 33.6 (2023).

[181] Nicolas Brunel and David Hansel. "How noise affects the synchronization properties of recurrent networks of inhibitory neurons". In: *Neural Computation* 18.5 (2006), pp. 1066–1110.

[182] Bastian Pietras. “Pulse shape and voltage-dependent synchronization in spiking neuron networks”. In: *Neural Computation* 36.8 (2024), pp. 1476–1540.

[183] FlyWire Consortium et al. “Neuronal wiring diagram of an adult brain”. In: *Nature* 634.8032 (2024), pp. 124–138.

[184] Albert Lin et al. “Network statistics of the whole-brain connectome of Drosophila”. In: *Nature* 634.8032 (2024), pp. 153–165.

[185] Christopher W Lynn, Caroline M Holmes, and Stephanie E Palmer. “Heavy-tailed neuronal connectivity arises from Hebbian self-organization”. In: *Nature Physics* 20.3 (2024), pp. 484–491.

[186] Michael W Reimann and Daniela Egas-Santander. “An algorithm to model the non-random connectome of cortical circuitry”. In: *bioRxiv* (2025), pp. 2025–05.

[187] Richard F Betzel et al. “Generative models of the human connectome”. In: *Neuroimage* 124 (2016), pp. 1054–1064.

[188] Francesca Mastrogiuseppe and Srdjan Ostojic. “Linking connectivity, dynamics, and computations in low-rank recurrent neural networks”. In: *Neuron* 99.3 (2018), pp. 609–623.

[189] Ljubica Cimeša, Lazar Ciric, and Srdjan Ostojic. “Geometry of population activity in spiking networks with low-rank structure”. In: *PLoS computational biology* 19.8 (2023), e1011315.

[190] Ferdinand Tixidre, Gianluigi Mongillo, and Alessandro Torcini. “Is the cortical dynamics ergodic? A numerical study in partially symmetric networks of spiking neurons”. In: *arXiv preprint arXiv:2508.04354* (2025).

[191] Denis S Goldobin et al. “Synaptic shot noise triggers fast and slow global oscillations in balanced neural networks”. In: *Physical Review E* 112.3 (2025), p. 034301.

[192] Sven Dorkenwald et al. “FlyWire: online community for whole-brain connectomics”. In: *Nature methods* 19.1 (2022), pp. 119–128.

[193] Jagruti J Pattadkal et al. “Synchrony dynamics underlie irregular neocortical spiking”. In: *bioRxiv* (2024), pp. 2024–10.

[194] Arnaud Tonnelier, Hana Belmabrouk, and Dominique Martinez. “Event-driven simulations of nonlinear integrate-and-fire neurons”. In: *Neural Computation* 19.12 (2007), pp. 3226–3238.

[195] Rainer Engelken. “Sparseprop: Efficient event-based simulation and training of sparse recurrent spiking neural networks”. In: *Advances in Neural Information Processing Systems* 36 (2023), pp. 3638–3657.

[196] N Ghofraniha et al. “Experimental evidence of replica symmetry breaking in random lasers”. In: *Nature communications* 6.1 (2015), p. 6058.

[197] Ekkehard Ullner, Antonio Politi, and Alessandro Torcini. “Ubiquity of collective irregular dynamics in balanced networks of spiking neurons”. In: *Chaos: An Interdisciplinary Journal of Nonlinear Science* 28.8 (2018), p. 081106.

[198] Alessandro Torcini, Helge Frauenkron, and Peter Grassberger. “Studies of phase turbulence in the one-dimensional complex Ginzburg-Landau equation”. In: *Physical Review E* 55.5 (1997), p. 5073.

[199] Alessandro Torcini and Paolo Politi. “Coarsening process in one-dimensional surface growth models”. In: *The European Physical Journal B-Condensed Matter and Complex Systems* 25 (2002), pp. 519–529.

[200] David Schüler et al. “Spatio-temporal dynamics induced by competing instabilities in two asymmetrically coupled nonlinear evolution equations”. In: *Chaos: An Interdisciplinary Journal of Nonlinear Science* 24.4 (2014).

[201] Ernest Montbrió, Diego Pazó, and Alex Roxin. “Macroscopic description for networks of spiking neurons”. In: *Physical Review X* 5.2 (2015), p. 021028.

[202] Wulfram Gerstner et al. *Neuronal Dynamics: From Single Neurons To Networks And Models Of Cognition*. Cambridge: Cambridge University Press, 2014.

[203] Norbert Hájos et al. “Spike timing of distinct types of GABAergic interneuron during hippocampal gamma oscillations in vitro”. In: *Journal of Neuroscience* 24.41 (2004), pp. 9127–9137.

[204] Paolo Bonifazi et al. “GABAergic hub neurons orchestrate synchrony in developing hippocampal networks”. In: *Science* 326.5958 (2009), pp. 1419–1424.

[205] Masanori Shimono and John M Beggs. “Functional clusters, hubs, and communities in the cortical microconnectome”. In: *Cerebral cortex* 25.10 (2015), pp. 3743–3757.

List of Figures

1 Left: the murmuration of starlings over Lough Ennell. Credit: James Crombie. Middle: group-averaged structural connectome reconstructed from 20 human brains. White-matter fiber pathways are shown with colors indicating their direction (x, y, z directions mapped to red, green, and blue). Credit: Andreas Horn. Right: the city of Paris as a complex system: a dynamic network of people, infrastructures, institutions, and interactions that together give rise to emergent social, economic, and spatial patterns. Credit: Thomas Pesquet. 1

1.1 (A) Typical representation of a neuron Taken from [19]. Green cylinders around the axon represented the myelin sheath. In different colours we see pre- and postsynaptic neurons of the orange neuron. Taken from [19]. (B) Pyramidal neurons of the prefrontal cortex are sparsely labeled with a fluorescent protein to visualize their morphology. Joseph Zak, Lab of Venkatesh Murthy, Harvard University 5

1.2 Constituents of extra- and intracellular fluids for a resting neuron, in milliequivalents per liter. Taken from [20]. 6

1.3 The density of potassium ion is higher inside the cell than outside, this chemical gradient tends to make ions cross the membrane via specific leak channels. As theses positively charged particles move out, an electrical gradients builds up. Eventually the two processes balance out. Taken from [20]. 7

1.4 The two layers of phospholipid molecules making up the cell membrane, typically the membrane is 30–50 Åthick. Taken from [20]. 8

1.5 (A) An illustration of the neuronal membrane. The lipid bilayer, which width ranges around 30–50 Åelectrically isolates the cell. Ionic channels, embedded in the membrane act as gates, letting charged particles cross. (B) The electrical circuit modelling the membrane. The membrane acts as a capacitor, the channels can be modelled by a resistance and the resting potential of the cell as a battery. Taken from [23]. 8

1.6 RC circuit modeling a passive membrane with injected current. 9

1.7 Time course of the membrane potential when a step current is applied. We turn on the current at $t = 0$ and turn it off at $t = 100$ ms. The left panel shows the current above and the membrane potential below. Different colours represent different values of the current $I(t)$. On the right side we see the rise and fall of the membrane potential when the current is turn on and off. Different colours represent different values of the membrane time constant τ_m. 10

1.8 Low-pass filtering property of the RC membrane circuit. (A) Sinusoidal input current with frequency $f = 20$ Hz. (B) The resulting membrane potential, $V_m(t)$. The dashed line denote the steady state potential V_∞. (C) The phase delay in degrees as a function of the input frequency. $I_0 = 0.20$ nA, $R = 100$ MΩ, $V_{rest} = -70$ mV and $\tau = 10$ ms. 10

1.9 Representation of a typical action potential showing its various phases. The membrane potential starts out at approximately -70 mV at time zero. A stimulus is applied at time = 1 ms, which raises the membrane potential above -55 mV (the threshold potential). After the stimulus is applied, the membrane potential rapidly rises to a peak potential of +40 mV at time = 2 ms. Just as quickly, the potential then drops below the resting state potential to -90 mV at time = 3 ms, and finally the resting potential of -70 mV is re-established at time = 5 ms. . . . 11
1.10 (A) Electrical synapses allow a continuous transmission of ions through gap junctions from one cell to the next. (B) Chemical synapses are separated by the synaptic cleft. The presynaptic neuron releases neurotransmitters, which open or close ion channels in the postsynaptic membrane. The movement of ions then generates a synaptic current through the postsynaptic neuron. Taken from [26]. 12
1.11 Chronological description of the different events allowing the transmission of electrical signals via a chemical synapse. Taken from [26] 13
1.12 Transmission at the crayfish giant motor synapse. Simultaneous intracellular recordings from the presynaptic lateral giant axon (upper trace) and the postsynaptic motor giant axon (lower trace). (a) One-to-one transmission: the presynaptic spike evokes a postsynaptic potential that reaches threshold and triggers a postsynaptic action potential. The arrow indicates the point where the postsynaptic potential crosses threshold and triggers a postsynaptic spike (a_1) and (a_2) were recorded from the same synapse at different amplifications. (b) Subthreshold cases in which the presynaptic spike evokes a fast depolarisation in the postsynaptic axon without triggering a spike. Taken from [30] 14
1.13 A pair of electrically coupled low-threshold-spiking neurons. An action potential in one cell often triggers a synchronized spike in the other cell. The periods marked 1 and 2 on top traces are expanded in time in the lower traces. Taken from [31]. 14
1.14 Summation of postsynaptic potentials. (A) A neuron receives inputs from excitatory (E_1 and E_2) and inhibitory (I) synapses. An electrode records the membrane postential of the postsynaptic neuron. (B) Effect of different input combinations on the postsynaptic membrane potential. Taken from [26]. 15
1.15 Time course of postsynaptic current following a presynaptic spike at time $t = 0$. Typical time constants: AMPA: $\tau_{rise} \simeq 0.2$–1 ms, $\tau_{decay} \simeq 2$–5 ms; NMDA: $\tau_{rise} \simeq 3$–5 ms, $\tau_{decay} \simeq 50$–200 ms. $GABA_A$: $\tau_{rise} \simeq 1$–2, $\tau_{decay} \simeq 5$–10 ms. $GABA_B$: $\tau_{rise} \simeq 50$–150, $\tau_{decay} \simeq 300$–1000 ms. Taken from [38]. 16

2.1 The typical shape of an action potential (dashed line) can be modeled by a δ pulse (solid vertical line). The hyperpolarisation after the pulse is replaced by a reset of the membrane potential to a chosen value V_r. 18
2.2 Periodic firing of a LIF neuron driven by constant current. Adapted from [46]. . 19
2.3 LIF neurons responding to a step current input. (A) A fast spiking neuron showing short interspike intervals with no adaptation. (C) A regular spiking neuron, showing adaptation. Adapted from [38]. 20
2.4 Fixed points in a nonlinear integrate-and-fire model. The black (white) dot represent a stable (unstable) fixed point. Arrows show the direction of flow: $dV/dt > 0$ to the right, $dV/dt < 0$ to the left. The horizontal dashed line shows the 0 and the vertical dotted line the threshold. (a) At $I = 0$, the zero crossings indicates the resting potential V_{rest} and the firing threshold V_c. (b) For inputs larger than the rheobase current I_c, no fixed points remains, the membrane potential is driven to threshold, leading to repetitive firing. Adapted from [46]. 21

2.5 F-I curves from recordings of a rat's brain. Comparison of typical response of two neurons to steps of DC current of various magnitudes I. (a) Type I neuron: the frequency ν is almost a continuous function of I. (b) Type II neuron: the F-I curve has a discontinuity. Taken from [47]. 22
2.6 Sketch of the SNIC bifurcation. Black (white) dots show stable (unstable) fixed points. From left to right: excitable state, critical state, repetitive firing. Taken from [47]. 22
2.7 Comparing the sharpness of the threshold in the exponential and leaky integrate-and-fire models. We can see that as we reduce Δ_T (lighter shades of grey) in the EIF model, it becomes closer and closer to the LIF model represented by the red line. The inset shows a zoom around the boxed region. Taken from [38] 23
2.8 Experimental data fitted by the EIF model with parameters: $\tau_m = 17.2$ ms, $V_{\text{rest}} = -57.0$ mV, $V_T = -42.0$ mV and $\Delta T = 1.51$ mV. The curve crosses zero at two points: -57 mV and -38 mV, respectively the resting potential and spike initiation threshold. 23
2.9 Quadratic (black) and exponential (red) integrate-and-fire models. (a) $I = 0$. Without external current the model has two fixed points, a stable one V_{rest} in black and another, unstable, V_c in white. (b) $I \simeq I_c$. The quadratic integrate-and-fire model can be seen as an approximation of an exponential integrate-and-fire model (or any other type I model) depolarised to a state close to repetitive firing. Adapted from [38]. 24
2.10 Tonic neuron. The red vertical asymptotes represent the firing times t_f, expressed by Eq. (2.10), in which the neuron emits an action potential. Function graph of V(t) in Eq. (2.8) with $\eta = 3$, $V(t0) = 1$. 26
2.11 Excitable neuron, Sub-threshold dynamics. In blue, the value of the resting membrane potential, $V_{\text{rest}} = -\sqrt{-\eta}$, to which the neuron tends. Trend of $V(t)$ in Eq. (2.12) with $\eta = -3$ and $V(t_0) = -\eta - 0.05$. 27
2.12 Excitable neuron, supra-threshold dynamics. The red vertical asymptote shows the time of spiking as predicted by Eq. (2.13). In blue, the resting value of the membrane potential, $V_{rest} = -\sqrt{-\eta}$ to which the neuron's potential converges after spiking. This curve represent eq.Eq. (2.14), with $\eta = -3$ and $V(t_0) = \sqrt{-\eta}+0.05$. 28

3.1 Spike trains (left) and their corresponding normalised interspike interval distributions (right). From top to bottom each row shows increasingly regular spike trains. The spikes trains are generated from Gamma renewal processes, they have a total duration of 100 s and a 10 Hz mean rate. 31
3.2 Examples of experimental measurements of interspike interval variability in cortical neurons. 31
3.3 Observed and predicted neuronal variability. 32
3.4 Asynchronous irregular activity in a balanced network of leaky integrate-and-fire neurons. (a) Raster plot showing 150 neurons from a network of 10 000. (b) The average firing rate (in green 0.1 ms binning, in white 5 ms binning) of the entire population is roughly constant and (c) the voltage trace of single randomly picked neuron shows that it fires irregularly. (d) The excitatory (green) and inhibitory (red) currents that the single neuron above receives in time. The total current (blue) fluctuates around zero. (e) Histogram of the time averaged firing rates of each neuron in the network. The arrow show the population average at 8 Hz. (f) Distribution of the time averaged interspike intervals of each neuron in the network. (g) Distribution of the CV for the network neurons. Arrows indicate the means of the distributions. Taken from [65]. 36

3.5 Amplitudes of unitary EPSPs (red, n = 261) and IPSPs (blue, n = 99) versus K. The inset shows the data in a log-log scale, the slope of the linear fit combining E-I data is −0.59. Taken from [69]. 37

4.1 (a)–(c) PDFs of the single-neuron firing rates $\{\nu_i\}$. Dashed lines denote the mean and the dotted lines represent the first and third quartiles. The insets display the activity of thirty randomly selected neurons. (d)–(f) PDFs of the coefficients of variation $\{CV_i\}$ of individual neuron firing rates. The dotted vertical lines indicate the means of the PDFs. (g)–(i) PDFs of the pairwise correlation coefficients ρ_{ij} of the neuronal firing activity. The dotted horizontal lines indicate the full widths at half maximum of the PDFs. The solid black curves in (d)–(f) and (g)–(i) represents Gaussian fits to the data, the corresponding mean and standard deviation are denoted by μ and σ, respectively. The top row (blue) corresponds to $q = 0.0$; the middle row (magenta) to $q = 0.25$ and the bottom one (green) to $q = 0.5$. The PDFs were obtained by aggregating data from 10 independent replicas. Simulation parameters: $N = 4000$, $K = 1200$, $g_0 = 5$, and $h_{\text{ext}} = 0.10$. 47

4.2 (a) Spike-triggered average input STA(τ) for $q = 0.0$ (blue), $q = 0.25$ (magenta) and $q = 0.5$ (green). In the inset of (a) we compare the STA obtained from the network simulations (grey), with a single neuron's dynamics under the diffusive approximation [15] (sky blue) and subject to Poissonian shot noise (orange). (b) Firing rates of the neurons versus the time averaged (mean) input currents for different levels of symmetry in the network $q = 0.0$ (blue), $q = 0.25$ (magenta), $q = 0.5$ (green); the Population Frequency-Input curves are shown in the inset and obtained by fitting the logistic function to the raw data (details in [116]). (c) Cumulative distribution functions (CDFs) of the mean input currents. The curves reported in (a) were obtained by averaging over 200,000 spike events, while data in (b) and (c) has been obtained by averaging over a time interval of 250 seconds. Same parameters used as in Fig.4.1 48

4.3 The autocorrelations are shown as a function of the time lag for different levels q of symmetry in the synaptic connections: $q = 0.0$ (blue), $q = 0.25$ (magenta), $q = 0.5$ (green), $q = 0.8$ (orange) and $q = 0.9$ (red). The inset shows a zoomed-in view for $q = 0.9$, where different shades of the red color denotes different initial conditions. The autocorrelations were averaged over 500 selected neurons and over 3 replicas. The same parameters as in Fig.4.1 were used. 49

4.4 (a),(c) The "instantaneous" firing rate for the same neuron and replicas, using time bins of $\Delta = 10$ seconds, for 5 different replicas for $q = 0.8$ (orange) and $q = 0.9$ (red). Different shades of the main color represent different replicas. (b),(d) Running averages of the firing rate of a single selected neuron versus time. All other parameters are the same as in Fig. 4.1. 50

4.5 (a) D as a function of time for different values of q: $q = 0$ (blue), $q = 0.5$ (green), $q = 0.7$ (yellow), $q = 0.8$ (orange), $q = 0.9$ (red), $q = 1.0$ (black). Five realizations (replicas) of the same network have been considered to estimate D. (b) Bidimensional phase diagram in the (q, g_0) plane, showing the ergodic and non-ergodic regimes in the red and blue regions, respectively. (c) Percentage of neurons with a firing rate lower than $0.01\langle\nu\rangle$ (i.e., almost silent). The black dots in (b-c) indicate the parameter values for which the reported quantities in the plane have been measured. All other parameters are fixed as in Fig. 4.1. 51

4.6 D as a function of $\tilde{T}$ for exponentially decaying synapses with different values of q and of the synaptic time constant: namely, $\tau_s = 0.02$ s (solid lines); 0.1 s (dashed lines); and 1 s (dotted lines). The colors refer to $q = 0$ (blue), $q = 0.5$ (green), $q = 0.7$ (yellow), $q = 0.8$ (orange), $q = 0.9$ (red), and $q = 1.0$ (black). These results were obtained using five replicas; other parameters are fixed as in Fig. 4.1 53
4.7 Trajectories in a 3D neural space defined by the total synaptic input of three random neurons; each point corresponds to $(h_1(\tilde{T}), h_2(\tilde{T}), h_3(\tilde{T}))$ at the same time. The different colors represent the five different replicas displayed. The upper row corresponds to instantaneous synapses with $q = 0.8$, while the other two refer to $\tau_s = 1$ s and $q = 0.8$ (middle row) and $q = 0$ (bottom row). The same parameters as in Fig.4.1 were used. 54
4.8 Ergodic to non-ergodic transition as a function of network connectivity and coupling strength. Phase boundary between the ergodic and non-ergodic regimes in networks of size N = 2000 (blue) and N = 4000 (red), shown in the (K, g_0) plane. Below the curves, network activity is ergodic: $D(T)$ eventually decays as $1/T$. Above the curves, activity becomes non-ergodic, $D(T)$ saturates for the entirety of the simulation ($1O^4$ s). The critical coupling decreases with increasing connectivity and saturates for large K, indicating a mean-field limit. The boundary also shifts downward with N, showing that larger networks enter the non-ergodic regime at weaker coupling strengths. 55

5.1 Population firing rates $\nu(t)$ versus time for $i_0 = 0.00055$: $K = 10$ (a) and $K = 210$ (b); $i_0 = 0.00033$: $K = 100$ (c) and $i_0 = 0.00027$ and $K = 60$ (d). The black lines represent network simulations with $N = 80\,000$ neurons, the violet lines to Langevin simulations with shot noise [Eq. (5.7)] and the red lines to Langevin simulations obtained within the DA [Eq. (5.9)] with $N = 20\,000$ (a, b) and $N = 80\,000$ (c, d). The solid turquoise lines denote the results of the CMF approach [Eq. (5.17) and (5.23)]. All data are for $g_0 = 1$. Details on the integration of the Langevin equations are reported in Appendix B.1. 61
5.2 Population firing rates $\nu(t)$ versus time for $i_0 = 0.02$, $K = 200$ (a) and $i_0 = 0.006$, $K = 400$ (b). The black circles refer to network simulations with $N = 80\,000$ (a) and $N = 20\,000$ (b); the violet (red) solid lines to integration of the continuity equation (5.10) [FPE (5.12)]. The green solid lines denote the results of the integration of the GFPE including third-order terms (5.13). All data are for $g_0 = 1$; the numerical integration of the partial differential equations has been performed by employing time splitting pseudo-spectral methods with a time step $\Delta t = 10^{-4}$ ms and with 128–512 Fourier modes (for more details see Appendix B.2). 63
5.3 Relative error in the estimation of the firing rate ν for a stationary situation (asynchronous dynamics) computed with (5.17)–(5.23) plotted versus the in-degree K for $M = 10$ (black line), 20 (red line) and 40 (green line). The reference firing rate was estimated by employing $M = 80$, and it is shown in rescaled units as a blue line. Parameters: $(i_0, g_0) = (0.006, 1)$. 66
5.4 Spectrum of the eigenvalues $\{\lambda_i\}$ for a stationary solution of the system (5.17,5.23) for $(i_0/g_0^2, K) = (0.02, 400)$ (a) and $(0.00055, 10)$ (b). An enlargement is reported in the inset in (b). Black circles represent the CMF, the red squares the DA and the green plus signs are for the D3A. 69

5.5 (a) Phase diagram for the QIF network in the plane $(i_0/g_0^2, K)$: the black (blue) solid line is the supercritical HB line obtained within the DA (D3A); the orange solid (dashed) line is the super- (sub-) critical HB line given by the CMF; the symbols refer to numerical estimations of the HBs and SNBs. The green (violet) circles denote HBs obtained by performing quasiadiabatic simulations by varying K (i_0) for constant i_0 (K) values; the cyan stars indicate SNBs. The dimension of symbols takes into account for the error bar in the transition point evaluation. The vertical red dotted line is the critical value defined in [157] within the DA for the emergence of fluctuation-driven balanced asynchronous dynamics (for more details see the text). (b) The coefficient Re C_3 in rescaled units at the critical points $K = K_{cr}$ versus i_0/g_0^2: CMF (orange solid line), DA (black line), and D3A (blue line). In all simulations we set $g_0 = 1$. 72
5.6 Average order parameter χ_A versus K (a) and versus the system size N (b) for $K = 10$ (black circles), $K = 60$ (blue circles) and $K = 210$ (green circles). In (a) the vertical magenta lines denote the HBs obtained within the CMF approach. In (b) the dotted lines are a guide for the eye, while the red dashed line denotes a power-law decay $\propto N^{-1/2}$. The values of χ_A have been averaged over 5–20 network realizations for a time interval $t_E = 20$–30 s following a transient of $t_T = 20 - 30$ s. (c-d) Firing rates $\nu(t)$ versus time t for $K = 10$ (black line) and $K = 60$ (blue line) in (c) and $K = 210$ (green line) in (d). The data in (a) refer to quasiadiabatic simulations for fixed i_0 obtained by increasing (decreasing) K in steps $\Delta K = 10 - 20$. All are for $i_0 = 0.00055$ and $g_0 = 1$; the simulations in (a), (c) and (d) concern networks of size $N = 80\,000$. 73
5.7 (a) Average order parameter χ_A versus i_0 for $K = 100$. The blue dashed line in (a) denotes the subcritical HB given by the CMF and the magenta dot-dashed line: numerically estimated SNB. In (b-c) the population firing rates $\nu(t)$ versus time are reported for the states indicated by the corresponding coloured filled circles; the results for the CMF are also shown as green solid lines. The data in (a) refer to quasiadiabatic simulations for fixed in-degree obtained by increasing (decreasing) i_0 in steps $\Delta i_0 = 0.00003$. The values of χ_A in (a) have been averaged over five network realizations for $t_E = 30$ s following a transient of $t_T = 20$ s. For all data $N = 80\,000$ and $g_0 = 1$. 74
5.8 (a,c) Average order parameter χ_A versus i_0 for different system sizes: $N = 10\,000$ (black circles), 20 000 (red circles), 40000 (green circles) and 80000 (cyan circles). The values of χ_A have been averaged over 5-20 network realizations for a time interval $t_E = 20 - 30$ s following a transient of $t_T = 20 - 30$ s. (b,d) Order parameter $\langle \chi \rangle$ for a single network realization multiplied by $\sqrt{N}$ versus i_0 for different network sizes. The sizes are identified by the same symbols as in panel (a) apart $N = 160000$ (blue circles). The parameter χ has been averaged in time for a time interval $t_E = 20$ s following a transient of $t_T = 60$ s and refers to a single network realization. The magenta dash-dotted line in (a) and (b) is the SNB numerically estimated via finite-size scaling analysis of χ_A, while the blue dashed line in (c-d) is the subcritical HB obtained from the CMF approach. All data refer to quasiadiabatic simulations of QIF networks with $g_0 = 1$ for fixed in-degree $K = 100$ by varying i_0: the data in (a) and (b) (in (c) and (d)) have been obtained by increasing (decreasing) i_0 in steps $\Delta i_0 = 0.00003$. 76

5.9 (a) Frequency f^H of the GOs at the HB versus i_0/g_0^2: symbols are simulations for $N = 20\,000$ and the solid line is the CMF result. (b) Frequency f_G of the GOs as a function of the parameter β, where $i_0 = \beta \times 0.01$, $g_0 = \sqrt{\beta}$, $K = 200$. Circles are network simulation data with $N = 20\,000$ and the red dashed line represents the curve $\nu_{GO} = 11\sqrt{\beta}$ Hz. The corresponding population averaged coefficients of variation CVs are shown above the two panels with the same symbols employed to denote simulation data. The vertical red dotted line shown in the upper part of panel (a) is the critical value defined in [157] within the DA for the emergence of fluctuation-driven balanced asynchronous dynamics (for more details see the text). All data have been obtained by considering a time interval $t_E = 100$ s, after discarding a transient of $t_T = 20$ s. In (a) we set $g_0 = 1$. 78
5.10 Raster plots of 5000 neurons for $K = 10$ (a) and $K = 250$ (b). In both cases the firing times of four neurons are evidenced by coloured circles. Parameters $g_0 = 1$, $i_0 = 0.00055$, and $N = 20\,000$. 79
5.11 (a) R_G versus K in the lower panel, while in the upper panel is reported the population averaged coefficients of variation CVs versus K. The green dashed lines refer to the HBs found within the CMF: GOs are expected for $K \leq 28$ and $K \geq 230$ in this case. (b) f_G versus K, the blue solid lines denote ν_0. Parameters $g_0 = 1$, $i_0 = 0.00055$, and $N = 40\,000$ for the empty black circles, $g_0 = 20$, $i_0 = 0.22$, and $N = 20\,000$ for the red stars. 80
5.12 (a, b) Effective input currents $A(t)$ versus time: black lines (orange dots) refer to CMF (network simulations) results. (c, d) Membrane potential evolution in time: black lines (other colors) refer to $V_0(t)$ (single-neuron dynamics). Data correspond to $i_0/g_0^2 = 0.00055$ (with $g_0 = 20$) and to $K = 10$ (a, c), $K = 210$ (b, d), network simulations realised for $N = 80\,000$ 80
5.13 (a) Effective input currents $A(t)$ versus time : black line ($K = 10$), red line ($K = 60$), blue line ($K = 100$), and green line $K = 250$. (b) Population firing rates $\nu(t)$ versus time the panels from bottom to top are for $K = 10$, $K = 60$, $K = 100$ and $K = 250$. Solid lines are CMF results obtained via the integration of Eq. (5.10); black symbols denote network simulation for $N = 80\,000$. Data correspond to $i_0/g_0^2 = 0.00027$ (with $g_0 = 20$). 81

A.1 In- and out-degree distributions for varying reciprocity q. $N = 3000$, $K = 100$. . 92
A.2 (a) The population averaged CV (a) and order parameter χ (b) as a function of q and for different synaptic strengths. $N = 3000$, $K = 100$. 92
A.3 (a) Probability density functions of the firing rate, the inset shows the distribution for $q = 0.99$ in a semi-logarithmic scale. (b) The population averaged firing rate as a function of q. (c) Raster plots for different values of q. (d) The distribution of the coefficient of variation of individual neurons. Again, the inset shows the distribution when $q = 0.99$. $N = 3000$, $K = 100$, $g_0 = 5$. In the distributions we have combined data from 25 realizations (5 networks and 5 replicas per network). 93
A.4 Distance indicator in highly symmetric networks, $q = 0.99$, with homogeneous synaptic couplings. $N = 3000$, $K = 100$. The data have been obtained by considering 5 different replicas for each network realization, i.e. by averaging over 20 unique pairs of replicas for each network, and then by averaging over 5 different network realizations. In total this makes 100 unique pairs. 93
A.5 (a) $D(T)$ for different level of symmetry, 5 networks with 5 to 45 replicas per network. (b) Overlap distributions, using 45 replicas. (c) The maximum value of the overlaps as a function of q. $N = 3000$, $K = 100$, $g_0 = 5$. 94

A.6 Distribution of the time averaged input currents of individual neurons, for different symmetry levels of the network. In the inset we show the standard deviation of the distributions. $N = 3000$, $K = 100$, $g_0 = 4$. 95
A.7 In- (solid lines) and out-degree (dashed lines) distributions of nodes in the network, for different levels of symmetry. 96
A.8 The coefficient of variation (a) and the order parameter χ (b) as a function of q for different synaptic strength. $N = 3000$, $K = 100$. 96
A.9 (a) Firing rate distribution for different levels of symmetry in the network. 2 networks and 50 replicas of each. The inset (b) shows the population averaged firing rate as a function of q, the error bars represent the standard deviation. (c) The 95th percentile as a function of q. (d) Distribution of the coefficient of variation of individual neurons firing rate. Data aggregated from 5 networks using 3–5 realisations of each. The insets show the firing activity for different levels of symmetry. We used the following parameters: $N = 3000$, $K = 100$ and $g_0 = 5$. 97
A.10 (a) The distance $D(t)$ as a function of time in fully symmetric networks, for different synaptic couplings strength. (b) Fixing the synaptic couplings to $g_0 = 5$, we vary the level of symmetry q in the connectivity matrix. (c) The distribution of the overlaps Q for $g_0 = 5$ and different symmetry levels. (d) The standard deviation of the overlaps distributions as a function of the symmetry. 98
A.11 Left: distribution of the overlaps Q between different replicas for different levels of symmetry q and different synaptic couplings. Right: the absolute maximum value of the overlaps. 100 replicas of a single network with $N = 3000$, $K = 100$. 99
A.12 (a) Firing rate distribution for different levels of symmetry in the network. The inset (b) shows the population averaged firing rate as a function of q, the error bars represent the standard deviation. (c) The 95th percentile as a function of q. (d) Distribution of the coefficient of variation of individual neurons firing rate. The insets show the firing activity for different levels of symmetry. We used the following parameters: $N = 3000$, $K = 100$ and $g_0 = 5$, data aggregated from 4 networks and 45 replicas of each. 100
A.13 Left: effect of the width A of the synaptic strength distribution on the average distance $D(t)$ between replicas. The black dashed line show the decay of $1/T$. Right: Effect of the mean synaptic strength g_0 on the average distance $D(t)$ between replicas. Solid lines represent simulations with a fully symmetric network ($q = 1$), while dashed lines are for a fully random network ($q = 0$). In both cases synaptic weights were uniformly distributed $g_{ij} \sim \mathcal{U}(g_0, A)$, 5 replicas of the same network were used to compute the distances, other parameters were set to $N = 3000$, $K = 100$, $\eta = 0.1$. 100

B.1 Population firing rates $\nu(t)$ versus time for exponentially decaying PSPs. The black line refers to network simulations with $N = 20\,000$, and the red (violet) line to Langevin simulations for diffusive (shot) noise with $N = 20\,000$ uncoupled neurons. The data are from QIF networks with exponentially decaying PSPs (B.24) with $K = 200$, $i_0 = 0.16$, $g_0 = 4$, and $\tau_s = 0.1\tau_m$. 106